Department of Electrical and Electronic Engineering
Communication Research Group

Design and Measurement of mm-wave Dielectric Resonator Antennas with Improved Performance

By:

Meshari D. Alanazi

Department of Electronic and Electrical Engineering
University of Sheffield

A thesis submitted in partial fulfilment of the requirements for the degree of
Doctor of Philosophy

September 2022

Dedicated to:

To my parents and grandmother.

To my lovely family, my son **Mazen** and my daughter **Yafa.**

To my brothers and sisters.

Acknowledgements

First and foremost, I would like to express my sincere gratitude to Dr Salam Khamas for his helpful guidance and invaluable supervision throughout my PhD study. His helpful advice throughout my PhD has significantly contributed to the completion of this thesis. Moreover, his numerous suggestions and feedback during the research works are gratefully praised.

I would also like to give special thanks to Dr Gavin and Mr Pater for helping me during my work at the Clean Room facility. Additionally, many thanks to Mr Steven for his kind assistance and support during the lab experiments, and to Mr Mario and Mr Andy for their kind support at the workshops. Their help is highly appreciated.

Last but not least, I would like to thank my lovely family for their deepest love and unconditional support all these years.

Publications

Journal articles

[1] Alanazi, M.D.; Khamas, S.K. A Compact Dual Band MIMO Dielectric Resonator Antenna with Improved Performance for mm-Wave Applications. *Sensors* **2022**, *22*, 5056.

[2] Alanazi, M.D.; Khamas, S.K. Wideband mm-Wave Hemispherical Dielectric Resonator Antenna with Simple Alignment and Assembly Procedures. *Electronics* **2022**, *11*, 2917.

[3] Alanazi MD, Khama S. Dual-band circularly polarized cylindrical dielectric resonator antenna for millimeter-wave applications. InInternational Journal of Simulation: Systems, Science and Technology **2022** May 14 (Vol. 23, No. 2). UK Simulation Society.

[4] Alanazi, M.D.; Khamas, S.K. Wideband Circularly Polarized Millimeter Wave Hemispherical Dielectric Resonator Antenna. *Micromachines* **2023**, *14*, 436.

[5] Alanazi, M.D.; Khamas, S.K. A Review of Dielectric Resonator Antenna at Mm-Wave band. *Eng* **2023** (Accepted)

Conference proceedings papers

[1] Alanazi MD, Khamas SK. High gain on-chip hemispherical dielectric resonator antenna for 60 GHz applications. In2020 International Workshop on Antenna Technology (iWAT) 2020 Feb 25 (pp. 1-4). IEEE.

[2] Alanazi MD, Khamas SK. Dual-Band On-Chip Rectangular Resonator Antenna for Millimetre Wave Application. In2021 International Wireless Communications and Mobile Computing (IWCMC) 2021 Jun 28 (pp. 715-717). IEEE.

[3] Alanazi MD, Khamas SK. On-Chip Multiband MIMO Dielectric Resonator Antenna for MillimeterWave Applications. In2021 30th Wireless and Optical Communications Conference (WOCC) 2021 Oct 7 (pp. 174-177). IEEE.

[4] Alanazi MD, Khamas SK. Circularly polarized on chip dielectric resonator antenna at 60 GHz. In2022 International Workshop on Antenna Technology (iWAT) 2022 May 16 (pp. 118-120). IEEE.

List of Abbreviations

DRA	Dielectric Resonator Antenna
Mm wave	Millimetre-Waves
LF	Lower Frequency Bands
5G	5th Generation
IoT	Internet Of Things
HDRA	Hemispherical Dielectric Resonator Antenna
RDRA	Rectangular Dielectric Resonator Antenna
CDRA	Cylindrical Dielectric Resonator Antenna
RHCP	Right Hand Circular Polarization
LHCP	Left Hand Circular Polarization
LDRA	Federal Communications Commission
DWM	Dielectric Waveguide Model
CST MWS	Computer Simulation Technology Microwave Studio
SIW	Surface Integrated Waveguide
CPW	Coplanar Waveguide
BW	Bandwidth
AR	Axial Ratio
TE	Transfer Electric
TM	Transfer Magnetic
HE	Hybrid Electric
λ_0	Wavelength
λ_g	Guide Wavelength
ε_r	Dielectric Constant

Abstract

Dielectric Resonator Antennas (DRAs) have been extensively studied over the past four decades due to their attractive features, such as a compact structure, high radiation frequency, design flexibility, lightweight, and high gain. These advantages make DRAs a preferred choice over other 1-D and 2-D antennas. With the increasing demand for higher bandwidth in 5G communication systems, the mm-wave band has proven capable of providing wider bandwidth, operating on frequencies between 30 GHz and 300 GHz. This thesis aims to provide a novel approach to enhance radiation efficiency, gain, impedance, circular polarization (CP) bandwidth, minimize mutual coupling, and reduce errors caused by misalignment. Furthermore, this thesis investigates the use of hemispherical DRAs, which adds to the existing literature while highlighting their limitations.

A wideband hemispherical DRA with an enhanced gain is proposed at a frequency band of 20 to 28 GHz. The precise alignment and assembly of the hemispherical DRA have been implemented using three novel approaches, the first is based on highlighting the DRA position on the ground plane, the second involves creating a groove in the ground plane in which the DRA is placed, and the third is based on the 3D printing of the DRA on a perforated substrate. A CP hemispherical DRA is usually achieved with a narrow CP bandwidth since the DRA offers zero degree of freedom, which limits the options of designing an antenna with a reasonably wide axial ratio bandwidth. As a result of the numerous limitations that could occur, a novel approach is proposed in this work to achieve a wider CP bandwidth from a hemispherical DRA by incorporating an additional dielectric substrate between the DRA and the ground plane that accommodates cross-slot feeding. Furthermore, a compact multiple-input-multiple-output (MIMO) DRA is proposed with reduced mutual coupling between the elements. In the proposed design, two rectangular DRAs have been placed on the opposite sides of a Rogers substrate, and each is fed using a coplanar waveguide (CPW) feed with slots etched in a dedicated metal ground plane that is located under each DRA. Also, the fixing and precise alignment of a 60 GHz DRA represent a stronger challenge compared to that at the lower 28 GHz band. A 3D-printed integrated DRA-substrate configuration has been utilised with a separate feeding substrate that has been attached to the lower side of the configuration. The printed antenna has been fabricated using Alumina, which has the same dielectric constant as the Gallium Nitride.

The novel contributions of this study include designing mm-wave DRAs with improved performance and measuring them whilst addressing solutions to several challenges, such as DRA assembly and alignment for rapid prototyping. Also, the study determined methodologies that result in higher gain, enhanced circular polarization as well as impedance bandwidths for compact MIMO DRAs and DRAs that operate at 60 GHz. For all the proposed designs, the reflection coefficient, radiation pattern, axial ratio and gain have been measured to verify the simulations that have been carried out using the CST microwave studio. Closed agreement has been achieved between simulated and measured results.

Contents

List of figures

List of tables

Chapter 1

Introduction

1.1 Millimetre wave communications

Wireless communications have been extensively focusing on lower frequency bands (LF) over the frequency ranges of 300 kHz to 3 GHz. As a result of the substantial increment in the number of mobile devices and customers, the bandwidth of the microwave band is becoming scarce [1]. Consequently, mobile users have to face problems in achieving a very high speed, low latency, and good coverage, ultimately reducing the quality of service [2]. On the other hand, wide bandwidths at higher frequencies offer transmission rates of several gigabits per second even in wide scale establishments [3].

The 5th generation network (5G) is the most recent commercially available wireless communications system. Even though its intended objective was to facilitate the mobile users' communication, it is evident that massive architectures, like the Internet of Things (IoT) and institutional systems, have also been supported. However, terminal devices that are integrated to 5G networks have increased the access demands for the limited spectrum below 6 GHz.

In this context, it is essential to explore operating bandwidths at higher frequencies [4]. For example, millimeter wave (mm-wave) frequency range has been identified as a potential band [5]. A white paper developed by the MiWaveS, a project that was established in 2015 and funded by the European Union, suggested the development of technologies to access mm wave wireless and backhaul [6]. In 2016, the Federal Communications Commission (FCC) of the United States introduced four frequency bands to develop 5G mm-wave communication systems and to research further. They were deployed by US vendors in the field of communications. Further, acquiring a key position in the global mm wave mobile communication technology was attempted [7]. Contemporarily, US wireless communications operators such as Verizon, T-Mobile and AT&T acquired the license to use the mm-wave spectrum. Particularly, Verizon has dynamically promoted the indoor placement of mm-wave systems. In China, ministries of Industry and Information Technology, Science and Technology as well as the National Development and Reform Commission cooperatively worked to launch 5G band of IMT-2020. The team is responsible to study issues related to the 5G spectrum [8]. China provided a commercial license for 5G in 2019 [9] enabling its telecommunications operators to officially introduce 5G-related services.

On the other hand, mm-wave frequencies are associated with limitations such as the short-range communications as well as maintaining line of sight. Main factors that affect the transmission range are short wavelengths (1-10mm) and high atmospheric attenuation caused by fog, rain, or moisture as illustrated in Figure 1.1. This has triggered a significant interest in the design of high gain antennas and arrays, which improve the effective radiated power over an enhanced the transmission range.

In comparison to other communication systems that operate at lower frequencies, the mm-wave communication systems have a higher propagation loss. At the 60 GHz band, with directional antennas, the multi-path is most obvious because of the small-scale propagation effects [10]. In addition to the high-data rates that can be attained at 60 GHz, the energy propagation at this frequency has characteristics that make it suitable for use to attain high security, high immunity to interference, and frequency re-use. The mm-wave frequencies that range between 28 GHz and 38 GHz are suitable for use at 5G and Beyond-5G communication systems. Therefore, it has been proposed by previous studies to employ 28 GHz and 38 GHz mm-wave frequencies in Hyperconnected F-RANs. Furthermore, the use of mm-wave at 28 GHz, 38 GHz, and 71-76 GHz is useful because it can operate at the 5G enhance local area (eLA). It is evident that the eLA system can attain high data rate in excess and edge, that would be 10 Gbps and more than 100 Mbps, respectively[11].

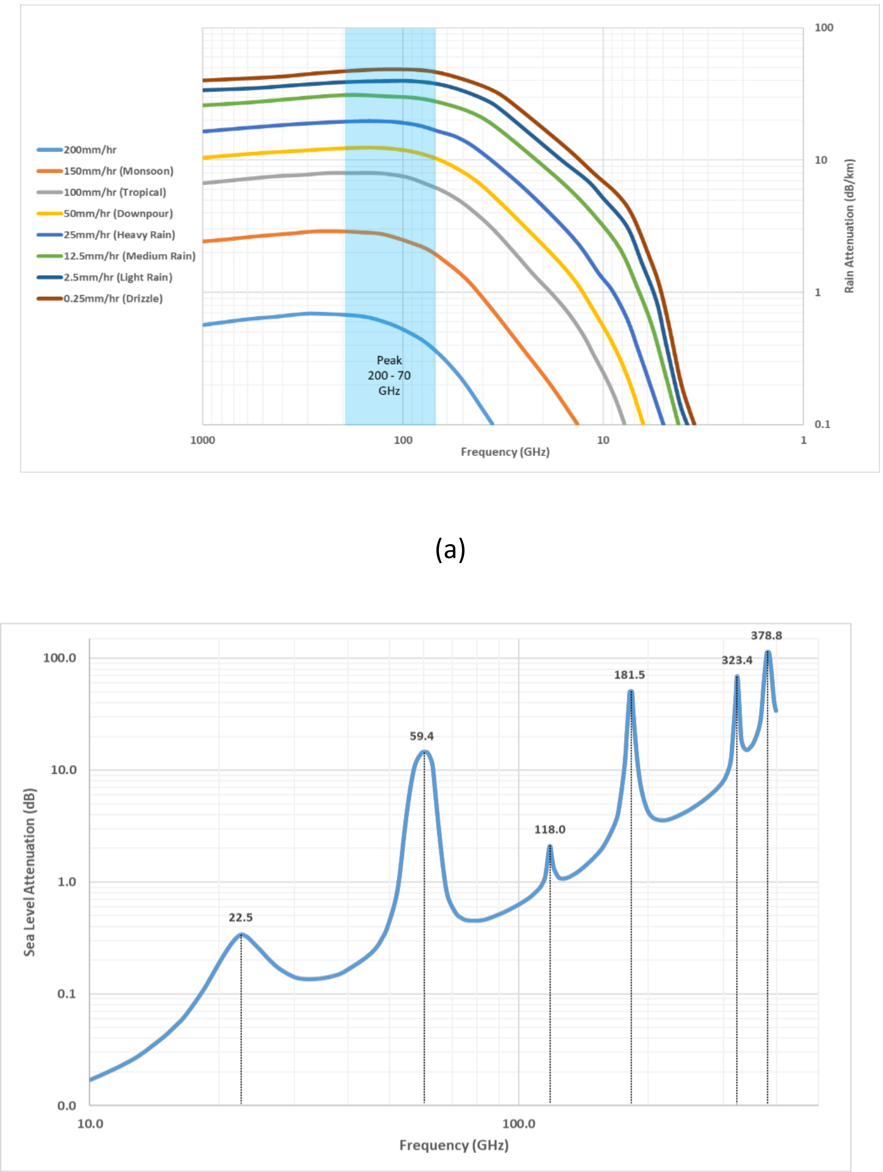

(a)

(b)

Figure 1.1: (a) Rain attenuation, (b) Atmospheric and molecular absorption [12].

1.2 Dielectric Resonator Antenna

In 1939, R. D. Richtmyer, who studied the resonant properties of dielectric materials in different shapes such as spherical, ring, and toroidal, predicted the concept of generating electromagnetic radiation from such dielectric geometries [13]. Nevertheless, such a concept was unpopular among scientists as low-loss dielectric materials were unavailable. Later, dielectric resonators (DRs) of cylindrical, rectangular, and hemispherical geometries have been introduced using materials with low losses and high permittivity that have received considerable popularity [14]. Due to the advancements in the ceramic industry and with the accessibility to low loss dielectric materials, in the early 1960s, the use of dielectric resonators was initiated to provide a substitute for metallic microwave resonators. Hence, the preliminary research on dielectric resonators was focused on their electronics applications, particularly in oscillators and filters [15, 16]. In 1962, Okaya and Barash reported that rutile crystals with low dielectric losses can provide an unloaded quality factor (Q) greater than that of cavity resonators with metal walls [17]. Gastine et al. discovered the radiation Q-factor of isolated spherical dielectric resonators in 1967 [18]. Many research studies have been conducted on the investigation of the electromagnetic field distribution of modes and nomenclature in dielectric resonators with a high dielectric constant [19-22]. Accordingly, during this period, primary attention was given to explore the potential of using dielectric resonators as circuit elements and their properties were explored for suitability in such applications.

With the aforementioned objectives, dielectric resonators were covered by a metallic cavity to keep the Q-factor high and hence to reduce radiation leaks. However, when the metallic cover is removed and the dielectric constant is reduced, dielectric resonators can act as effective radiators of electromagnetic waves. Therefore, scientists developed dielectric resonator antennas (DRAs) based on this concept and this was the transition period of dielectric resonators from circuit components to radiating elements. The transition was based on the fact that the electromagnetic fields could leak out of the cavity when the metallic enclosure is removed.

Accordingly, dielectric resonators can radiate when their permittivity is lowered, and the metallic surrounding is removed. The systematic study on the use of dielectric resonators as antenna elements began in early 1980s. Long, McAllister, and Shen [22-24] studied the characteristics of dielectric resonator antennas with cylindrical, hemispherical, and rectangular shapes and calculated their radiation pattern theoretically. As per the findings of the aforementioned research studies, DRAs exhibit better performance than traditional metallic antennas that have lower radiation efficiencies and gain. Since then, numerous research studies have been conducted on simple dielectric resonator shapes as well as the possible resonance modes. In the 1990s, numerical and analytical methods were applied to determine the input impedance, resonance frequency, and radiated Q-factor of DRAs of different shapes. In mid to late 1990s, various feeding mechanisms such as aperture coupling, probe feeding, and microstrip coupling were focused on exciting dielectric resonators [25] as illustrated in Figure 1.2. Since 2000, and with availability of 3D commercial electromagnetic simulators, research studies on DRAs have been directed towards the design of DRAs with improved characteristics, such as wideband, dual band, circular polarisation, high gain, re-configurability as well as array structures. In addition, DRAs with complex geometries and improved performances have been proposed, such as stair-shaped and trapezoidal DRAs, as well as other shapes [26]. In addition, to achieve high electromagnetic coupling between the source and resonator, the DRA must be made from high dielectric constant material. Conversely, the DRAs must be made from low dielectric constant material to operate over a wide bandwidth.

As per the findings of the aforementioned research studies, DRAs exhibit better performance than traditional metallic antennas that have lower radiation efficiencies and gain. However, there are various limitations to the use of DRAs when compared to traditional metallic antennas, as the DRAs need to be more aligned and fixtured and may have a higher profile, which could limit their use.

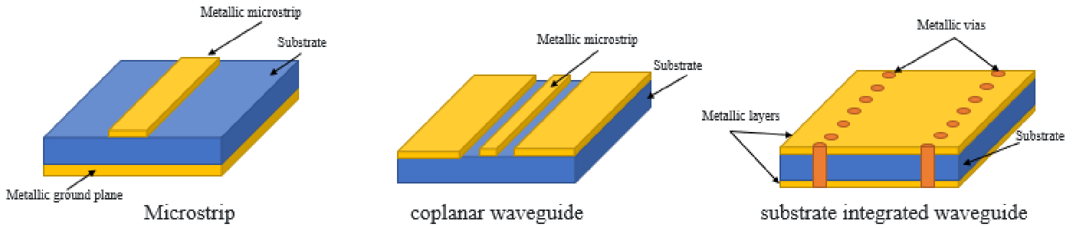

Figure 1.2: Feeding methods for the dielectric resonator antenna.

1.3 Mm-wave dielectric resonator antennas

There are a couple of modes in which DRAs operate, namely TE and TM. Each one of them has a fundamental and high-order mode. In general, fundamental modes operate at wide bandwidths as well as low resonant frequencies. However, high-order modes operate with narrow bandwidths as well as high operating frequencies.

The hemispherical, cylindrical, and rectangular DRAs are the basic conventional shapes that are often used in studies. For the hemispherical DRAs, two fundamental modes are often used, namely the TE_{111} mode as well as the TM_{101} mode. In each one of the modes, three subscript numbers are present, and they represent the field change in the radial, azimuthal, and elevation directions of the spherical coordinate system, respectively. The operating modes of cylindrical DRAs are relatively different from those of hemispherical DRAs. The two fundamental modes of the cylindrical DRAs are $HEM_{11\delta}$ mode as well as $HEM_{01\delta}$ mode. Unlike the hemispherical DRAs, the three subscripts represent the azimuthal, radial, and z-axial directions, respectively, of a cylindrical coordinate. The value of δ ranges from 0 to 1. As for the rectangular DRA, it has only two fundamental modes, which are $TE_{\delta 11}$ and $TE_{1\delta 1}$ mode. The two modes only different in the direction. The three subscripts in it refer to the field change in the x, y, and z-axis, respectively, of a Cartesian coordinate system. Figure 1.3 illustrates the field distributions of fundamental modes in Hemispherical, Cylindrical and Rectangular DRA.

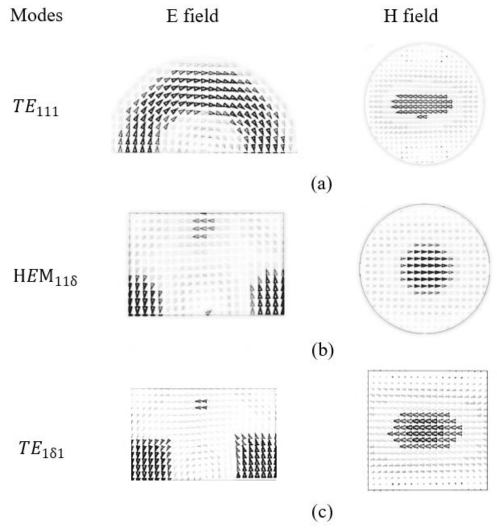

Figure 1.3: Field Distributions of Fundamental Modes in (a) Hemispherical (b) Cylindrical (c) Rectangular DRAs.

Various studies investigated the difference in performance between DRAs and microstrip antennas (MSAs) and concluded that the DRA is more beneficial on many aspects in particular at higher frequencies, where ohmic losses are more significant [27]. After analysis of the data of [27], it can be concluded that there are clear differences in the performance of both designs in key areas. Firstly, the DRA produced a remarkable increase in bandwidth compared to the MSA. The results also demonstrated a clear increase of ~14% in the radiation efficiency when the DRA is utilised owing to the absence of ohmic losses. Furthermore, using a higher-order DRA resonance modes has several benefits. For example, the higher-order modes transverse electric, TE, modes; TE_{115} and TE_{119} have excited to design and fabricate larger dimensions of DRA at 24 GHz in order to minimise the fabrication errors and tolerance [28]. Compared to a DRA operating in the fundamental resonance mode, TE_{111}, the results demonstrated DRA size increments by factors of 7 and 14.4 times when the TE_{115} and TE_{119} modes are excited. This helped the authors of [28] to confirm that electrically large antennas (ELAs) offer higher tolerance to the fabrication errors. Additionally, the DRA has achieved at an impedance bandwidth of 5.75% and gain of 6 dBi. This study is focused on three of frequency bands, namely: K, Ka, and V bands that correspond to the following frequency ranges 18-27 GHz, 27-40 GHz, and 40-75 GHz, respectively.

A wide-band high-gain three-layer mm-wave hemispherical DRA has been proposed in [29] with impedance bandwidth of 35.8% and maximum gain of 9.5 dBi as well as a radiation efficiency of 90%. One of the limitations of such a technique is the complexity in the assembly of the three dielectric layers and the higher cost. Likewise, the gain of a multilayer DRA has been increased by introducing air holes in the antenna [30]. The study was conducted using a low-profile hybrid multi-permittivity DRA with perforated structure for mm-wave applications. To create the air holes, the DRA should be drilled to enhance the bandwidth. However, this is not possible with physically small DRAs because it would be difficult to maintain the same size and space between the air holes. In total, 21 identical cylindrical holes were created inside the dielectric resonator. The operating bandwidth has been increased by 27.4%, i.e., from 48.4% to 75.8% without any change in the achieved gain of 5.65 dBi.

Another approach to enhance the gain was implemented by using a DRA with plastic-based conical horn for mm-wave applications [31]. The antenna has been excited using a slot-coupled micro-strip line with achieved bandwidth, radiation efficiency and gain of 16.6%, 94%, and 11.3 dBi, respectively. It is worth it to mention that without the plastic-based conical horn, the DRA gain is 8 dBi. Nevertheless, the resultant antenna configuration is complex. A different experiment that aims to increase the DRA gain has been reported in [32], whereby the high-permittivity DRA has been placed over an H-slot on-chip antenna with an impedance bandwidth of 4.15% at 35 GHz. The measured gain and efficiency after the addition of the DRA on top of the chip are 1 dBi and 48%, respectively.

The surface integrated waveguide (SIW) technology has been utilised to maximize the efficiency and gain of the DRA [33]. For example, a cylindrical millimetre-wave DRA has been fabricated using the Low Temperature Co-fired Ceramics (LTCC) process to increase the gain and the efficiency [34]. Instead of using microstrip feed line, the slot has been used in a SIW, which resulted in a significant decrease in the back lobe radiation levels. This technique achieved impedance bandwidth of 2.5%, a gain of 10.8 dBi, and efficiency of 87%. Another study used PCB process to fabricate a low-profile substrate integrated dielectric resonator antenna (SIDRA) with bandwidth of 33-36 GHz, gain of 5.5 dBi and an efficiency of 94% upon being fed by SIW [33].

1.4 Dielectric resonator antennas arrays

In order to increase the gain, several studies have been conducted using multiple elements to design DRA arrays. Notably, [35-38] have used SIW as a feed network. Abdel-Wahab et al. [35] has conducted a research that would improve the radiation efficiency using N-element linear arrays based on two different feeding slot configurations. Likewise, in another study, [39], that was conducted by the same author of [35], an array of four DRA elements has been designed using SIW feeding network at 33.9 GHz and achieved gain of 11.70 dBi, a bandwidth if 4.7%, and an efficiency of 90%. Yet, the weakness of [35] is that it lacked a matching circuit which could have been used to improve the coupling in the SIW longitudinal slot case.

Alternatively, different structures for SIW were utilized in [36, 37]. In [36], an 8×8 rectangular 2D DRA array has been proposed using an SIW hybrid feeding network. The results of the study demonstrate gain of 22.6 dBi, bandwidth of 6.1%, and radiation efficiency of 89%. In [37], the study that involved analysis, design, and measurements of an SIW-Integrated Parasitic DRA array to minimise the metallic loss at the mm-wave band. The resulting gain increased from 11 dBi using 4 driven DRAs to 13 dBi by adding 8 parasitic DRAs. The bandwidth and the efficiency remained the same as 2.5% and 91%, respectively.

Even though SIW has also been employed in [38], the shape of the DRA is neither conventionally cylindrical nor rectangular, as it is grid-shaped. It is noteworthy to mention that this is the only paper that proposes a grid shape for the DRA a with a fabrication process that involves many steps. In another study [39], it has been demonstrated a gain enhancement of 5.6 dBi by using 8 DRA elements. The bandwidth has also been increased from 12.1% for a single element to 18.46% for the 8 elements array.

An LTCC fabricate integrated-DRA has been proposed for 5G applications [40], where sixteen cylindrical DRA elements have been utilised. An inverted micro-strip corporate feeding network has been used to feed the array and to fabricate in the same LTCC stack as resonators. To enhance the overall performance of the array and to facilitate the alignment of the individual array elements, a grooved and grounded superstrate has been used. with achieved bandwidth of 9.81%, gain of 15.68 dBi, and radiation efficiency of 88%.

Another DRA array design has been reported using directive LTCC fabricated DRA elements that operates at the HEM_{113} higher-order mode at 25.7 GHz [41]. They used an antenna array design. For an array of 1×4 elements, the achieved respective bandwidth, gain, and efficiency are 1%, 16.3 dBi and 87%. Even though [40] and [41] have mutually proposed LTCC technology to fabricate DRA arrays, different materials have been use to fabricate the DRA and substrate in [40] compared to using the same material in [41].

A high gain planar array with 8×8 elements has been proposed for mm-wave vehicular wireless communication [42], where comparison has been reported between series-parallel hybrid feed network and parallel-cascaded feed network in terms of impedance bandwidth, gain and radiation efficiency. The series-parallel hybrid has wider impedance bandwidth, higher gain and effective suppression of the sidelobes. The study also involved a comparison between the performances of patch antenna and DRA arrays where the latter has outperformed the former.

A structure of four connected rectangular ring DRA elements has been proposed at 28 GHz [43], where a glue has been utilised to reduce the air gaps between the connected DRAs and the ground plane. Also, to overcome the alignment limitations, dielectric arms have been added to the structure. However, it has been noted that the positions of the dielectric arms significantly affect the performance of the DRA in terms of the mutual coupling, radiation efficiency, and gain. The attained bandwidth, gain, efficiency are 31.6 %, 8 dB, and 86%, respectively.

1.5 V band dielectric resonator antennas

The following section presents the studies that operated at a V band frequency that ranges between 40 and 75 GHz. A high-gain hybrid DRA and the micro-strip antenna has been proposed at 60 GHz [44], that where a circular micro-strip patch has been used to feed a ring-shaped DRA placed on a thin grounded dielectric layer with low permittivity. The antenna gain has been improved upon the excitation of a higher-order mode. One of the limitations of such a study is that fact a super glue has been used to bond the driven patch and DRA. They have been fabricated separately using a complex manufacturing process. The resulting bandwidth is 15%, gain is 11.9 dBi, and the radiation efficiency is 75% [44].

A micro-machined on-chip cylindrical DRA that operates at 60 GHz has been reported using high resistivity silicon for the DRA and the feeding circuit [45]. The cylindrical DRA has been fed using a coplanar waveguide, which results in a simple and cost-effective design. The deep reactive ion etching process has been employed to etch one side of the wafer and create a cylindrical shape that has respect radius and height of 1.18 mm and 0.4 mm. The backside of the wafer has not been-etched as it acts as a substrate for the feeding structure, which has a thickness of 0.275 mm. This design results in an impedance bandwidth of 3.78%, gain of 7 dBi, and radiation efficiency of 79.35%.

A60 GHz slot-coupled rectangular DRA, with a small size of 1×1×0.6 mm^3 has been designed to attain high-efficiency monolithic integration [46]. Even though the RDRA had. The dielectric that was used to fabricate the DRA has been intended for on-chip system applications. The direct generation of the signal at the intrinsic port results in a maximized efficiency for the integrated mm-wave system. Hence, this proves that the use of intrinsic port DRAs with on-die multi-chip modules (InP MMIC) technology can result in a high efficiency with respective bandwidth and gain of 6.1% and 6 dBi. Studies [46] and [45] implemented different fabrication techniques of MMIC in [46] and micro-machine in [45]. Moreover, the shapes of the DRAs were different as well. Yet, both studies design on-chip antenna using a semiconductor material.

A compact wide-band cubic DRA for 60 GHz Miniature Hybrid Microwave Integrated Circuits (MHMIC) short-range transceivers has been report in [47]. The array's feed network consists of a rounded Wilkinson power divider that uses MHMIC technology. In contrast to the conventional T-junction power divider, the output ports of the Wilkinson power divider have a high isolation which aids in eliminating of any potential mismatch of the radiating elements. This provided an impedance bandwidth of 16%, gain of 6.5dBi, and efficiency of more than 96%. Hence, the proposed antenna is most suitable for the MHMIC fabrication process.

In [48], the authors conducted a study that aims to increase the dimensions of the DRA, the wide-band capability, and the gain performance. They proposed the use of a mm-wave rectangular DRA that would accomplish the aforementioned aims. The SIW cavity has been used as a high-pass filter. The use of the conventional backed cavity design with a 2×2 array demonstrated an impedance bandwidth of 8.7%. In contrast, the use of the stacked enlarged DRA demonstrated an improved impedance bandwidth of 15%. To increase the, a 4×4 array has been used and resulted in in a significantly higher gain of 17.2 dBi.

A template-based DRA array has been presented in [49] in which a cavities have been fabricated in acrylic templates in order to compose a monolithic polymer-based DRA array layer. The results demonstrate an impedance bandwidth of 12% and gain of 10.5 dBi. The studies, [47-49] have focused on increasing the gain through the design of 60 GHz arrays. Nevertheless, each study has utilised a different process with different number of elements. In addition, the methods employed in [48] and [49] are sophisticated and expensive compared to that in [47].

Table 1-1: Comparison between the performance of linear polarized DRAs at mm-wave, NM: not mentioned.

Ref.	DRA Shape	Frequency (GHz)	Bandwidth (%)	Gain (dBi)	Efficiency (%)	Mode
[27]	Cylindrical	36	15.6	6.9	95	NM
[28]	Rectangular	24	5.75	6	NM	TE_{119}
[29]	Hemispherical	25	35.8	9.5	90	TE_{711}
[30]	Cylindrical	20	75.8	5.65	92	HE_{11}
[31]	Cylindrical	30	16.6	11.3	94	HE_{11}
[32]	Rectangular	35	12	1	48	$TE_{11\delta}$
[33]	Rectangular	35	12	5.5	94	TE_{10}
[34]	Cylindrical	26	2.15	10.8	87	HEM_{133}
[35]	Rectangular	35	12.5	5.51	95	TE_{111}
[36]	Rectangular	35	6.1	21.5	85	TE_{111}
[37]	Rectangular	38	2.5	13	91	$TE_{11\delta}$
[38]	Grid	32	18.46	12	76	TE_{10}
[39]	Rectangular	34	4.70	11.7	90	TE_{10}
[40]	Cylindrical	28	9.81	15.68	88	$HEM_{11\delta}$

[41]	Cylindrical	24	1	16.3	87	HEM_{133}
[42]	Rectangular	26	2.18	20.5	92	TE_{111}
[43]	Rectangular	28	31.6	8	86	$TE_{3\delta 1}$
[44]	Cylindrical	60	15	11.9	75	TM_{110}
[45]	Cylindrical	60	3.78	7	79.35	$HE_{11\delta}$
[46]	Rectangular	60	6.1	6	98	TE_{111}
[47]	Rectangular	60	16	6.5	90	NM
[48]	Rectangular	67	16.4	17.2	72.3	TE_{112}
[49]	Rectangular	60	12	10.5	NM	NM

1.6 Multiple-input and multiple-output (MIMO) dielectric resonator antenna

Mutual coupling between MIMO elements can drastically affect the antenna characteristics by reducing the performance of the MIMO systems. Hence, studies have been conducted to examine the efficient approaches that can be utilised to reduce the mutual coupling between MIMO, by incorporating w metamaterials walls [50, 51] and the mutual coupling was significantly reduced.

In [50], a meta-surface shield has been used for 60 GHz MIMO systems and 1×7 elements array of split-ring resonator with respective bandwidth, gain and efficiency of 13%, 7.9 dBi, and 91%. On the other hand, a metamaterial polarization rotator wall has been used to reduce the spatial electromagnetic fields between two DRAs in a MIMO system with respective bandwidth and efficiency of 13.3% and 88% [51].

A low-mutual-coupling 60-GHz MIMO antenna system with frequency selective surface (FSS) wall to increase isolation has been reported [52]. The usage of an FSS wall resulted in an insertion loss enhancement of more than 15 dB. However, using FSS wall and slots resulted in an achievement of a better isolation, that is 30 dB. These methods demand an element spacing of more than 0.6 λ, which is relatively large and can result in a higher profile. Therefore, these methods are not applicable in the development of dense arrays.

A simple decoupling method has been used proposed to improve the isolation using metallic vias [53]. The decoupling and self-decoupled methods have been mainly focused on two-element arrays and do not provide approaches that can be applied on massive MIMO arrays with bandwidth of 7.3% and gain of 6 dBi. Similarly, another study has been conducted using a similar technique to enhance the isolation among the DRA elements with bandwidth of 4.8% and gain of 9.9 dBi [54]. It should be noted that metal vias have been used in [53], whereas metal micro-strips have been utilised in [54]. Antennas that have metallic patches as radiating elements, as evident in these studies, lead lower radiation efficiencies. This could be remedied through the use of DRAs. The efficiency has not been mentioned in these two studies because it is relatively low due to the usage of metallic patches as radiating elements.

A Ka-band frequency of 30 GHz has been designed using two arrays MIMO of eight-element linear cylindrical DRAs [55]. A passive microstrip feed network has been implemented to excite the design. Nevertheless, the achieved isolation achieved 15dB, which is considered to be low as literatures report [52]. The achieved bandwidth is 3.33% and the gain is 7dBi, and the efficiency is 80%.

In the recent study [56], a MIMO DRA has been used at 28 GHz, which has been excited using a rectangular slot at the fundamental TE_{111} resonance mode. Two simple metallic sheets have been symmetrically embedded into the DRA to minimize the mutual coupling. The attained isolation is 17 dB. The bandwidth and gain attained are 3.9% and 6 dBi, respectively. The method used to embed the metallic sheets into the DRA has not been extensively clarified in the study. This poses a limitation on the study, since the technique needs to be accurate to avoid fabrication errors that could potentially affect the performance of the antenna in future studies.

Table 1-2: Comparison between the performance of mm- wave MIMO DRAs, NM: not mentioned.

Ref.	DRA Shape	Frequency (GHz)	Bandwidth (%)	Gain (dBi)	Efficiency (%)	Mode
[50]	Cylindrical	60	13	7.9	91	NM
[51]	Cylindrical	60	13.3	NM	88	$HEM_{11\delta}$
[52]	Cylindrical	60	11.5	NM	90	NM
[53]	Rectangular	26	7.3	6.4	NM	TE_{111}
[54]	Rectangular	28	4.8	9.9	NM	TE_{311}
[55]	Cylindrical	30	3.33	7	80	$TE_{11\delta}$
[56]	Rectangular	28	3.9	6	NM	TE_{111}

1.7 Circularly polarised dielectric resonator antenna

The section below illustrates studies that have been conducted on mm-wave CP DRAs at K and Ka-bands, Section 1.7.1, as well as the V-band, Section 1.7.2. Table 1-3 compares the performance of various mm-wave CP DRAs.

1.7.1 CP dielectric resonator antenna at K and Ka bands

Conventionally, the feed structure and DRA are designed and fabricated using different dielectric materials. When mounting the DRA on the feed network, errors are expected, which would significantly affect the antenna’s performance. This is especially the case if the operation takes place in the millimetre wave band. To minimize the aforementioned errors, the integrated DRA- substrate concept has been proposed through designing the 4 DRA elements and feed network together using the same material and fabrication process. This method has been implemented in [57] with achieved bandwidth of 1.6% and gain of 13.6 dBi for the linear polarization case. On the other hand, bandwidth of 16.48% and gain of 12.7 dBi have been achieved for the CP antenna with an axial ratio bandwidth of 1.1%. One of the limitations of [57] is the fact that no attention has been paid to the element's profile.

A wide bandwidth high gain circularly polarised mm-wave rectangular dielectric resonator antenna has been reported [58], where a two-layer DRA has been utilised By adding the coat layer, a CP bandwidth of 13.75% has been achieved in conjunction with impedance bandwidth of 36.5% and gain of 12.5 dBi. However, using two different material increases the complexity and cost of the design.

A wideband circularly polarised substrate-integrated dielectric resonator antenna (CP SIDRA) has been reported with respective gain, impedance, and CP bandwidths of 8.15 dBi, 34.6% and 26.3% [59]. However, this technique is expensive and sophisticated with a relatively large size. An experiment has been conducted on a wide-band CP 2×2 DRA array with a feed that consists of sequential network and cross slots [60]. Each unit element is the rotation from the adjacent element and the results demonstrate impedance and CP bandwidths of 33.8% and 5%, respectively, with a gain of 9.5 dBi.

In [61], the authors proposed a CPDRA that would operate at 24 GHz. Remarkably, their aim was to design a larger DRA and they achieved that through operating the antenna at a higher mode of TE_{117}. A rectangular DRA and three rectangular slots make up the antenna structure, such that one of the slots is at the centre and the two other slots are equilaterally inclined with regards to the centre slot. The results illustrate that when the antenna operated at a higher mode of TE_{117}, the antenna size was increased by 61%. A phase difference was provided by the two stubs and the main microstrip feed that are used to design the modified microstrip. The study achieved an impedance bandwidth of 15.06%, a gain of 7.9dBi, and an axial ratio of 5.8% [61].

The studies above operated at a Ka-band frequency. Yet, the main difference between them is that they incorporated different structures onto or under the DR to increase the CP band. For instance, [58] and [59] both used cross-slot with unequal length. The authors [60] combined sequential network and cross slots. Nevertheless, in [57] and [61] , they incorporated different structures as they used U-metal strip patterns on the DR, and three rectangular slots with two stubs at the feed network, respectively. In addition to that, the aforementioned studies, except [58], have not mentioned the radiation efficiency due to the use of material that results in a reduction in the radiation efficiency.

Recent studies have been conducted to achieve the CP bandwidth using DRAs with different shapes, and measuring their performance in terms of the bandwidth, gain, efficiency, and axial ratio. In [62], a trapezoid DRA has been used at a frequency of 26 GHz, and the bandwidth and the axial ratio attained are equal to 26.3% and 5.2%. Yet, there have been fabrication errors that may have resulted from the angular cuts of the rectangular DRA structure into a trapezoid.

In [63], a cylindrical DRA has been used at a frequency of 26 GHz, which is excited using coaxial probe, such that the DRA is drilled. This is a complex procedure, and it has not been implemented by many studies. There needs to be a high tolerance for fabrication. To convert the LP to CP, the meta-surface is applied. The axial ratio and gain are improved significantly when the meta-surface is applied. The CP bandwidth is 26.3% and the axial ratio is 1.35%. In [64], a stacked rectangular DRA structure has been used at a dual frequency of 20 GHz and 30 GHz, which is excited using SIW feed. Two rectangular DRAs are stacked on top of each other, and a metal strip is placed on top of the second DRA to obtain CP in both frequency bands. However, this process is complicated and costly since it demands numerous steps and materials. At 20 GHz and 30 GHz, the CP bandwidth attained is equal to 6.4% and 12.8%, respectively, and the axial ratio attained is equal to 5.2% and 4.1%, respectively. It is remarkable that in the study, alignment has not been sufficiently addressed when it should have been given critical attention since the structure is complex.

1.7.2 Dielectric resonator antenna at V band

This Section presents the studies that operate at a frequency of 60 GHz. The chief difference between them is that in [65] , the researchers used a cross slot and a half mode SIW, whereas in [66], they loaded the DR with a slotted circular patch at the top. In [65], aperture-coupled cylindrical DRAs that are fed by a half-mode SIW (HMSIW) were proposed with a measured circular bandwidth of 4%. The CP bandwidth should be improved, but overall, the HMSIW served as efficient feeds for DRAs that operated in the mm-wave frequency band. This design achieved an efficiency between 80 and 92% [65]. The gain in the linear DRAs is 5.5dBi and is not mentioned for the circular DRAs. At frequencies above 40 GHz, the HMSIW has the ability to present a lower attenuation constant than a standard micro-strip line that is fed at the same substrate. The gain in the design is minutely affected by the variations of glue layer in the design of the DRAs that would operate in the mm-wave band. The impedance of the whole band can be affected by a minor increase in the thickness of the glue layer. Nonetheless, it is not practical to control the thickness of the glue. Hence, it would be useful to use another method to fix the DRAs in future replications of [65].

In [66], a CP-SIW cylindrical DRA was proposed for mm wave applications. Before the introduction of the loading patch, the impedance bandwidth was 5.7%. When the loading patch was added, CP radiation was produced, and the results show a bandwidth of 9.33% and a CP bandwidth of 1.35%. The CP bandwidth is narrow, so the researchers in [66] proposed a

2 x 2 sequential rotation feeding to enhance the CP bandwidth to 15.9% and the gain was 10.3 dBi. In addition to that, the gain was improved with the metalized vias as they can aid in the suppression of the back radiation and on the enhancement of the front radiation. The efficiency of the experiment is between 69.9% and 98.6% [66].

Table 1-3: Comparison between the performance of circular polarized DRAs at mm wave, NM: not mentioned.

Ref.	DRA Shape	Frequency (GHz)	Bandwidth (%)	Gain (dBi)	Efficiency (%)	Mode	Axial ratio bandwidth (%)
[57]	Rectangular	30	16.48	12.7	NM	$TE_{11\delta}$	1.1
[58]	Rectangular	26	36.5	12.5	90	TE_{119}	13.75
[59]	Cylindrical	25	34.6	8.15	NM	$HEM_{11\delta}$	26.3
[60]	Flower	30	33.8	9.5	NM	NM	5
[61]	Rectangular	24	15.06	7.9	NM	TE_{117}	5.8
[62]	Trapezoidal	26	26.3	3.28	NM	TE_{x21}	5.23
[63]	Cylindrical	26	26.3	6.6	NM	TE_{412}	1.35
[64]	rectangular	20/30	6.4/12.8	6.6/8.2	NM	TE_{111}	5.2/4.1
[65]	Cylindrical	60	24.2	5.5	92	$HEM_{11\delta}$	4
[66]	Cylindrical	60	11.8	11.43	84.25	$HEM_{11\delta}$	15.9

1.8 Alignment and assembly

Many studies have examined different techniques that could be used to simplify the bonding and alignment of mm-wave DRAs. The bonding and alignment of DRAs is a highly critical procedure that should be implemented in the most efficient way, as any slight inconsistency could affect the performance. This is important as the manual DRA-feed alignment can be a cumbersome and time-consuming process. Therefore, time and cost saving techniques need to be developed.

Some studies proposed double and multi-layers in an attempt to assemble the DRA and examining the benefits and limitations of these methods. For example, 8×8 DRA array has been proposed attempts to achieve precise alignment following. a strenuous procedure whereby the feeding slot would be located exactly at the centres of the 64 DRAs [42]. This study demonstrates that alignment and assembly are two critical factors that can significantly affect the results, as any alteration in the position could impact the outcome, and manual alignment can be associated with human errors. An evolved form of DRA has been proposed, which transformed the conventional island DRA to a substrate-integrated DRA (SIDRA) including a double PCB layers that have been bonded using a little glue [33]. The limitation of using bonding glue is that it is not possible to control the consistency of thickness, which could lead to altering the outcomes of the study due to the nonuniform gap between the DRA and feed.

In [35] and [57], the rectangular DRA has been assembled using a multi-layer and multi-step PCB process. The board is composed of three PCB layers, which include the DRA elements and SIW feed layer. The limitation of both studies is the use of a 2 mm thermally stabilized bonding film as a bonding layer between the top SIW feed layer and bottom layers of the DRA, which can subsequently impact the overall performance.

The studies [59] and [66] proposed an SI-CDRA, which is configured from two substrates; the upper substrate for the DRA fabrication as well as a lower substrate for feeding structure. Two concentric circular arrays of metallic vias have been used to isolate the cylindrical DRA from the upper substrate. The studies propose this technique to automate the alignment of the DRA and the substrate. However, the limitations of such a technique are that the air gaps lead to weak radiation because the sidewalls of the DRA are not well-defined.

Moreover, the use of glue to affix the DRA has been given special attention in the literature as several studies mentioned the disadvantages of using glue as an adhesive material, which implies that there should be other techniques to affix the DRA. Both, [65] and [44] used glue to stick the DRA on feeding network, however the glue was placed on different structures in each study. In [65], the glue was placed on over the slot, whereas in [44], it was placed on the edge. It is important to take into consideration the impact of glue layer thickness on the outcome of the study especially in the mm-wave band. It is evident that a subtle change in the thickness of the glue can affect the overall impedance of the band. Also, the study [43] has not discussed how to align correctly. The alignment between the elements has been addressed by implementing the use of dielectric arms. However, the alignment in the whole structure has not been addressed in the study. In other words, the researchers did not clarify how the dielectric arms were placed on top of the ground plane whilst ensuring that the edges are precisely positioned. Moreover, in the study, glue was used, and it has not been mentioned how the thickness of the effective glue was controlled. This could explain the high discrepancy between the simulated and measured results, as recorded.

Other studies have also implemented acrylic in their experiments as a fixture to assemble the DRA and show the drawbacks of this technique that help future studies when using this technique. The study [39] proposed a new way to design the mm-wave DRA, such that the DRA element and the whole feeding network are co-fabricated and co-designed using the PCB technology. To align the DRA in the most accurate way possible, a fixture is designed and implemented. The following studies were conducted at a frequency of 60 GHz. In studies [48] and [49], an acrylic material is fabricated and used as a template between the PRA elements. Using PCB process, the feeding layers are fabricated, and then they are aligned and bonded together. However, in [48], a non-conductive adhesive is used to bond two DRA's. The use of the non-conductive adhesive can significantly impact the results if not managed correctly due to its thickness, especially at a high frequency. It's remarkable that the introduction of a template in [39], [48], and [49] leads to increasing size, complexity, and cost of the study. Therefore, it is not convenient to use templates to assemble the DRA.

The aforementioned literature works demonstrate that there are still many limitations that should be avoided in studies and experiments. Hence, this study aims to find an efficient method to align the DRA at minimal cost, error, and complexity.

1.9 Problem Definition

It is well known that employing the DRA at mm-wave leads to undesirable practical results since mm-wave DRAs have extremely small dimensions. Misalignment of the DRA can impact the impedance bandwidth. The adhesive material that fixes the DRA on the feeding structure has unpredictable errors. This is due to the fact that it is difficult to control the thickness and distribution of the glue material.

At mm-wave band, the performance of channel is affected by various problems caused by weather conditions like rain, fog, snow, and wind. In addition, mutual coupling between the DRAs can also degrade the signal. These problems are the reasons why this study has been conducted, as it aims to limit the aforementioned limitations by developing alternative methods that would conveniently enhance the performance of the mm-wave DRAs.

This thesis presents novel designs that provide solutions to the aforementioned limitations, whereby the wide and dual impedance and axial ratio bandwidths, alignment, assembly, and high data rate are going to be introduced and will be validated by measurements.

1.10 Thesis aims and objectives.

The main aim of this thesis is to establish novel designs that allow the DRA to have an improved performance at mm-wave communication systems. In detail, the objectives that have been set to achieve the main aim are as follows:

1. Investigate the precise and simple alignment and assembly methods to accelerate the prototyping of mm-wave DRAs.
2. Develop a novel DRA configuration with an additional degree of freedom that results in an enhanced CP bandwidth.

3. Propose more than one technique to reduce the mutual coupling between a dual band MIMO DRA elements, which results in a compact structure.
4. Investigate a compact and simple dual band 60 GHz DRA with circular and linear polarisations while ensuring that there are no misalignment issues.

1.11 Thesis Structure

The thesis is made up of six chapters, as listed below:

Chapter 1: Introduction, literature review, contributions in the research, and the layout of the thesis.

Chapter 2: Investigates techniques to improve the performance, assembly, and alignment of linearly polarized hemispherical DRA using three approaches.

Chapter 3: Presents a wideband circularly polarized hemispherical DRA that incorporates and addition sold, or perforated, dielectric substrate between the feeding slot and the DRA. It is evident that the simulated results have a good agreement with measurements.

Chapter 4: Investigates MIMO rectangular DRA system that operates at 28 and 38 GHz with reduced mutual coupling between the DRAs. The findings are supported by experimental measurements.

Chapter 5: Investigates 60 GHz cylindrical and rectangular DRAs that operate in a dual band with a suitable alignment method.

Chapter 6: Conclusion and implications for future research.

Chapter 2

Wideband mm-wave Hemispherical DRA with Simple Alignment and Assembly Procedures

2.1 Introduction

The rapid growth of wireless communications systems, such as mobile communications and the Internet of Things (IoT), has triggered a notable interest in developing new systems that can operate efficiently at the millimeter wave (mm-wave) frequency band, which provides the required high data rates and capacity [67, 68]. However, the main challenge of the mm-wave communications is the short propagation range due to the attenuation caused by the oxygen molecules absorption [69]. Therefore, high gain antennas with a stable operation over a wide bandwidth, need to be utilized to overcome the signal path loss while transferring massive data in particular for 5G-and-beyound applications.

Popular antenna types such as dipole [70], microstrip [71], and monopole [72] have been used in the mm-wave frequency band albeit with well-known drawbacks such as narrow bandwidths and increased ohmic losses. On the other hand, a DRA represents a suitable alternative due to the absence of ohmic losses and attractive radiation characteristics that can be achieved through a proper combination of the resonator's dimensions and dielectric constant as well as a properly chosen feeding technique [73]. Therefore, mm-wave single DRAs as well as arrays have been reported in several studies over the last few years [31, 42, 60, 74-76]. However, the DRA alignment and assembly represent key challenges at mm-wave frequencies since any marginal misalignment between the feeding network and DRA can have a significant impact on the antenna's performance [35, 55] due to the shorter wavelengths and the physically smaller antenna size. The same is true for the DRA bonding since the thickness and permittivity of any glue layer can also impact the performance at mm-wave frequencies [33, 65]. In addition, another limitation of using bonding glue layer is the difficulty of achieving a uniform thickness, which could alter the mm-wave antenna's performance. At lower frequencies, the DRA-feed alignment is usually achieved by manually adjusting the DRA position for maximum coupling and any misalignment errors are of a less significance since the resultant difference in the DRA position is considerably smaller than the operating wavelength. Similarly, the thickness of any bonding material is negligible compared to the wavelength at lower frequencies.

Therefore, DRA prototyping and precise measurements can be cumbersome and time-consuming processes at mm-wave frequencies. As a result, several approaches have been proposed in the literature to address the above limitations. For example, metal fixings and various glue distributions have been utilized in [49], which still affect the antenna performance to some extent and involves a relatively complex process. In another study, an acrylic template has been proposed in-which monolithic polymer-based DRA array elements were placed [66]. However, the acrylic template has a dielectric constant of 2.5, which may impact the mutual coupling between the array elements and excites surface waves that deteriorate the radiation efficiency. Furthermore, a 60 GHz circularly polarized substrate integrated cylindrical DRA array has been reported in which the DRA elements have been fabricated and positioned in a single process with no need for additional assembly steps [40]. However, the substrate integrated DRA approach is most suitable for DRA geometries with uniform cross section such as rectangular and cylindrical DRAs. In addition, the height of the DRA is determined by the thickness of the used substrate. An alternative approach has been proposed by fabricating an integrated DRA using Low Temperature Cofired Ceramics (LTCC) technology to address the DRA alignment and assembly issues [40, 77]. However, LTCC technology has a higher prototyping cost and can be associated with surface waves due to the substrate thickness.

In this work, simple and low-cost alignment methods are proposed that considerably reduce the required time and effort needed for the assembly and accurate measurements of mm-wave DRAs. Further, the proposed methods can be utilized for DRA geometries of non-uniform cross sections, such as hemispherical, pyramidal and stair shaped DRAs. Therefore, a wide band hemispherical DRA has been utilized as a case study to demonstrate the potential of the proposed methods in expediating the DRA prototyping. The antenna parameters have been investigated using the hemispherical DRA mode characteristics equation, CST simulations as well as measurements. Good agreement has been achieved between the simulated and measured results.

The chapter is organized into four sections that describe the theoretical and experimental results of three prototypes. The hemispherical DRA configuration and resonance modes are introduced in Section 2.2. Section 2.3.1 presents the technique of outlining the DRA position on the ground plane. Section 2.3.2 describes the method of utilizing a grooved compound ground plane in which the DRA is placed. Section 2.3.3 is focused on the 3D printing of the DRA on a perforated substrate. Finally, the conclusions are stated in Section 2.4.

2.2 Hemispherical DRA configuration and resonance modes

A hemispherical DRA has been selected using Alumina with a dielectric constant of $\varepsilon_r = 9.9$ and a radius of a = 3.8 mm. The hemispherical DRA supports both transverse electric (TE_{nms}) modes with the TE_{111} as the lowest order TE mode and transverse magnetic (TM_{nms}) modes with the TM_{101} as the lowest order TM mode. The subscript *n* denotes the order of the Bessel function and can be used to determine the elevation variations of the mode's fields. On the other hand, the subscript *m* represents the number of full wave field's variation along the azimuth axis with $0 \leq m \leq n$. Finally, the subscript *s* refers to the number of half wavelength field's variation along the *r* axis [23]. The resonance frequencies of the supported TE modes can be determined from the roots of the following mode characteristics [23]:

$$\frac{j_n(ka)}{j_n'(ka)} = \sqrt{\varepsilon_r}\frac{h_n(k_0 a)}{h_n'(k_0 a)} \tag{2.1}$$

where j_n and h_n represent the first kind spherical Bessel function and the second kind of spherical Hankel function of order n, respectively. j_n' and h_n' represent the derivatives of the aforementioned functions, respectively. k_0 is the free space wavenumber and k is the dielectric wavenumber defined as $k = \sqrt{\varepsilon_r} k_0$. The roots ($k_0$a) of equation (2.1) have been determined numerically from which the resonance frequency of each mode can be calculated as [78]:

$$f_r = \frac{4.775 \times 10^7 \ \mathrm{Re}\,(k_0 a)}{\sqrt{(\varepsilon_r) a}} \tag{2.2}$$

For the hemispherical DRA under consideration, the resonance frequencies of the first few TE modes have been calculated using equations (2.1) and (2.2) as listed in Table 2-1.

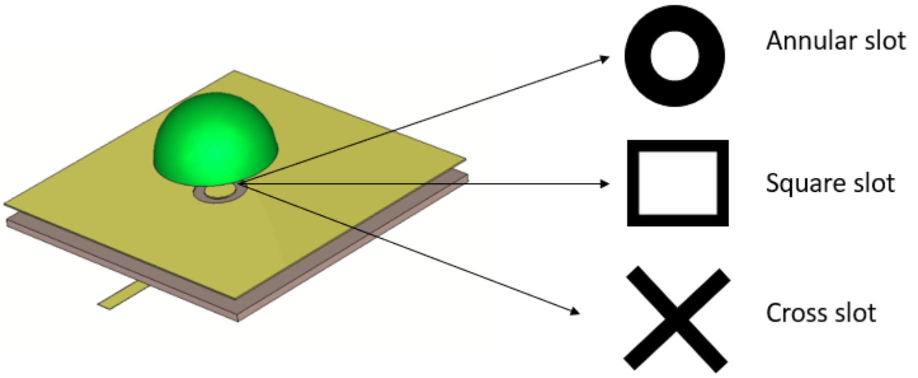

Figure 2.1: A slot fed hemispherical DRA configuration 3-D view with different slot shapes.

Table 2-1: Resonance frequencies of few TE modes of the used alumina hemispherical DRA

Resonance TE mode	Resonance Frequency $f_{TE_{nms}}$ (GHz)
TE_{111}	11.8
TE_{211}	17
TE_{311}	22.5
TE_{112}	27

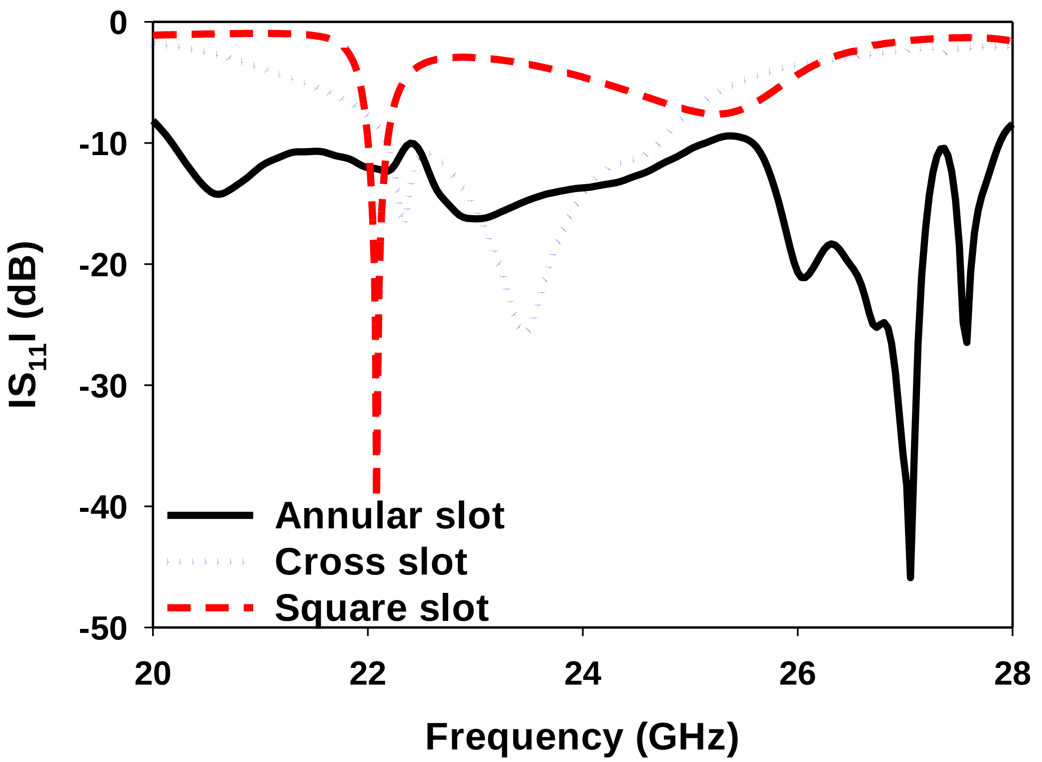

Figure 2.2: Effect of the different slots (Annular slot, cross slot, and square slot) on the single element hemispherical DRA performance.

The slot-coupling mechanism and feed-coupling mechanism play a vital role in the enhancement of the bandwidth. To investigate the performance of the hemispherical DRA, different shapes of slots are analyzed and compared in order to determine the most convenient slot shape. The aim is to choose the slot which results in the widest bandwidth. As shown in Figure 2.1, different slot shapes, namely the cross, square, and annular, which have the same area, have been investigated. First, at a frequency band of 22 GHz to 24.7 GHz, the bandwidth of the antenna with a cross slot is nearly 10%. Second, at a frequency of 22 GHz, the bandwidth of the antenna with a square slot is nearly 1%. Finally, at a frequency band of 20 GHz to 28 GHz, the bandwidth of the antenna with an annular slot is nearly 33%. These results imply that the antenna with an annular slot can operate at a wider frequency band. Thus, it has the widest bandwidth. Furthermore, the annular slot has good impedance matching and a larger coupling area between the micro-strip line and the DRA.

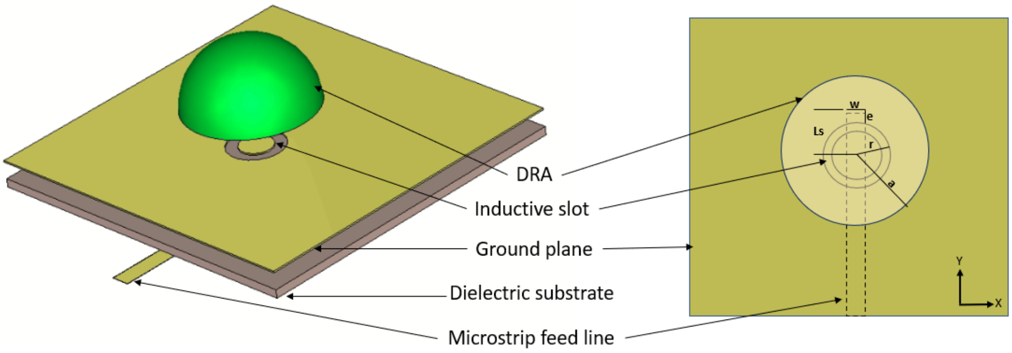

(a) (b)

Figure 2.3: A slot fed hemispherical DRA configuration (a) 3-D view (b) 2-D top view.

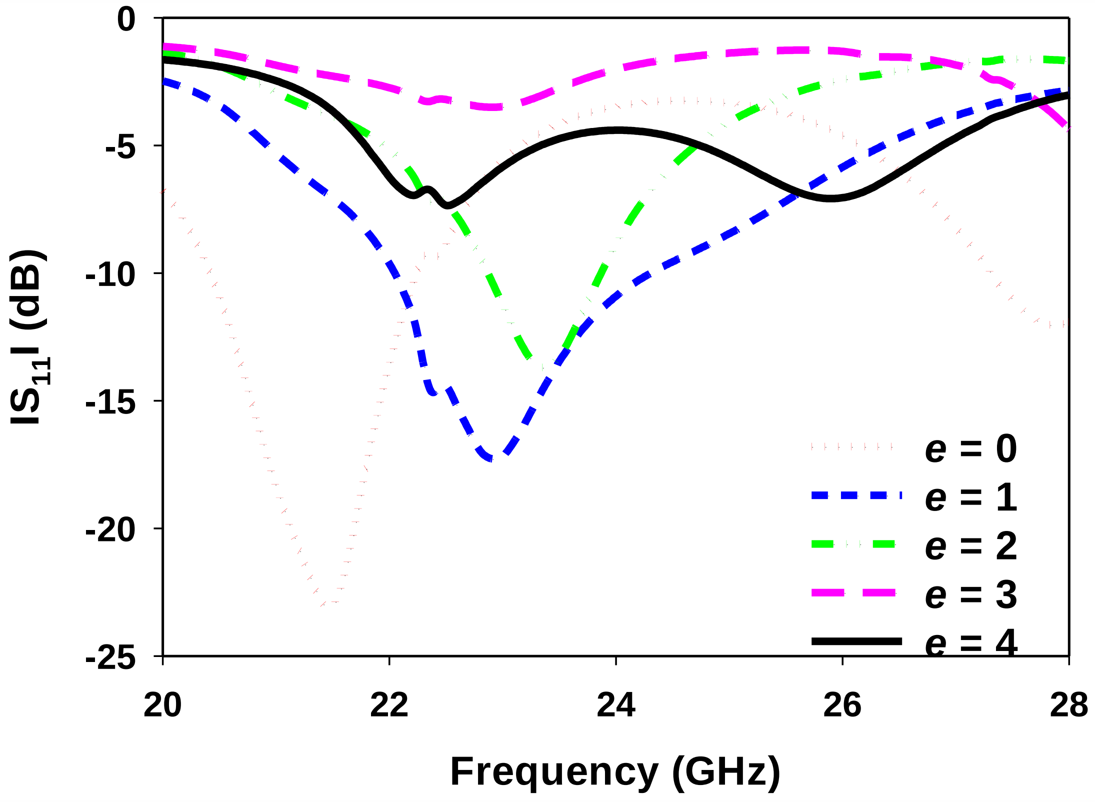

(a)

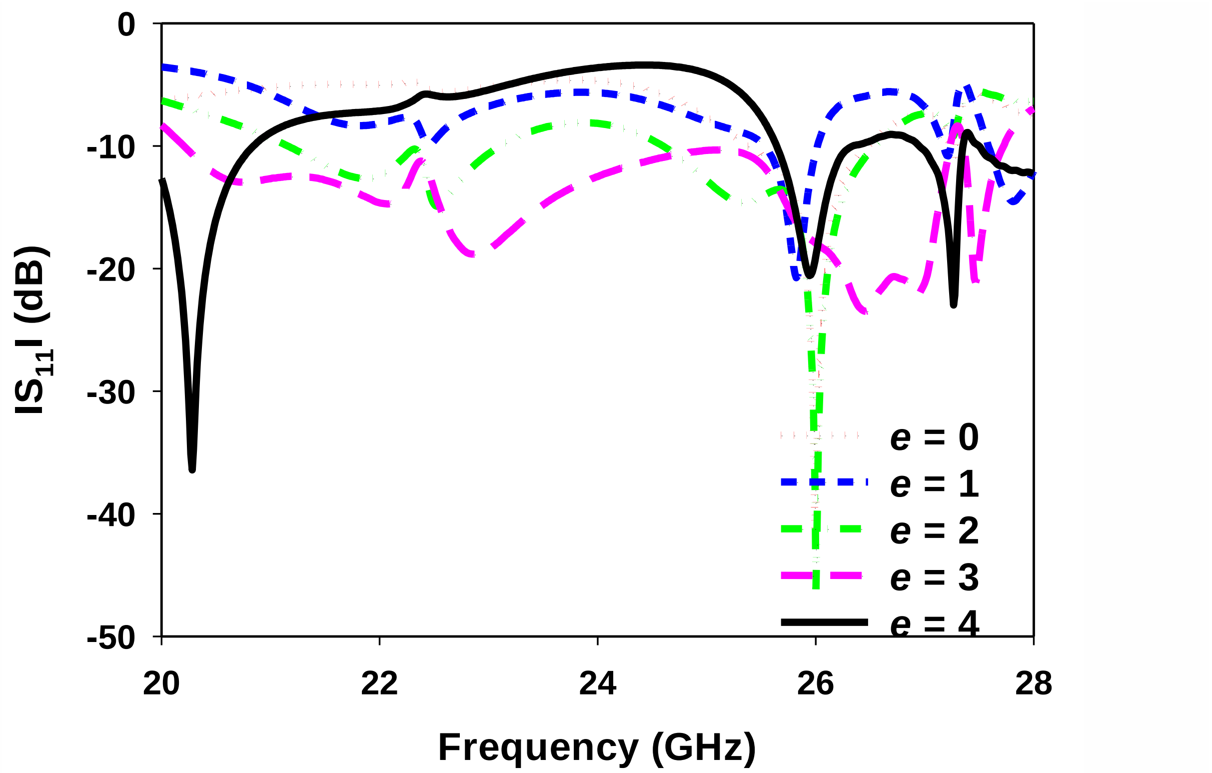

(b)

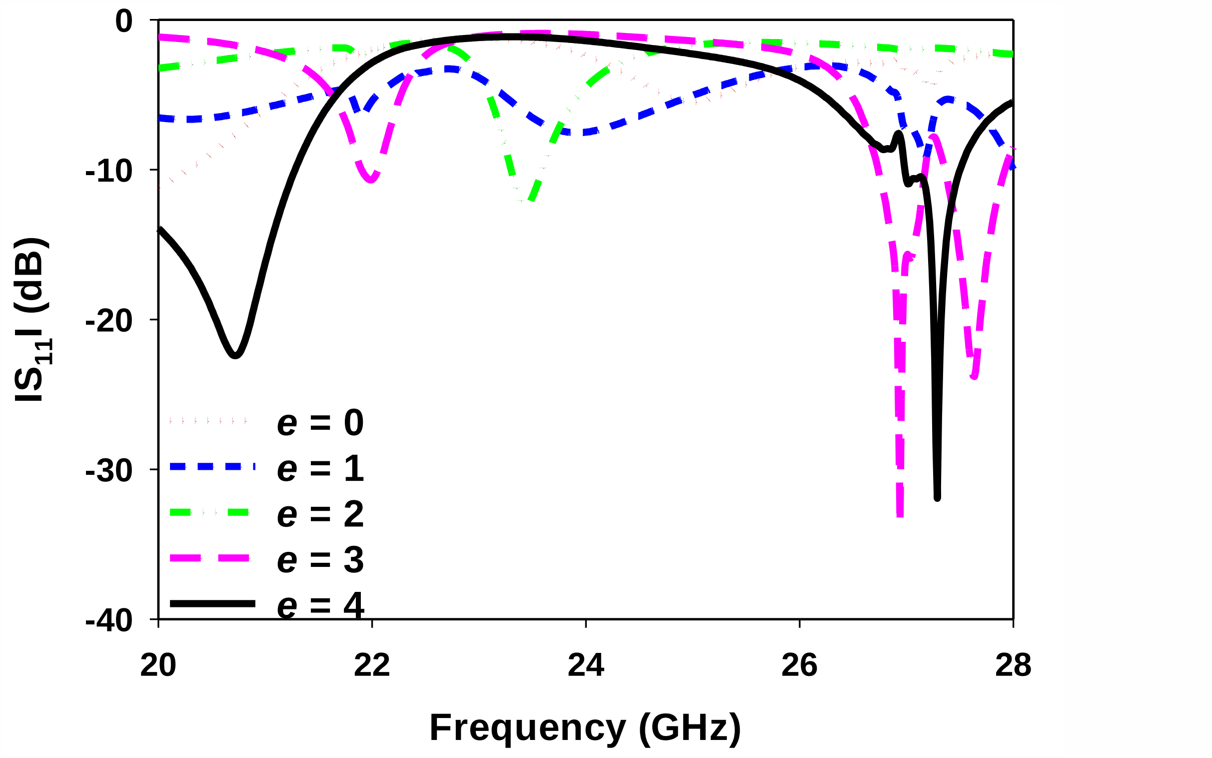

(c)

Figure 2.4: Effect of the stub length (e) on the Single element hemispherical DRA performance (a) r = 1.5 mm (b) r = 1.6 mm (c) 1.7 mm

The stub length (*e*) of the feeding line can significantly affect the matching of the hemispherical DRA. Moreover, the radius of the annular slot (*r*) can affect the performance of the hemispherical DRA. Therefore, the effect of changing the values of the r and the *e* have been examined, as shown in Figure 2.2. When $r = 1.5$ mm and the *e* is changed from 1 mm to 4 mm, the matching of the antenna is changed, as suspected. From 22 GHz to 24 GHz, a wide bandwidth is achieved at $e = 1$ mm, as illustrated in Figure 2.2 (a). When $r = 1.6$ mm and the *e* is changed from 1 mm to 4 mm, the best matching is achieved from 20 GHz up to 28 GHz at $e = 2$ mm as illustrated in Figure 2.2 (b). Finally, when the $r = 1.7$ mm and *e* is changed from 1 mm to 4 mm, the wideband operation is achieved at frequency band from 26 GHz to 28 GHz as shown in Figure 2.2 (c). Therefore, from the previous parametric study, the structure and dimensions of the proposed single hemispherical DRA have been chosen.

The hemispherical DRA configuration is illustrated in Figure 2.3(a), where it can be observed that the antenna is placed on top of a square ground plane with a size of 20 mm that has an etched annular ring feeding slot. The antenna is fed using a 50 Ω microstrip line with a width of $w = 1$ mm. The microstrip line is printed on the lower side of a Rogers (RO4350B) dielectric substrate with a respective dielectric constant and thickness of 3.48 and 0.5 mm as demonstrated in Figure 2.3 (b).

As demonstrated in Table 2-1, the proposed hemispherical DRA supports two higher order resonance modes over a frequency range of 20-30 GHz as well as the fundamental TE_{111} mode at 11.8 GHz. The radius of the annular slot, *r*, has been adjusted for the widest impedance bandwidth that has been achieved over a frequency range of 20-28 GHz using $r = 1.6$ mm with a matching stub length of $L_s = 2$ mm. The reflection coefficient is presented in Figure 2.4, where it can be noted that the TE_{111} mode has been excited in conjunction with the higher-order modes of TE_{311} and TE_{112} at 22.5 GHz and 27 GHz, respectively. The simulated resonance frequencies are in close agreement with those calculated using equation (2.2). As a result, a wide operating bandwidth of ~33% has been achieved over the expected frequency range. In addition, the antenna offers a stable broadside pattern over the entire frequency range with a maximum gain of ~10 dBi at 22.7 GHz.

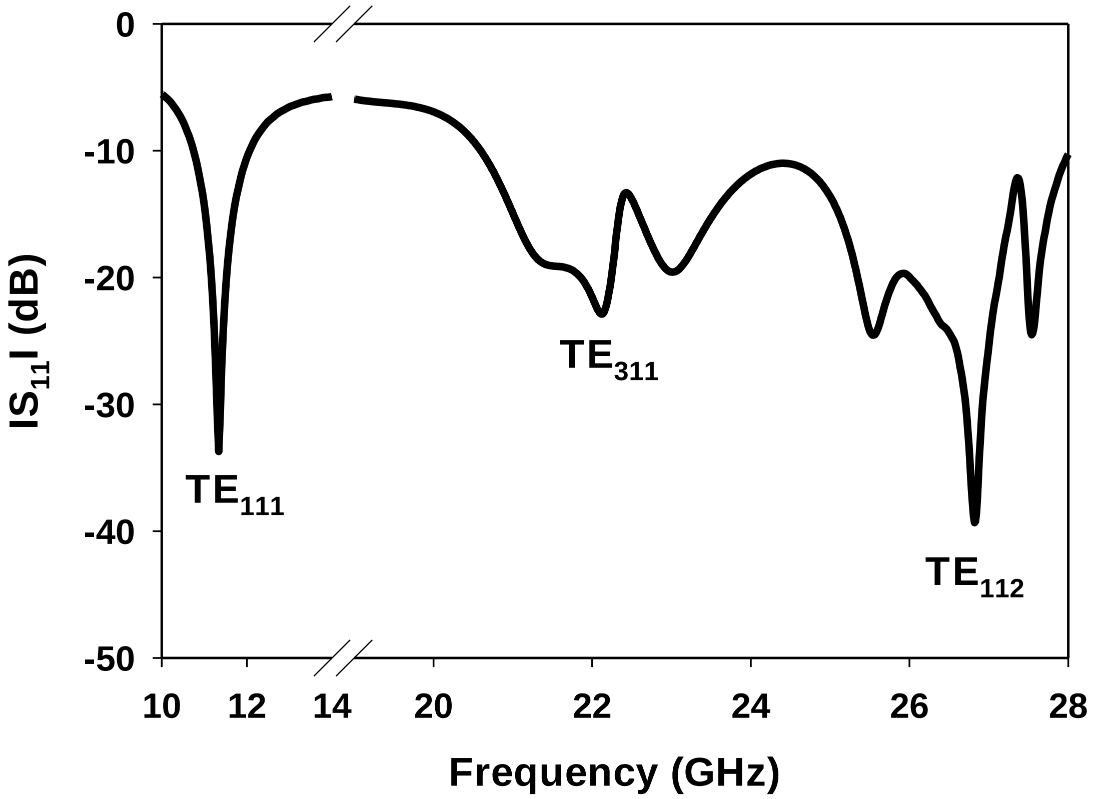

Figure 2.5: Simulated S_{11} of the slot fed hemispherical DRA that excited three modes: TE_{111}, TE_{311} and TE_{112}.

2.3 Experimental results

A prototype of the proposed hemispherical DRA has been fabricated and measured. DRA was fabricated using alumina material that has a permittivity of 9.9 by T-CERAM company. The reflection coefficient has been measured using a 2.92 mm SMA and a N5245B vector network analyzer (VNA). In addition, the radiation pattern has been measured using the SNF-FIX-1.0 Spherical Near-field mm-Wave Measurement System. The proposed simple and low-cost alignment and assembly methods have been utilized in the experimental work as demonstrated in the following sections.

2.3.1 Highlighting the DRA position on the ground plane

The first alignment method is based on highlighting the DRA position on the metal ground plane using a white ink as illustrated in Figure 2.5. The highlighting can be added during the feed network fabrication at no extra cost or subsequently added using a standard 3D printer. In addition, the automated highlighting provides the needed alignment precision for accurate measurements and saves a considerable time that is usually spent in adjusting the DRA position. Besides, it eliminates any human errors that can be introduced in the attempts to align the mm-wave DRA manually. However, adhesive copper tape is still needed to bond the DRA to the feed network. Therefore, two short-length pieces of a double-sided adhesive copper tape with a thickness of 0.5 mm have been utilized to attach the DRA to the ground plane. It should be noted that such a thickness of the copper tape has been incorporated in the simulations and proved to have a negligible impact on the antenna performance at frequencies up to 70 GHz.

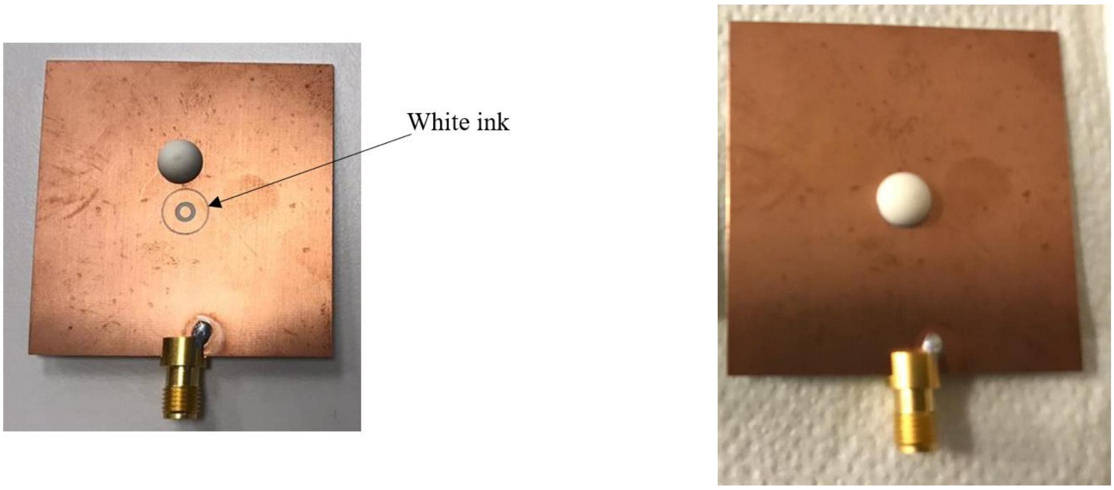

(a) (b)

Figure 2.6: The prototype of a hemispherical DRA (a) Highlighted DRA position on the ground plane, (b) Assembled DRA

The measured S_{11} of the proposed DRA is illustrated in Figure 2.6, where it can be noted that the impedance matching bandwidth extends over the expected frequency range of 20 to 28

GHz, which corresponds to 33.3% with close agreement between measurements and simulations. The normalized E-plane and H-plane patterns are presented in Figure 2.7 at 22.7 GHz and 27 GHz. The respective simulated and measured half power beamwidths are 61° and 54° at 22.7 GHz as well as 70° and 73° at 27 GHz. Once more, a close agreement has been achieved between the simulated and measured results with a stable broadside radiation throughout the operating frequency range. Figure 2.8 illustrates the simulated and measured realized gain, where it can be noted that the antenna offers an average gain bandwidth of circa 7 dBi with a peak of circa 10 dBi at 22.7 GHz, which can be attributed to the excitation of a higher order mode at this frequency. Finally, the simulated and measured gains are in close agreement with each other.

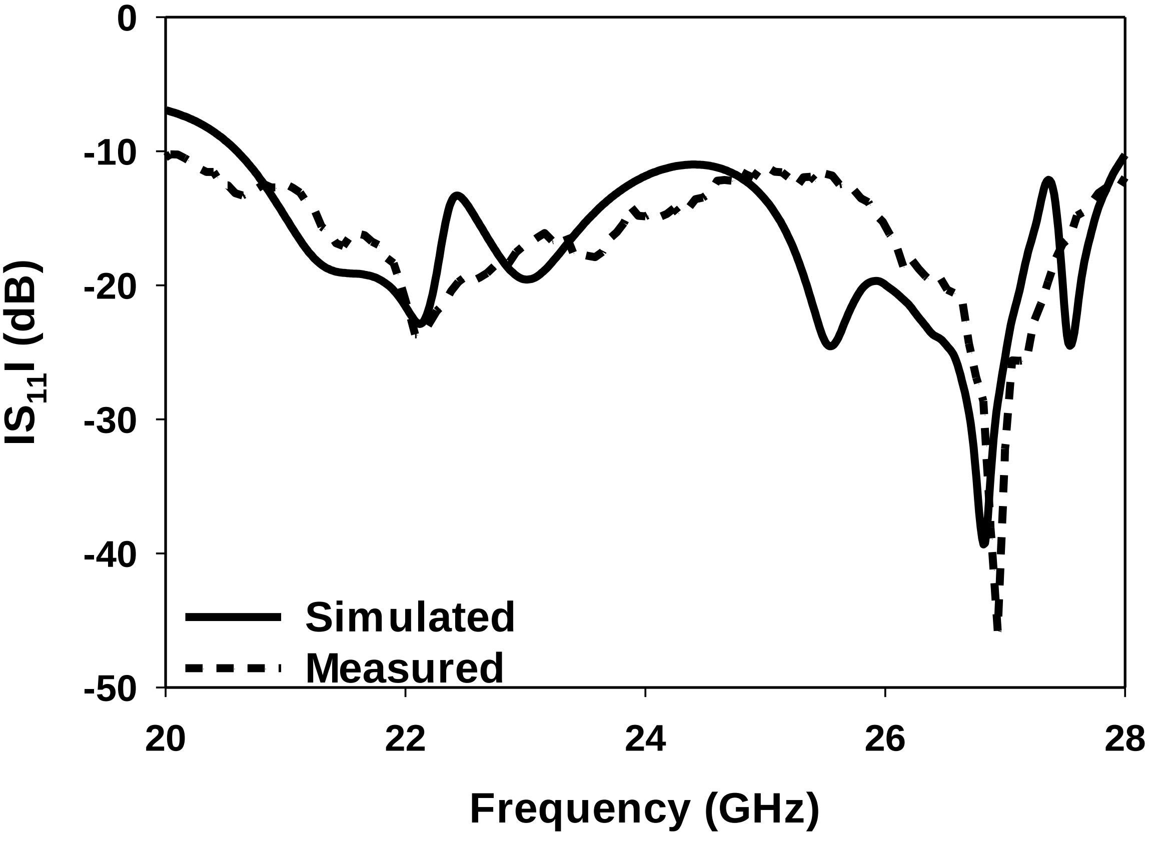

Figure 2.7: The $\mathbf{S_{11}}$ of a linearly polarized hemispherical DRA with a highlighted position on the ground plane at ε_r= 9.9, ε_s= 3.48, a = 3.8 mm, r = 1.6, l_s = 2 mm and h_s= 0.5 mm.

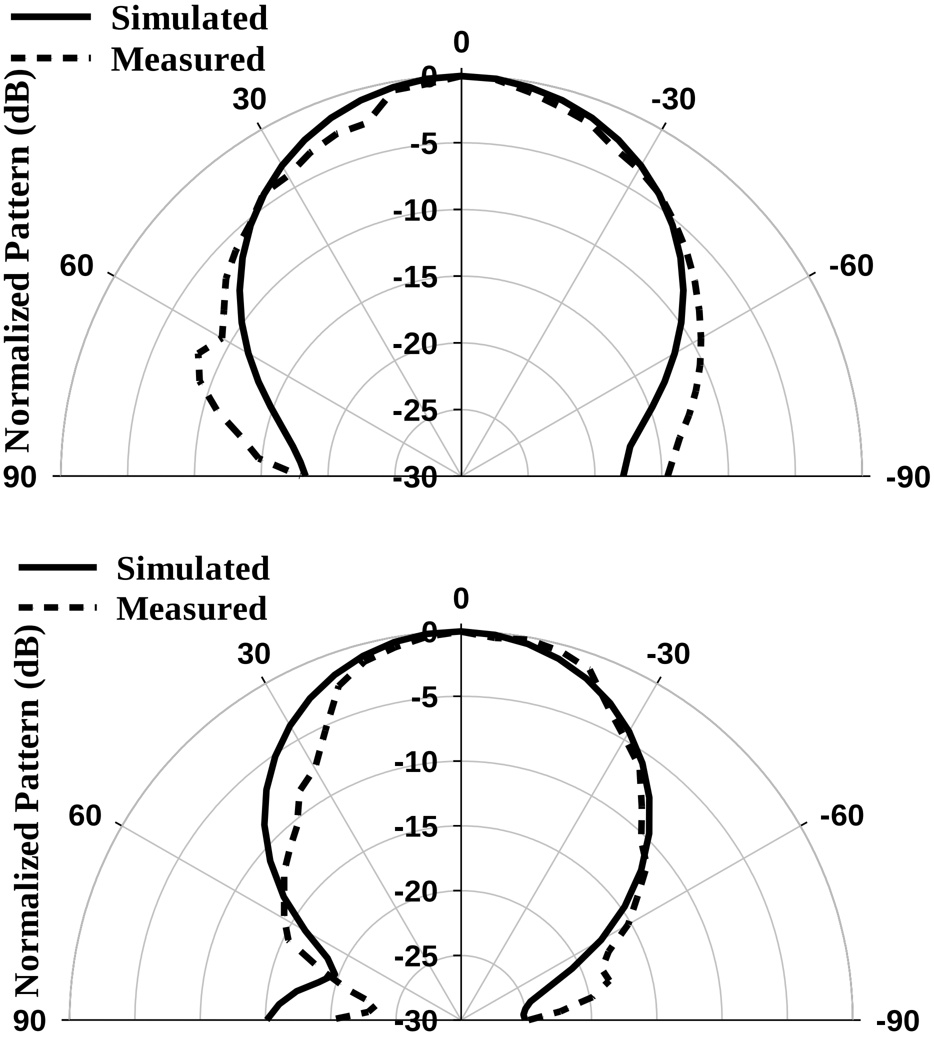
Simulated
Measured
Normalized Pattern (dB)
0
30
-30
60
-60
90
-90
0
-5
-10
-15
-20
-25
-30
Simulated
Measured
Normalized Pattern (dB)
0
30
-30
60
-60
90
-90
0
-5
-10
-15
-20
-25
-30

(a)

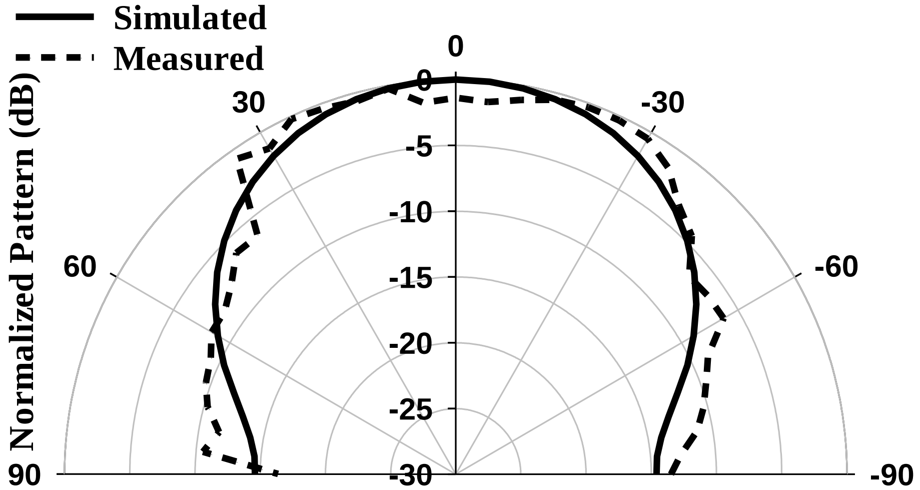
Simulated
Measured
Normalized Pattern (dB)
0
30
-30
60
-60
90
-90
0
-5
-10
-15
-20
-25
-30

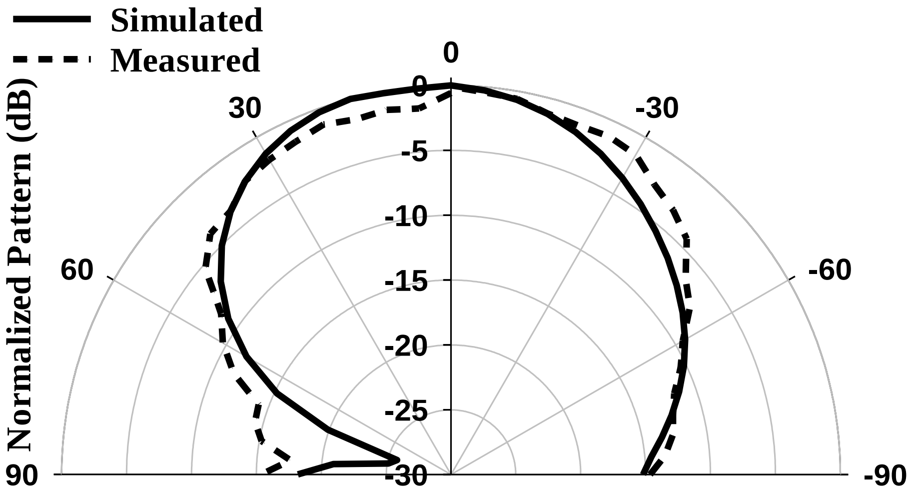

(b)

Figure 2.8: The E and H planes radiation patterns of a hemispherical DRA with a highlighted position on the ground plane (a) 22.7 GHz (b) 27 GHz at ε_r= 9.9, ε_s= 3.48, a = 3.8 mm, r = 1.6, l_s = 2 mm and h_s= 0.5 mm.

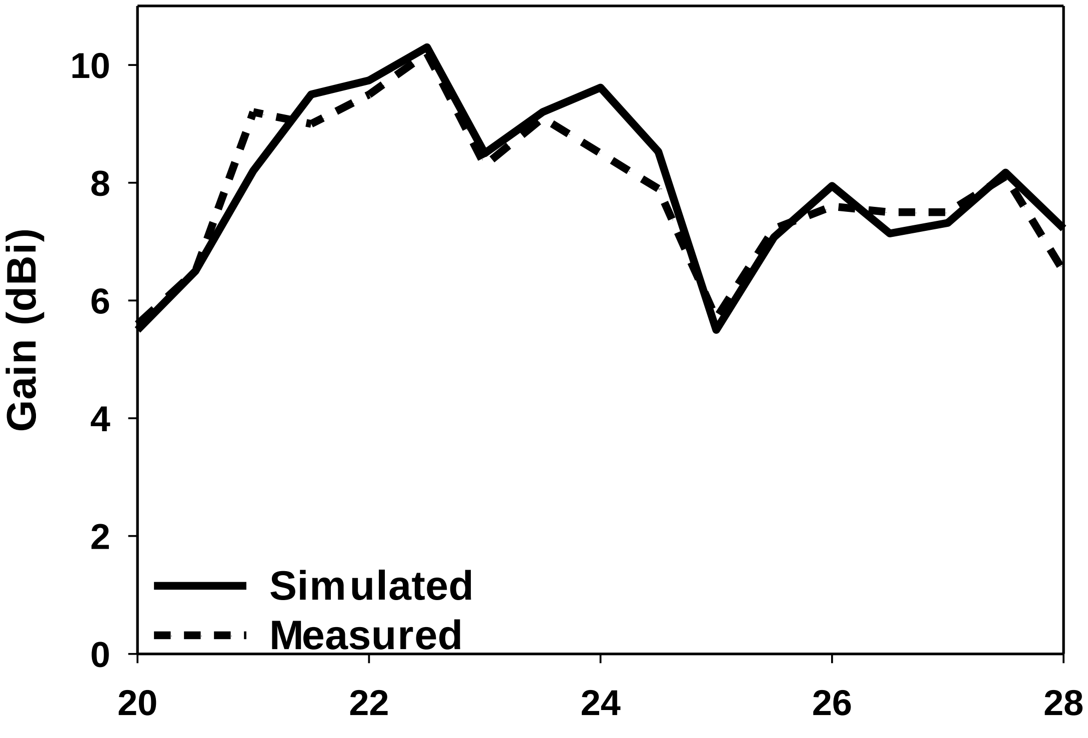

Figure 2.9: The gain of a hemispherical DRA with a highlighted position on the ground plane at ε_r= 9.9, ε_s= 3.48, a = 3.8 mm, r = 1.6, l_s = 2 mm and h_s= 0.5 mm.

The same approach has been utilized for an array of two DRAs that are separated by a distance of 6.6 mm, where the positions of the DRAs have been highlighted as demonstrated in Figure7 (b). Again, close agreement has been achieved between the simulated and measured s_{11}

of the array as demonstrated in Figure 2.10 over the desired bandwidth in which the same resonance modes have been excited. Figure 2.11 illustrates the simulated and measured radiation patterns of the hemispherical DRA for E and H planes at TE_{311} and TE_{112} modes whereby the frequency is equal to 22.7 GHz and 27 GHz, respectively. The figures demonstrate that the measured and simulated radiation patterns are in a relatively good agreement.

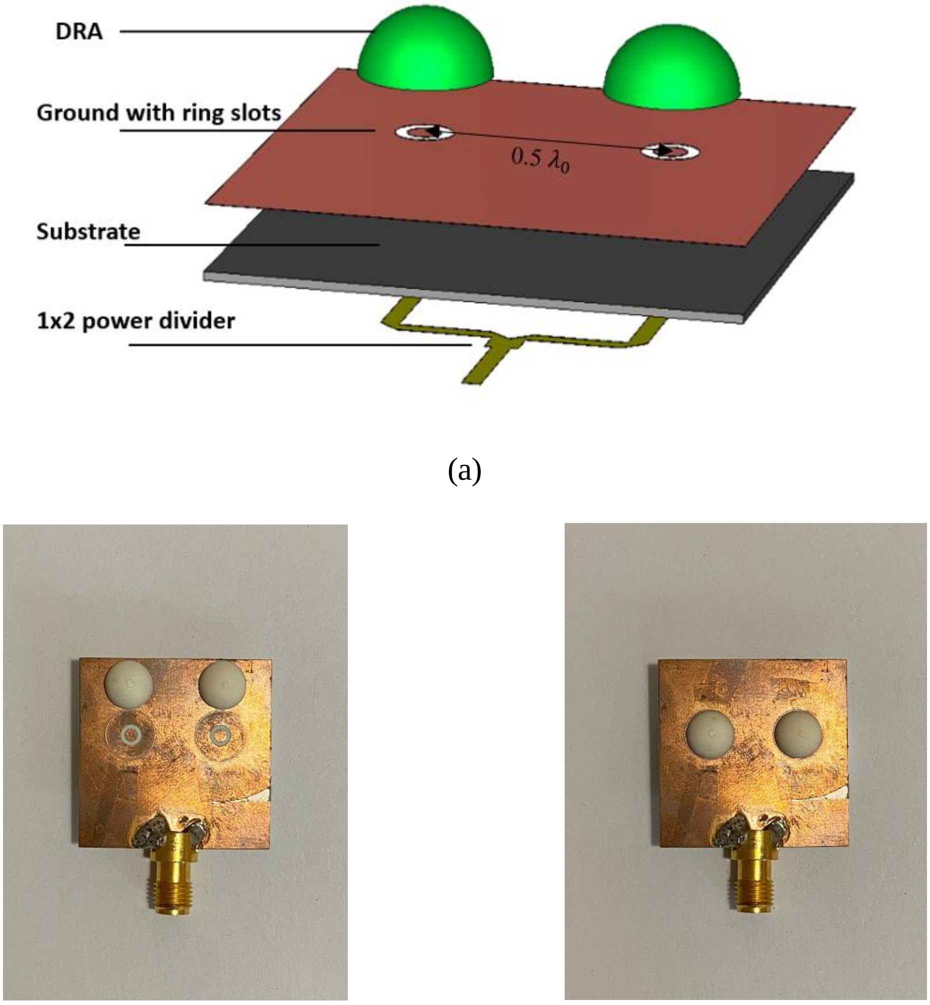

(a)

(b) (c)

Figure 2.10: Configuration of the two hemispherical DRAs (a) 3-D layout (b) Highlighted DRA positions (c) Assembled DRAs.

From these results it can be noted that highlighting the DRA’s position on the ground plane represents a simple and a cost-effective approach that facilitates a precise alignment between the DRA and the feeding slot as well as saves considerable time and effort compared to the case when the DRA position is not highlighted. However, the process involves the utilization of an adhesive copper tape below the DRA, which may be unsuitable at higher frequencies of more than 70 GHz due to the increased impact of the 0.5 mm gap between the DRA and feeding slot. In addition, the used ink to mark the DRA position may fade with time and usage, and hence the highlighting step may need to be repeated as needed. This is problematic because the highlighting step is used to mark the position of the DRA, so if it fades away, then this will affect the alignment of the DRA, and the step may have to be repeated again, which is time-consuming and not very precise and accurate. Therefore, another process for the alignment and assembly of a DRA prototype is proposed in the next section, which provides the same advantages of simplicity, timesaving, and accurate measurements.

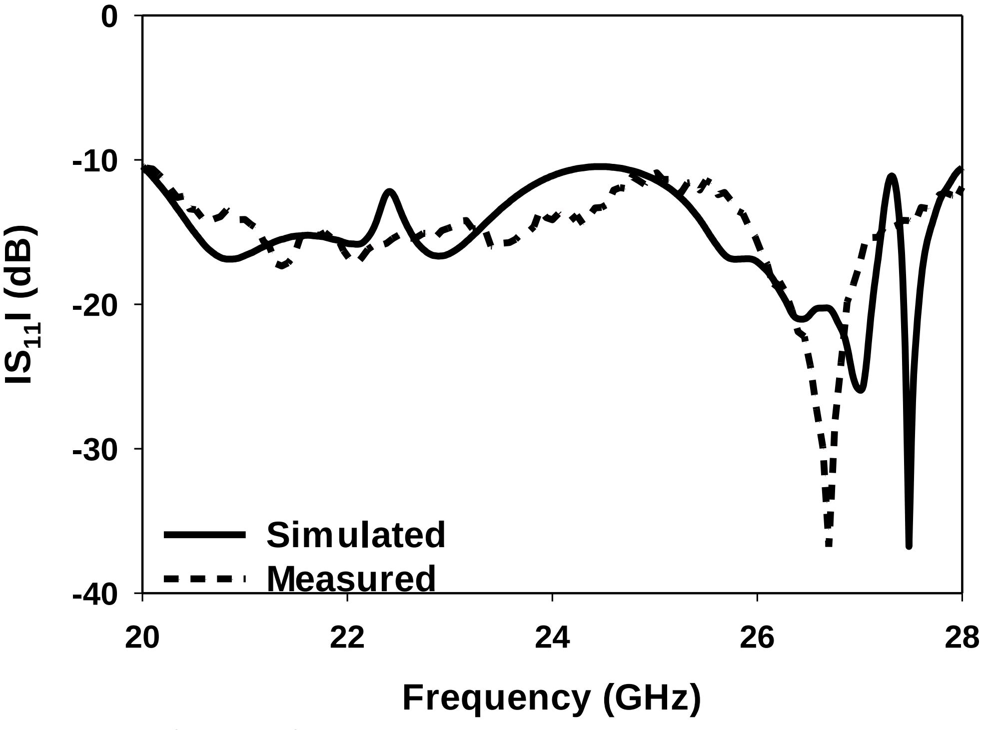

Figure 2.11: The S_{11} of an array of two hemispherical DRAs with highlighted antenna positions on the ground plane at ε_r= 9.9, ε_s= 3.48, a = 3.8 mm, r = 1.6, l_s = 2 mm and h_s= 0.5 mm.

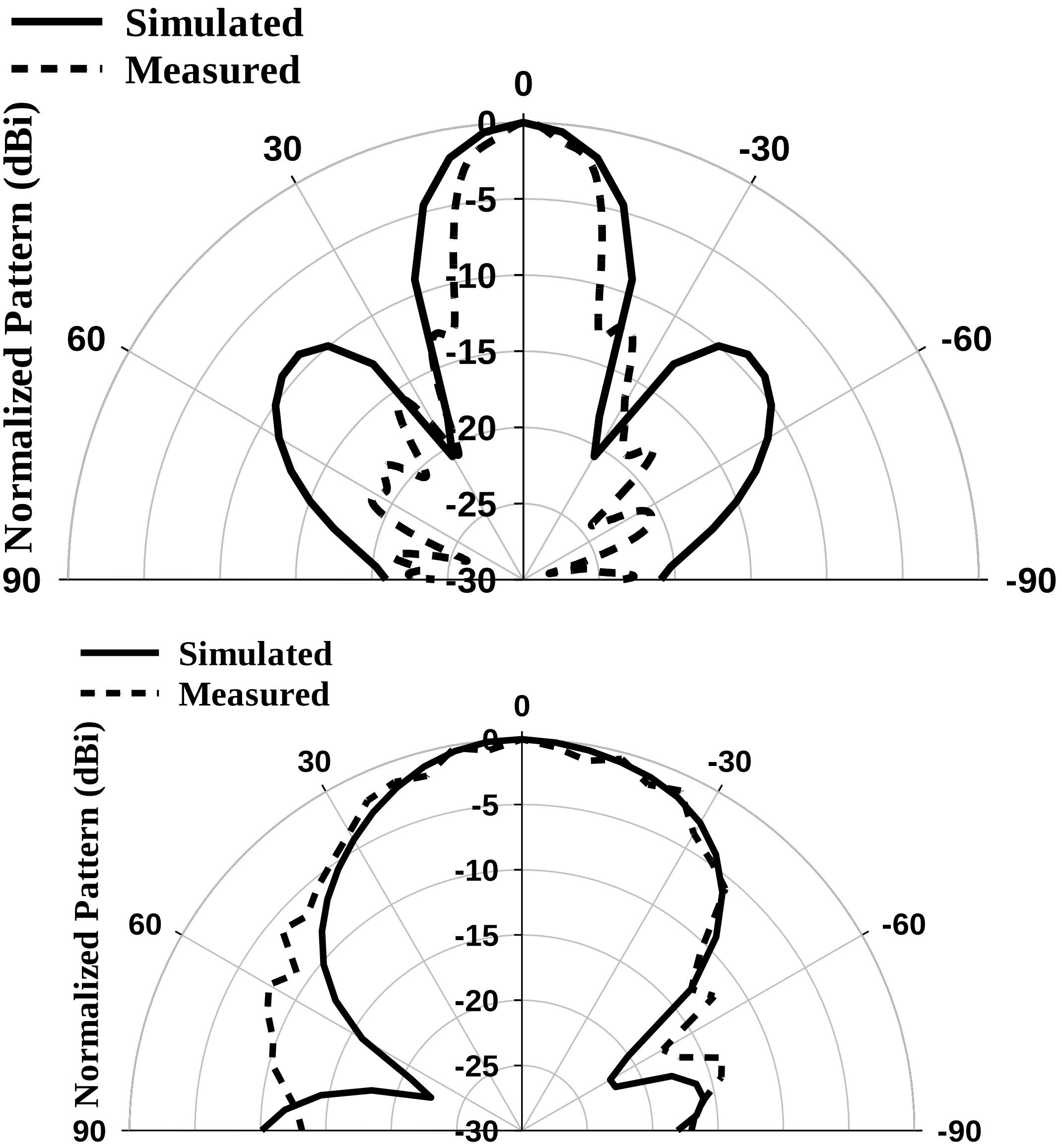
Simulated
Measured
Normalized Pattern (dBi)
0
30
-30
60
-60
90
-90
0
-5
-10
-15
-20
-25
-30
Simulated
Measured
Normalized Pattern (dBi)
0
30
-30
60
-60
90
-90
0
-5
-10
-15
-20
-25
-30

(a)

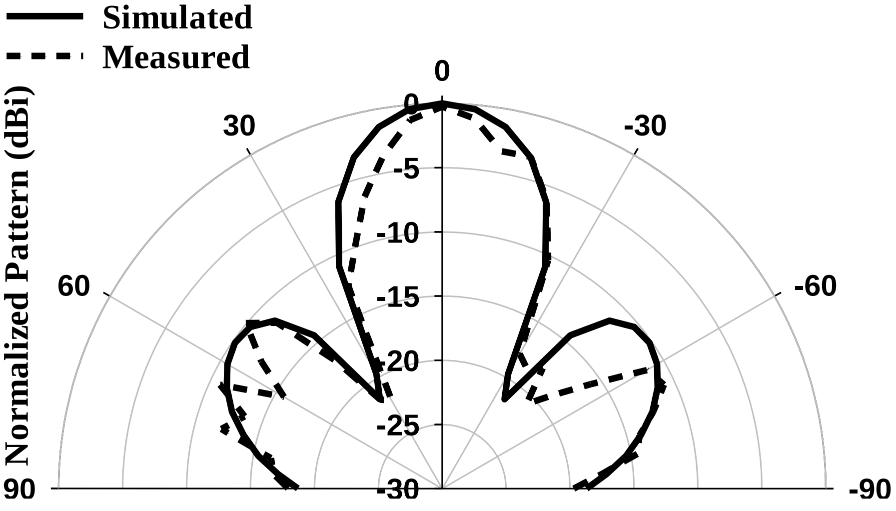
Simulated
Measured
Normalized Pattern (dBi)
0
30
-30
60
-60
90
-90
0
-5
-10
-15
-20
-25
-30

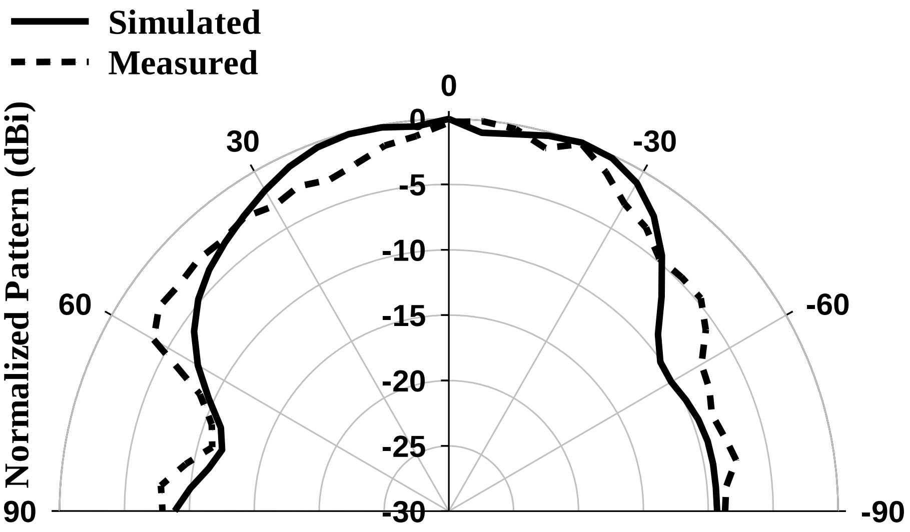

(b)

Figure 2.12: The E and H planes radiation patterns of a hemispherical DRA with a highlighted position on the ground plane (a) 22.7 GHz (b) 27 GHz at ε_r= 9.9, ε_s= 3.48, a = 3.8 mm, r = 1.6, l_s = 2 mm and h_s= 0.5 mm.

2.3.2 Grooved ground plane alignment and assembly process

Introducing a secondary grooved ground plane has been proposed earlier to eliminate the need of using a bonding glue, where two separate ground planes were utilized on top of each other with potential air gaps in-between that could have a notable impact at higher frequencies [79]. In addition, a small hole needed to be drilled inside the DRA in which a metal holder can be placed to attach the DRA to the ground plane. However, at mm-wave frequencies, it is difficult to drill hole inside a solid DRA considering the small physical size of the antenna. In this work, the two ground planes concept has been utilized, where the thickness of each ground plane has been chosen as 18 μm. In addition, the required DRA position has been determined by etching a circular groove in the top ground plane with a radius that is larger than that of the DRA by 100 μm as illustrated in Figure 2.12 (a). Furthermore, the feeding annular ring slot was etched in the lower ground plane. The two ground planes have been bonded together by inserting a thin pre-preg layer in-between with a small thickness of ~5 μm. Besides, a circular groove that is identical to, that in the top ground plane, has been created in the pre-preg layer so that the DRA can be placed directly above the feeding slot without airgaps in-between.

The automated ground planes' bonding process has been achieved through compression to eliminate potential airgaps between the two ground planes. This compression is a part of the feed network fabrication and has been implemented by placing the ground planes and pre-preg layer under a vacuum chamber and heated to 180° C under a pressure of 300 psi. Moreover, due to the compression, the final thickness of the pre-preg layer has been reduced further to ~2 μm. Therefore, the resulting structure involves a circular groove with a depth of ∼20 μm that precisely accommodates the DRA above the annular ring feeding slot. As mentioned earlier, the diameter of the groove has been made larger than that of the DRA by 100 μm, i.e., there is a gap of 50 μm between a centrally located DRA and the surrounding ground plane from all sides. This gap has been filled by adding a double-sided adhesive copper tape along the inner side of the groove, which also serves the purposes of bonding the ground plane to the DRA sides. Therefore, no potential airgaps are expected between the DRA and feeding slot. The fabricated grooved ground plane and the assembled DRA prototype are presented in Figures 9 (b) and (c), respectively. As in the case of a ground plane with a highlighted DRA position, an annular slot radius of 1.6 mm has been utilized with a matching stub length of $L_s = 2$ mm.

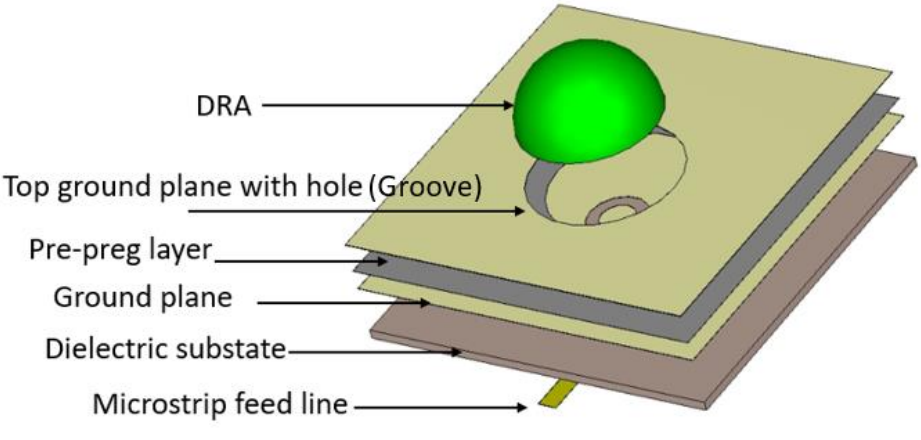

(a)

(b) (c)

Figure 2.13: A hemispherical DRA above a grooved ground plane; (a) 3-D layout, (b) Fabricated grooved ground plane, (c) Assembled DRA.

Figure 2.13 illustrates the simulated and measured reflection coefficient for a mm-wave DRA that is placed in a grooved ground plane. The results demonstrate close agreement between the simulated and measured impedance bandwidths of approximately 33%. Figure 2.14 demonstrates the simulated and measured radiation patterns at $TE_{311}$and TE_{112} modes for the E and H planes, such that the frequency is equal to 22.7 GHz and 27 GHz, respectively. The results show that there is close agreement between the simulated and measured results. In addition, good agreement has been achieved between simulated and measured realized gains, as demonstrated in Figure 2.15. Furthermore, the grooved ground plane offers a simple low-cost process in terms of the DRA assembly and bonding. Therefore, both of highlighting the DRA position and using a grooved ground plane represent simple and effective processes for rapid prototyping and accurate measurements of mm-wave DRAs. The choice between the two processes depends on the project timeline and budget.

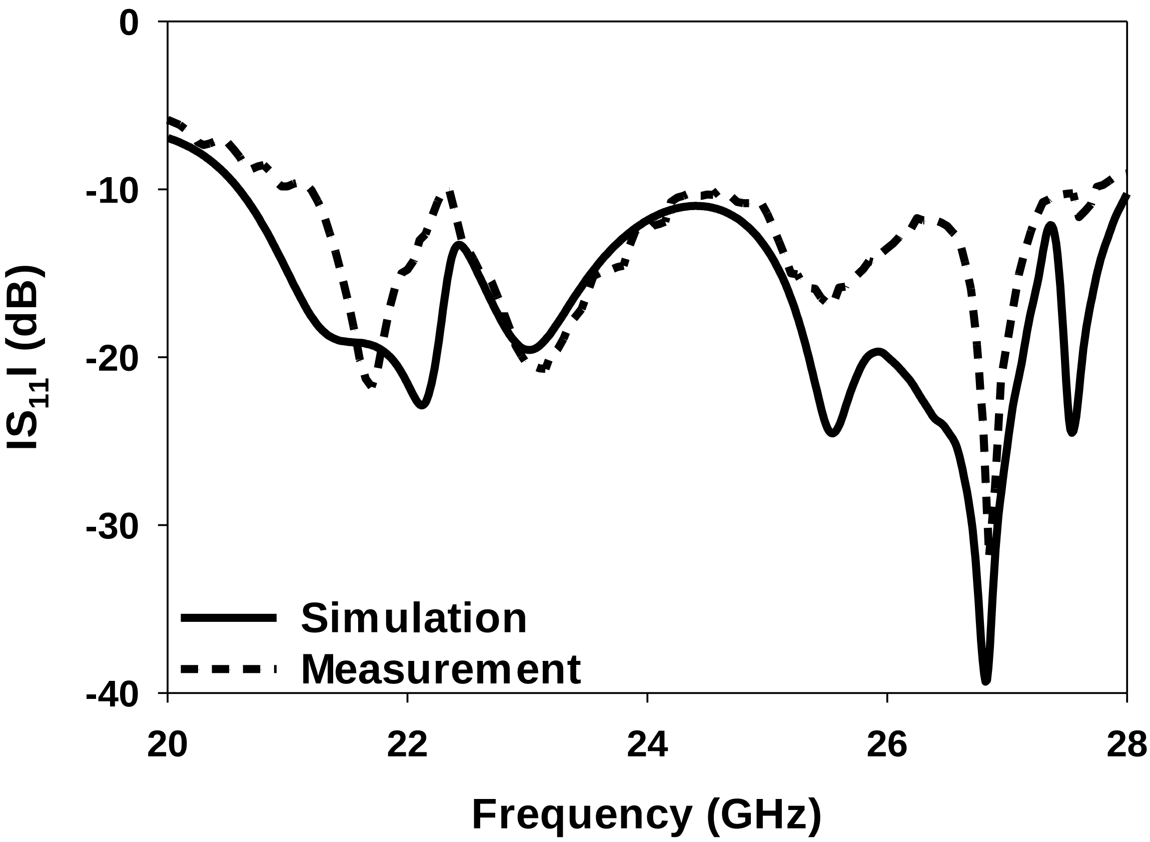

Figure 2.14: The S_{11} of a hemispherical DRA placed on a grooved ground plane at ε_r= 9.9, ε_s= 3.48, a = 3.8 mm, r = 1.6, l_s = 2 mm and h_s= 0.5 mm.

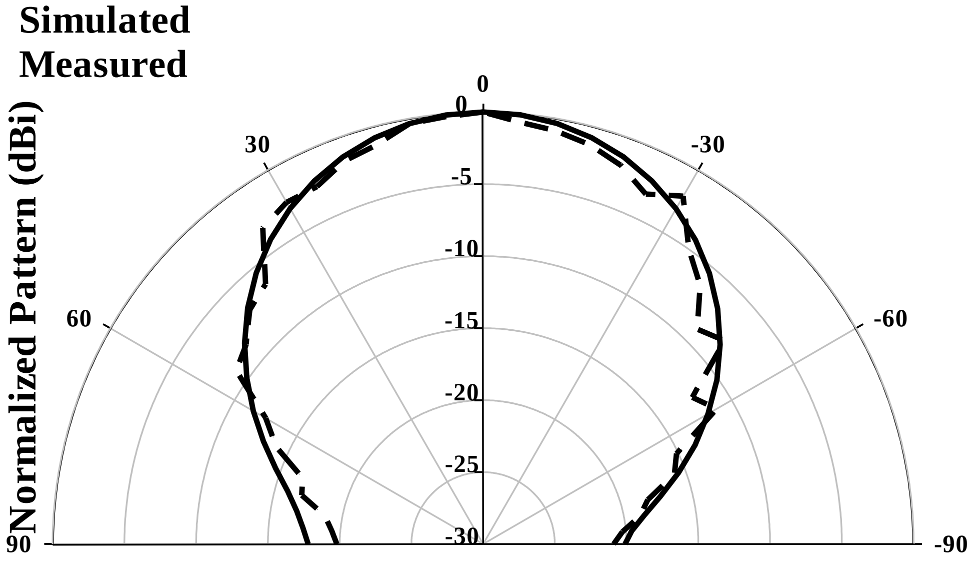

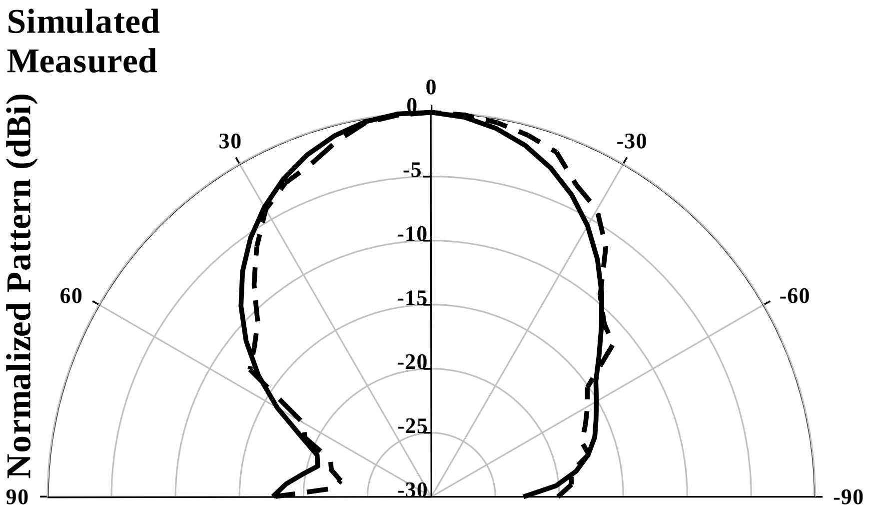

(a)

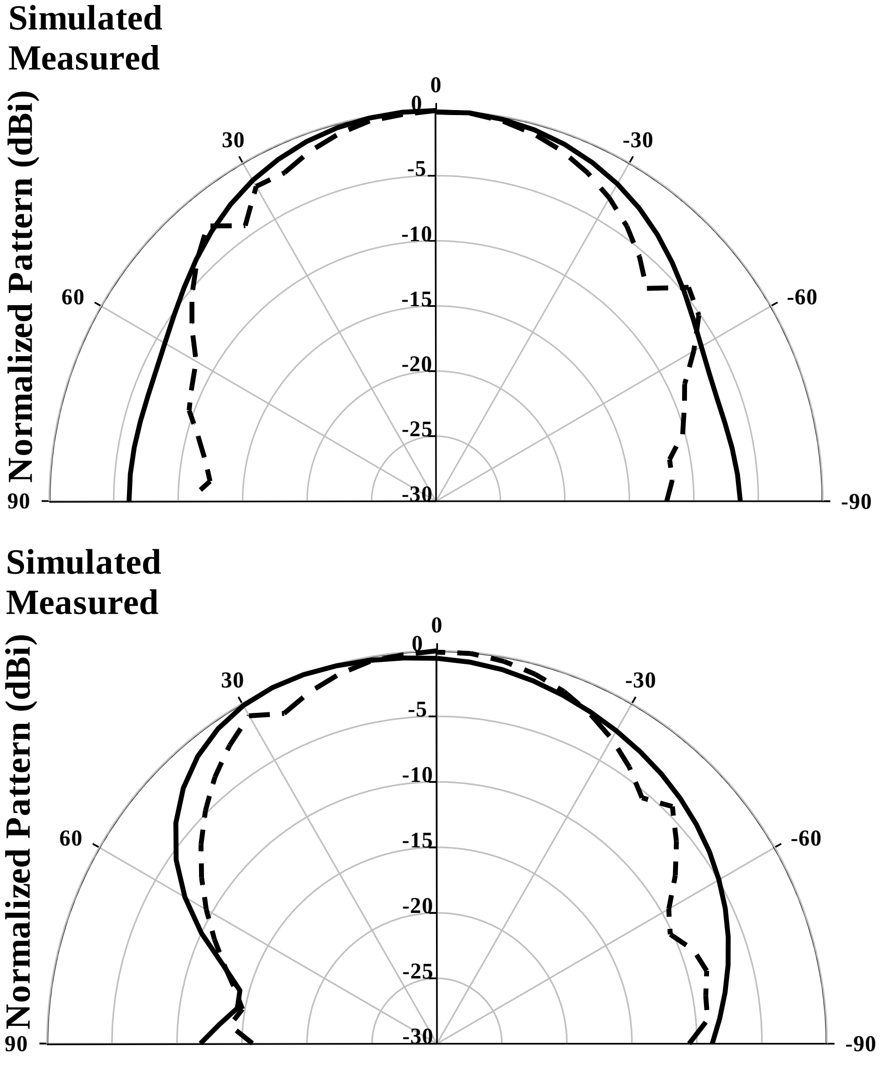

(b)

Figure 2.15: The E and H planes radiation patterns of a hemispherical DRA with a highlighted position on the ground plane (a) 22.7 GHz (b) 27 GHz at ε_r= 9.9, ε_s= 3.48, a = 3.8 mm, r = 1.6, l_s = 2 mm and h_s= 0.5 mm.

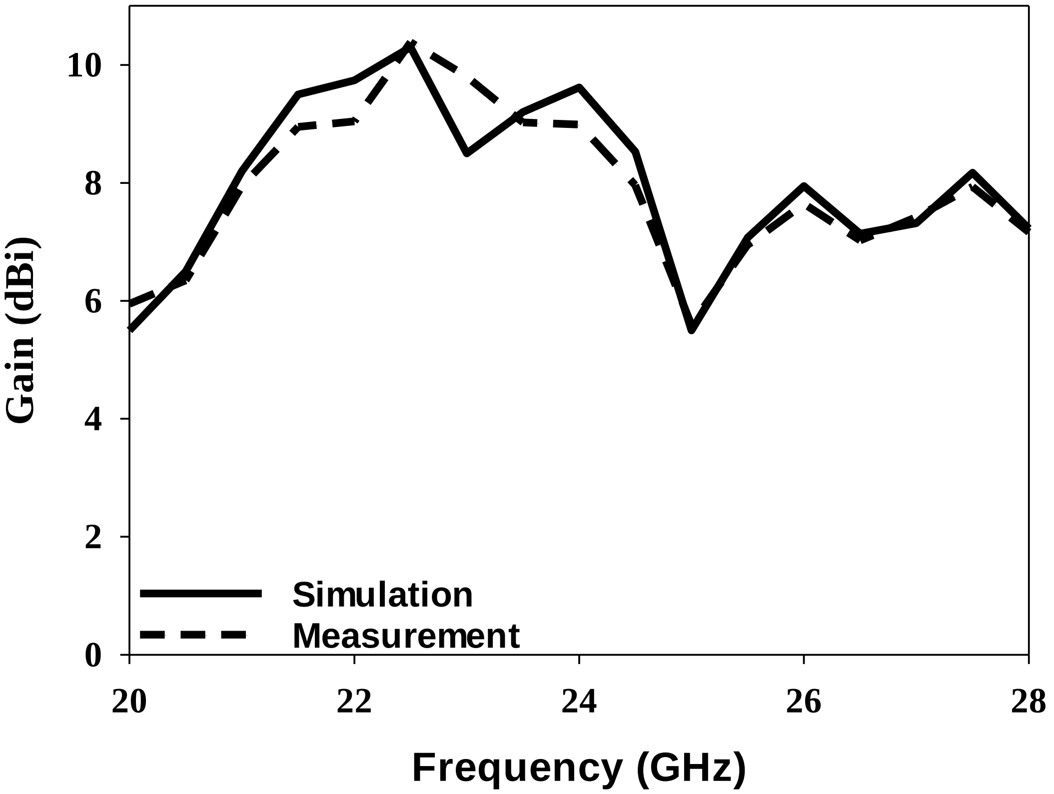

Figure 2.16: Realized gain of a hemispherical DRA placed on a grooved ground plane at ε_r= 9.9, ε_s= 3.48, a = 3.8 mm, r = 1.6, l_s = 2 mm and h_s= 0.5 mm.

2.3.3 3D printing the DRA on a perforated substrate with the same material

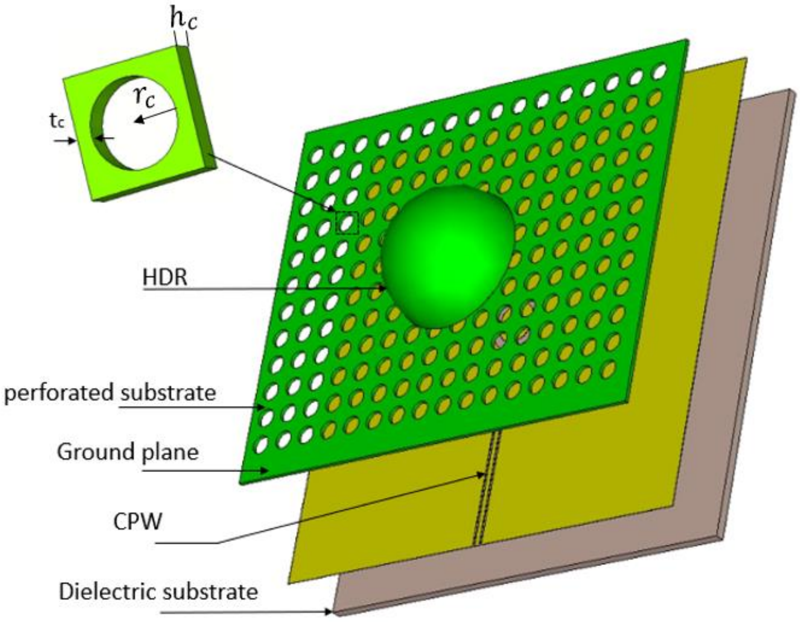

(a)

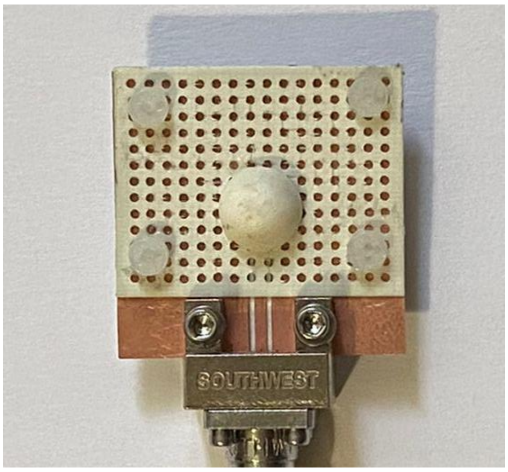

(b)

Figure 2.17: The integrated DRA and perforated substrate configuration (a) 3-D layout, (b) Fabricated DRA.

The configuration in Figure 2.16 presents an alternative approach that aims to avoid any misalignment or bonding problems during the DRA assembly. The proposed configuration integrates an Alumina hemispherical DRA with a square dielectric substrate of the same material, which facilitates the utilization of 3D printing technology (Raptor 3D Printer for Fused Filament Fabrication (F.F.F.)) to fabricate the integrated DRA-substrate structure without needing an adhesive material for bonding. Once more, this is largely an automated process that simplifies the antenna assembly. However, the higher permittivity of the Alumina substrate represents a key challenge, and it needs to be considerably reduced to minimize the chance of exciting surface waves. A reduced effective dielectric constant can be achieved by creating a perforated Alumina substrate with a regular pattern of cylindrical air-filled holes, which means the DRA and substrate can be 3D printed simultaneously using the same material and 3D printer. The Raptor 3D Printer uses Fused Filament Fabrication (FFF) to produce cost-effective ceramic parts. The process involves using specially fabricated bound filaments of metal or ceramic that are melted and deposited layer by layer to create the desired geometry. After printing, the parts can be machined and heat-treated to eliminate the binder and sintered, resulting in parts with a high relative density of over 99%.

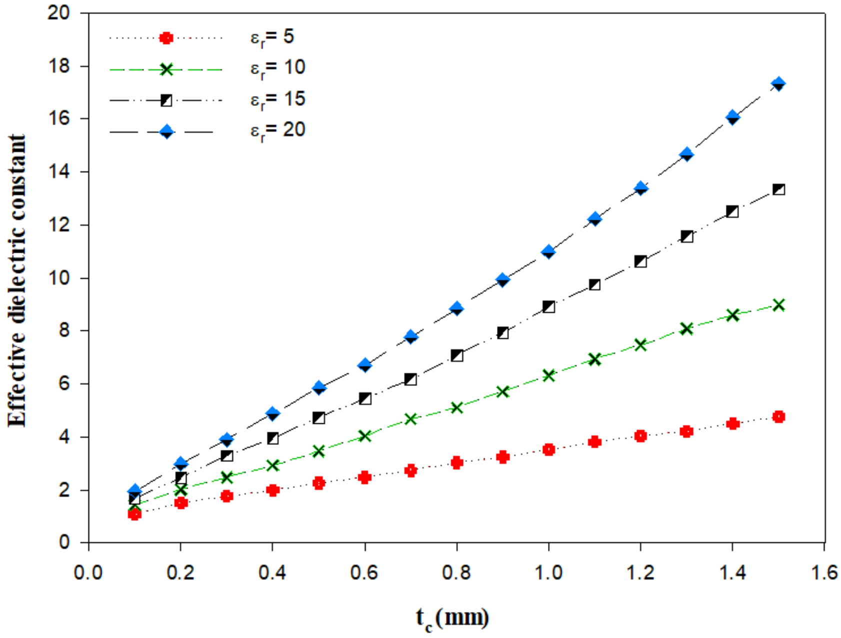

Figure 2.18: The effective permittivity of perforated hemispherical DRA.

The resultant perforated substrate's effective dielectric constant, ε_{eff} , can be calculated as [80]:

$$f_r = \frac{4.775 \times 10^7 \ \mathrm{Re}\,(k_0 a)}{\sqrt{(\varepsilon_r)}a} \tag{2.3}$$

where the spacing between centers of two adjacent air-filled holes, $2t_c$, can be adjusted for a given ε_r so that the required effective relative permittivity is achieved. Figure 2.17 demonstrates the achieved ε_{eff} as a function of t_c by changing the substrate dielectric constant from 5 to 20. As can be observed, a linear relationship exists between t_c and ε_{eff}, when the unit cell radius and substrate height are fixed as 0.5 and 0.3 mm, respectively. In addition, it is also easy to control the effective permittivity of the perforated substrate by adjusting the diameter of the air-filled holes based on the filling ratio theory [81]. Therefore, for an Alumina substrate with $\varepsilon_r = 9.9$, t_c has been chosen as 0.4 mm so that the effective dielectric constant of the perforated substrate is reduced to $\varepsilon_{eff} = 3$, which results in a radiation efficiency of ~ 94% across the operating frequency range. Furthermore, the 3D printed hemispherical DRA has been designed using the same DRA radius of previous sections, i.e., a = 3.8 mm.

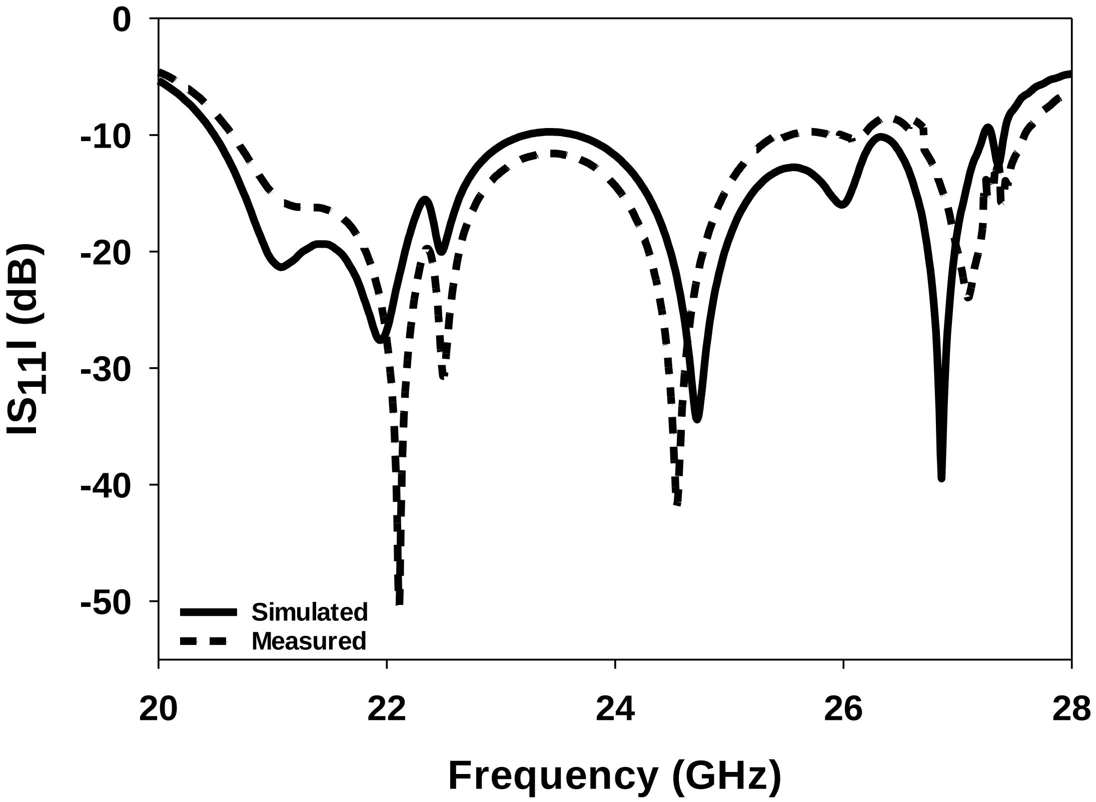

Figure 2.19: The simulated and measured S_{11} of the integrated DRA-perforated substrate configuration at ε_r= 9.9, ε_s= 3.48, a = 3.8 mm, r = 1.6, t_c = 0.4 mm and h_c= 0.3 mm.

The integrated DRA-substrate structure has been fed using a separate feed network that consists of an annular slot with a radius of 1.5 mm combined with coplanar waveguide (CPW) feeding line that has a slot width and separation of 0.35 mm and 0.9 mm, respectively, as illustrated in Figure 2.16. The 2.4 mm end-launch connector was affixed to the CPW line that has been printed on a Rogers substrate with a relative permittivity of 3.48 and a thickness of 0.5 mm. Figure 2.18 illustrates the measured and simulated reflection coefficients over a frequency range of 20-28 GHz, where the same bandwidth of 33% has been achieved in simulations and measurements with a maximum gain of 10 dBi at 22.7 GHz. Figure 2.19 depicts the simulated radiation patterns at 22.7 GHz and 27 GHz at TE_{311} and TE_{112} modes for the E and H planes. The proposed method has provided a close agreement between the measurements and simulations since an automated process has been adopted without using a bonding layer between the DRA and the feeding slot that can impact the performance.

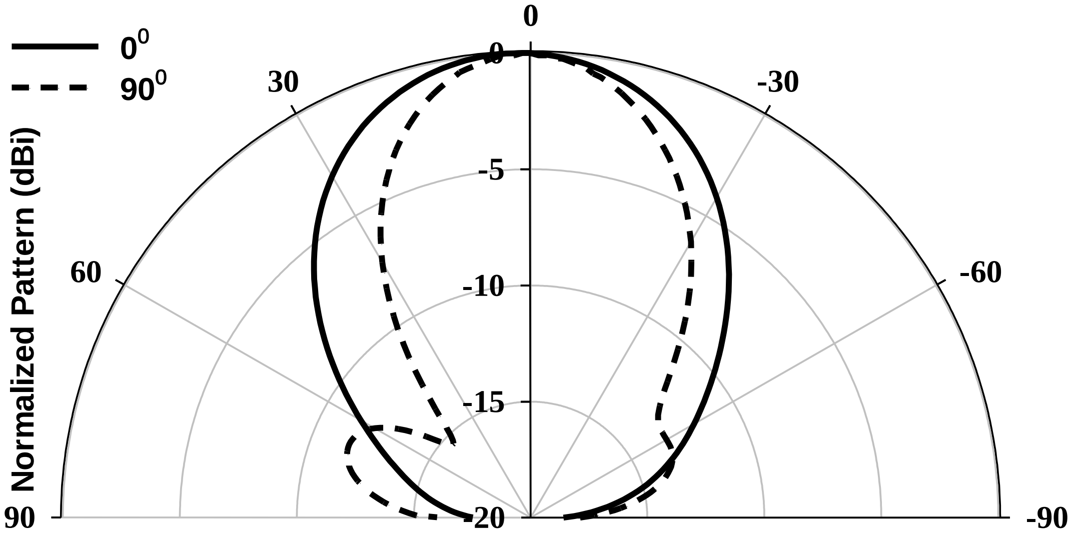

(a)

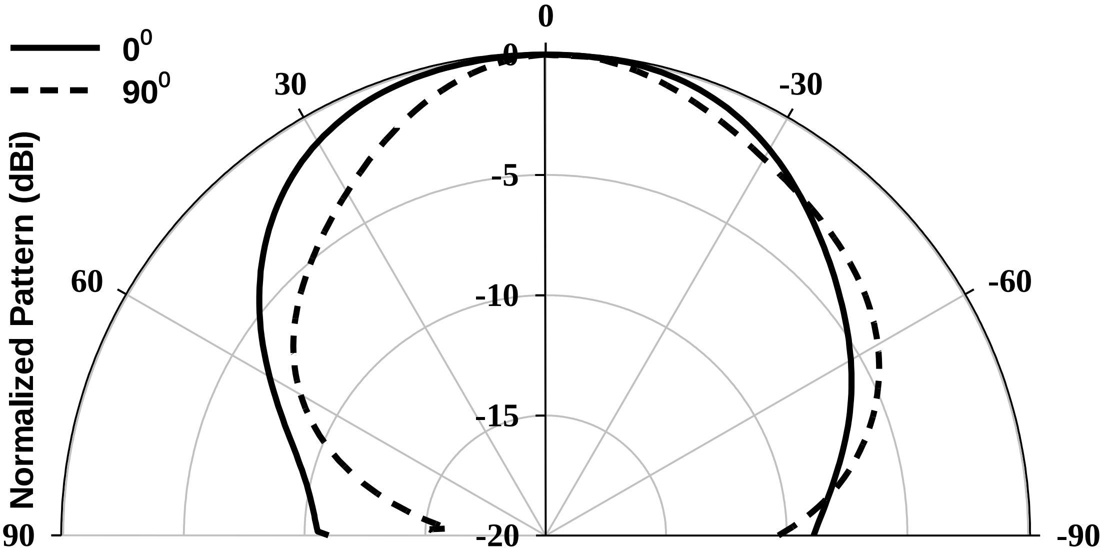

(b)

Figure 2.20: The E and H planes radiation patterns of a hemispherical DRA with a highlighted position on the ground plane (a) 22.7 GHz (b) 27 GHz at ε_r= 9.9, ε_s= 3.48, a = 3.8 mm, r = 1.6, t_c = 0.4 mm and h_c= 0.3 mm.

Table 2-2: Comparison between different techniques of fixture and alignment with the proposed designs

Ref.	Feeding Technique	Comments
[35]	SIW	Applicable for DRAs with uniform cross sections only

[65]	Half-mode SIW	Glue over the slot is used to fix the DRA which resulting in significantly influence
[33]	SIW	Glue is used
[49]	Microstrip	Extra layer of acrylic that increases the size of structure
[66]	SIW	Using fixture holes that create a gap between air holes and vias that effect the performance
[44]	Microstrip	Super glue is used around the DRA and the alignment mark
[57]	SIW	Etching markers and a layer of fixture
This work	Microstrip	Glue is not used under the DRA (Glueless) or mask. Even the outlining approach used a printer to avoid any influence like etching.
	Microstrip	The groove approach overcome any ink fading in case of using the prototype frequently.
	CPW	The integrated DRA offers easy alignment that does not requires any adhesive tape.

Table 2-2 Compares different feeding structures of designs that have been proposed by other studies. The limitations of the alignment and fixture methods are listed for each structure, which leads to the development of the most convenient technique for alignment and fixture in this study. The different feeding techniques investigated by other studies are SIW, Microstrip, Hybrid DRA. One of the alignment techniques used is the application of glue [33, 44, 65]. It has been shown that the use of glue is disadvantageous since it affects the performance of the DRA. Other techniques of fixture involve adding an extra layer of acrylic [49], using fixture holes [66],

and etching markers [57]. The disadvantages of each are mentioned in Table 2-2. This study proposes a simple feeding structure, namely microstrip and CPW, whereby neither glue nor mask are used to avoid affecting the magnitude and performance of the DRA.

2.4 CONCLUSION

The challenges of the alignment and bonding of mm-wave DRA have been addressed by proposing three procedures that are based on highlighting the position of the DRA on the ground plane, introducing a circular groove in a secondary ground plane to accommodate the DRA and the 3D printing of an integrated DRA-perforated substrate structure. An array of two DRAs has also been built and measured using a ground plane over which the DRA positions are highlighted. All the prototypes have been measured with close agreement between simulated and measured results. The proposed methods save a considerable time that is usually needed for mm-wave DRAs prototyping in a cost-effective approach. In addition, they can be used with any the DRA geometries that have uniform or non-uniform cross sections. The same DRA was used in the three proposed procedures with a consistent performance in terms of the attractive radiation characteristics such that, the impedance bandwidth of 33% and a maximum gain of 10 dBi. In addition, the proposed methods are largely automated with minimum manual assembly, which improves the measurements’ accuracy. The choice of which method to utilize depends mainly on the project’s time frame and fabrication cost. Although all the suggested processes offer low-cost and rapid prototyping of single DRA and arrays with finite number of elements, the 3D printing of an integrated DRA-perforated substrate is also suitable for large DRA arrays and large-scale production for 5G-and-byeond communication systems.

Chapter 3

Wideband Circularly Polarized Hemispherical Dielectric Resonator Antenna

3.1 Introduction

When a signal is sent using a linearly polarised (LP) wave, there should be an accurate alignment between the transmitting and receiving antennas. On the other hand, a circularly polarised (CP) radiation offers a greater flexibility in the orientation of the transmitting and receiving antennas, which means the alignment requirements are not as strict as that in the LP radiation. Hence, circular polarisation is advantageous in such cases. In addition, CP radiation can help in establishing a reliable communication at constantly changing weather that could be harsh at times. The CP wave can also suppress multipath interference as well as reduce any polarisation mismatch since a CP signal is received and sent in all planes, where the strength of the signal is not lost compared to LP.

In mm-wave communication systems, the weather conditions play a significant role in affecting the performance of the antenna. Circular polarisation can be used to overcome polarisation rotation effects that result from atmospheres like reflections from obstacles as well as multi path fading. Furthermore, another reason to use CP antennas is that there is a direct line of sight path across the radio link [82]. On the contrary, in linear polarisation, if a matched polarisation is not maintained, then the interruptions that result from the increased polarisation losses could happen frequently. Therefore, circularly polarised antennas are used since there would be no need to track polarisation with transmitter and receiver lines in space.

When a plane radio wave propagates over a long distance, it has no field components along the travelling *z* direction, thus is in the form of a transverse electromagnetic (TEM) plane wave. The instantaneous field of such a plane wave can be expressed as:

$$E = E_x + E_y \tag{3.1}$$

where the E_x and E_y components are specified as:

$$E_x = E_{xm}\cos\left(\omega t + k_{\mathrm{o}z} + \phi_x\right) \tag{3.2a}$$

$$E_y = E_{ym}\cos\left(\omega t + k_{\mathrm{o}z} + \phi_y\right) \tag{3.2b}$$

where E_{xm} and E_{ym} are the maximum values and k_{0z} is the free-space wavenumber defined as $k_{0z} = 2\pi/\lambda$. The radiated wave's polarisation can be classified into linear, circular, or elliptical, based on the direction of its electric field vector E. When $z = 0$, equation (3.2) can be simplified as [83]:

$$E_x = E_{xm}\cos\left(\omega t + \phi_x\right) \tag{3.3a}$$

$$E_y = E_{ym}\cos\left(\omega t + \phi_y\right) \tag{3.3b}$$

The polarisation is circular only when both of E_x and E_y field components have the same magnitude and in quadrature, i.e.

$$E_{xm} = E_{ym} = E_m \tag{3.4}$$

$$\Delta\phi = \phi_y - \phi_x = \pm\frac{\pi}{2} + 2n\pi, \quad n = 0,1,2,\ldots. \tag{3.5}$$

When $\phi_y - \phi_x = \pi/2$, equation (3.3) can be expressed as:

$$E_x = E_m\cos\left(\omega t + \phi_x\right) \tag{3.6a}$$

$$E_y = E_m\cos\left(\omega t + \phi_x + \frac{\pi}{2}\right) = -E_m\sin(\omega t + \phi_x) \tag{3.7b}$$

It is well-known that the magnitude of the electric field vector is constant, and the direction varies with time. Accordingly, the electric field vector rotates in a circle in the xy plane, i.e., it rotates along the propagation direction as illustrated in Figure 3.1. Further, in the case of circular polarisation, when the rotation of the electric field vector is counter clockwise then the polarisation sense is defined as a Left-Hand Circular Polarisation (LHCP) as illustrated in Figure 3.1(a). Moreover, when the electric field vector rotates clockwise, as illustrated in Figure 3.1(b), the polarisation sense is defined as Right-Hand Circular Polarisation (RHCP).

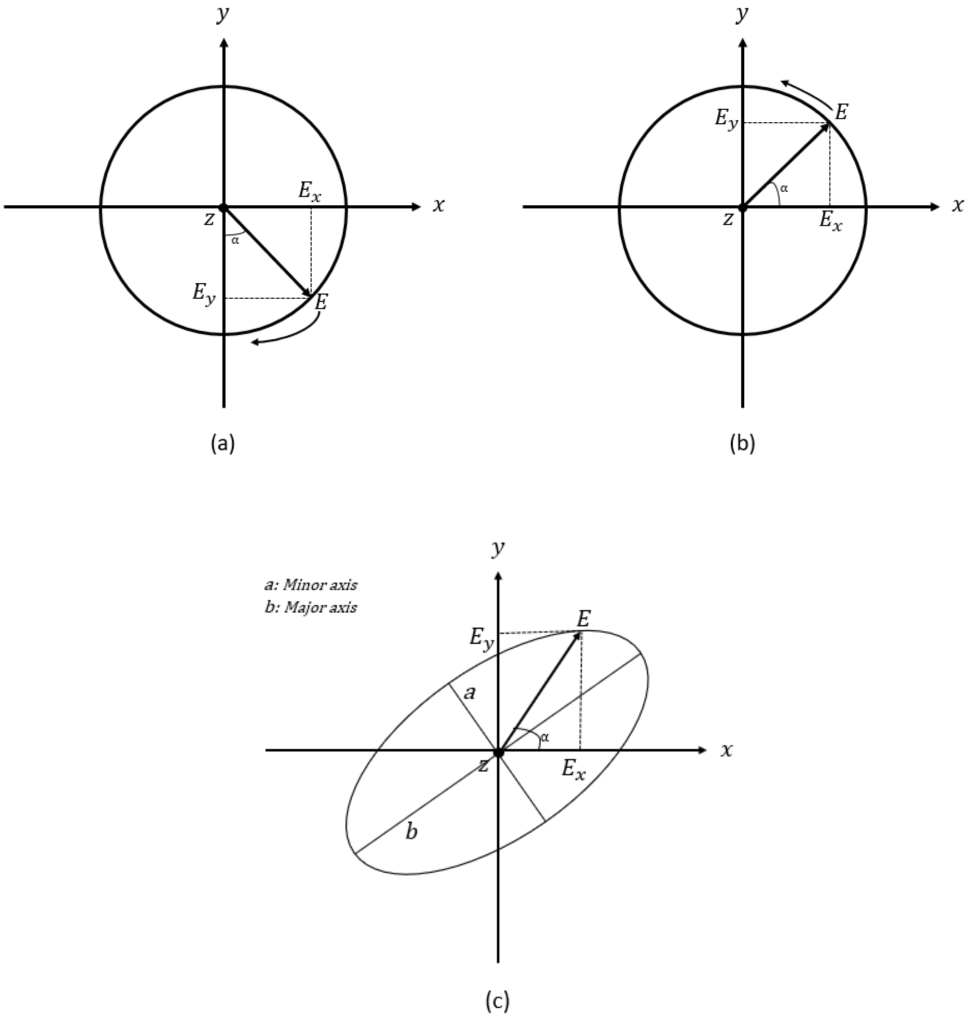

Figure 3.1: E-field vector of (a) Right-Hand Circular Polarisation and (b) Left-Hand Circular Polarisation (c) elliptical polarisation.

The quality of the circular polarisation is assessed using the axial ratio (AR) parameter, which is calculated by dividing the maximum by the minimum electric field strengths that correspond to the maximum and minimum radii of the ellipse, respectively, as illustrated in Figure 3.1(c). Therefore, the mathematical expression of the axial ratio is:

$$\mathrm{AR} = 20\log\left(\frac{E_{max}}{E_{min}}\right) \tag{3.8}$$

where $|E|_{\substack{max \\ min}} = \sqrt{\frac{1}{2}\left(E_x^2 + E_y^2 \pm \sqrt{E_x^4 + E_y^4 + 2E_x^2 E_y^2 cos2\Delta\phi}\,\right)}$. From the aforementioned equation, it can be noted that when E_x and E_y have the same magnitudes and out of phase by 90°, then the $E_{max} = E_{min}$ and AR = 0 dB, which means the wave's polarisation is circular. Practically, AR ≤ 3 dB is the acceptable level of AR in which a circular polarisation is considered to be achieved, i.e., a linear polarisation exists when if AR>3 dB.

3.2 Circularly Polarised Hemispherical DRA

This Chapter will introduce three different DRA configurations that have been implemented to improve the CP performance of the designed mm-wave antennas. The first configuration involves optimising the feeding slot size. The second configuration introduces a new substrate layer between the DRA and the slotted ground plane. Such a layer is added to improve the CP bandwidth and reduce the sensitivity of misalignment between the DRA and the feeding slot as will be demonstrated later. The third configuration develops an integrated DRA-perforated substrate configuration, which is used for the first time to improve the CP bandwidth.

As mentioned earlier, a circularly polarised radiation can be achieved by modifying the DRA dimensions and/or the feeding method to excite the two orthogonal degenerate modes that are needed to generate the CP radiation. Unlike rectangular and cylindrical DRAs, the hemispherical DRA radius offers zero degree of freedom, which limits the options of designing an antenna with a reasonable CP bandwidth. This limitation is more noticeable at mm-wave frequencies since many of the lower frequency feeding methods, such as probe and conformal strip feedings are impractical due to the physically small antenna dimensions. Another challenge is the increased probability of working at higher order modes at the mm-wave frequency, where it is well-know that such modes support narrow bandwidths. Besides, compared to S_{11}, the axial ratio is much more sensitive to any misalignment between the DRA and feeding slot position as well as the addition of a glue layer.

An annular ring slot fed hemispherical DRA has been reported with a CP bandwidth of ~6% using a coaxial cable and backing hemispherical metal cavity at 2 GHz [84]. Another study reported a hemispherical DRA that has been excited by a conformal strip or a rectangular slot with a CP bandwidth of 2.4% and 3.4%, respectively [85, 86]. Remarkably, the CP bandwidth of the rectangular slot is higher than that of the conformal-strip fed-DRA. Yet, to excite the CP, grounded parasitic patches have been used with both feeding methods. However, a coaxial cable feed, backing cavity and grounded parasitic patches are difficult to utilise at the mm wave frequency range. Further studies have investigated the impact of using spiral slot, shorted annular slot with and without parasitic slot, and U-slot as excitation slots for the Hemispherical DRAs at lower frequencies on the CP bandwidth. It has been found that the CP bandwidth ranges between 2.6% and 4.5% [87-91]. It is worth mentioning that the investigation of the mm-wave CP hemispherical DRA has not been reported earlier. Additionally, the CP bandwidths attained in this study are higher than those attained at low frequencies.

Therefore, a new approach is proposed in this work to design a hemispherical DRA with a wide CP bandwidth. The proposed approach involves incorporating an additional dielectric substrate between the DRA and a ground plane that accommodates a cross slot feeding. In addition, there is another feed substrate that has the ground plane on the upper side and a feeding strip-line on the lower side. Adding another substrate on top of the ground plane provides an additional degree of freedom in the design that can help in utilising CP radiation over a wide bandwidth.

3.2.1 Effect a slot shape on the circular polarisation.

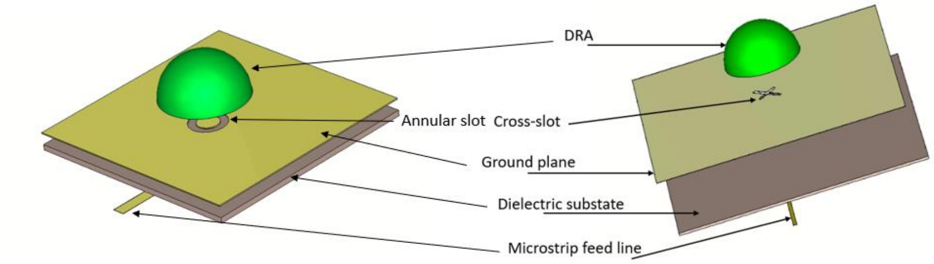

(a) (b)

Figure 3.2: Geometry of the configuration (a) Annular slot (b) Cross slot.

Different feeding slot shapes can be used to generate circular polarisation, but it is evident that some of them are more advantageous than others in terms of improving the CP bandwidth. In this Chapter, a hemispherical DRA that is fed two kinds of slots, namely the annular and the cross slots, has been studied. The annular slot is less flexible compared to the cross slot, which has multiple arms' widths and lengths that can be adjusted. It is noteworthy to mention that the annular slot has been used in Chapter 2 with a wider impedance bandwidth for a linearly polarised hemispherical DRA. However, this is not the case when a circular polarisation is required, as the study demonstrates that cross slots exhibit wider axial ratio bandwidths compared to annular slots. Therefore, cross slots have been used for circular polarisation in this study.

Figures 3.3 and 3.4 illustrate the S_{11} and AR bandwidths, respectively, for an Alumina DRA with a radius of 3.8 mm. The results illustrate that the impedance matching bandwidth of

27.1% in the case of annular slot is wider than that of 7.2% when a cross slot is utilised. However, the results also demonstrate that the circular polarisation is only achieved by the cross slot and not by the annular slot. It should be noted that a coaxial cable-fed annular slot has been used successfully to excite a CP hemispherical DRA in [89] since the antenna was working at the fundamental resonance mode.

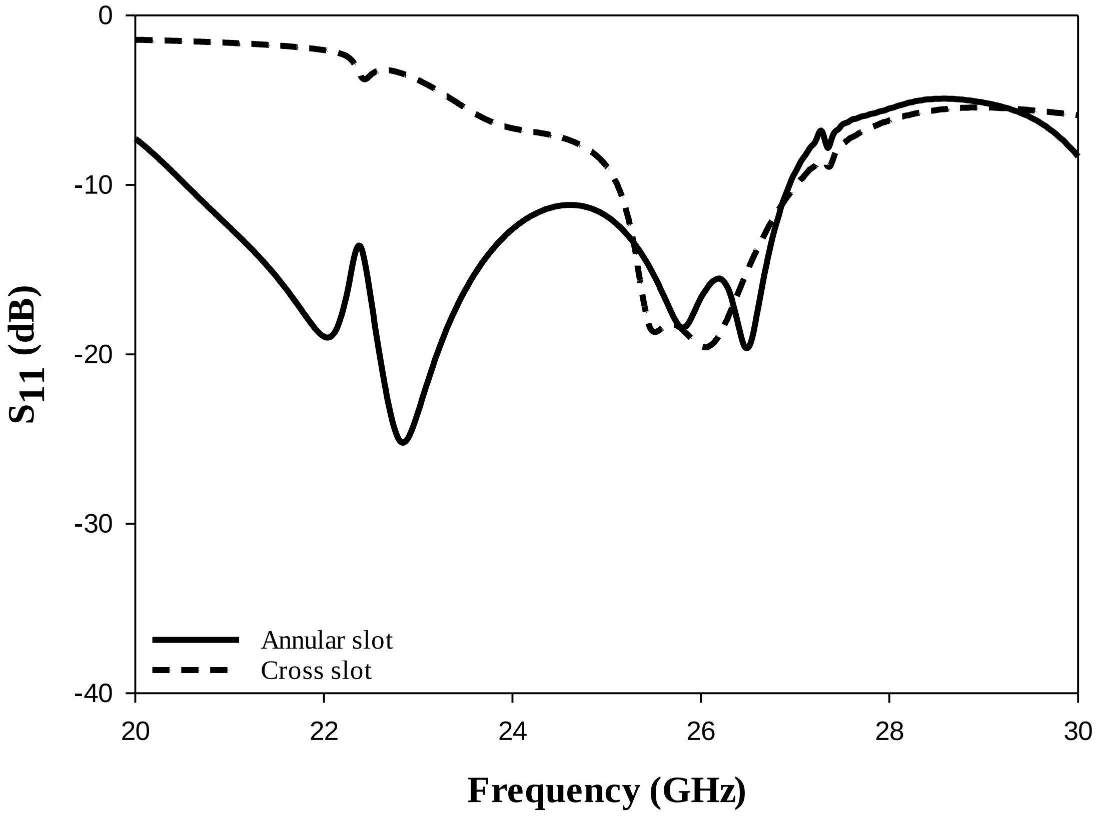

Figure 3.3: Effects of the feeding slot’s shape on the hemispherical DRA return losses.

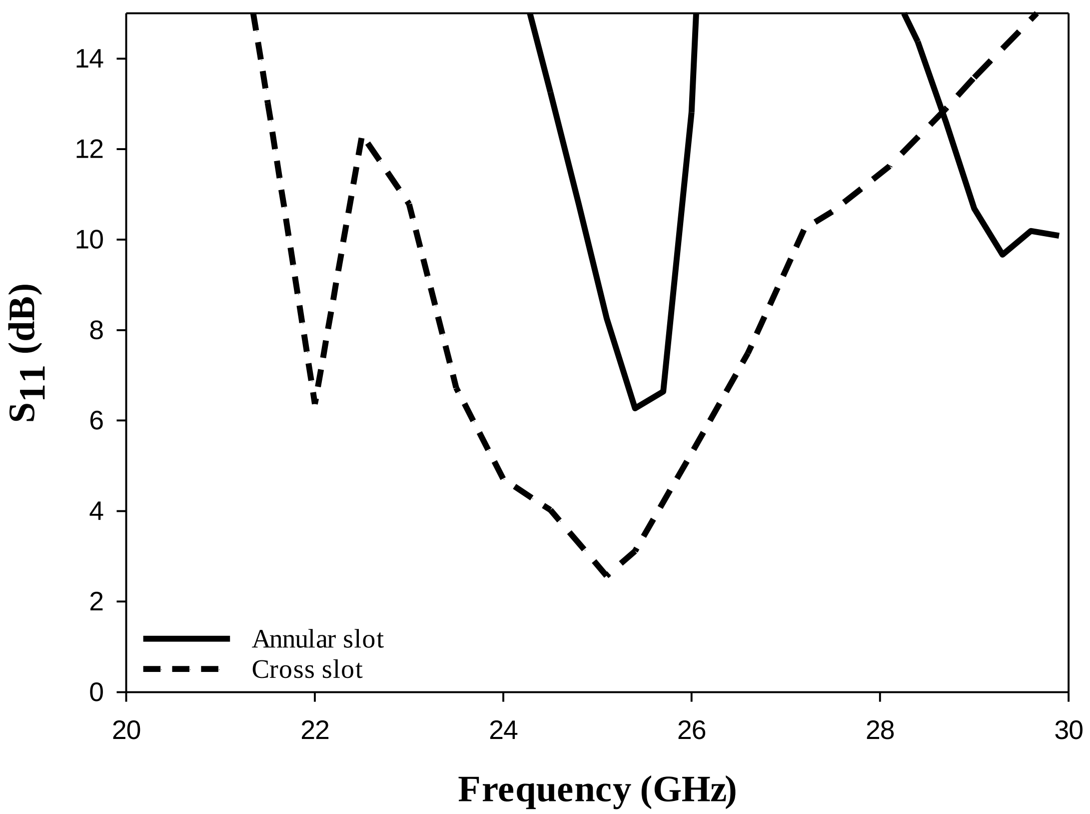

Figure 3.4: Effects feeding slot’s shape on the axial ratio of a hemispherical DRA.

3.2.2 Antenna Configuration

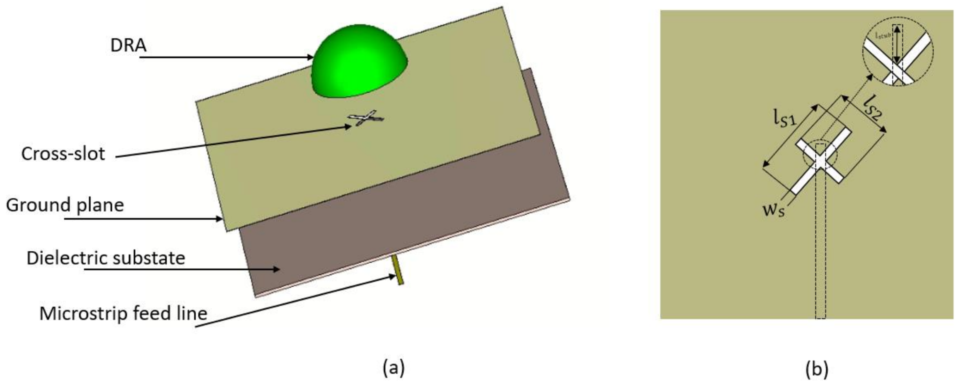

Figure 3.5: Geometry of the configuration (a) 3D view(b) Top view of the feed network

The proposed configuration includes a hemispherical DRA with a radius of r that is placed on a ground plane, which is etched by a cross slot. The cross slot has respective arm lengths of $l_{s1}$and l_{s2} and arm widths of $w_{s1}$and w_{s2}. If the cross-slot lengths were equal, then a linearly polarised wave is radiated. However, in this study, the lengths of the cross-slot arms are unequal while the widths are equal, and this excites the required orthogonal degenerate modes that generate a circularly polarised wave. The utilised substrate beneath the ground plane is a Roger Ro3006, which has a dielectric constant of 6.5 and loss tangent of 0.002 and a thickness of 0.3 mm. Below the substrate, there is a microstrip line that extends beyond the cross slot's centre to form matching stub with a length of l_{stub}. It is worth to mention that the substrate with a dielectric constant of 6.5 was chosen because at the time of fabrication, it was the only material available from the supplier.

3.2.3 Parametric study of the cross slot

A parametric sweep study has been carried out to investigate the effect of different cross slot sizes on the input impedance, gain, and CP bandwidth. Conventionally, a cross slot has three parameters; l_{s1}, l_{s2}, and $w_{s1} = w_{s2}$. Only one of the parameters has been changed at a time while the rest were fixed, as they would represent independent variables to see the effect of changing a particular parameter.

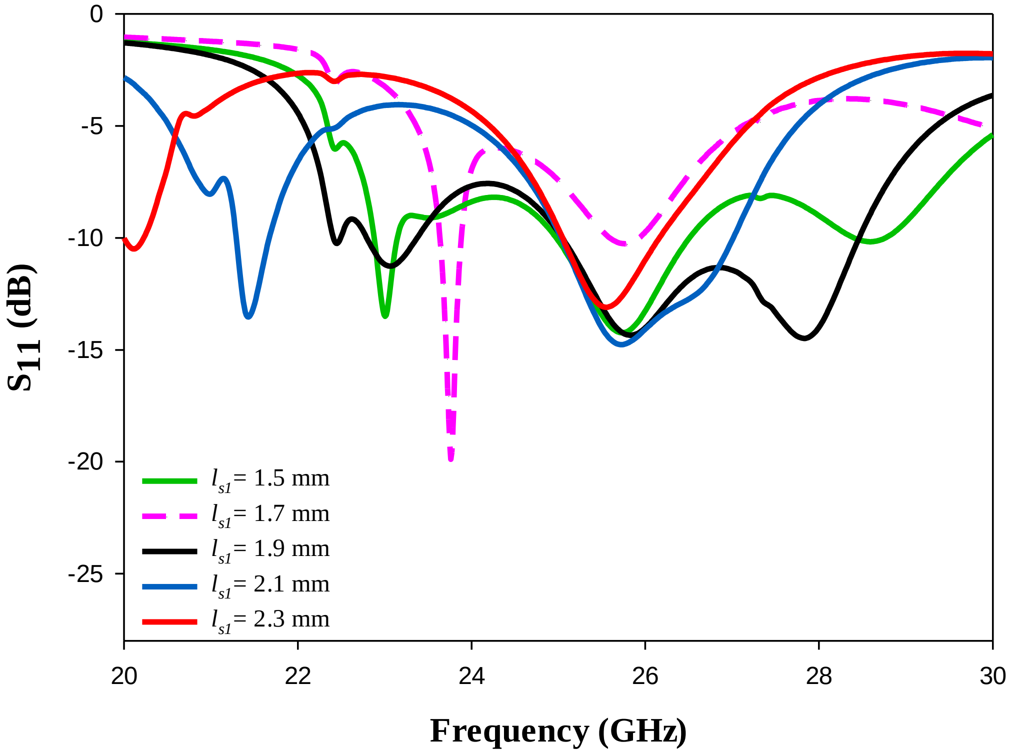

(a)

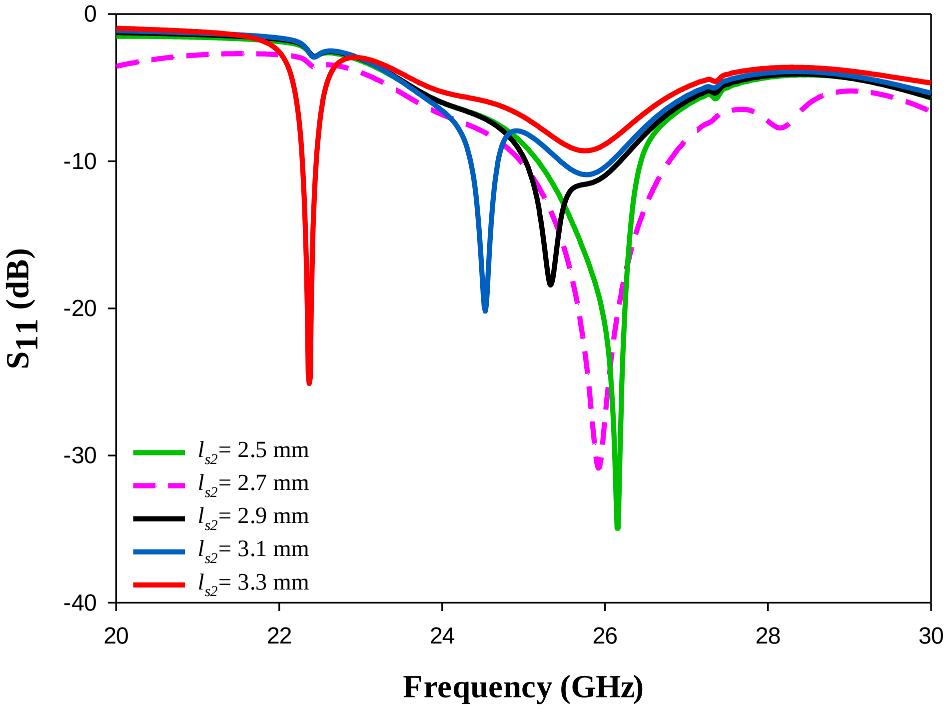
0
-10
-20
-30
-40
20
22
24
26
28
30
S11 (dB)
Frequency (GHz)
ls2= 2.5 mm
ls2= 2.7 mm
ls2= 2.9 mm
ls2= 3.1 mm
ls2= 3.3 mm

(b)

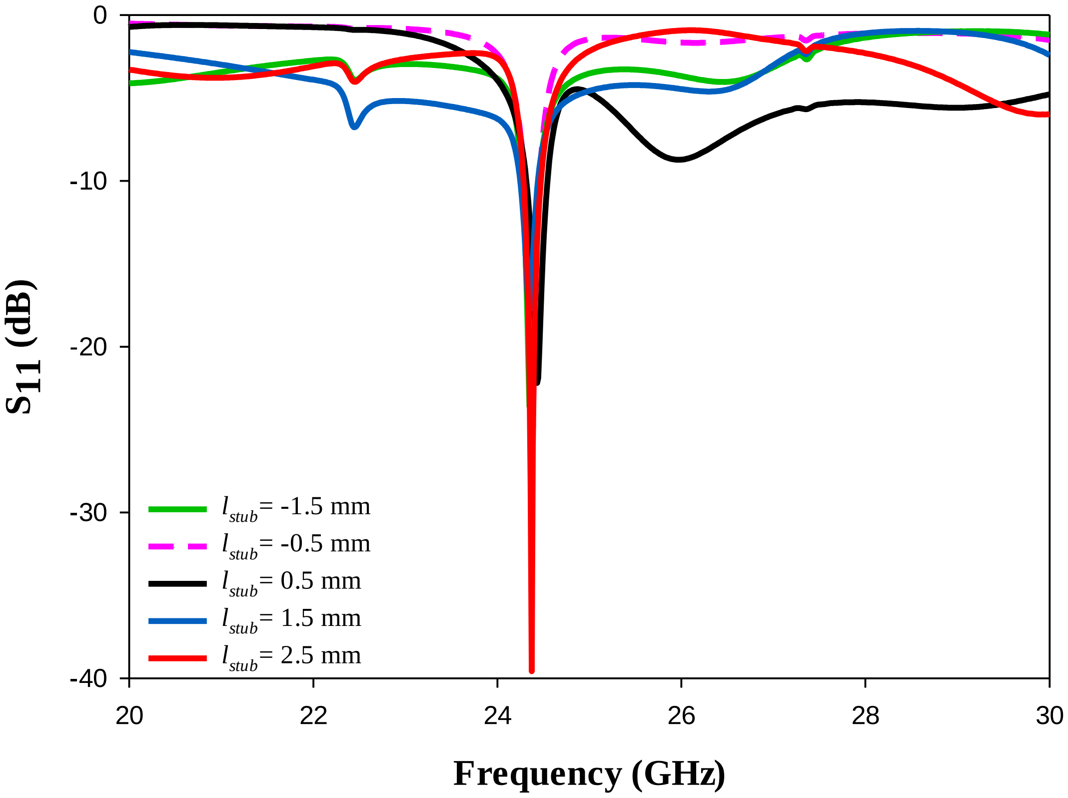
0
-10
-20
-30
-40
20
22
24
26
28
30
S11 (dB)
Frequency (GHz)
lstub= -1.5 mm
lstub= -0.5 mm
lstub= 0.5 mm
lstub= 1.5 mm
lstub= 2.5 mm

(c)

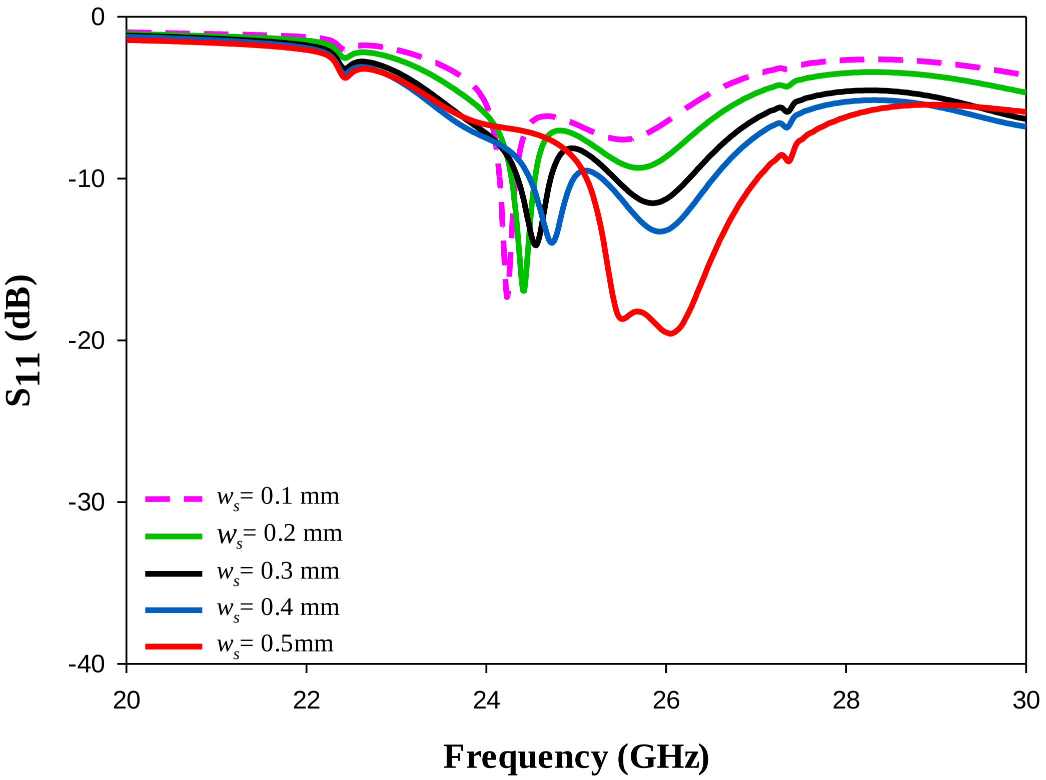

(d)

Figure 3.6: The effect of changing the feed dimensions on the reflection coefficient (a) l_{s1} (b) l_{s2} (c) l_{stub} and (d) w_s .

The effect of changing the slot's arm length and width as well as the stub's length on the impedance, CP bandwidth, and gain is demonstrated in Figure 3.6, 3.7 and 3.8, respectively. In summary, it is evident that changing the lengths and widths can significantly affect the excited resonance mode, which impacts the impedance and CP bandwidths. However, there is marginal variation of the gain against the slot dimensions. The cross-slot arm' length, l_{s1}, has been changed from 1.5 mm to 2.4 mm by a step size of 0.2 mm, while the other slot dimensions were kept constant as l_{s2} = 3 mm and w_s= 0.35 mm. When l_{s1}= 1.5, 1.7, 1.9, 2.1 and 2.3 mm, the DRA achieved impedance bandwidths of 5, 1.2, 11.3, 9.2 and 4.6%, respectively. However, the CP has been achieved only when l_{s1}= 1.7 mm and l_{s2} = 3 mm. Next, the cross-slot arm's length, l_{s2}, has been changed over a small range from 2.5 mm to 3.3 mm by a step size of 0.2 mm, while the other slot dimensions were kept constant as l_{s1}= 1.7 mm and w_s= 0.35 mm. The

CP bandwidth has been attained at all the aforementioned cross slot arm lengths (l_{s2}) with the widest CP bandwidth attained at l_{s2} = 3.1 mm.

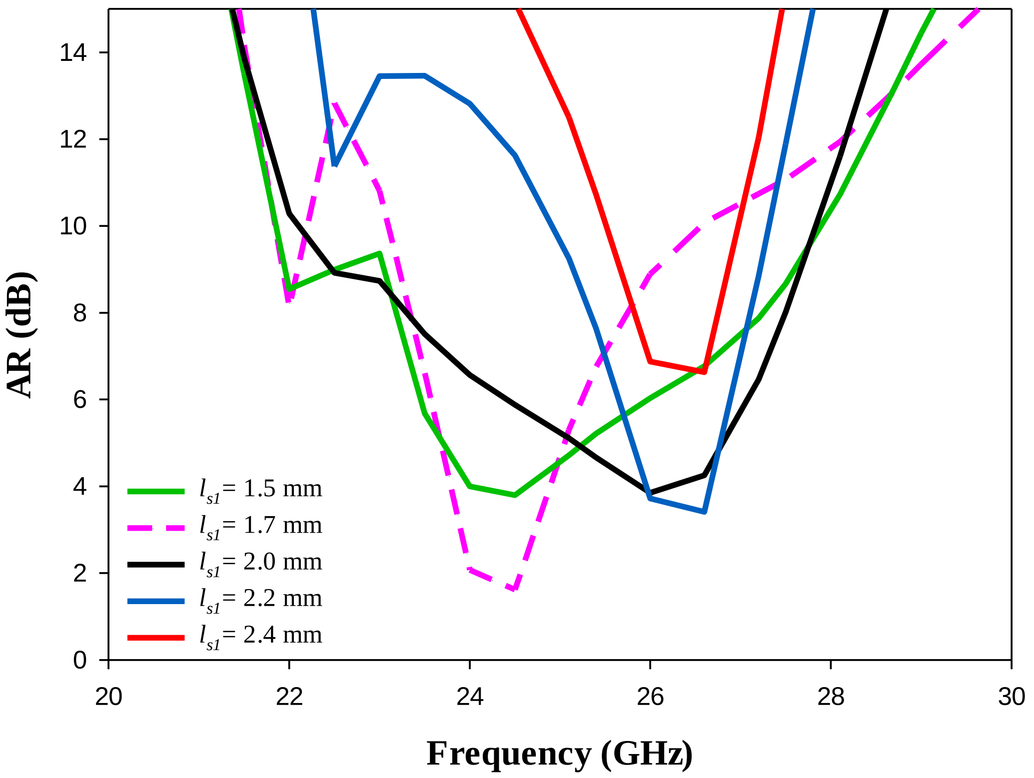

(a)

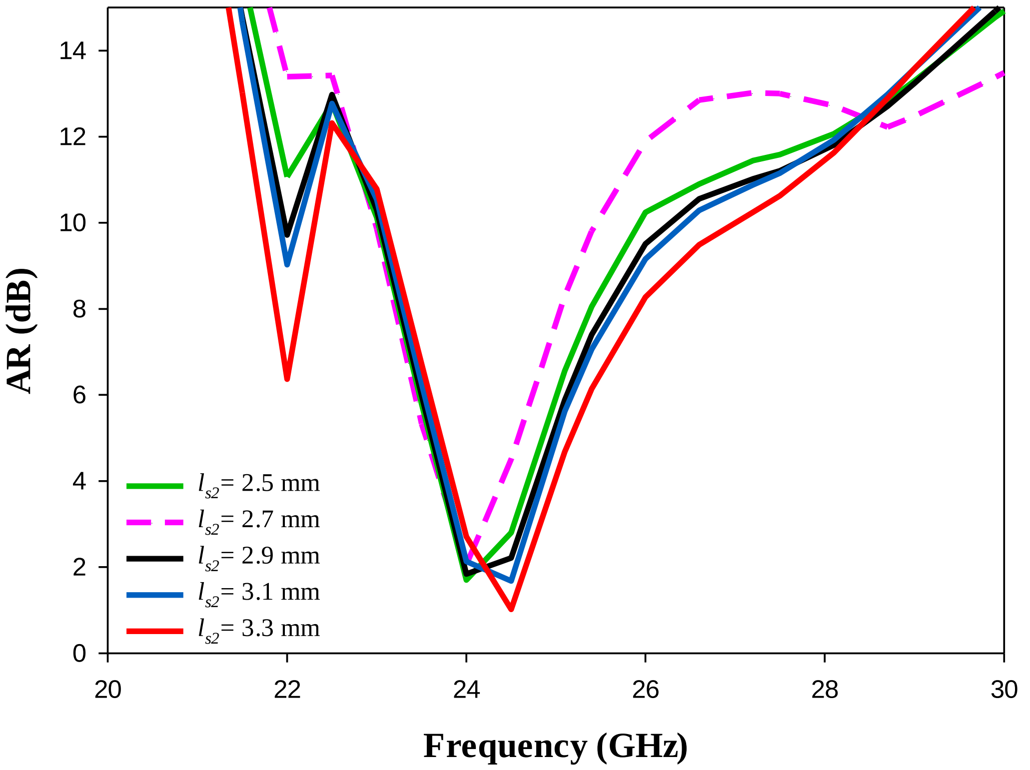

(b)

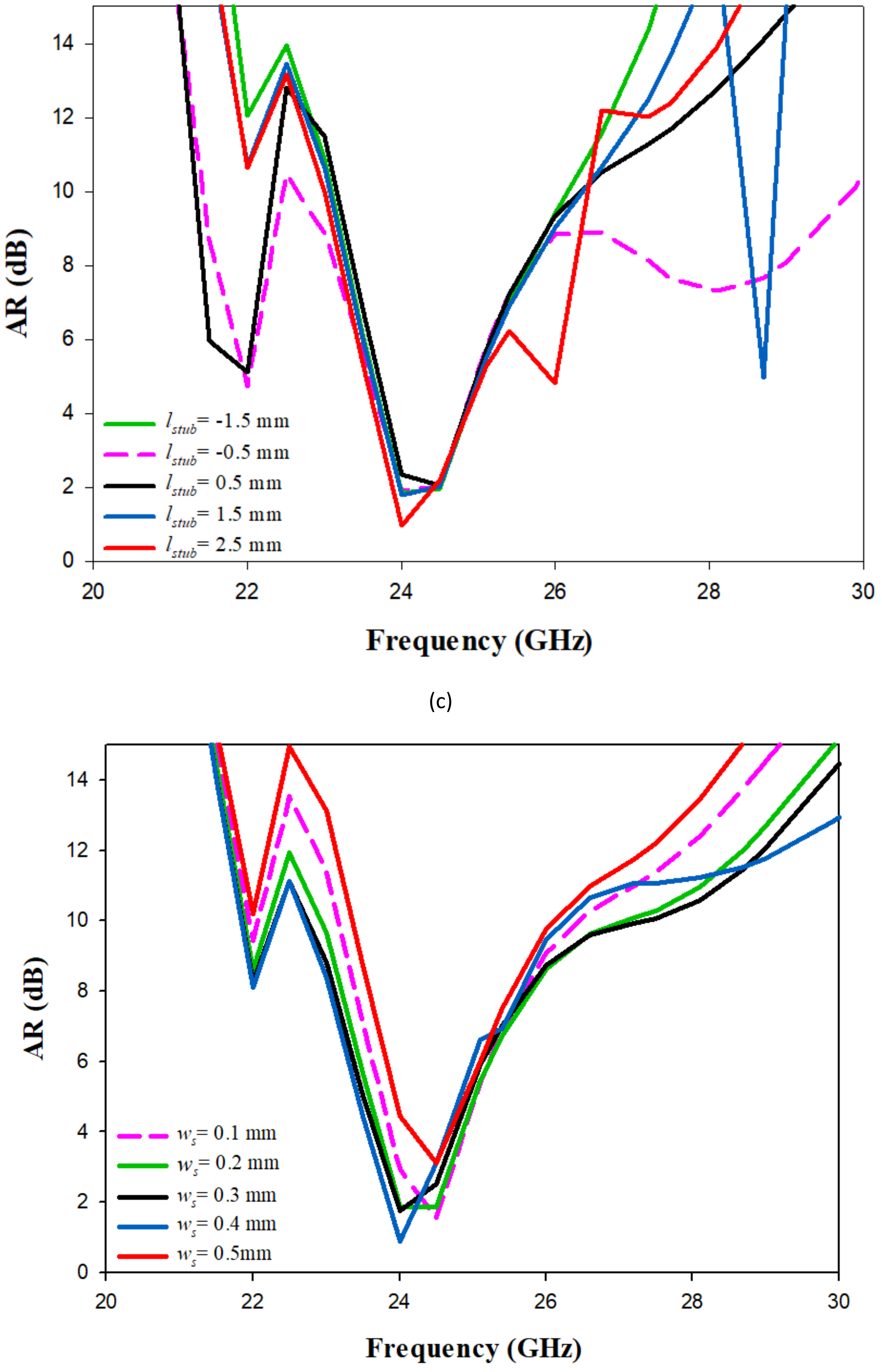

(c)

(d)

Figure 3.7: The effect of changing the feed dimensions on the axial ratio (a) l_{s1} (b) l_{s2} (c) l_{stub} and (d) w_s

Moreover, the width of the slot has been changed from 0.1 mm to 0.5 mm to observe the impact on return loss and CP bandwidth, while the lengths of slots were kept constant (l_{s1}= 1.7, l_{s2}= 3.1 mm). The results in Figure 3.6(d) suggest that when the slot's arm is wider, the impedance matching bandwidth improves. At w_s = 0.4 mm, the return loss and CP bandwidths are 4% and 7.8%, respectively, as the bandwidth shifted to lower frequencies when the width increased. Therefore, the parameters that offer the best results in terms of S_{11} and AR bandwidths have been chosen as l_{s1}= 1.9, l_{s2}= 3.1 and w_s = 0.4 mm. As illustrated in Figure 3.8, a notable change in the directivity is achieved when the cross-slots' dimensions are varied. It should be noted that the radiation is RHCP when l_{s2} is longer than l_{s1}. On the contrary, when $l_{s1}$is longer, a LHCP radiation is achieved.

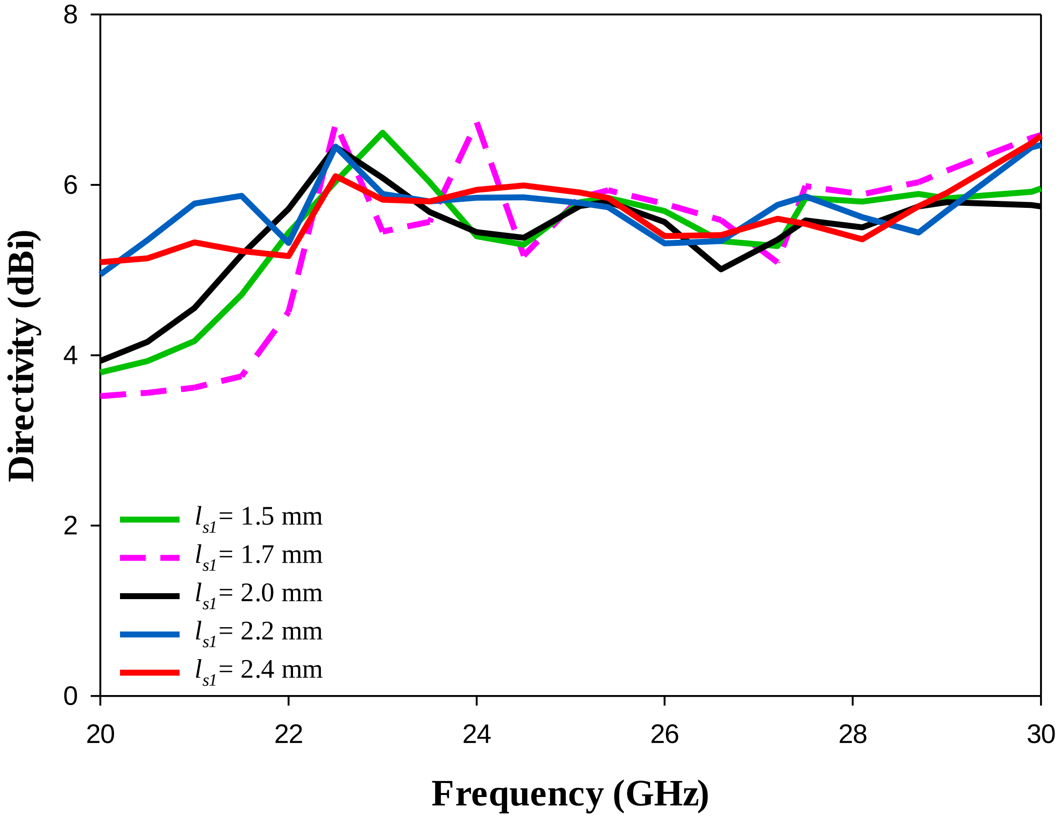

(a)

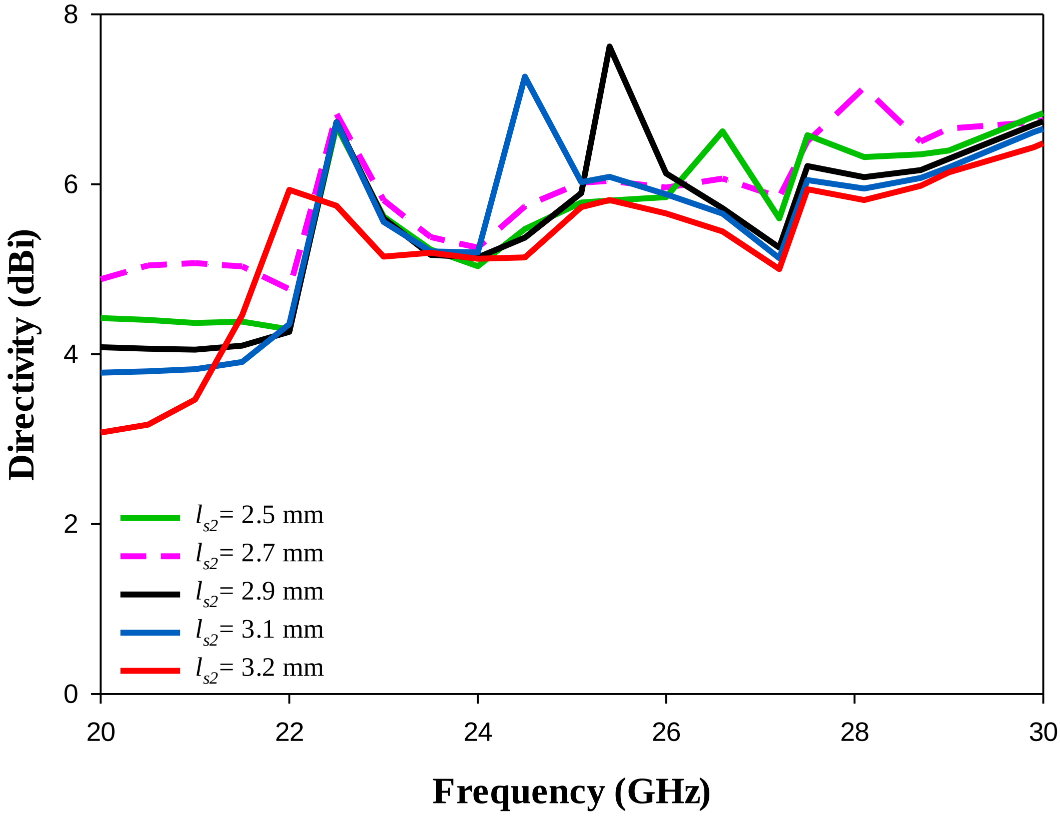
Directivity (dBi)
Frequency (GHz)
0
2
4
6
8
20
22
24
26
28
30
l_{s2}= 2.5 mm
l_{s2}= 2.7 mm
l_{s2}= 2.9 mm
l_{s2}= 3.1 mm
l_{s2}= 3.2 mm

(b)

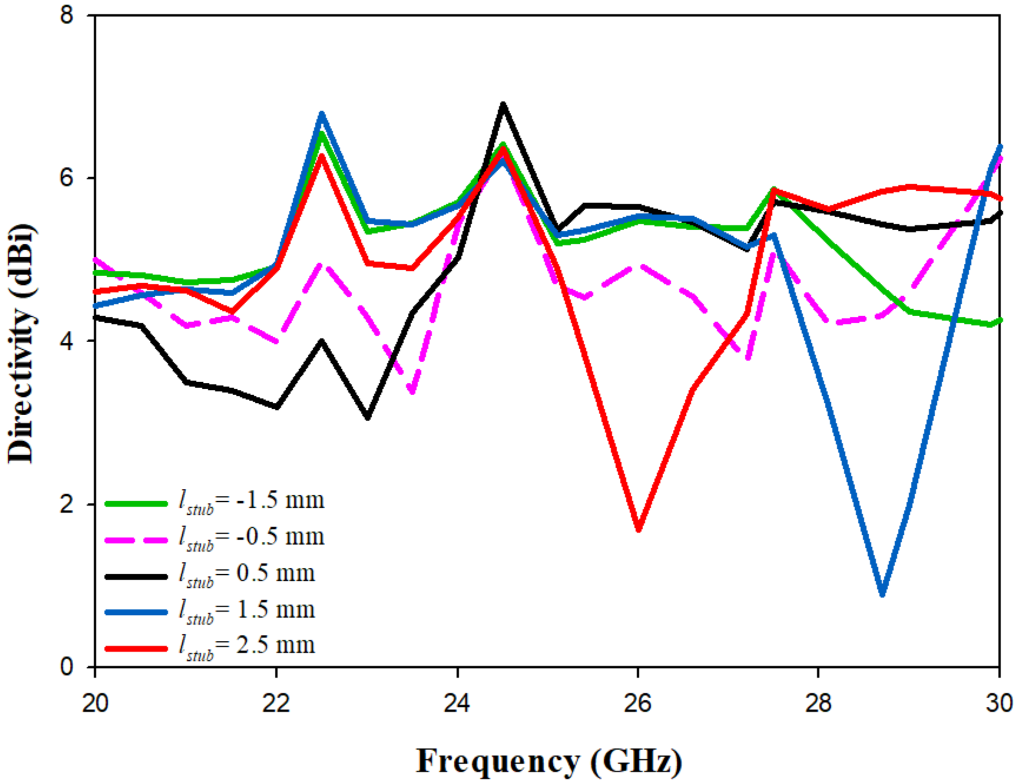
Directivity (dBi)
Frequency (GHz)
0
2
4
6
8
20
22
24
26
28
30
l_{stub}= -1.5 mm
l_{stub}= -0.5 mm
l_{stub}= 0.5 mm
l_{stub}= 1.5 mm
l_{stub}= 2.5 mm

(c)

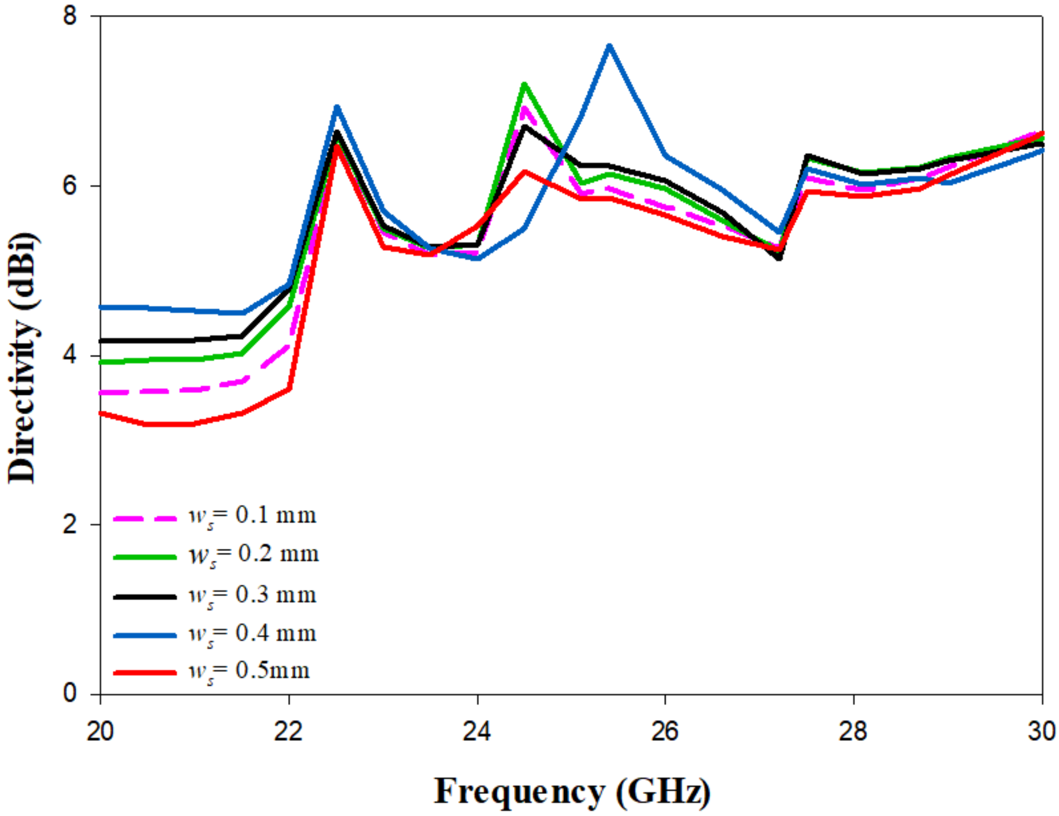

(d)

Figure 3.8: The effect of changing the feed dimensions on the directivity (a) l_{s1} (b) l_{s2} (c) l_{stub} and (d) w_s .

3.3 Incorporating an Additional Dielectric a Substate between the hemispherical DRA and Cross Slot

3.3.1 Antenna Configuration

This section presents the second configuration, which involves the incorporation of another dielectric substrate layer to improve the CP bandwidth. In addition, the added substrate adds another degree of freedom, which allows more flexibility and control over the design. The substrate has a dielectric constant of ε_{r2} and a thickness of h_2, which can be optimised to produce the require CP radiation. The added substrate has the same size, 20 mm × 25 mm, as the ground plane and the original feeding substrate to avoid any errors that could occur from misalignment.

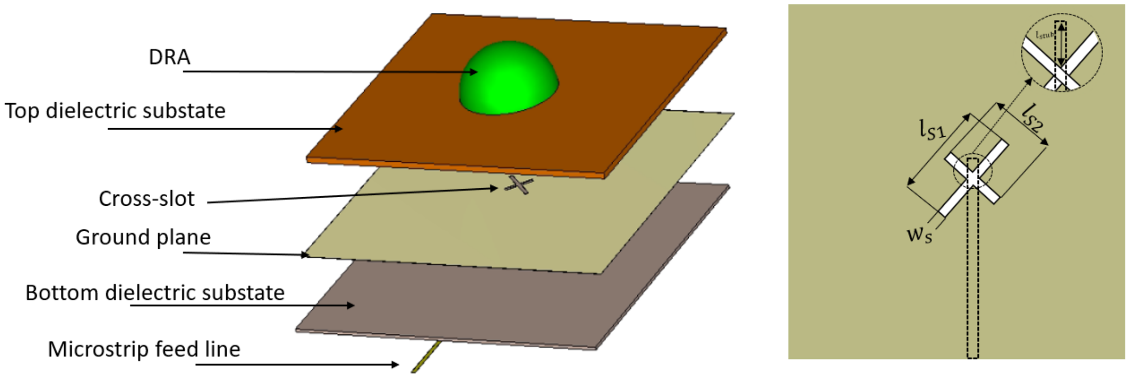

(a) (b)

Figure 3.9: The proposed configuration (a) 3D view(b) Top view of the feed network

The impact of changing the relative dielectric permittivity (ε_{r2}) has been investigated as demonstrated in Figures 3.10 and 3.11 when the height of the top substrate is maintained at 0.6 mm. The examined dielectric constant range is $2 \leq \varepsilon_{r2} \leq 6$. As expected, when the dielectric constant is increased, the resonance frequency and impedance matching bandwidth are reduced. Figure 3.11 demonstrates an overlapping between the impedance and the AR bandwidths at $\varepsilon_{r2} = 3$ only. For the other dielectric constants, the CP bandwidth has been achieved without any overlapping with the impedance bandwidth. As a result, the dielectric constant of the top substrate has been chosen as 3.

Next, the height of the added substrate has been changed from 0.1 mm to 0.9 mm, where it has been observed that increasing the height of the substrate results in a reduction in the impedance bandwidth as illustrated in Figure 3.12. Moreover, the CP bandwidth is achieved when $0.1 \leq h_2 \leq 0.6$ only with the widest CP bandwidth of 11.7% has been achieved using a substrate height of 0.3 mm as demonstrated in Figure 3.13. Therefore, the optimal relative permittivity and height have been determined as 3 and 0.3 mm, respectively.

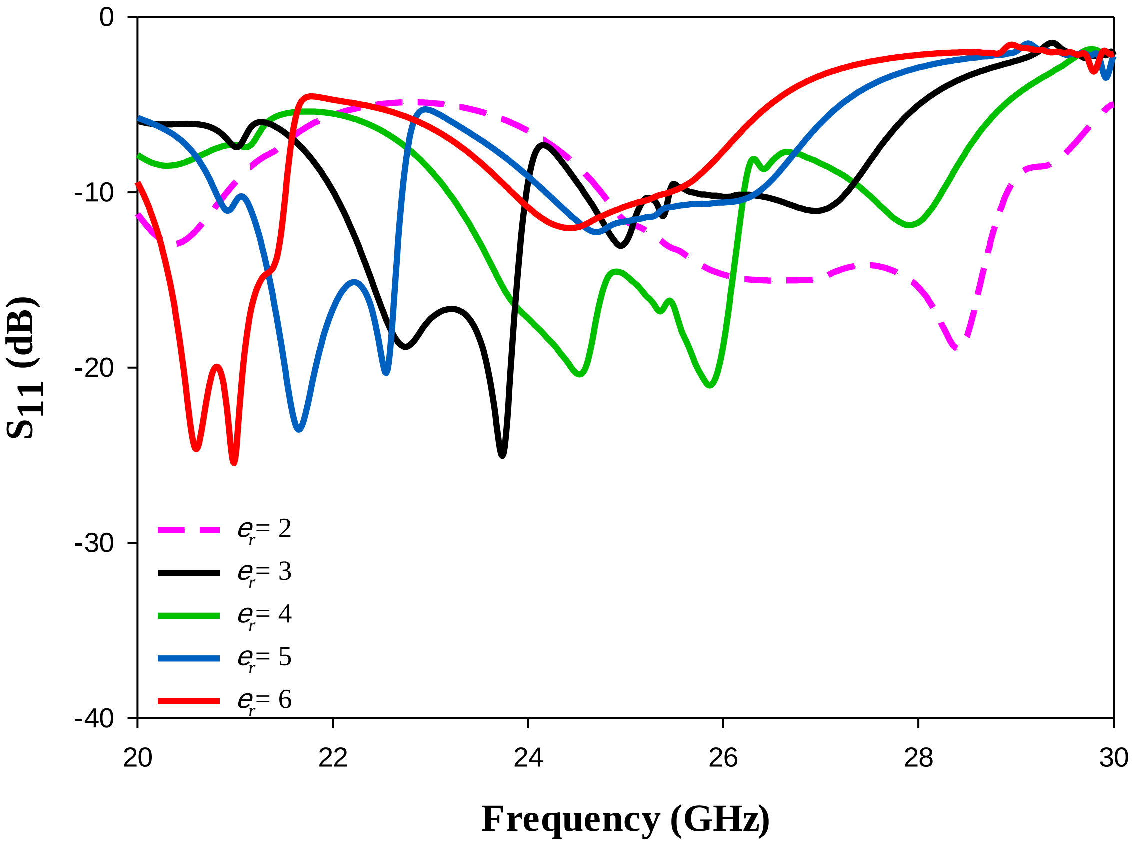

Figure 3.10: Reflection coefficient of a hemispherical DRA as a function of the dielectric constant of the added substrate and frequency.

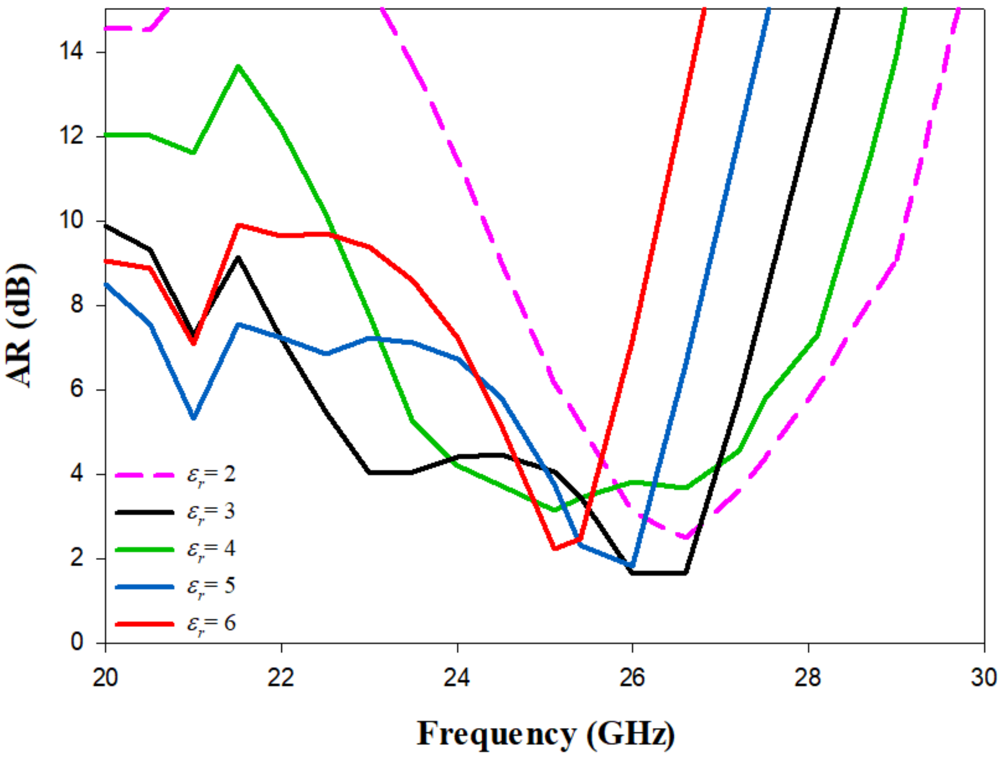

Figure 3.11: Axial ratio of a hemispherical DRA as a function of the dielectric constant of the added substrate and frequency.

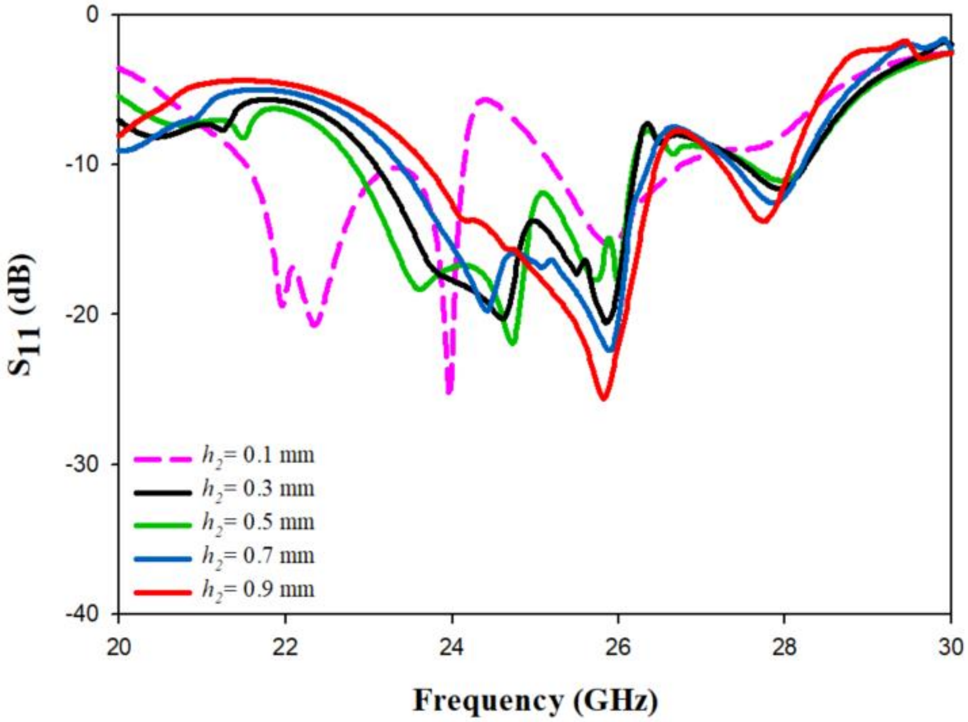

Figure 3.12: Reflection coefficient of a hemispherical DRA as a function of the thickness of the added substrate and frequency.

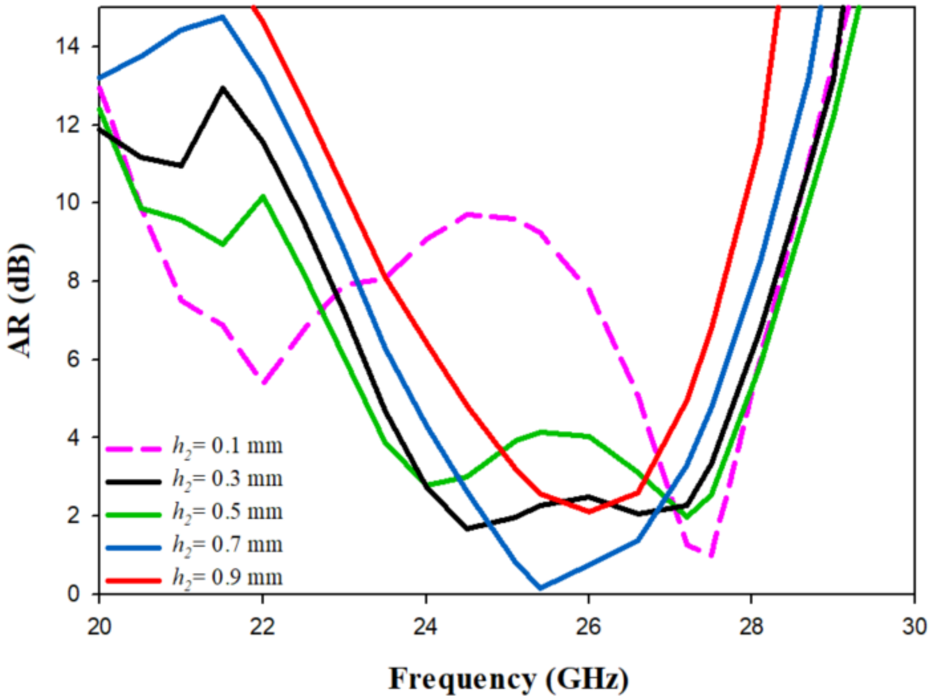

Figure 3.13: Axial ratio of a hemispherical DRA as a function of the thickness of the added substrate and frequency.

The reason why there is a wider bandwidth for the resonator mode is that a layer with a low dielectric permittivity is inserted between a high-permittivity DRA and ground plane. Thus, the electric fields are obliged to pass through low-permittivity region which increases the bandwidth.

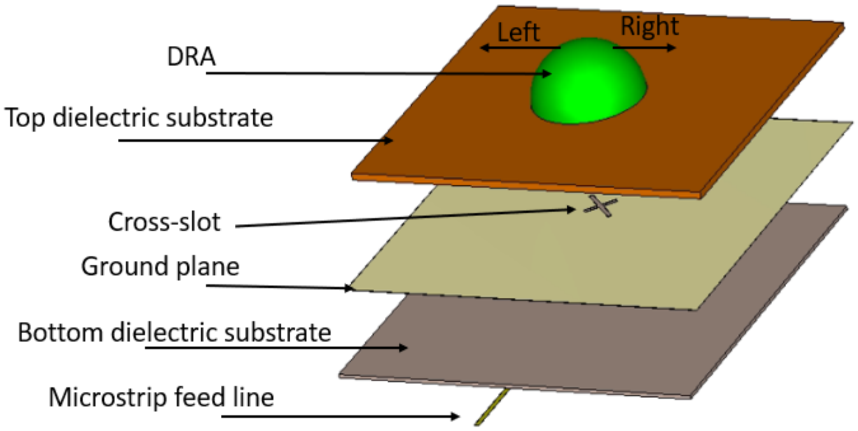

Figure 3.14: The proposed configuration 3D view with directions of shifting.

As well as improving the CP bandwidth, the impact of any misalignment between the DRA and the cross slot can be reduced by inserting a dielectric substrate in-between the DRA and the ground plane. As demonstrated in Figure 3.15, at the absence of the added substrate, a significant change in the performance exists when the DRA position is shifted by 1 mm with respect to the feeding slot. However, this impact is reduced significantly when a substrate is added between the DRA and the feeding slot. As mentioned earlier, at mm-wave frequencies, a slight misalignment in the DRA position can have a significant impact on the results.

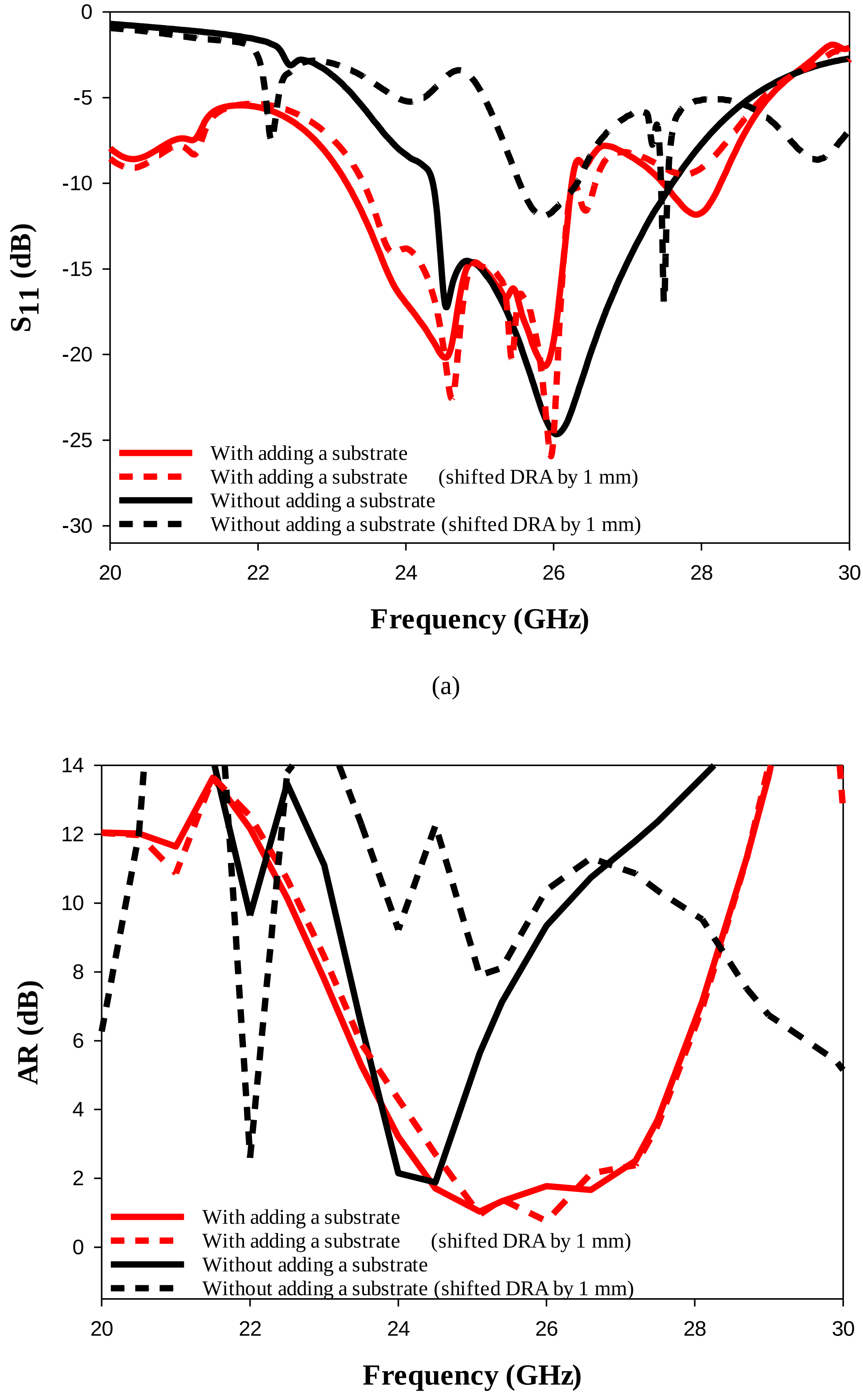

(a)

(b)

Figure 3.15: The impact of misalignment on the performance of a hemispherical DRA with/without adding a top substrate (a) Reflection coefficient (b) Axial ratio.

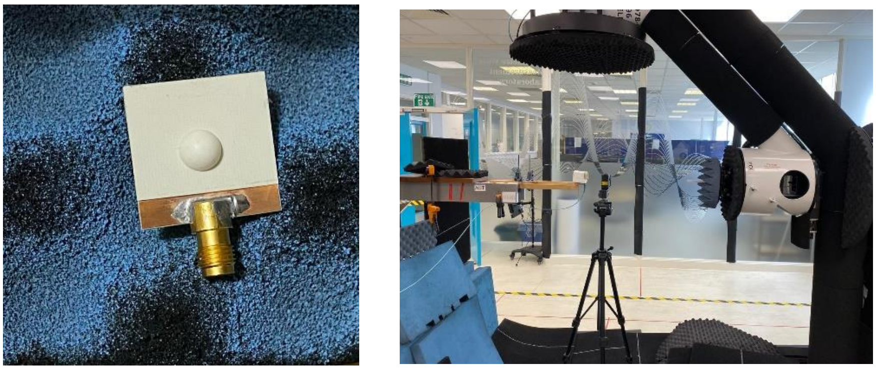

(a) (b)

Figure 3.16: Photographs of (a) Hemispherical DRA with added substrate (b) Hemispherical DRA in the anechoic chamber.

3.3.2 Experimental setup and measured results

Practically, it was not possible to use the theoretically identified optimal height and relative permittivity, as this combination of parameters is not available commercially. As a result, a Roger Ro4350C dielectric substrate with a height of 0.35 mm, a relative permittivity of ε_{r2} = 3.45, and a loss tangent of 0.0037, has been used. The size of the DRA and feeding substrate are kept the same as proposed in Section 3.2, which implies that the DRA has a radius and dielectric constant of 3.8 mm and ε_r = 9.9, respectively. The optimised lengths of the cross-slot arms, 1.7 mm and 3.1 mm, have been used with a stub length of $l_{\text{stub}} = 0.5$ mm. However, the introduction of an additional substrate layer results in a marginal increase of the configuration's profile, which can be justified considering the achieved CP bandwidth.

Figure 3.16 (a) illustrates the DRA prototype that has been fabricated with the add top substrates. It is noteworthy that the position of the DRA was highlighted in an attempt to avoid any misalignment that could occur. The measurements have been conducted using the E5071C mm-wave vector network analyser and the spherical near-field mm-wave measurement system (SNF-FIX-1.0). The reflection coefficient has been measured using a 2.92 mm SMA. An anechoic chamber is an antenna spherical measurement system that is designed by NSI-MI Technologies measurement system. It is located in a mmWave Measurement Laboratory at the

Sheffield university where the measurements are taken, and it can measure frequencies that range from 10 GHz to 110 GHz. Additionally, it is a room that is designed to inhibit reflections of electromagnetic and sound waves, as well as energy from entering the surrounding.

Figure 3.17 illustrates the simulated and measured reflection coefficients, where it can be noted that there is a close agreement between the simulated and measured bandwidths of 12.1% and 14%, respectively. Once more, the impedance matching bandwidth has been achieved by exciting the $TE_{311}$and TE_{112} resonance modes at 23 GHz and 26 GHz, respectively. In addition, the axial ratio is illustrated in Figure 3.18, where it can be observed that the achieved simulated and measured CP bandwidths are 11.7% and 12.1%, respectively. It should be noted that the impedance bandwidth extends from 21.2 GHz to 25.6 GHz, which the CP bandwidth extends from 24 GHz to 27.1 GHz, i.e., there is an overlap of 2 GHz between the two bandwidths that corresponds to 8%. Further, the achieved CP bandwidth is considerably wider than those reported in the literature for hemispherical DRAs. Figure 3.19 illustrates the simulated and measured broadside gain with an average gain bandwidth of 7.5 dBi and a close agreement between simulation and measurements. Figure 3.20 demonstrates a close agreement between the simulated and measured normalised radiation patterns of the excited TE_{311} and TE_{112} resonance modes at 24 GHz and 26 GHz, respectively. The respective simulated and measured half power beamwidths are 79° and 108° at 24 GHz as well as 84° and 110° at 26 GHz, respectively.

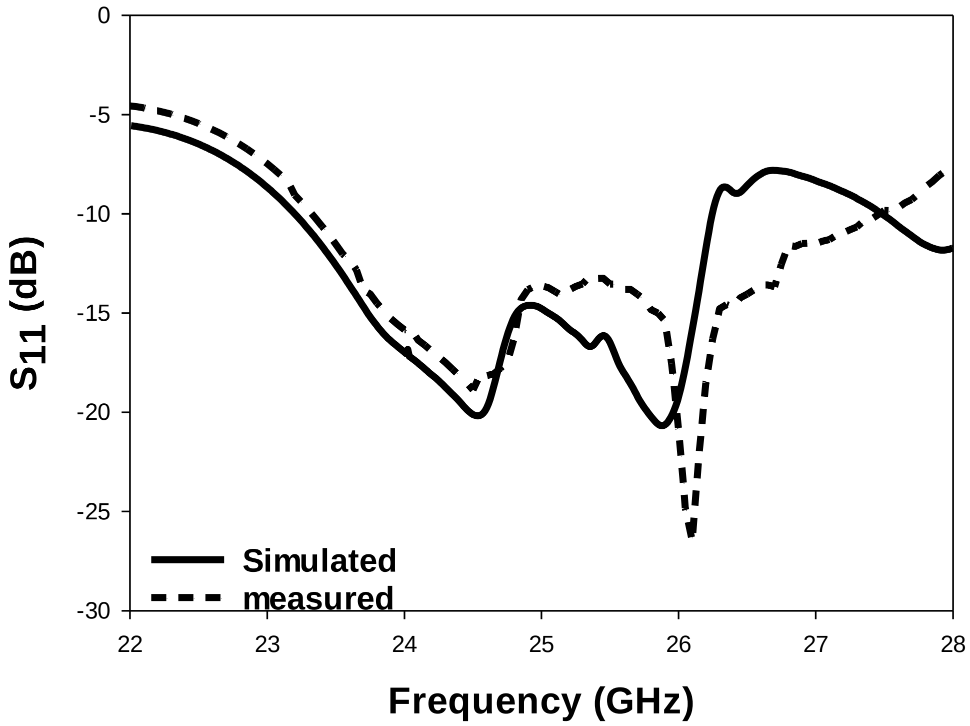

Figure 3.17: Reflection coefficient of a circularly polarised hemispherical DRA with added substrate between the DRA and feed at ε_r= 9.9, ε_s= 3.45, a = 3.8 mm, r = 1.6, l_{stub} = 0.5 mm = l_{s1}= 1.7 mm, l_{s2}= 3.1 mm.

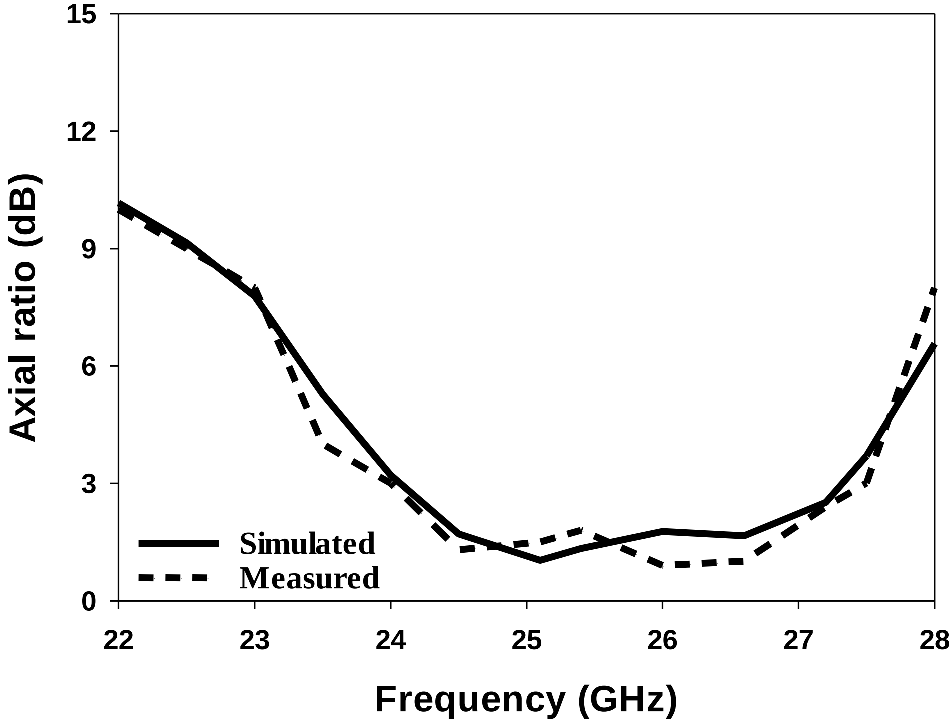

Figure 3.18: Simulated and measured axial ratio of a circularly polarised hemispherical DRA with added substrate between the DRA and feed at ε_r= 9.9, ε_s= 3.45, a = 3.8 mm, r = 1.6, l_{stub} = 0.5 mm = l_{s1}= 1.7 mm, l_{s2}= 3.1 mm.

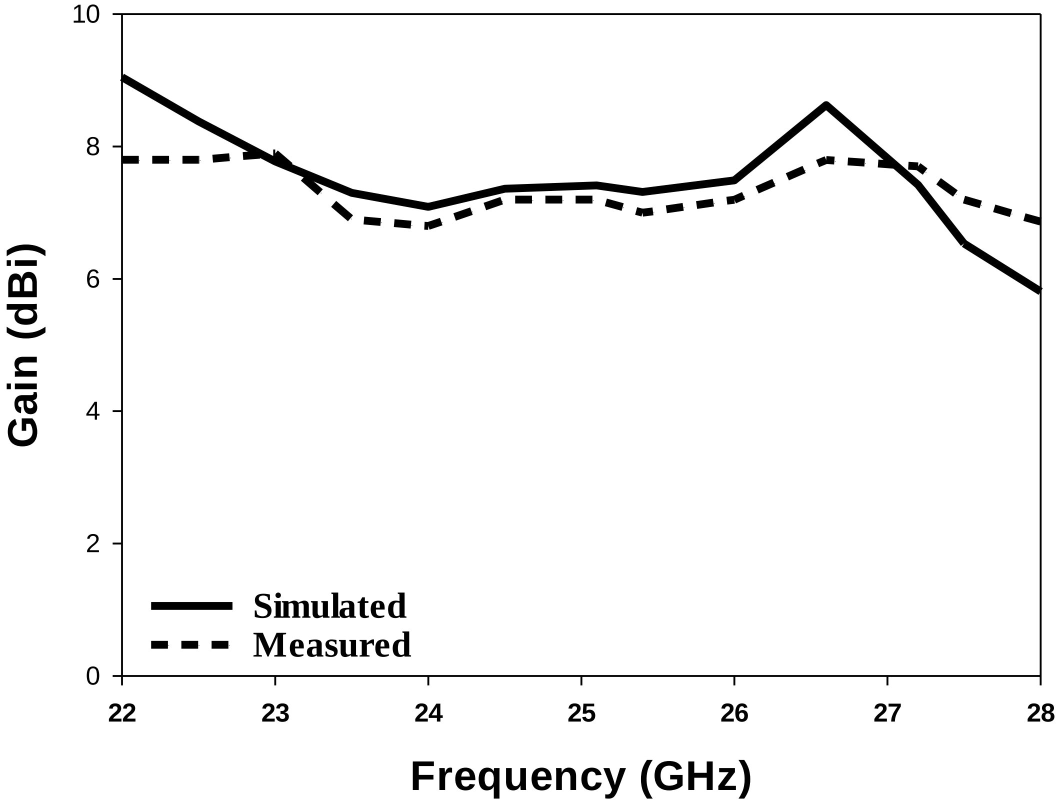

Figure 3.19: Simulated and measured gain of a circularly polarised hemispherical DRA with added substrate between the DRA and feed at ε_r= 9.9, ε_s= 3.45, a = 3.8 mm, r = 1.6, l_{stub} = 0.5 mm = l_{s1}= 1.7 mm, l_{s2}= 3.1 mm.

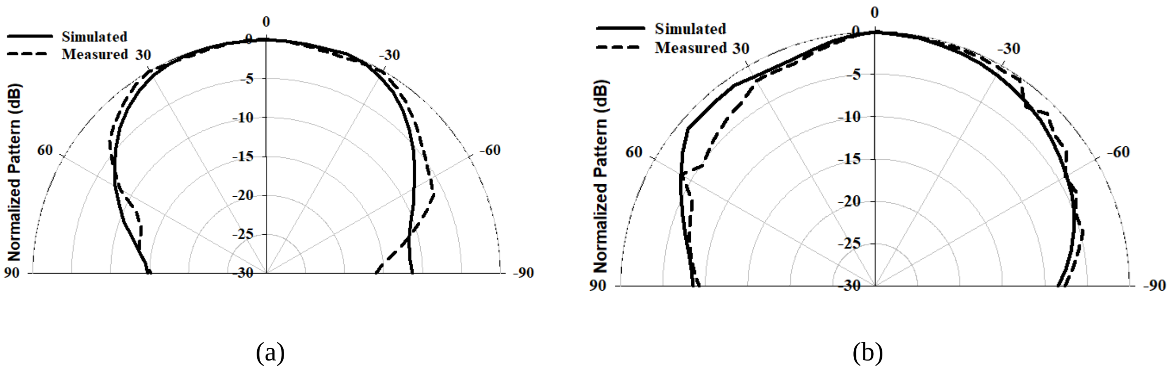

(a)

(b)

Figure 3.20: Radiation pattern of a hemispherical DRA with added substrate at 24 GHz (a) $\phi = 0°$ (b) $\phi = 90°$ at ε_r= 9.9, ε_s= 3.45, a = 3.8 mm, r = 1.6, l_{stub} = 0.5 mm = l_{s1}= 1.7 mm, l_{s2}= 3.1 mm.

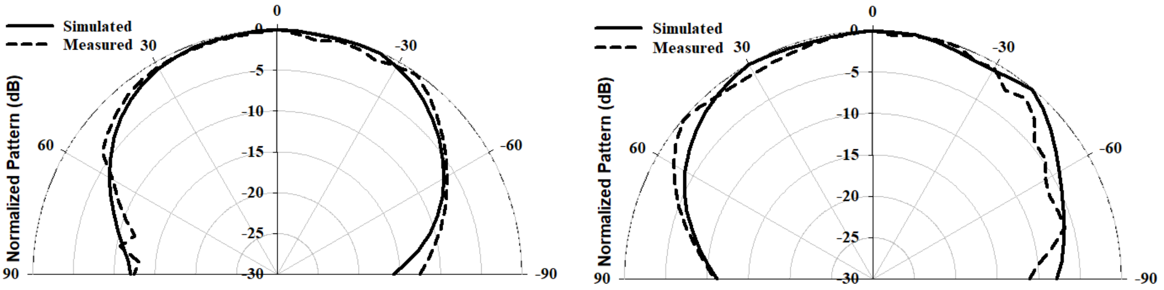

(a) (b)

Figure 3.21: Radiation pattern of a hemispherical DRA with added substrate at 26 GHz (a) $\phi = 0°$ (b) $\phi = 90°$ at ε_r= 9.9, ε_s= 3.45, a = 3.8 mm, r = 1.6, l_{stub} = 0.5 mm = l_{s1}= 1.7 mm, l_{s2}= 3.1 mm.

There are a couple of limitations that result from adding the top dielectric substrate. For instance, the DRA and substrate are not well-integrated, and there is a limited choice of substrates with the required permittivity. Therefore, the next section proposes a technique whereby the DRA is integrated to the substrate using 3D printing technology that does not demand the use of any fixture methods.

3.4 Integrated Hemispherical DRA and Perforated Substrate Configuration

3.4.1 Antenna Configuration

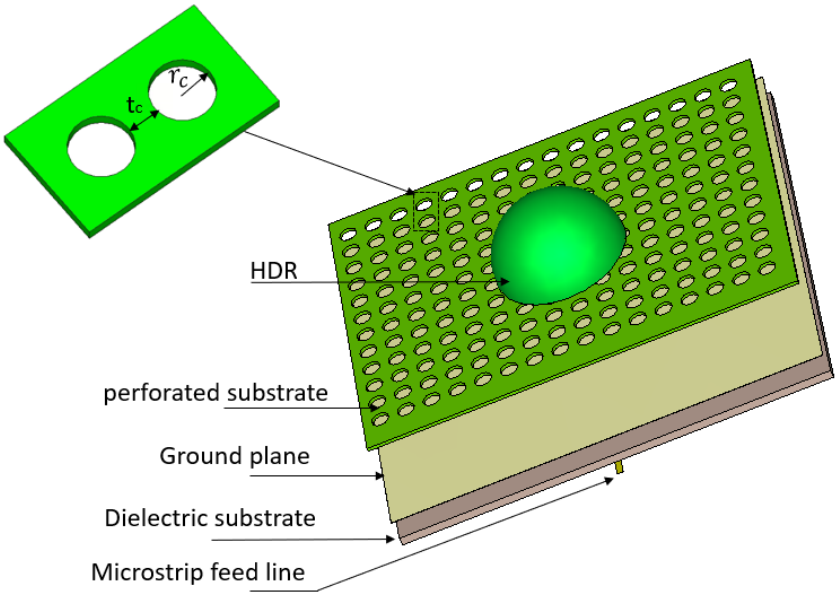

Figure 3.22: Geometry of the integrated hemispherical DRA and perforated top substrate.

This section aims to develop a design that will overcome the challenge of commercially unavailable substrate with specific dielectric constant and thickness. In addition, one of the advantages of the proposed configuration is eliminating the need for extra alignment and bonding steps between the DRA and a top substrate with different permittivities. As mentioned in Chapter 2, for a linearly polarised DRA, this configuration has utilised a perforated technique that involves the use of air-filled holes in a substrate, which is designed using the same material as the DRA. In addition, a perforated substrate offers the flexibility to adjust the effective permittivity by altering the diameter and thickness of the air-filled holes of the top substrate. The cross slot, transmission line, and thickness of the feeding substrate are maintained at the same dimensions that had been used in Section 3.3.

To obtain the optimal effective permittivity, a cylindrical unit cell has been studied as illustrated in Figure 3.23. The unit cell has a radius of r_c, and a thickness of t_c. In this study, the side length will be fixed at 0.3 mm, i.e. the thickness of the top substrate. In accordance with the theory of air-filled holes, the spacing between holes of its cylindrical shape determines the effective permittivity.

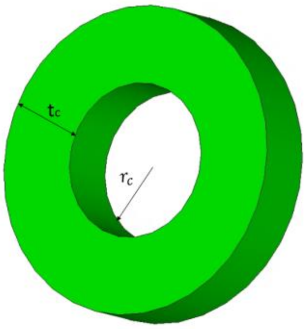

Figure 3.23: Unit cell of the perforated top substrate

The unit cell has been examined using CST to determine the effective permittivity when it is placed in a waveguide with perfect magnetic and electric boundaries. The effective permittivity of the unit cell can be extracted from S-parameter by changing the material's dielectric constant from 5 to 20, as demonstrated in Figure 3.20. The results illustrate a linear relationship between the thickness of unit cell and effective permittivity. For example, when ε_r = 5 and 20 and t_c = 0.1 and 1.4 mm, the effective dielectric constant is ε_{eff} = 1.3 and 4.7, respectively. The increase in the thickness and effective dielectric constant result in an increase in the effective permittivity.

For the sake of simplicity, to find the suitable radius and thickness of a unit cell, a curve-fitting formula has been developed, as stated in the equation below [80]:

$$\varepsilon_{eff} = 0.55\, t_c \varepsilon_r - 0.04\varepsilon_r + 1.3 \tag{3.9}$$

It is easy to find the obtained effective permittivity (ε_{eff}) by determining the thickness t_c parameter. The graph in Figure 3.24 illustrates a close agreement between the original data and the curve-fitting results.

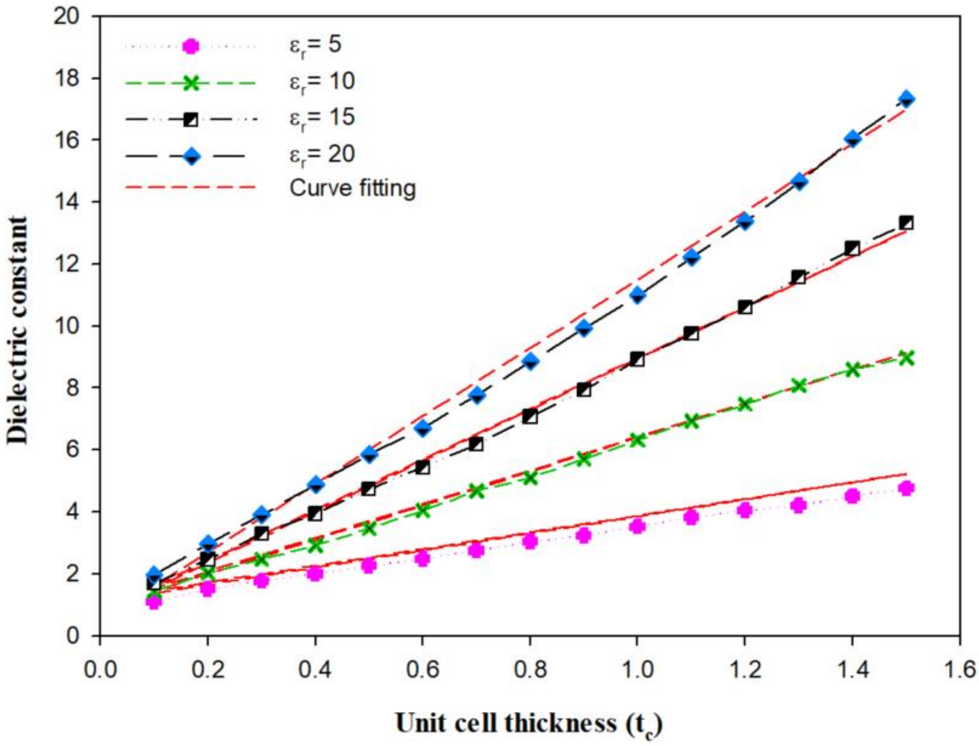

Figure 3.24: Effective relative permittivity of perforated hemispherical DRA

As mentioned in the previous section, when the dialectic constant of the top substrate is increased, the impedance bandwidth and resonance frequency are reduced, Therefore, the perforated technique is introduced to overcome this challenge by reducing the effective permittivity of the integrated top substrate made using Alumina. The radius (r_c) of the air-filled holes and spacing (t_c) between the sides of the adjacent air-holes should be increased to reduce the effective permittivity as shown in Figure 3.24.

By fixing the radius of the holes at $r_c = 0.5$ mm which is correspond to 0.08 λ_0 [80] and changing t_c significant impact on the impedance bandwidth as shown in Figure 3.25 (a) but it has as significant impact on the axial ratio bandwidth as demonstrated in Figure 3.25 (b). The aforementioned studies demonstrate the effect of changing the spacing between the air-filled holes on the impedance and AR bandwidths. The dimensions used should be chosen on a trade-off basis by focusing on the desired result so t_c has been chosen as 0.4 mm so that the effective permittivity of the perforated substrate is reduced to 3.

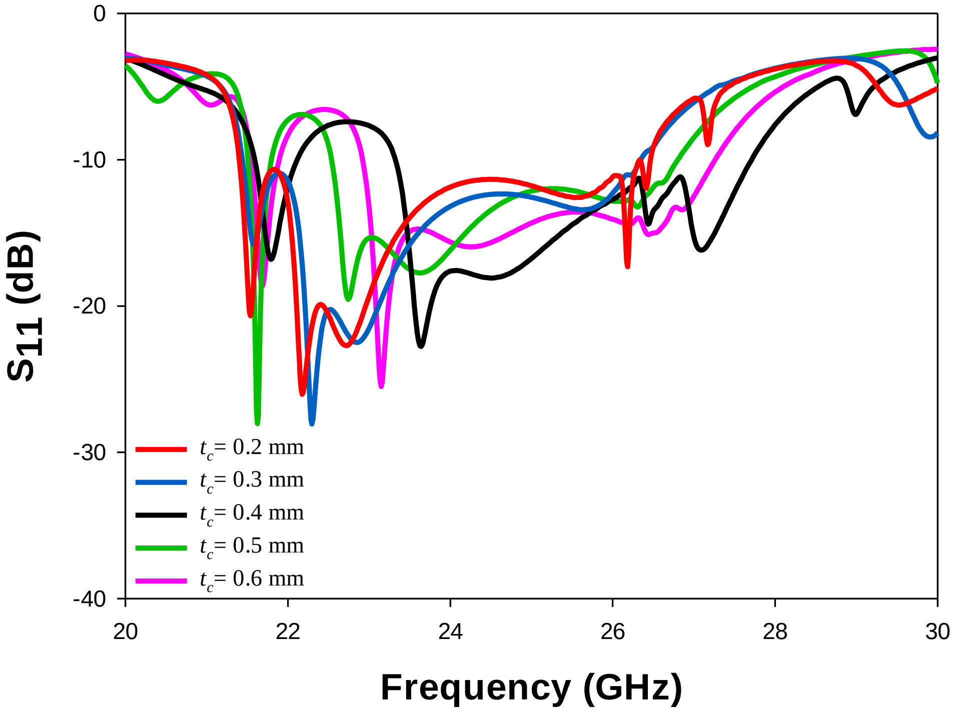

(a)

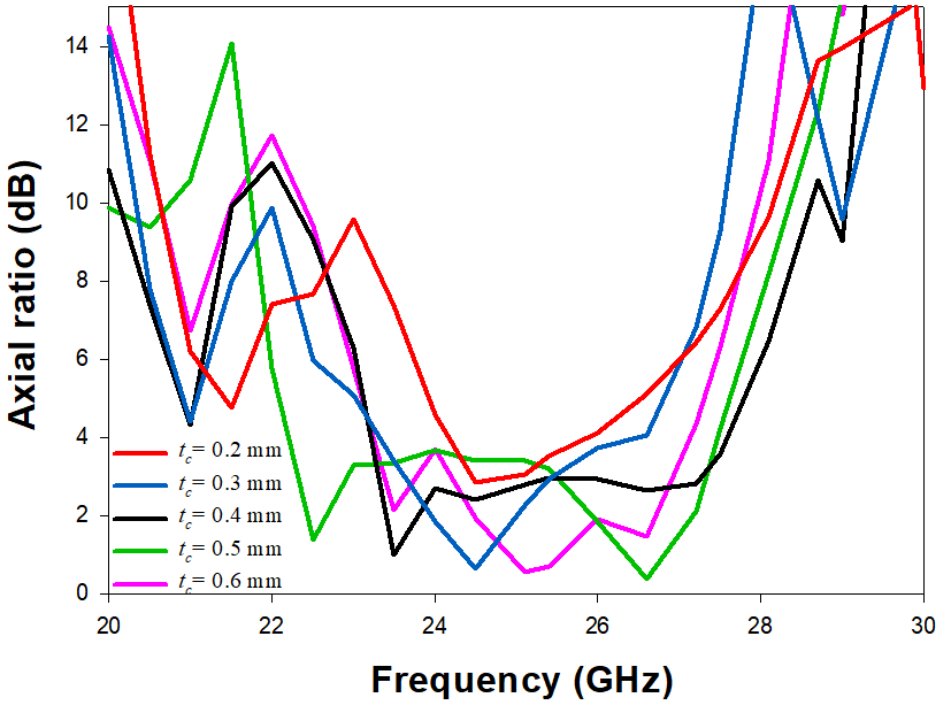

(b)

Figure 3.25: Effects of t_c of perforated top substrate on the performance of the hemispherical DRA (a) Reflection coefficient (b) Axial ratio.

3.4.2 Measured Results

(a) (b)

Figure 3.26: Integrated hemispherical DRA and a perforated substrate(a) Assembled (b) In the anechoic chamber.

Figure 3.26 illustrates the configuration of the integrated hemispherical DRA and perforated substrate. The DRA has been fabricated using Alumina and integrated to the perforated substrate using 3D printing. The feeding structure has been fabricated separately, and it consists of the cross slot and feeding substrate that is fabricated using of Ro3006 substrate with a dielectric constant of 6.5, a loss tangent of 0.002, and a thickness of 0.3 mm. To validate the results, the CP bandwidth, reflection coefficient, gain, and radiation pattern have been measured and recorded.

From these results, it can be noted that the simulated and measured reflection coefficients extend over frequency range of 23.3 to 27.6 GHz and 23.2 to 27.8 GHz, respectively. These frequency ranges correspond to percentage bandwidths of 16.8% and 18% for the simulated and measured results. These results show that the simulated and measured reflection coefficients bandwidths are in good agreement. The radiation pattern, CP bandwidth, and gain have been measured using the spherical near-field mm-wave measurement system (SNS-FIX-1.0).

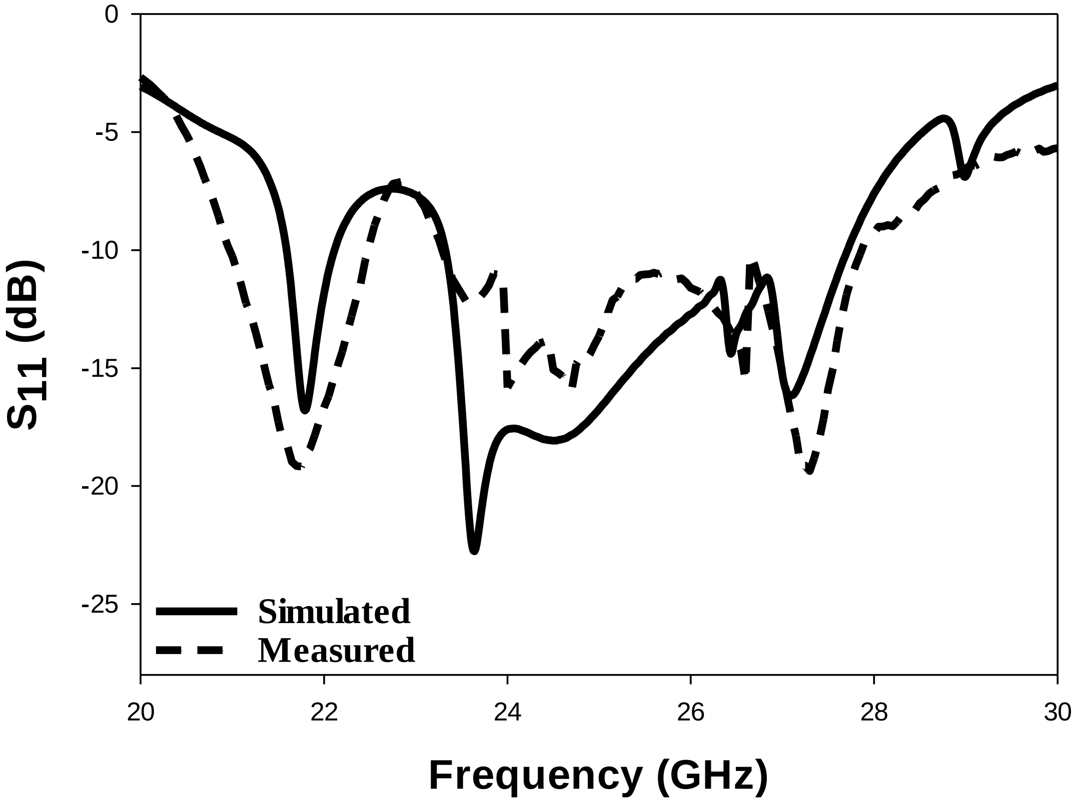

Figure 3.27: Reflection coefficient of a circularly polarised integrated hemispherical DRA and a perforated substrate at ε_r= 9.9, ε_s= 3.45, a = 3.8 mm, r = 1.6, l_{stub} = 0.5 mm = l_{s1}= 1.7 mm, l_{s2}= 3.1 mm.

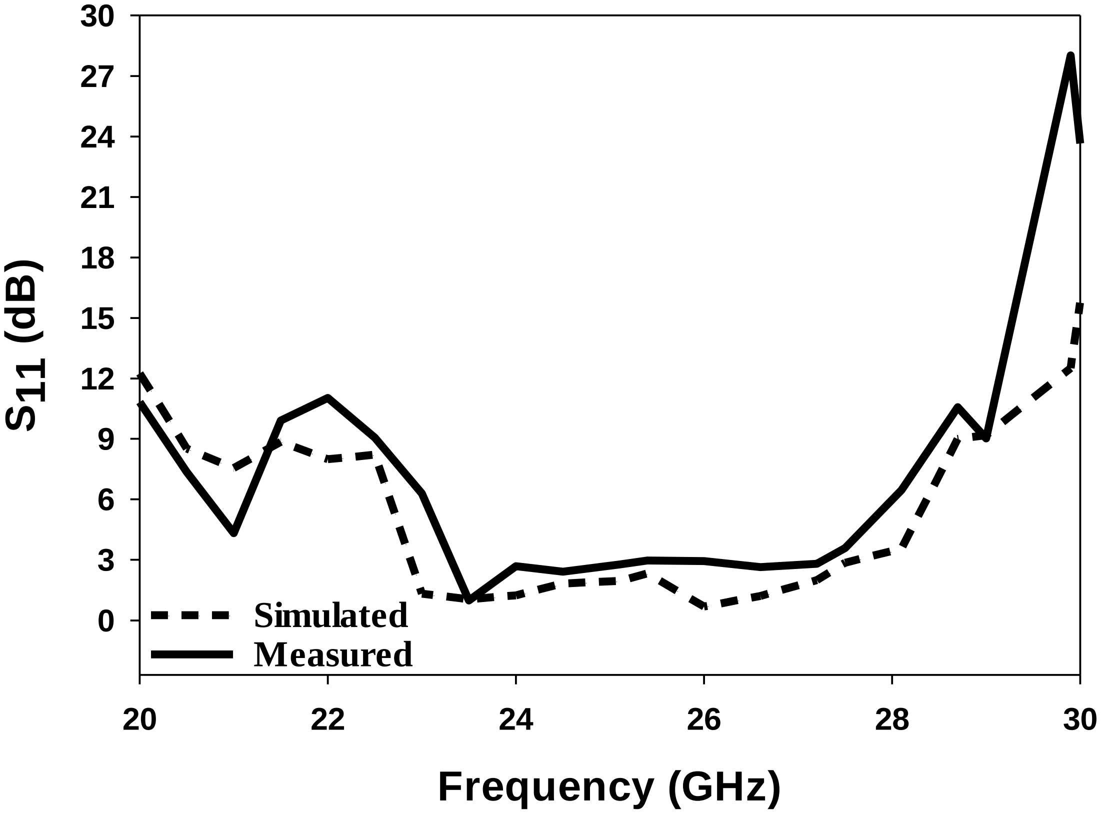

Figure 3.28: Axial ratio of a circularly polarised integrated hemispherical DRA and a perforated substrate at ε_r= 9.9, ε_s= 3.45, a = 3.8 mm, r = 1.6, l_{stub} = 0.5 mm = l_{s1}= 1.7 mm, l_{s2}= 3.1 mm.

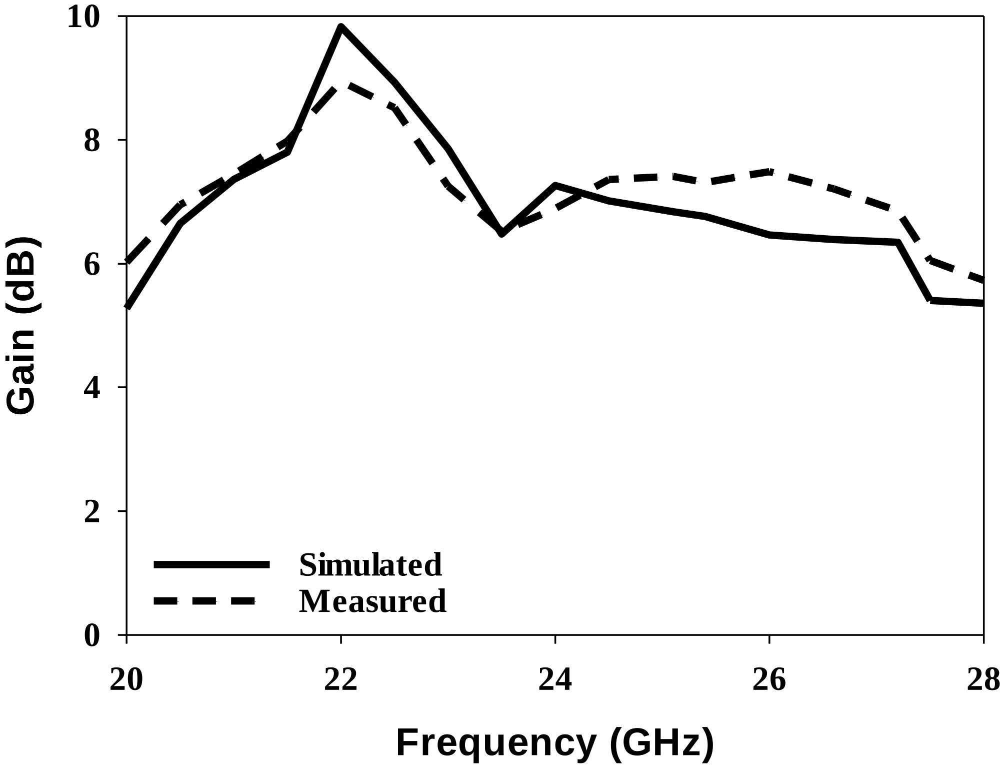

Figure 3.29: Broadside gain of a circularly polarised integrated hemispherical DRA and a perforated substrate at ε_r= 9.9, ε_s= 3.45, a = 3.8 mm, r = 1.6, l_{stub} = 0.5 mm = l_{s1}= 1.7 mm, l_{s2}= 3.1 mm.

The simulated and measured CP bandwidths are equal to 16.2% and 18.3%, respectively. At 27 GHz, the simulated and measured gain are equal to 6.4 dB and 7.1 dB, respectively. The simulated and measured broadside radiation patterns are presented in Figures 3.29 at the two principal plane cuts at 27 GHz with close agreement between measurements and simulations. However, there is a marginal discrepancy between simulated and measured results owing to fabrication errors and experimental.

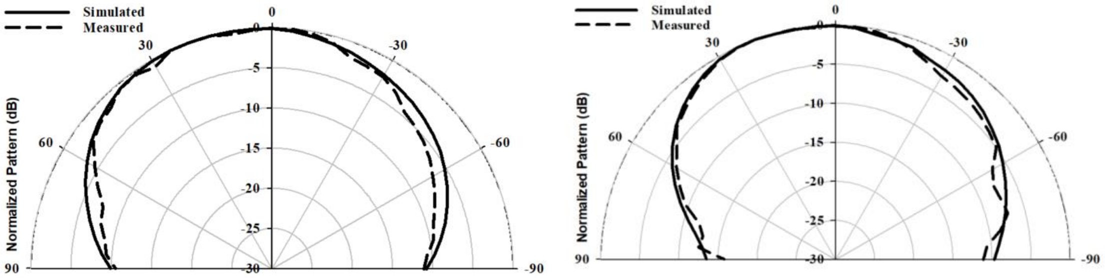

Figure 3.30: Radiation pattern of the integrated hemispherical DRA with perforated substrate excited in the TE112 mode at 27 GHz (a) $\phi = 0°$ (b) $\phi = 90°$ at ε_r= 9.9, ε_s= 3.45, a = 3.8 mm, r = 1.6, $l_{\text{stub}} = 0.5$ mm = l_{s1}= 1.7 mm, l_{s2}= 3.1 mm.

Table 3-1: Comparison between the performances of the measured proposed configurations

	Configuration	S_{11} bandwidth (%)	AR bandwidth (%)	Gain (dBic)
1	Cross slot	7.8	4	6.5
2	Solid top substrate	14	12.1	7.5
3	Perforated top substrate	18	18.3	7.1

3.5 Conclusions

In this Chapter, three circularly polarised hemispherical DRA configurations have been proposed. It is evident that each subsequent configuration aims to overcome a limitation that was demonstrated in the preceding configuration.

In Section 3.2, a cross-slot with unequal arms’ length has been considered. The design provided respective impedance and AR bandwidths of 4.2% and 4% with a gain of 6.5 dBi and an efficiency of 95%. The effect of cross slot dimensions has been discussed.

In Section 3.3, a top dielectric substrate has been added, which reduced the impact of misalignment and provided a significant increase in the impedance and CP bandwidth to 14% and 12.1%, respectively. Since the DRA and top substrate have different permittivities, it was not possible to fabricate them together through 3D printing. However, this configuration has a limitation as it requires an adhesive material to fix the DRA to the substrate firmly. In addition, the permittivity and thickness of the substrates are controlled by the market and may not be available at the proposed parameters, which are required to optimise the configuration.

In Section 3.4, air-filled holes were introduced in the top substrate. This configuration used an integrated DRA-perforated substrate, which offered the flexibility to control the substrate parameters without being restricted to the commercially available substrates. In addition, the integrated DRA-perforated approach overcomes the limitations of using glue. As a result, an optimum effective dielectric constant has been achieved, which improved the CP bandwidth as it has been increased from 12% to 18.3% when the solid top substrate is replaced by a perforated counterpart. Moreover, the configuration resulted in a dual band operation with an increased impedance bandwidth of 18% and a gain of 7.1 dBi at the lower frequency band. The parameters and results attained in this Chapter can be used for future studies to maximise the CP bandwidth and to overcome the limitations of unavailable material.

Chapter 4

A Compact Dual Band MIMO Dielectric Resonator Antenna

4.1 Introduction

Dielectric resonator antennas have been used in a wide range of microwave related applications due to their well-known benefits, such as design flexibility, low loss, and high radiation efficiency [33, 92]. Modern wireless communications, such as video streaming and multimedia applications demand higher data rates. A solution that was proposed to cater for such applications is to utilize a MIMO system with improved data rate for transmitting and receiving applications. However, a major challenge in the MIMO antenna setup is the mutual coupling between multiple antennas that are placed in the proximity of each other. Mutual coupling causes significant impedance mismatch, high correlation and impacts the radiation patten. Therefore, compact MIMO antennas with improved isolation are needed in modern wireless applications [93].

Additionally, multi-band antennas have received considerable attention as they are capable of operating in multiple applications simultaneously and can replace several single band antennas that are needed otherwise. In order to meet the high data rates demanded by modern communications systems, multiband MIMO antennas have been proposed [94]. However, developing MIMO antenna structures with a multiband operation represents another challenge due to the space constraints in particular for applications that require compact structures. Yet, when the frequency is increased, the wavelength becomes shorter and so does the physical size of the MIMO antenna. This makes it more complex to implement techniques that improve the performance of the antenna, such as adding air-filled holes or a dielectric wall.

Several designs of 5G-and-beyond MIMO antennas working at a frequency range of 26 to 40 GHz have been proposed [54, 95-99]. For example, loading a dipole antenna with a metamaterial surface was suggested to increase the end-fire gain [95]. Similarly, a superstrate was used to improve the bandwidth and gain of a mm-wave microstrip antenna [96]. Even though such antennas exhibit high gain, the incorporation of the superstrate has increased the size and created mechanical complications. To address these issues, a patch antenna array of four elements with a defected ground was proposed and utilised in a MIMO configuration to obtain broadband and high gain simultaneously [97]. The impact of a defected ground plane was further investigated in [98] for the design of a 5G MIMO antenna with ultra-broadband and high gain. A MIMO antenna consists of eight H-shaped radiating elements that have been proposed for mm-wave applications [99].

On the other hand, DRAs offer higher gains and wider bandwidths, which makes them suitable to be used in mm-wave applications while avoiding the conductor losses of patch antennas [54]. In earlier research studies, approaches such as varying the placement [100], polarization [101], and main-beam direction [55] have been implemented to decrease the mutual coupling between the DRAs. In addition, electromagnetic band gap (EBG) structures [102], frequency selective surface (FSS) walls [103, 104], meta surface shields [50], metamaterial polarization-rotator walls [51], partially reflecting surfaces [105, 106], and many more structures have been employed to reduce the mutual coupling between DRAs. However, all those configurations share a limitation of being complex and bulky. In order to reduce the complexity of the decoupling structure, metal strips were printed on the top DRA surface [54], metallic vias were implanted [53], metallic strips were added on the ground plane side [107] or both metallic strips and slots were utilized [108]. However, at mm-wave frequencies, approaches such as printing on the DRA top or drilling the DRA sides can represent major challenges and require precise machining tools that are complex and costly due to the small DRA physical dimensions at such frequencies. The proposed design offers simple and low-cost approach to achieve a high isolation between mm-wave DRAs in a compact size MIMO system. Besides, to the best of the authors' knowledge, the achieved transmission coefficient, S_{21}, is lower than those reported in earlier studies. Furthermore, high broadside gain and wide bandwidth are achieved at the two operating frequency bands with low envelope correlation and high diversity gain. Therefore, the presented configuration addresses well-known limitations with respect to the structure and performance of mm-wave MIMO DRA systems. Furthermore, a dual band operation has not been reported earlier for MIMO DRAs. Each of the achieved bandwidth is ~5 GHz at the 28 GHz and 38 GHz frequency bands that are widely used for Internet of Things (IoT) applications [11, 109, 110]. Additionally, a high data rate and compact size makes the proposed antenna suitable for miniature 5G devices.

4.2 Proposed Configuration

4.2.1 Rectangular DRA

The rectangular DRA is excited using coplanar waveguide (CPW) with a combination of cross and square slots as illustrated in Figure 4.1b. For the chosen DRA's width, *w*, depth, *d*, and height, *h*, the modes' resonance frequencies have been calculated by employing the well-known dielectric waveguide model [53], i.e.,

$$k_y = \frac{n\pi}{w}, k_z = \frac{m\pi}{2d}, k_x^2 + k_y^2 + k_z^2 = \varepsilon_r k_0^2 \tag{4.1}$$

$$k_x \tan\left(\frac{k_x h}{2}\right) = \sqrt{\left((\varepsilon_{r1} - 1)k_0^2 - k_x^2\right)}, f_0 = \frac{c}{2\pi\varepsilon_r}\sqrt{\left(k_x^2 + k_y^2 + k_z^2\right)} \tag{4.2}$$

where k_x, k_y, and k_z are the wave numbers. For a rectangular DRA above a ground plane, the transverse electric, TE, modes are excited. With the aid of Equations (4.1) and (4.2), the required DRA dimensions have been calculated so that the fundamental and higher order modes of $TE_{111}$and TE_{311}can be excited at 28 GHz and 38 GHz, respectively. In addition, the DRA width and depth have been chosen so that a low DRA profile is achieved. Therefore, the calculated dimensions are *w* = *d* = 5 mm, and *h* = 1 mm, which offers a compact DRA with a profile that is lower than those reported in the literature. The magnetic field distribution of each mode is illustrated in Figure 4.2 using the CST Eigenmode solver, which is in line with the expected resonance modes using the dielectric wave guide model.

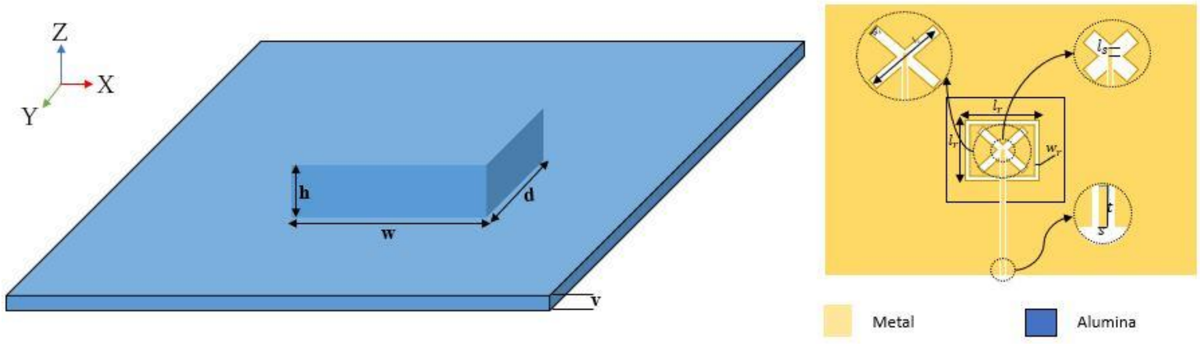

(a) (b)

Figure 4.1: (a) 3D printed Alumina rectangular DRA and substrate (b) feeding structure.

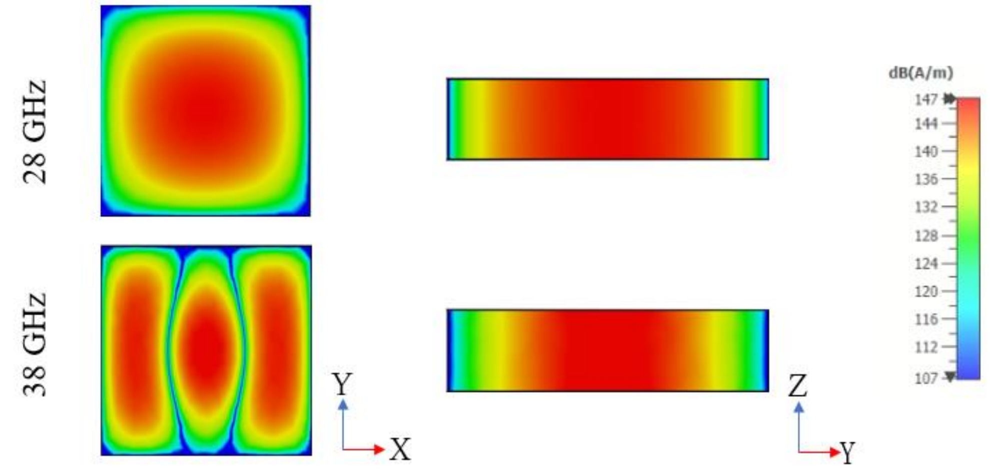

(a) (b)

Figure 4.2: Fields distribution of the excited modes TE_{111} at 28 GHz and TE_{311} at 38 GHz (a) xy plane. (b) xz plane.

The slots' dimensions need to be expressed in terms of the effective wavelength λ_{eff}, which can be calculated as $\lambda_{eff} = \lambda_0/\sqrt{\varepsilon_{eff}}$ and the effective permittivity is given by [111]:

$$\varepsilon_{eff} \approx \frac{\varepsilon_S \varepsilon_r (t+h)}{(\varepsilon_S h + \varepsilon_r t)} \tag{4.3}$$

In Equation (4.3), ε_S and t represent the permittivity and height of the Rogers substrate, respectively, and ε_r, and h represent the permittivity and height of the DRA, respectively. In this design, a combination of cross and square slots is utilized to excited two resonance modes and hence facilitates the dual band operation. The dielectric constant and height of the Rogers substrate are 2.3 and 0.25 mm, respectively. Therefore, the effective wavelengths have been calculated as 4.5 and 3.3 mm at 28 and 38 GHz, respectively. The cross slot has identical arms' length and width of l_c and w_c, respectively. The additional square slot was designed with a respective side's length and arm width of l_r and w_r. The PCB fabrication approach was followed to fabricate the feeding network using coplanar waveguide (CPW). The CPW feeding line incorporates a matching stub with a length of ls that is adjusted for optimum matching.

4.3 MIMO Configuration

As mentioned earlier, the proposed configuration involves two identical integrated DRAs that are placed on two separate feed networks printed on a Rogers 5881 substrate with thickness of 0.250 mm, relative permittivity of 2.3 and loss tangent, *d*, of 0.0007. As illustrated in Figure 4.1, each integrated DRA is placed above one of the two feed networks that involve slotted ground planes. In order to simplify the antenna's assembly, each DRA was printed on top of an Alumina substrate that has a thickness of $v = 0.2$ mm. The 3D printed Alumina DRA and substrate is illustrated in Figure 4.1a and will be referred to as an integrated DRA throughout this article. The evolution of the proposed design is demonstrated in Figure 4.3. The initial configuration of Figure 4.3a illustrates two integrated DRAs that are mounted on the same side of the Rogers substrate and the two CPW feeding lines are in parallel to each other. To minimise the coupling between the antennas, the configuration in Figure 4.3b was considered in which the CPW feeding lines' orientation was modified so that they are collinear to each other and fed from the opposite sides of the substrate since one CPW feeding line has been rotated clockwise by 90° and the other has been rotated counter-clockwise by 90°. For further reductions of coupling, the two integrated DRAs and feed structures were placed on opposite sides of the Rogers substrate as demonstrated in Figure 4.3c. It should be noted that the recommended distance between the DRAs' centres is $0.5\lambda_0$ [112]. The configuration's parameters are listed in Table 4-1.

Table 4-1: Dimensions of proposed MIMO antenna (unit: mm).

w	4	s	0.28
d	4	t	0.06
h	1	l_s	0.1
x	25	w_r	0.06
y	15	l_r	2.3
w_c	0.5	l_c	2.4

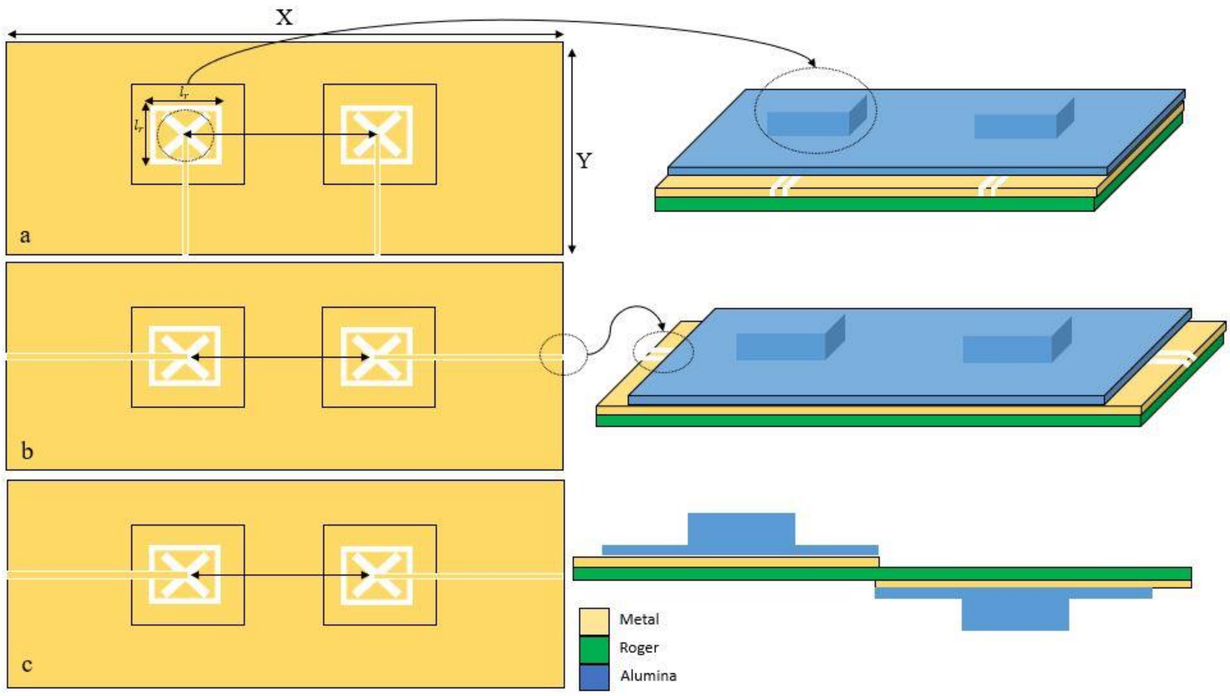

Figure 4.3: The MIMO rectangular DRA configurations (a) Initial design with parallel CPW feeding lines (b) Intermediate design with collinear CPW feeding line (c) Final design with DRAs at opposite sides of the Rogers substrate and collinear CPW feeding lines.

4.4 Surface Currents

The simulated current distributions at 28 GHz and 38 GHz have been studied by connecting a source to one DRA while the other DRA was parasitic and terminated by a 50 Ω lumped load. It should be noted that the current distributions in Figure 4.4a-c correspond to the configurations of Figure 4.3a-c, respectively. It is evident from Figure 4.4a that a noticeable current exists on the parasitic DRA's feed, which indicates a strong mutual coupling since the two DRAs are close to each other and the feeding CPW lines are in parallel. Therefore, it can be concluded that such arrangement of DRAs and feed networks exhibit mutual coupling that can significantly affects the performance. On the other hand, a weaker current on the feed of the parasitic DRA can be observed in Figure 4.4b owing to the increased distance between the collinear CPW feeding lines in the configuration of Figure 4.3b. In addition, it is evident from Figure 4.4c that a rather weak current exists on the parasitic DRA's feed when the antennas are placed on opposite sides of the Rogers substrate as in Figure 4.3c, which demonstrates a considerably reduced coupling and interference between the two integrated DRAs.

4.5 Results and Discussion

4.5.1 Performance of single and MIMO DRAs

Figure 4.5a illustrates the effect of changing the cross-slot arm's length, l_c, on exciting the required DRA resonance modes when the arm width was fixed at 0.5 mm. From these results it can be noted that the higher order mode is strongly excited when l_c = 2.4 mm, which corresponds to ~0.7 λ_{eff} at 38 GHz. On the other hand, Figure 4.5b demonstrates that a slot width of 0.5 mm is required to maintain the achieved resonance at 38 GHz. As mentioned earlier, a square slot has been added to excite the fundamental resonance mode TE_{111} at 28 GHz while maintaining the excited higher order mode at 38 GHz.

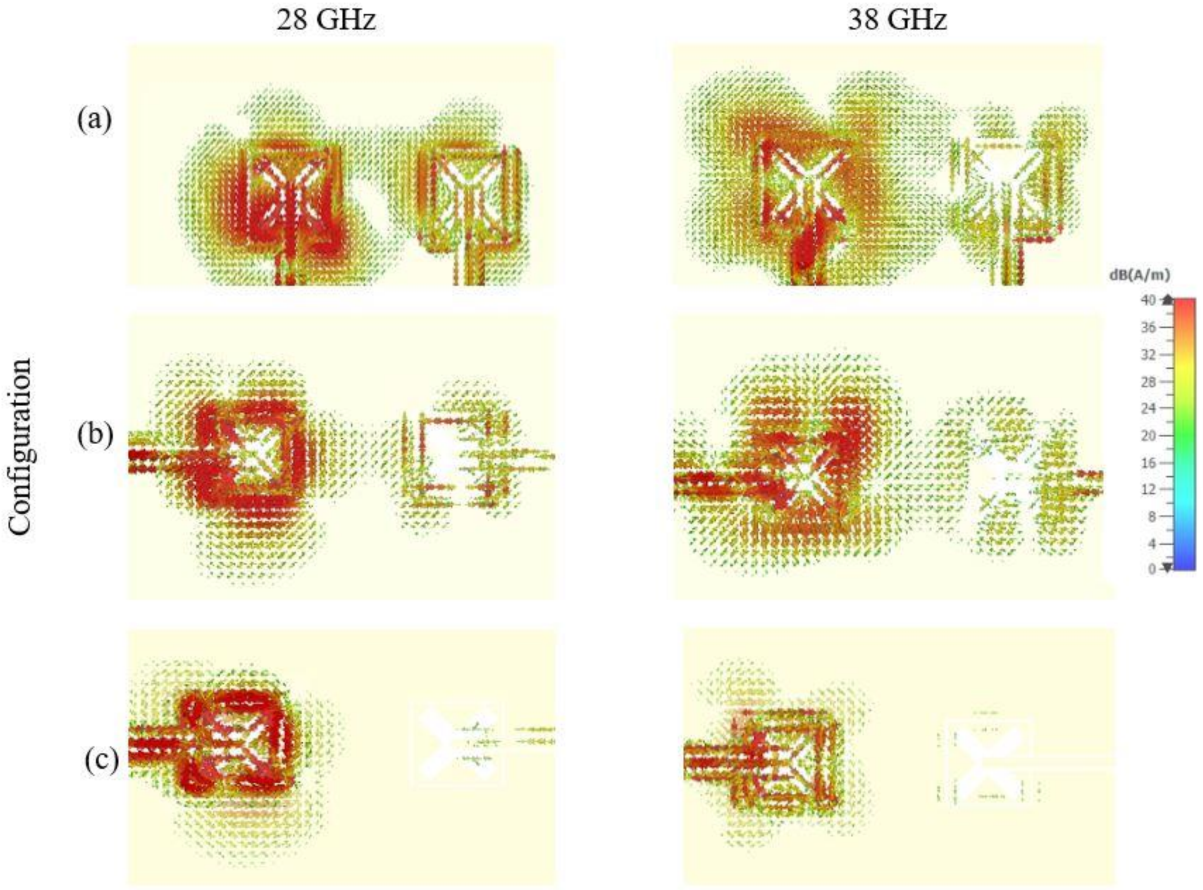

Figure 4.4: Surface current of the proposed MIMO antenna (a) Initial design with parallel CPW feeding lines (b) Intermediate design with collinear CPW feeding line (c) Final design with DRAs at opposite sides of the Rogers substrate and collinear CPW feeding lines.

The optimized square slot dimensions are illustrated in Figure 4.6, where it can be noted that having an arm's length of l_r= 2.3 mm and width of w_r = 0.06 mm provided the required dual band performance. It should be noted that l_r corresponds to ~0.5 λ_{eff} at 28 GHz. In addition, it can be noted from Figure 4.6a that by adding the square slot, the bandwidth of the upper band has also been increased by 5%. It is worth noting that a stub length of l_s = 0.1 mm has provided an optimum matching. The resulting impedance bandwidths for the lower and upper bands are 18% and 13%, respectively. The achieved bandwidth is ~5 GHz over each of the frequency bands of 28 GHz and 38 GHz, which results in an antenna configuration that is suitable for sensing, IoT and tracking applications.

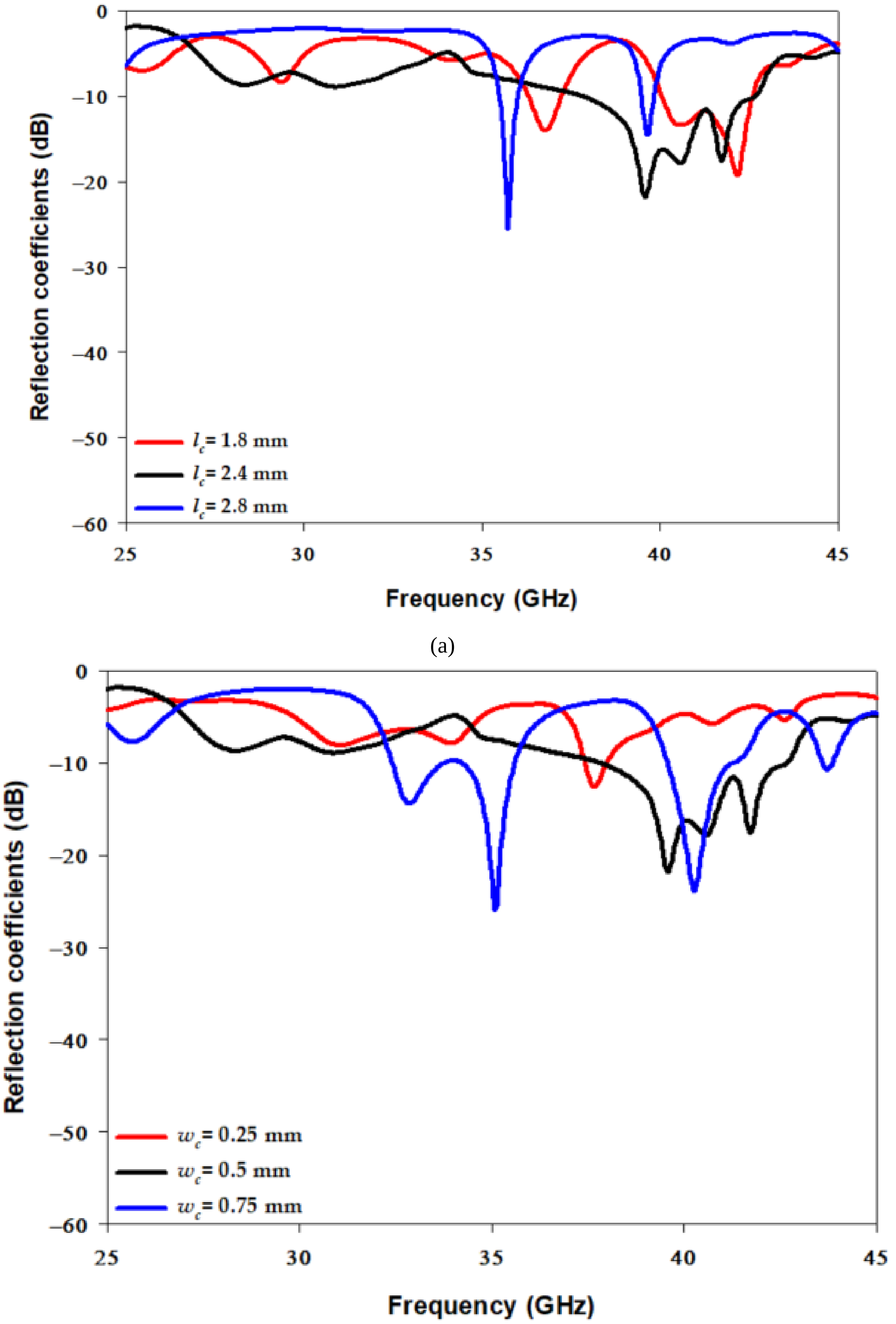

(a)

(b)

Figure 4.5: Effects of the cross-slot dimensions on the reflection coefficient (a) Lc (b) wc.

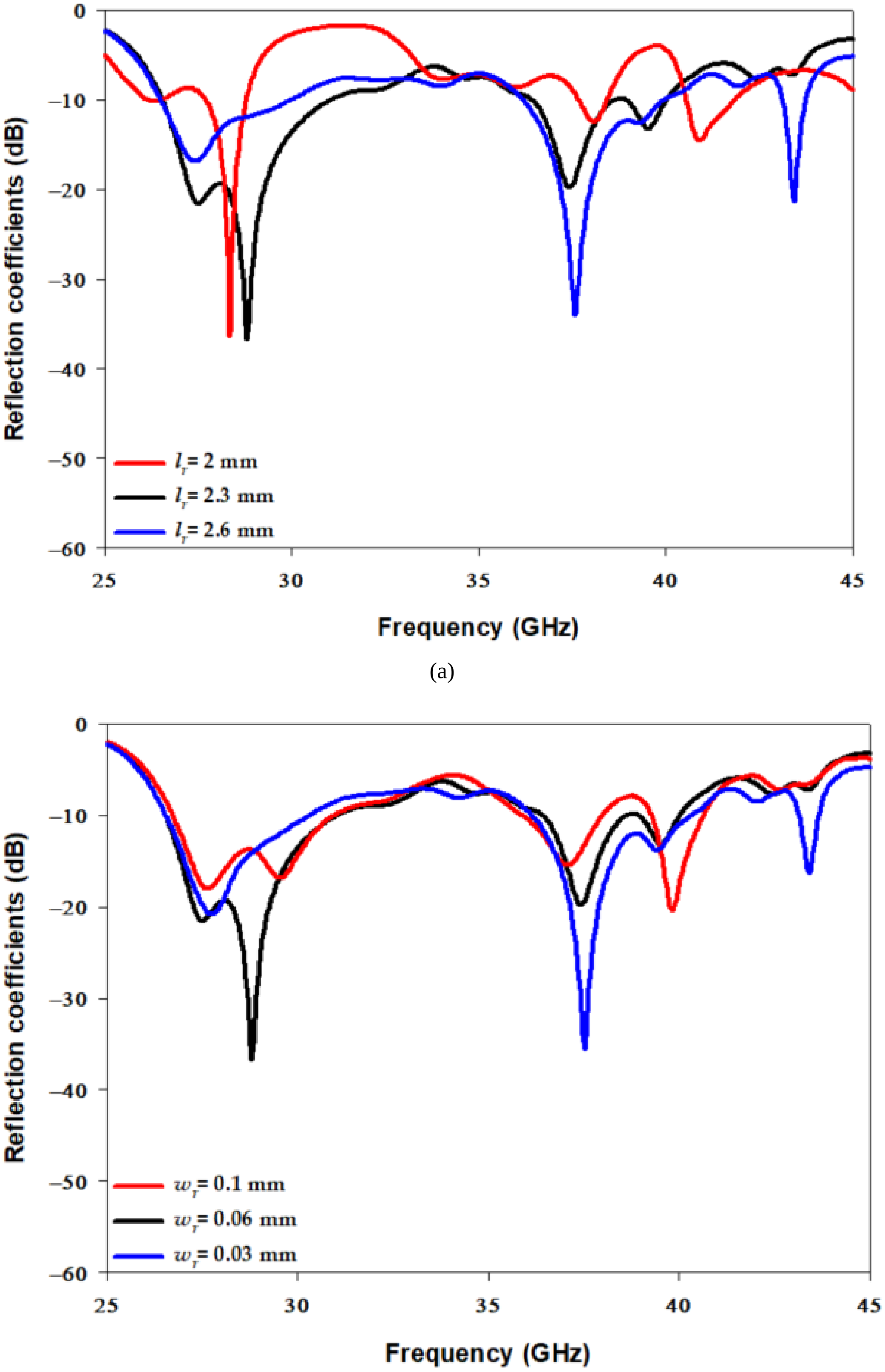

(a)

(b)

Figure 4.6: Effects of the square slot's dimensions on the reflection coefficient (a) L_r (b) w_r.

Furthermore, the impacts of altering the arrangement of the DRAs on the transmission coefficient, S_{21}, has been investigated for the three configurations of Figure 4.3, where it has been observed that altering the DRAs' arrangement can significantly improve the isolation between elements. These results are demonstrated in Figure 4.7 in which the shaded areas indicate the frequency ranges over which impedance matching is achieved. The S_{21} graph that corresponds to Figure 4.3a, offers transmission coefficients of -12 dB and -9.5 dB at 28 GHz and 38 GHz, respectively. This demonstrates that the upper frequency band has a stronger coupling between the DRAs, which may be attributed to the increased DRAs electrical size at 38 GHz. Furthermore, the results also indicate a modest isolation between the two DRAs since the parallel CPW feeding lines are close to each other. In addition, the smaller separation between the CPW feeding lines implies that, physically, the SMA will not fit comfortably, and hence it will affect the performance of any prototype.

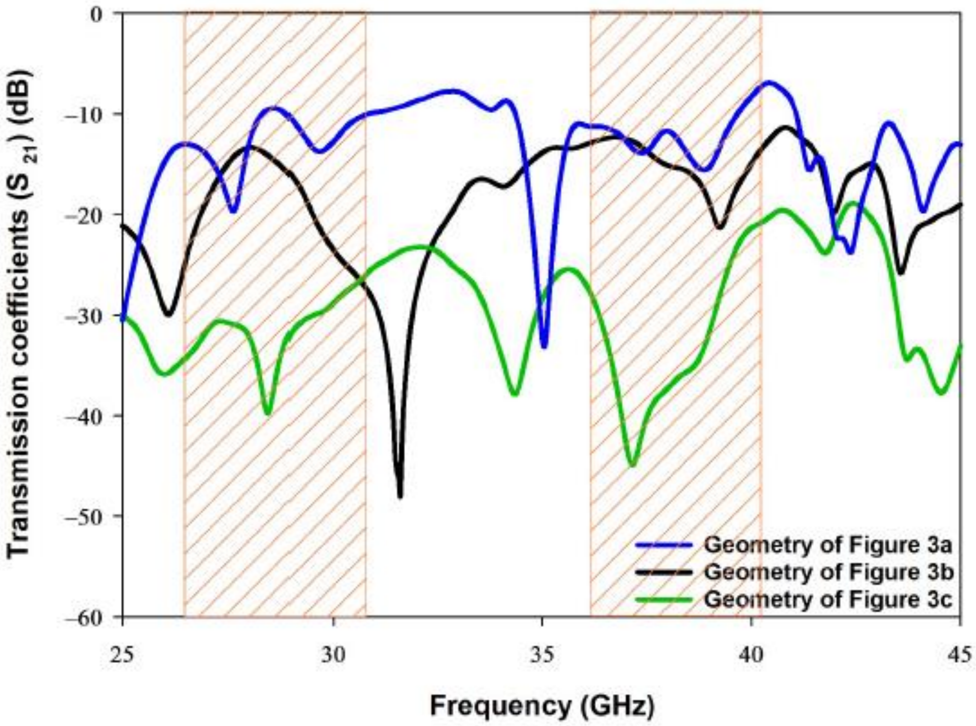

Figure 4.7: Simulated transmission coefficients for the configurations presented in Figure 4.3 at ε_r= 9.9, ε_s= 3.45, w=d = 4 mm, l_r = 2.3 mm = l_c= 2.4 mm, h= 1 mm.

On the other hand, the S_{21} curve that corresponds to Figure 4.3b offers a slightly lower isolation of -14 dB at 38 GHz. As mentioned earlier, the proposed configuration of Figure 4.3c provides a simple and compact structure in which one DRA, and its feed network, are kept at the top side of the Rogers substrate and the other DRA and feed network are placed at the lower side of the same substrate. As a result, the S_{21} has been reduced by 27 dB at 38 GHz compared to the case when the two DRAs are mounted at the same surface of the Rogers substrate. Therefore, reduced S21 of -36 dB and -41 dB have been achieved at 28 GHz and 38 GHz, respectively. It is evident that the S_{21} results of configuration of Figure 4.3c illustrates a considerably improved isolation. Another significant difference between the configurations is that a common ground plane was used in Figure 4.3a, b, whereas two separate ground planes were used in Figure 4.3c albeit with the same Roger substrate in all configurations. Therefore, the presence of the two ground planes on opposite sides of the Roger substrate has also contributed to the achieved in S_{21} since they effectively act as a metal surface between the two DRAs.

4.5.2 Experimental Verification

The proposed configurations in Figure 4.3b, c have been fabricated and measured using the E5071C mm-wave vector network analyser to measure the S-parameters through a 2.8 mm, 50 Ω, coaxial cable. Moreover, a 2.8 mm SMA was used between the coaxial cable and the CPW feeding structure. The return losses are presented in Figure 4.8, where it is evident that the simulated and measured impedance bandwidths are in close agreement with each other. It is worth noting that the measured resonance frequencies, i.e., frequency points with minimum S_{11}, are 28.8 GHz and 37.61 GHz which are in good agreement with the dielectric waveguide mode calculation of Equation (4.2). It should be noted that the return losses are presented for the configuration of Figure 4.3c only as they are identical to those of the configuration in Figure 4.3b. The respective simulated and measured impedance bandwidth are 18% and 19.5% for the lower band and 13% and 15% for the upper band. The transmission coefficient's results are also presented in Figure 4.8. For the configuration of Figure 4.3b, the respective simulated and measured transmission coefficients are -13 dB and -14.5 dB for the lower band, and -14 dB and -15.1 dB for the upper band. On the other hand, when the DRAs and their feed networks, are located at the opposite of the Rogers substrate, as in the geometry of Figure 4.3c, the respective simulated and measured transmission coefficients are -36 dB and -39 dB for the lower band, and -41 dB and -44 dB for the upper band. The simulated and measured transmission coefficients are in close agreement with each other. As expected, the transmission coefficient that corresponds to the configuration of Figure 4.3c is much lower than that of the counterpart in Figure 4.3b, which results in less interference and coupling between the DRAs in the proposed configuration.

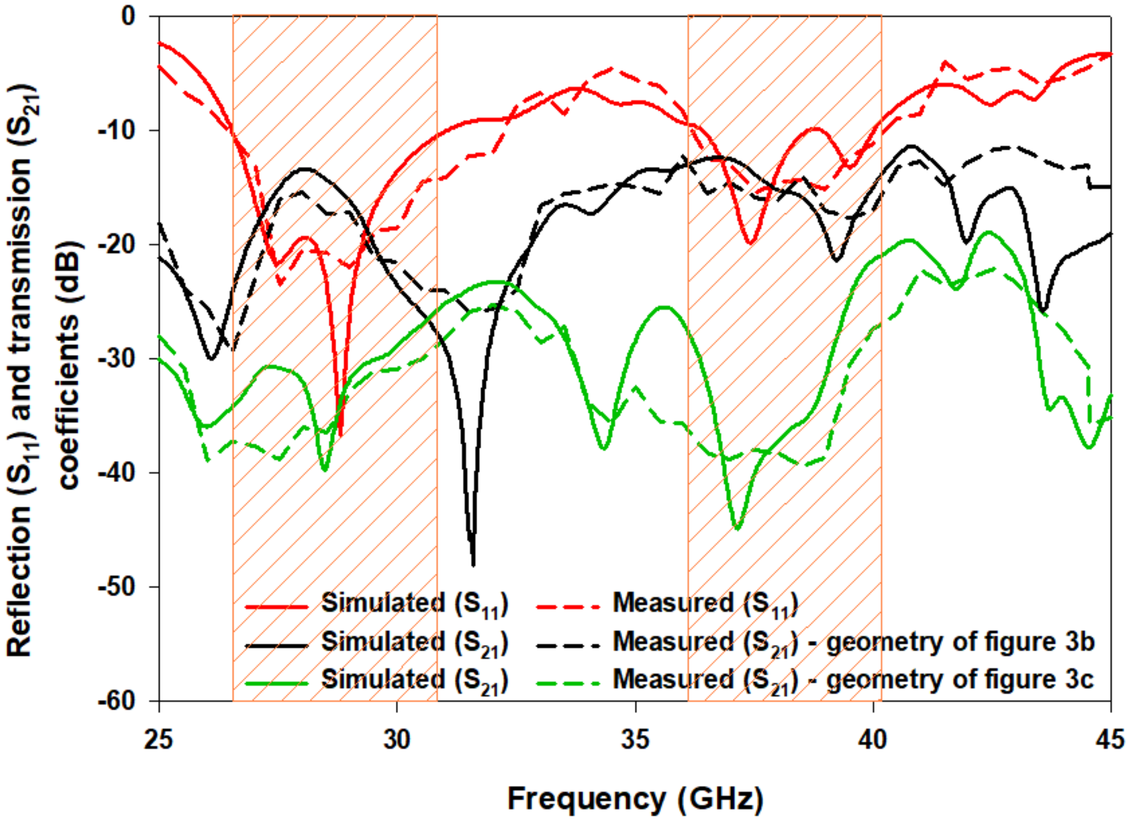

Figure 4.8: Simulated and measured S-parameters of the configurations in Figure 4.3b, c losses at ε_r= 9.9, ε_s= 3.45, w=d = 4 mm, l_r = 2.3 mm = l_c= 2.4 mm, h= 1 mm.

Figure 4.9: The photo of the MIMO rectangular DRA.

The spherical near-field mm-wave measurement system (SNF-FIX-1.0) was used to measure radiation pattern and the gain. The arm of the SNF-FIX-1.0 spherical system is restricted to rotating across the upper hemisphere to cover the elevation angle's range of θ = -90° to θ = 90°. The simulated and measured normalized broadside radiation patterns are presented in Figure 4.10 and 4.11 for the E and H-planes at 28 GHz and 38 GHz. Good agreement can be observed between simulated and measured radiation patterns. The measured gain of the DRA, G_{DRA}(dB), has been determined using the following Equation [113].

$$G_{\mathrm{DRA(dB)}} = G_{\mathrm{Hom(dB)}} + 10\log_{10} \frac{P_{\mathrm{DRA}}}{P_{\mathrm{Horn}}} \tag{4.4}$$

where G_{Horn} (dB) denotes the gain of the reference mm-wave horn antenna, $P_{DRA}$is the power received by the DRA and P_{Horn} is the power transmitted by the horn antenna. The respective simulated and measured gains are 6.2 dBi and 5.8 dBi at 28 GHz, and 7.57 dBi and 7 dBi at 38 GHz as illustrated in Figure 4.12 with close agreement between simulations and measurements. The increased gain at 38 GHz can be attributed to the excitation of the higher order DRA mode TE_{311} at this frequency compared to the excitation of the lower order mode TE_{111} at 28 GHz. In addition, the simulated efficiency is 90% over the operating frequency range as demonstrated in Figure 4.12, which is expected from the DRA due to the absence of ohmic and surface wave losses. There is a marginal discrepancy between simulated and measured results owing to fabrication errors and experimental tolerance. However, the discrepancies are more notable in the case of measuring the transmission coefficient for the configuration of Figure 4.3c, which can be attributed to a possible misalignment between two DRAs when they are placed on the opposite sides of the same substrate.

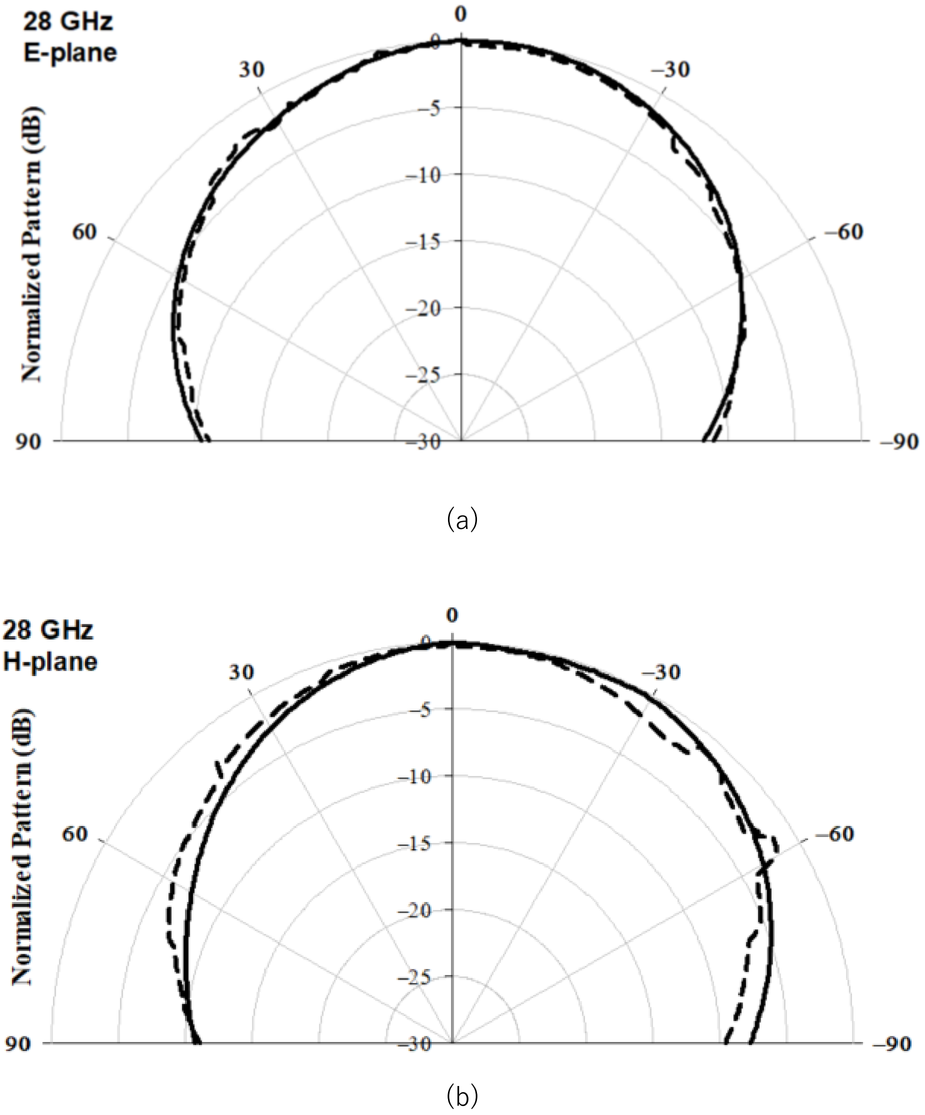

(a)

(b)

Figure 4.10: Radiation patterns of proposed MIMO configuration (a) E-plane (b) H-plane at 28 GHz at ε_r= 9.9, ε_s= 3.45, w=d = 4 mm, l_r = 2.3 mm = l_c= 2.4 mm, h= 1 mm.

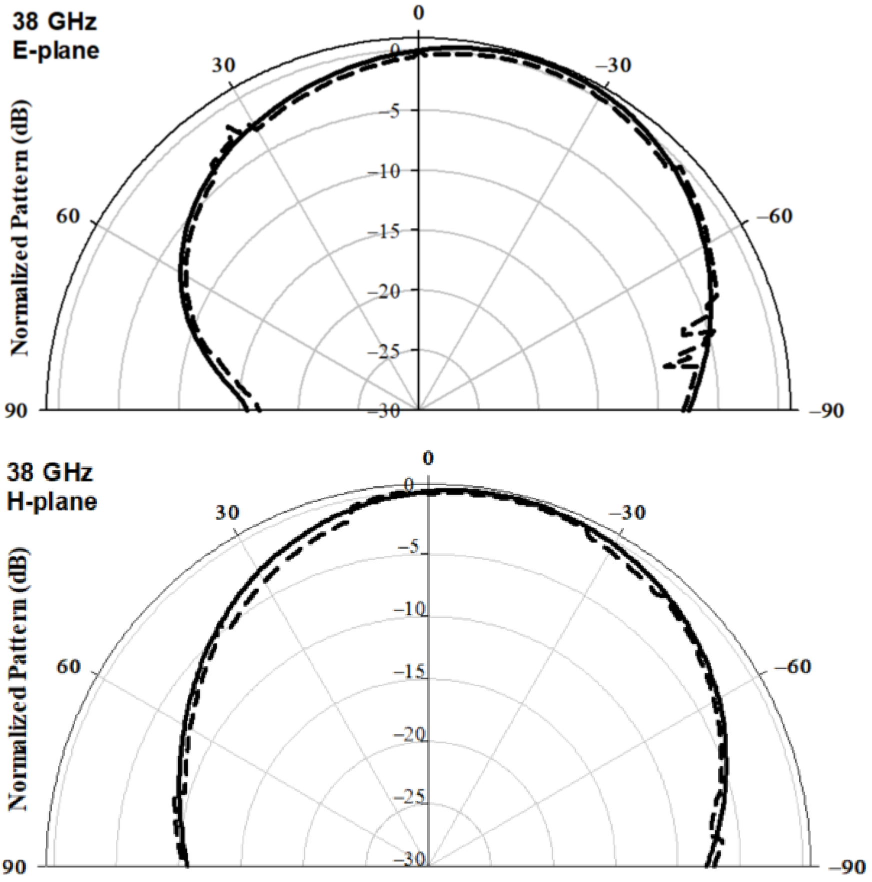

Figure 4.11: Radiation patterns of proposed MIMO configuration (a) E-plane (b) H-plane at 38 GHz at ε_r= 9.9, ε_s= 3.45, w=d = 4 mm, l_r = 2.3 mm = l_c= 2.4 mm, h= 1 mm.

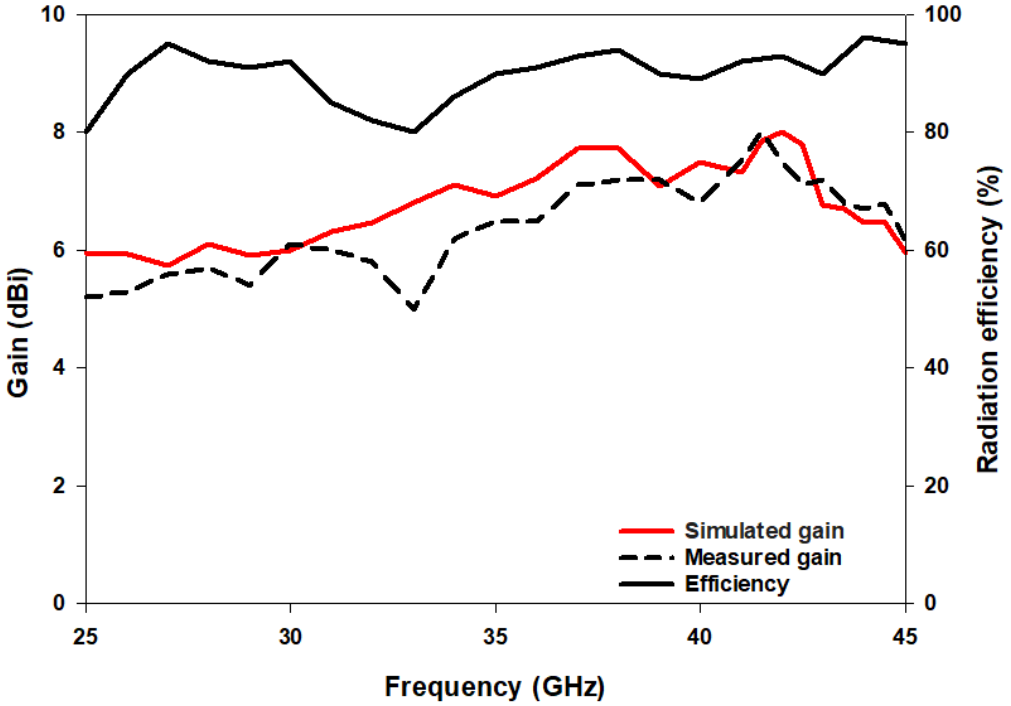

Figure 4.12: The broadside gain and simulated efficiency at ε_r= 9.9, ε_s= 3.45, w=d = 4 mm, l_r = 2.3 mm = l_c= 2.4 mm, h= 1 mm.

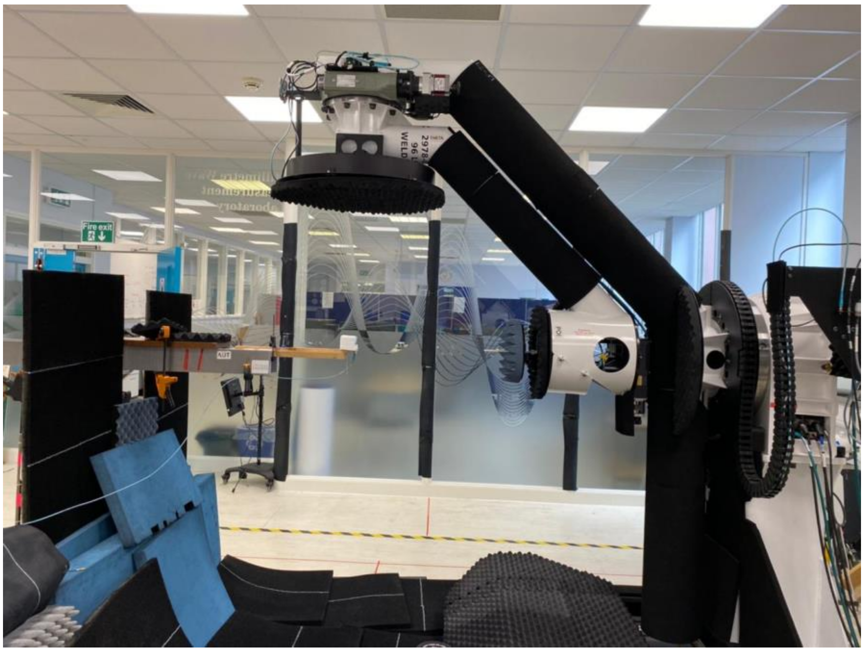

Figure 4.13: The prototype of rectangular DRA inside the anechoic chamber.

4.6 Performance of the MIMO Antenna

The characteristics of the MIMO antenna, particularly, the envelope correlation coefficient, the channel capacity loss, diversity gain, total active reflection coefficient, the mean effective gain and the multiplexing efficiency are evaluated in this section.

4.6.1 Envelope Correlation Coefficient

The diversity gain and other key parameters of the MIMO antennas are defined in terms of the envelope correlation coefficient (ECC). The isotropic envelope correlation coefficients were computed for the frequency bands of operation as illustrated in Figure 4.14. The calculated values are limited to 0.02, which demonstrates the suitability of the proposed antenna for wireless communication applications. The ECC of the dual MIMO antenna was computed by utilizing the following Equation [114].

$$\rho_e = \frac{|S_{11}^{*}S_{12} + S_{21}^{*}S_{22}|^2}{(1 - |S_{11}|^2 - |S_{21}|^2)(1 - |S_{22}|^2 - |S_{12}|^2)} \tag{4.5}$$

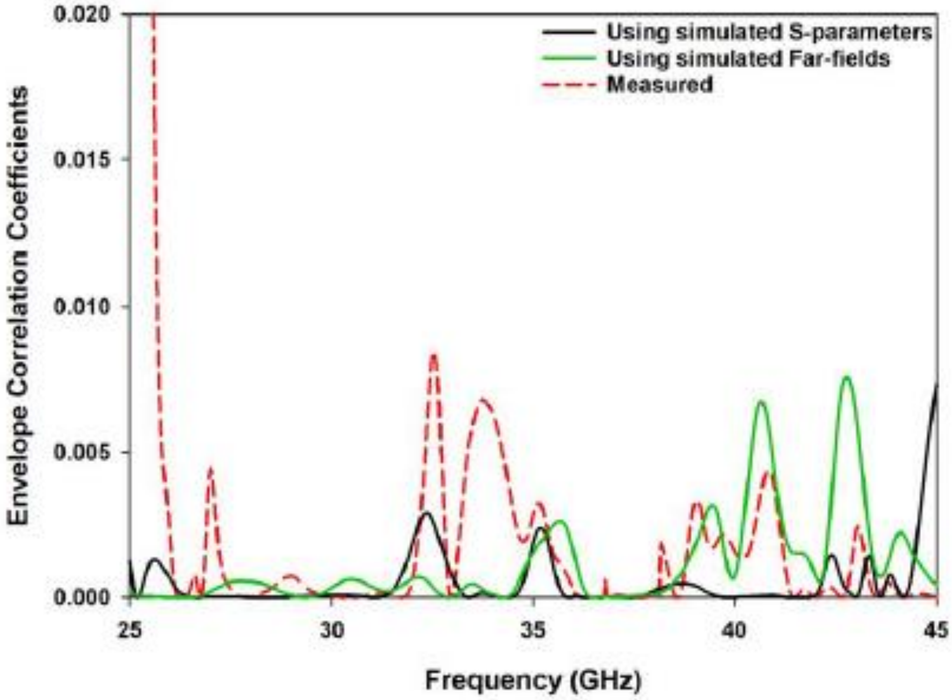

Figure 4.14: The simulated and measured ECC of the proposed MIMO antenna at ε_r= 9.9, ε_s= 3.45, w=d = 4 mm, l_r = 2.3 mm = l_c= 2.4 mm, h= 1 mm.

4.6.2 Analysis of Diversity Gain

The diversity gain for the frequency bands of operation has been determined from the far field and S parameters as illustrated in Figure 4.15. This parameter is calculated based on the envelope correlation coefficient, as [115],

$$DG = 10\sqrt{1 - |\rho_e|^2} \tag{4.6}$$

The simulated and measured diversity gains over the entire frequency band of operation are 9.98 and 9.97, respectively. The measured values are slightly lower than the simulated values due to fabrication and experimental tolerances.

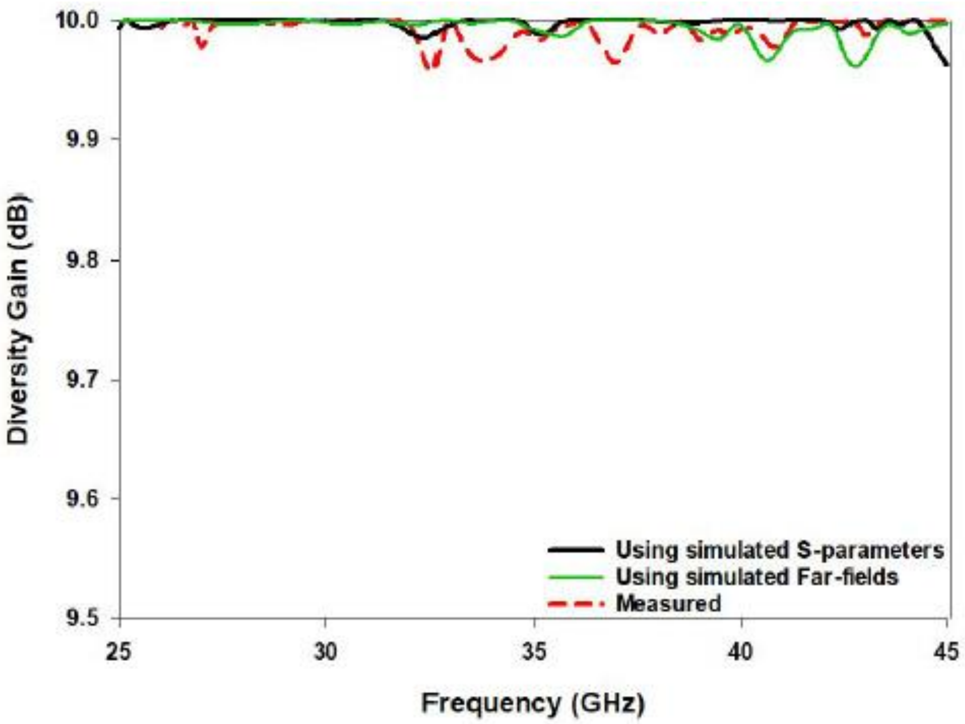

Figure 4.15: The simulated and measured diversity gain of the proposed MIMO antenna at ε_r= 9.9, ε_s= 3.45, w=d = 4 mm, l_{r} = 2.3 mm = l_c= 2.4 mm, h= 1 mm.

4.6.3 Channel Capacity Loss (CCL)

The CCL of an antenna indicates the quality of the transmitted data over the frequency band of operation. A high data transfer rate can be obtained for lower CCL. For example, a CCL higher than 0.4 bits/s/Hz indicates lossy data transmission while excellent transmission is assumed otherwise. As demonstrated in Figure 4.16, the calculated and measured CCLs are lower than 0.4 bits/s/Hz at the desired frequency bands. In detail, the CCL is equal to 0.3 and 0.1 at the lower and higher frequency bands, respectively. Accordingly, since the achieved CCL at both bands is ≤ 0.4 bits/s/Hz, the proposed MIMO antenna offers an efficient data transmission with low loss [116]:

$$C_{\mathrm{loss}} = -\log_2 \det(\psi) \tag{4.7}$$

where y is the correlation matrix,

$$\begin{gathered}\Psi = \begin{vmatrix}\psi_{11} & \psi_{12}\\ \psi_{21} & \psi_{22}\end{vmatrix}\\ \Psi_{11} = 1-(|S_{11}|^2+|S_{12}|^2)\\ \Psi_{22} = 1-(|S_{21}|^2+|S_{22}|^2)\\ \Psi_{12} = -\left((S_{11}^*S_{12})+(S_{21}^*S_{22})\right)\\ \Psi_{21} = -\left((S_{22}^*S_{21})+(S_{12}^*S_{11})\right)\end{gathered} \tag{4.8}$$

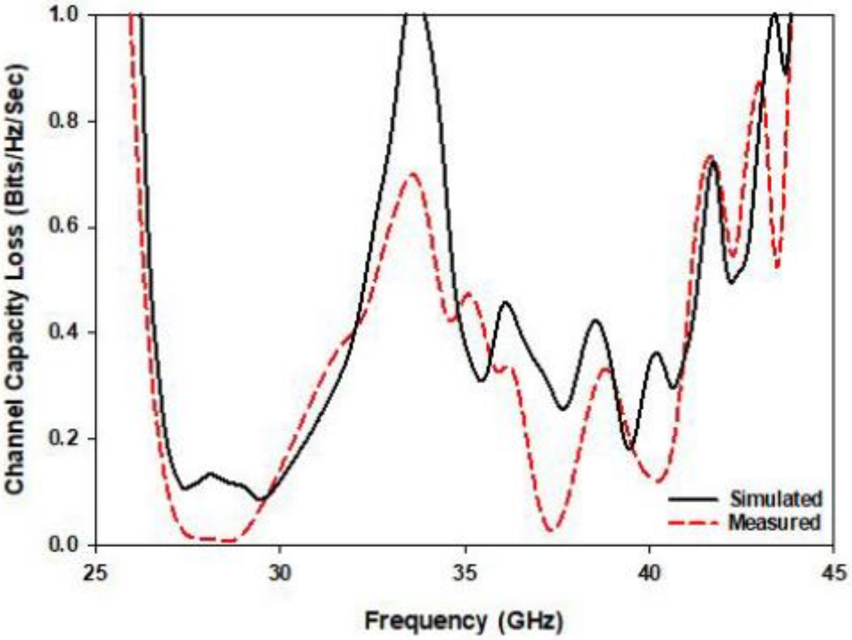

Figure 4.16: The simulated and measured CCL of the proposed MIMO antenna.

4.6.4 Total Active Reflection Coefficient

The total active reflection coefficient (TARC), as shown in Figure 4.17, illustrates the simulated and measured MIMO antenna systems' effective performances, namely the operating bandwidth. Equation (4.9) has been utilized, which explains how the S-parameters can be used to calculate the TARC, whereby q represents the input feeding phase [117].

$$\Gamma_a^t = \sqrt{\frac{(|s_{11}+s_{12}e^{j\theta}|^2)+(|s_{21}+S_{22}e^{j\theta}|^2)}{2}} \tag{4.9}$$

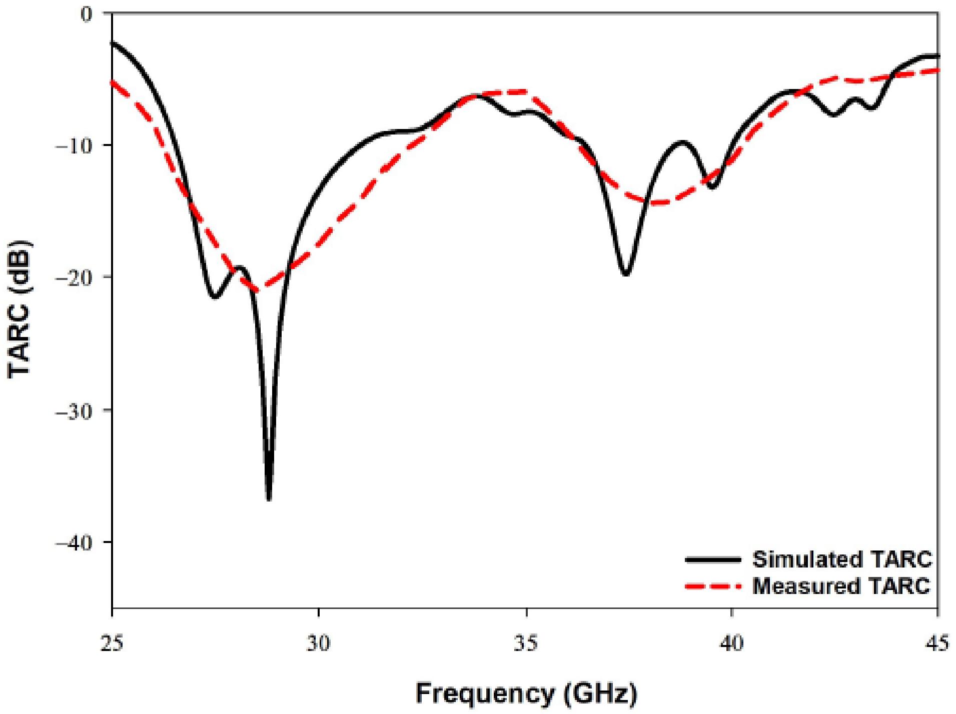

Figure 4.17: The simulated and measured TARC of the proposed MIMO antenna at ε_r= 9.9, ε_s= 3.45, w=d = 4 mm, l_r = 2.3 mm = l_c= 2.4 mm, h= 1 mm.

4.6.5 The Mean Effective Gain

The mean effective gain (MEG) is another key parameter that is commonly used to characterize the performance of the MIMO antenna systems. In fading environments, the MEG measures the performance of the antenna system. Equation (4.10) describes how the S-parameters of a MIMO antenna system can be used to calculate MEG [118].

$$\mathrm{MEG}_i = 0.5\eta_{i,\mathrm{rad}} = 0.51 - \left[\sum_{j=1}^{M} \left|S_{ij}\right|^2\right] \tag{4.10}$$

In the above equation, $\eta_{i,rad}$,M, and i represent the radiation efficiency, number of antenna elements, and the antenna under observation in the MIMO system, respectively. In order to attain practical results that can be validated, as shown in Figure 4.18, the MEG value should be between -3 dB and -12 dB [118]. It should be noted that *XPR* in Figure 4.18 denotes the cross-polarization power ratio where 0 dB and 6 dB refer to different mediums.

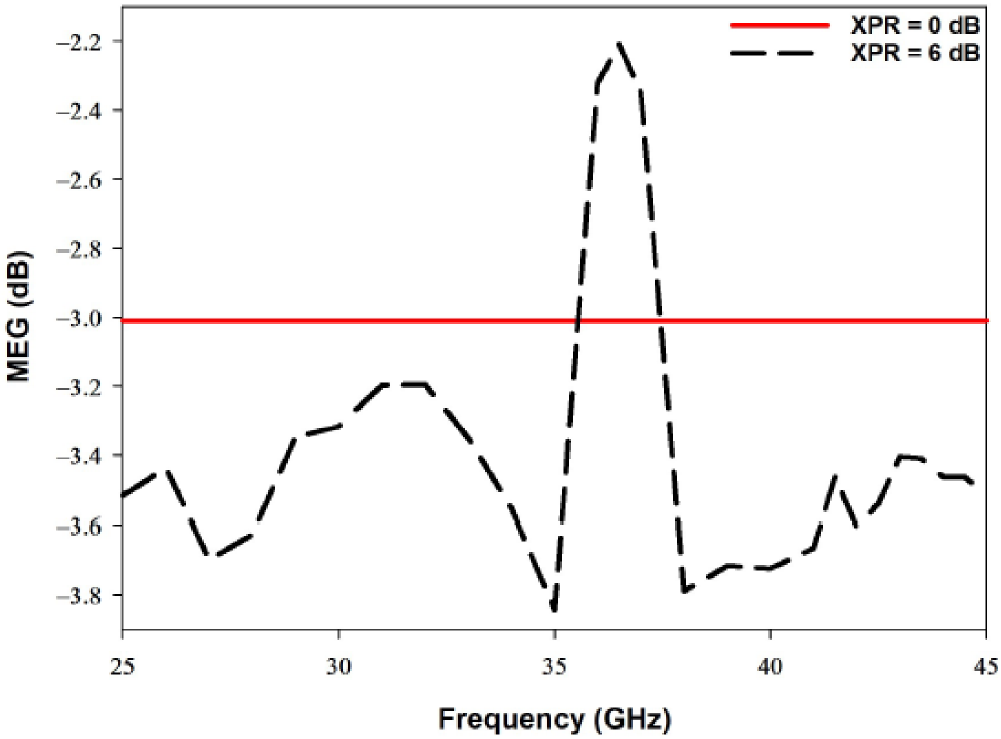

Figure 4.18: The mean effective gain (MEG) of the proposed MIMO antenna.

4.6.6 Multiplexing Efficiency

The multiplexing efficiency (η_{mux}) is defined as the signal-to-noise ratio between imperfect and an ideal MIMO antenna system. Equation (4.11) demonstrates how η_{mux} can be calculated [119].

$$\eta_{\text{mux}} = \sqrt{\eta_i \eta_j (1 - |\rho_c|^2)} \tag{4.11}$$

The parameters, η_i, η_j and ρ_c represent total efficiency, antenna port *i* or *j*, and complex correlation coefficient, respectively. As demonstrated in Figure 4.19, the multiplexing efficiency should not be lower than -3 dB at the operating dual frequencies of 28 GHz and 38 GHz.

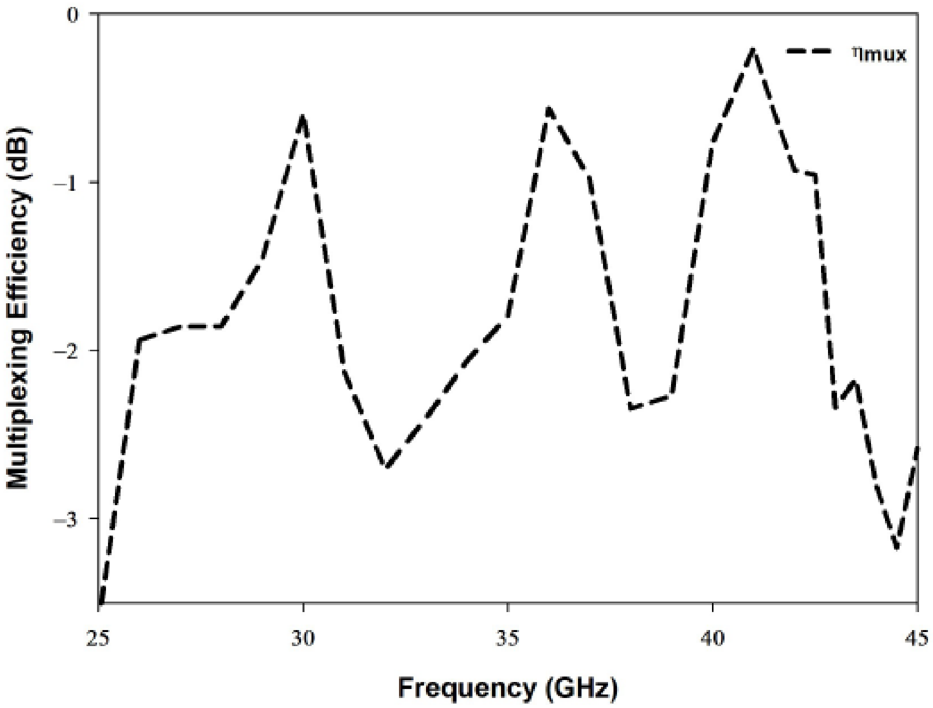

Figure 4.19: The multiplexing efficiency of the proposed MIMO antenna.

4.6.7 Comparison with Published MIMO DRA Designs

The performance of the proposed dual band mm-wave MIMO antenna has been evaluated and compared with recently published counterpart antennas as demonstrated in Table 4-2. As per the observations, the proposed antenna resonates at dual bands while all the reported MIMO DRAs operate in a single band. The data demonstrate that the proposed design offers the highest measured reduction in S_{21} over the dual frequency bands. Further, the achieved ECC in both frequency bands is very close to the highest value reported in [51, 103]. In addition, the proposed configuration offers the lowest profile of $0.11\lambda_0$ compared to the MIMO DRAs reported in the literature. Compared to published counterparts, the proposed antenna is advantageous on various aspects such as the compact size, dual band operation, and simple low-cost structure in which there is no need to incorporate additional components to improve the isolation between the two DRAs. In addition, it offers excellent performance at all the MIMO figures of merit across the bandwidths of the two considered operating frequency bands.

Table 4-2: Comparison the similar designs with proposed MIMO antenna.

Ref.	Number of Elements	Height (mm)	Operating Bands (GHz)	Average in S_{21} (dB)	ECC	DG	CLL
[50]	2	0.2 λ_0	60	22	-	-	-
[51]	2	0.25 λ_0	60	16	$< 0.1 \times 10^{-6}$	-	-
[53]	2	0.13 λ_0	28	22.7	-	-	-
[54]	2	0.24 λ_0	28	12	0.013	9.9	-
[99]	4	0.15 λ_0	28	14	0.0005	-	0.6
[103]	2	0.24 λ_0	60	19	$< 5 \times 10^{-6}$	-	-
This work	2	0.09/0.12 λ_0	28/38	25/27	0.007/0.003	9.98/9.99	0.06/0.09

4.7 Conclusions

A novel MIMO rectangular DRA configuration has been proposed. The design operates at a dual band, whereby the lower band is centered at 28 GHz and the higher band is centred at 38 GHz. It is worth mentioning that the main contribution is to modify the dual band DRA arrangements in order to reduce the coupling between antennas without affecting other key parameters, such as the gain, impedance bandwidth, efficiency, and radiation pattern. This is particularly important for a mm-wave antenna design for which the performance can be easily affected by any changes in the size as well as the addition of air holes or layers. Moreover, the proposed configuration reduces the transmission coefficient in a cost-effective approach. The optimum configuration of two DRAs on opposite sides of the Rogers substrate offers the minimum measured S_{21} of -41 dB and -44 dB at 28 GHz and 38 GHz, respectively. A significant diversity performance was demonstrated in terms of the ECC, DG, and CCL, which implies that the proposed antenna is most suitable for MIMO design. Owing to the dual band operation, the proposed configuration can be used in various applications, such as 5G mobile handsets. The proposed design principle has been demonstrated by utilizing two DRAs, but it is applicable for MIMO DRA systems with a higher number of elements.

Chapter 5

Low Profile Dielectric Resonator Antenna for the V Frequency Band

5.1 Introduction

This section proposes a DRA of different shapes, e.g., cylindrical and rectangular, that operates at the V frequency band of 40-75 GHz. At this frequency band, the DRA can operate in the unlicensed wider bandwidth as it offers more bandwidth compared to other antennas at 60 GHz that are used in different application like radar applications. The aim is to develop low-profile antennas that work at the V band using materials with properties that are close to those of semiconductor materials, such as silicon, Gallium Nitride and Gallium Arsenide in terms of thickness and permittivity. However, the aforementioned semiconductor materials take long to be fabricated, are expensive, and need to be fabricated in a clean room which is a restrained environment where contaminants like dust and floating microbes are purified in order to provide the cleanest environment. For example, in the previous Chapters, Alumina has been utilised which has a dielectric constant of with $\varepsilon_r = 9.9$, which is equivalent to that of Gallium Nitride, GaN, that has a dielectric constant of 9.5.

It should be noted that Gallium Nitride is also more advantageous than Silicon as it has a nearly three times higher bandgap that makes it suitable for equipping higher power applications, and it has higher electron mobility that makes it suitable to handle faster switching of frequencies.

Wireless communications have advanced in recent years and multi-band antennas represent an essential part of high-frequency applications. Satellite and Futuristic Mobile

Generations and Wi Gig applications utilise high frequencies that range between 22 GHz to 28 GHz and 55 GHz to 63 GHz, respectively. These applications have drawn more attention towards the development of multi-band antennas. As a result, designing such antennas would be more cost-effective than designing several antennas whereby each would operate at a single band.

As mentioned earlier, various feeding structures can be utilised to excite the DRA. However, at higher frequency bands, the CPW feed is a convenient feeding structure because it does not involve the use of a reducing metallization metal in the structure. This is important because when the ratio of metals increases, there would be a higher rate of losses [120]. Thus, it's important to choose the feeding structure that has a limited ratio of metals within it to avoid losses as much as possible. In addition, there is no need for multiple fabrication steps as in the case of a microstrip line. At 20 and 30 GHz, as illustrated in previous Chapters, it is certainly important to ensure that there is alignment. However, it is not as critical as it is at 60 GHz. This is because the size of the DRA would be much smaller at 60 GHz, and there are likely to be misalignment issues that could affect the results significantly. Therefore, it is important to pay additional attention to alignment at 60 GHz than at 20-30 GHz.

5.2 Resonance Modes of a Cylindrical DRA

A 3D view of a cylindrical DRA that is placed on a metallic ground plate is illustrated in Figure 5.1. The DRA can generate two different types of resonance modes namely TE (E_z= 0) and TM (H_z= 0) modes as well as hybrid modes (named EH and HE if the H_z and E_z component are dominants, respectively). The electromagnetic fields are symmetric axially in TE and TM modes with no deviations along the azimuth, φ, direction [121]. In contrast, the fields of hybrid modes vary along the φ direction. Hence, they are classified further into EH and HE modes [122, 123]. Moreover, these modes are asymmetric and characterize a superposition of the field of TE and TM mode. In the cylindrically shaped dielectric waveguide, E_z and H_z can generate an angular-based solution according to the Debye potential [121].

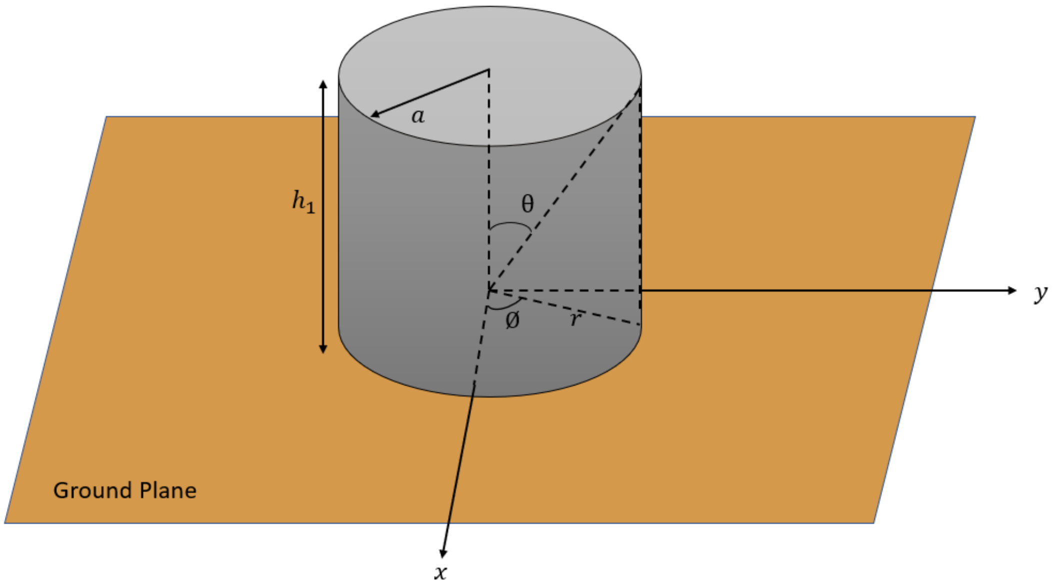

Figure 5.1: Cylindrical DRA mounted on a metal ground plane

The naming convention of the resonant modes in a cylindrical DRA are TE_{mnp}, TM_{mnp}, HE_{mnp}, and EH_{mnp}, where m represents the number of full-wavelength cycles along the azimuth (φ) direction, while n and p show the number of half-wavelengths field changes along the radial (ρ) and axial (z) axes, respectively.

In contrast to a rectangular DRA, accurate calculations of the resonant frequencies at higher order modes of a cylindrical DRA are difficult even with complex mathematical modelling [124]. Nevertheless, CST MWS Eigen mode is useful to determine the resonance frequencies of the higher order modes. In contrast, it is possible to approximately determine the resonant frequency at the fundamental mode of operation considering the diameter and height of the cylinder as well as its relative permittivity (ε_r). For example, if the aspect ratio range is within 0.4 ≤ a/h ≤ 6, the resonance frequency corresponds to the $HE_{11\delta}$ (mode can be specified as [124]):

$$k_0 a = \frac{6.324}{\sqrt{\varepsilon_r + 2}}\left[0.27 + 0.36\left(\frac{a}{2h}\right) - 0.02\left(\frac{a}{2h}\right)^2\right] \tag{5.1}$$

where the free space wave number is defined as $k_0 = 2\pi f_0/c$; c is the speed of light in free space, and f_0 is the resonant frequency. δ reaches 1 for higher dielectric permittivity values while varying between $0 \leq \delta \leq 1$. Likewise, if the aspect ratio is within 0.33 ≤ a/h ≤ 5, the resonance frequency corresponds to the $TE_{01\delta}$ mode can be specified as [125].

$$k_0 a = \frac{2.327}{\sqrt{\varepsilon_r + 1}}\left[1.0 + 0.2123\left(\frac{a}{h}\right) - 0.00898\left(\frac{a}{h}\right)^2\right] \tag{5.2}$$

when the aspect ratio remains within 0.33 ≤ a/h ≤ 5, the resonance frequency of the $TM_{01\delta}$ mode can be expressed as [126].

$$k_0 a = \frac{2\pi f_0 a}{c} = \frac{\sqrt{3.83^2 + \left(\frac{\pi a}{2h}\right)^2}}{\sqrt{\varepsilon_r + 2}} \tag{5.3}$$

5.3 On chip cylindrical DRA

The research carried out on DRAs can be classified in two categories. The first is focused at enhancing the antenna radiation characteristics such as gain, efficiency and radiation pattern. Non-semiconductor dielectric materials are commonly used for the substrate carrying the driving circuit and as a result, the antennas are unsuitable for the on-chip integration. The second category either applies to GaAs or silicon (Si) substrates, on which the driving electronics are placed. These are known as on-chip DRAs that are made of another material, so they require a hybrid integration.

To overcome the hybrid integration, the DRA and substate should use the same material which micromachined the DRA from the same wafer as GaAs, Si, and GaN. This kind of approach provided a good choice in terms of simplicity.

5.3.1 Linearly Polarised cylindrical DRA with Magnetic Dipole Excitation

In study [45], a novel design for a cylindrical DRA is presented: the structure of the DRA is illustrated in Figure 5.2. The CDRA which has radius a is fabricated from silicon wafer as illustrated schematically in Figure 5.2 (a). The resistivity of the silicon wafer is 2000 Ω.cm, its dielectric loss tangent (tan δ) is 0.003, and its relative permittivity ϵ_r = 11.9. The wafers used were 670 μm thick, and the height of the DRA is 400 μm, and the thickness of the substrate is 270 μm. Such a thin substrate thickness helps to prevent the excitation of the whole surface of the substrate [127]. The cylindrical DRA excitation takes place through a slot, which has the length and width of l and w, respectively. The slot terminates the feeding CPW lines, which consist of slots with 40 μm width that are separated by 68 μm. The dimensions of the line correspond to a characteristic impedance of 50 Ω as illustrated in Figure 5.2 (b). Figure 5.3 exhibits impedance bandwidth of 3.8% at 60 GHz. The radiation efficiency and gain are 80% and 7 dBi, respectively.

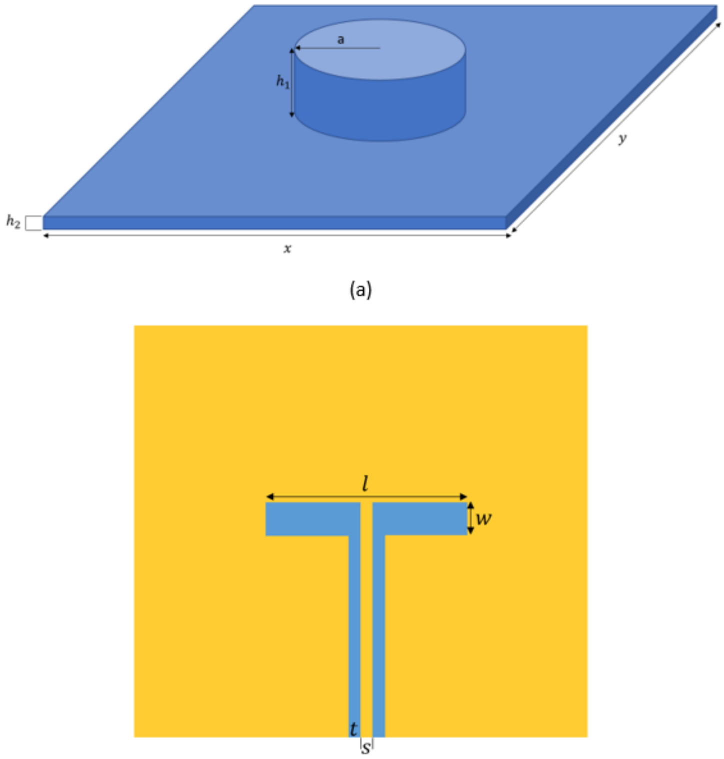

(a)

Figure 5.2: Geometry of on-chip DRA: (a) 3-D view of the design. (b) Projected top view.

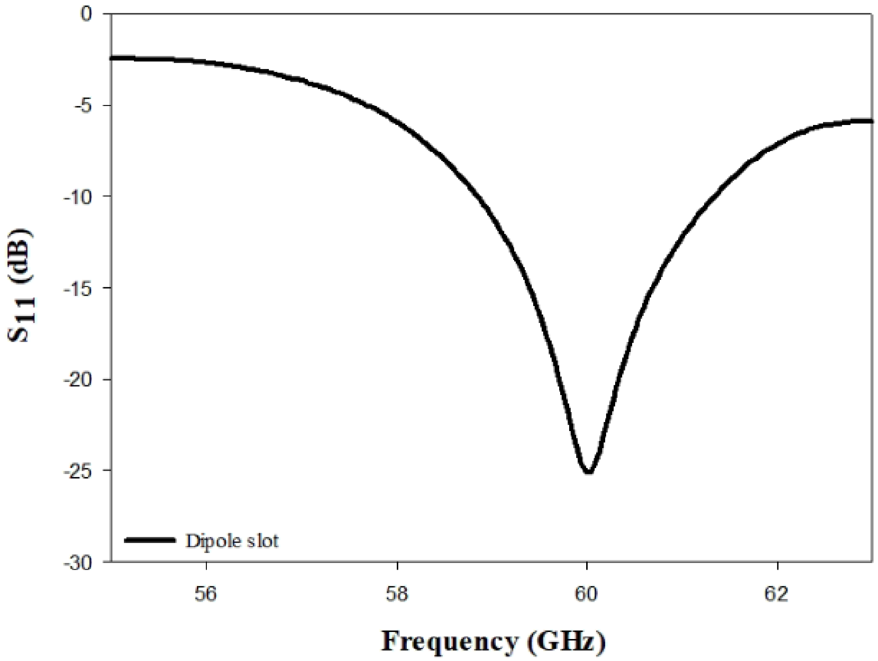

Figure 5.3: Return losses for the DRA with dipole and annular slots at ε_r= 11.9, ε_s= 11.9, h_1= 0.4 mm, a = 1.3 mm = h_2= 0.27 mm, h= 1 mm.

.

5.3.2 Linearly Polarised cylindrical DRA with dual loop excitation

The schematic configuration of the proposed dual-band linear polarization (LP) annular-ring slot antenna is illustrated in Figure 5.4. The antenna is printed on a copper of thickness ≥ 5μm, with a total dimension of x by y_2. Two concentric annular-ring slots with radii $r_1$and r_2 are etched into the ground plane, which is itself printed on the posterior of the substrate and coupled to a coplanar waveguide (CPW) feed line. The CPW is printed on the bottom side to achieve dual-band operation. The addition of this parasitic element can produce extra resonances that leads to significant enhancement in the bandwidth. Since the additional parasitic element is placed inside the original loop, there is no direct electrical connection to its surroundings. Additionally, there is no significant increase in size and complexity of the antenna structure.

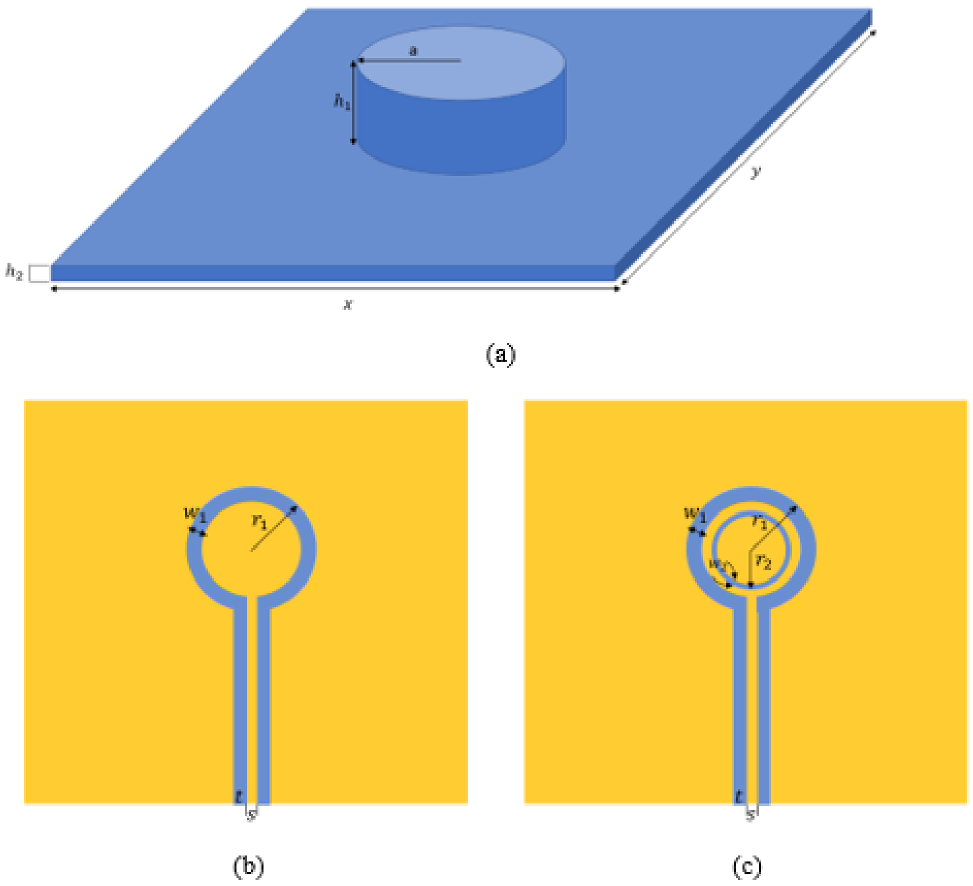

(a)

(b)

(c)

Figure 5.4: Projected top view illustrating the geometry: (a) On-chip DRA. Planar annular slot (b) without (c) with parasitic element

Figure 5.5 demonstrates the effect of the excitation of the annular slot as compared to the dipole slot in terms of the bandwidth. The graph illustrates that using the annular slot results in bandwidth of 8.18% and 4.14% at 38 GHz and 60 GHz, respectively, whereas using the dipole slot results in bandwidth of 3.78% at 60 GHz. It has been observed that the annular slot operates at dual band while the dipole slot operates at single band only. The single annular slot antenna is used to achieve dual-frequency whilst the parasitic annular slot increases the bandwidth by adjusting the key antenna parameters, which are the inner and outer radii of annular-slots. Figure 5.6 presents a comparison between the reflection coefficient of the annular slot antenna with the single loop and dual loops. The proposed antenna with the single slot is (8.18 - 4.14) % and dual loops have a bandwidth of (7.76 - 8.81) %. Consequently, it was noticed that the reflection coefficient improves by adding the parasitic loop inside the annular slot antenna. Moreover, DRA that has been proposed demonstrated good radiation characteristics. The gain is equal to 7.76 dBi and 8.81 dBi at 38 GHz and 60 GHz, respectively, and the radiation efficiency is equal to 89.1%.

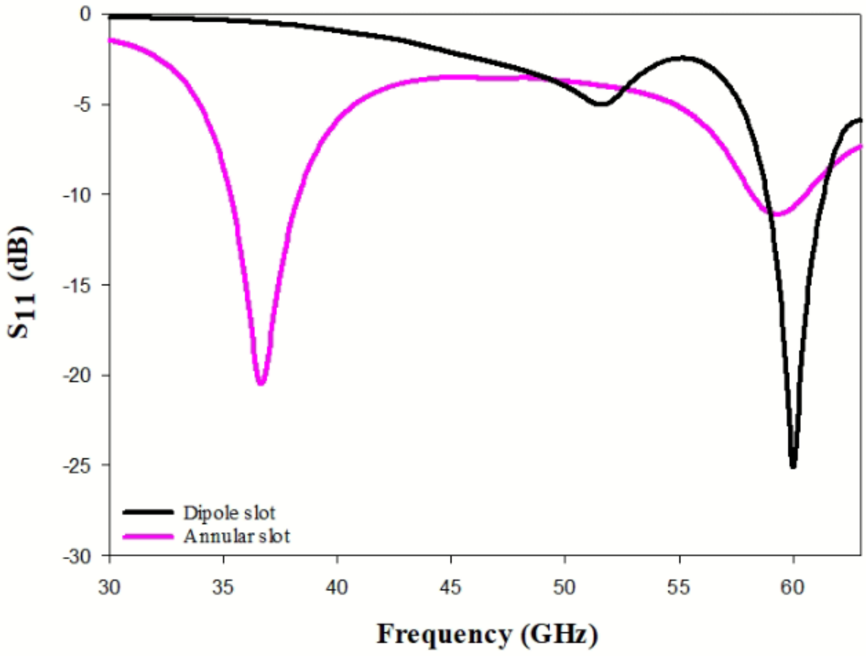

Figure 5.5: Return losses for the DRA with dipole and annular slots.

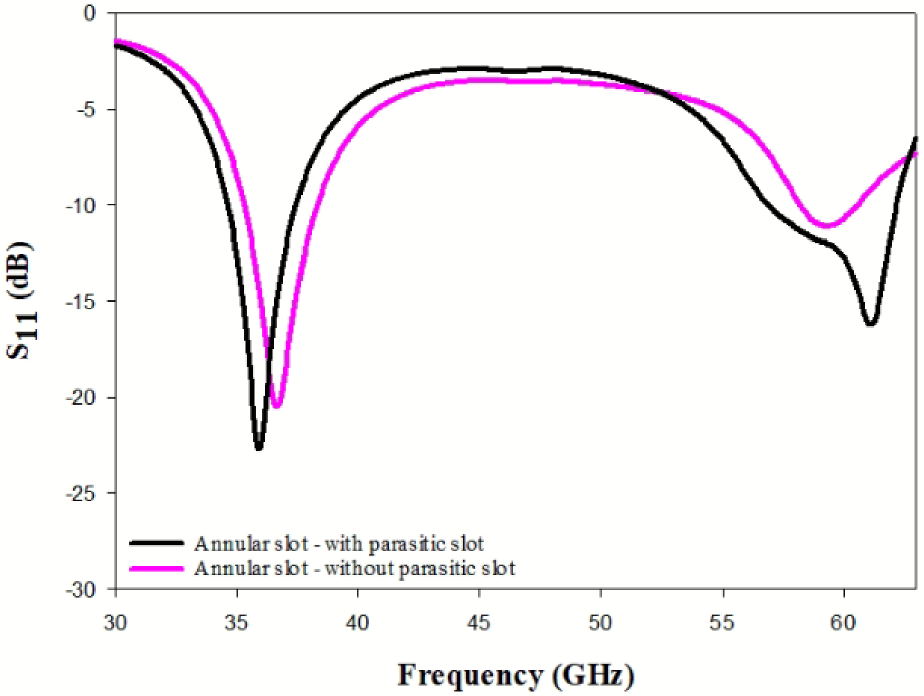

Figure 5.6: Return losses of cylindrical DRA with single and dual annular slot.

5.3.3 Circularly Polarized cylindrical DRA

The CP DRA has received increasing attention because of its distinct advantages over the LP counterpart, such as insensitivities to the antenna orientation and propagation effects [128]. The schematic configuration of the proposed dual-band circular polarization (CP) annular-ring slot antenna is illustrated in Figure 5.7, which is printed on a copper of thickness ≥ 5 µm, with a total dimension of x by y. Two concentric annular-ring slots with gaps G and G_p are etched in the ground plane printed on the back side of the substrate and coupled to a coplanar waveguide (CPW) feed line printed on the bottom side to achieve dual-band operation. Annular slot antennas are typically used as linearly polarized antennas. In previous research, it has been found that an annular slot antenna can radiate circularly polarized waves if a gap is cut in the loop. This CP radiation can be produced because the traveling wave current distribution gets excited along the open loop. The fundamental resonant mode will be split into two orthogonal degenerate modes. With an appropriate perturbation, the two orthogonal degenerate modes of the annular slot can be excited with 90◦ phase difference. As a result, CP radiation will be realised [86].

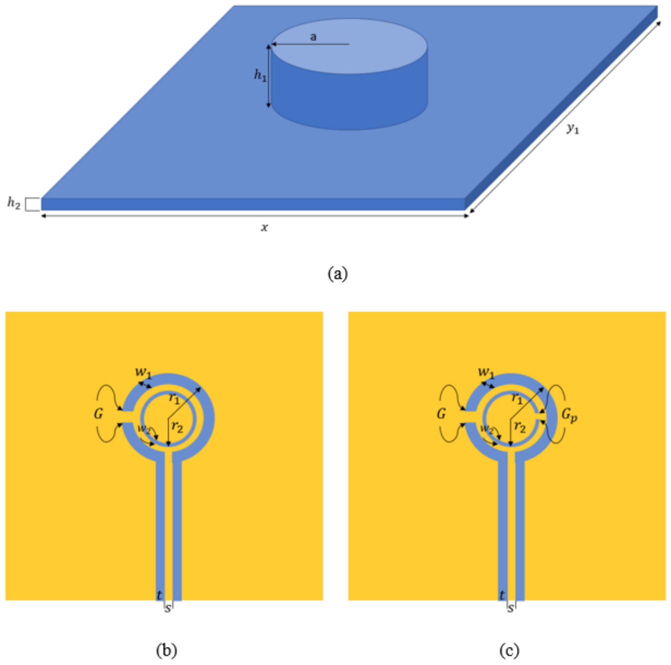

Figure 5.7: Projected top view illustrating the geometry: (a) On-chip DRA. Planar annular slot with (b) one gap and (c) two gaps for CP radiation.

It is found that the axial ratio (AR) bandwidth of a CP annular slot antenna can be significantly increased by adding another loop inside the original loop. The addition of this parasitic element can produce more resonant frequency bands that lead to a considerable enhancement for the AR bandwidth. Since the additional parasitic element is placed inside the original loop and there is no direct electrical connection to its surroundings, there is no significant increase in size and complexity of the antenna structure. As demonstrated in Figure 5.7 (c), the CP antenna consists of two open annular slots that are etched on a ground plane at the back of the silicon substrate. The outer slot acts as the driven element, while the inner counterpart acts as a parasitic element. A small gap is cut on each slot in order to radiate a CP wave. Furthermore, by adjusting the size of parasitic slot and the positions of two gaps, an optimal broadside axial ratio can be achieved. The single annular slot feed is used to achieve dual-frequency bands while incorporating the parasitic annular slot provided a dual-sense circular-polarisation by adjustment of the inner and outer radii of annular-slots.

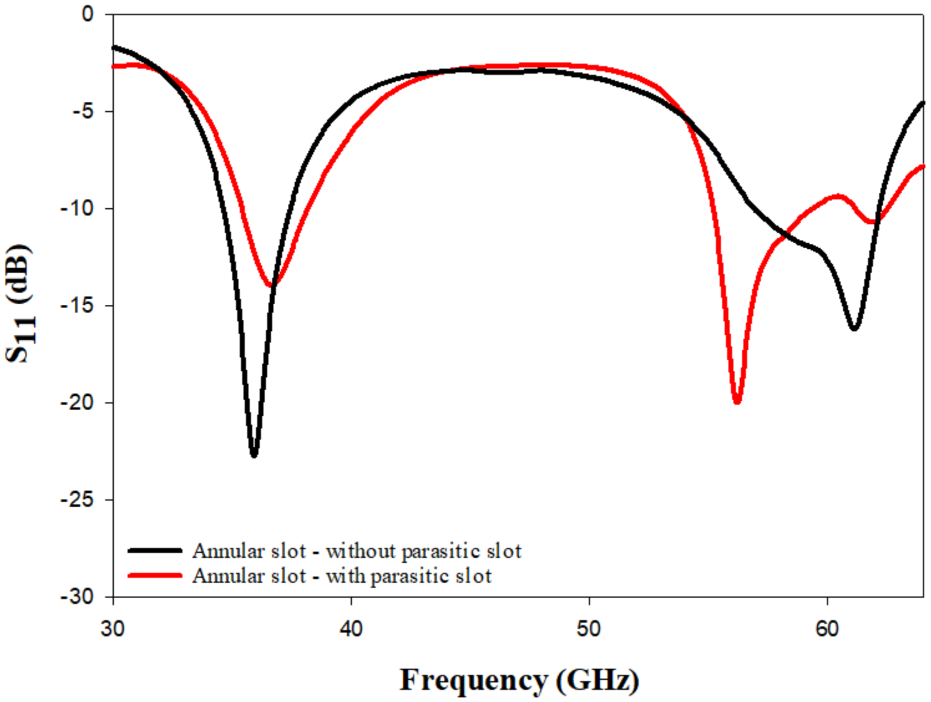

Figure 5.8: Return losses of cylindrical DRA with single and dual annular slot.

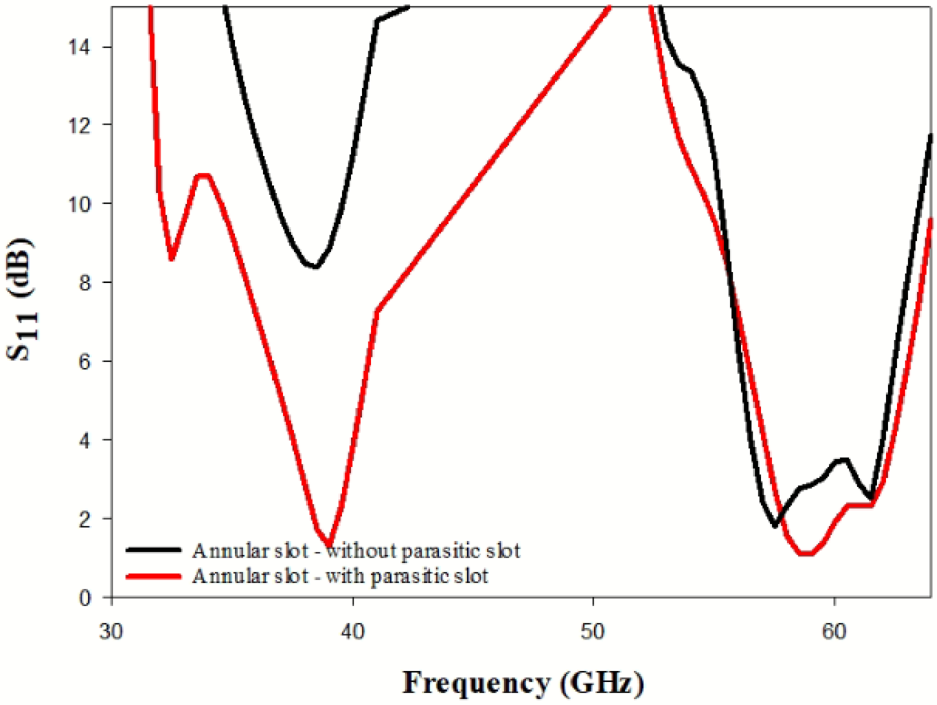

Figure 5.9: Return losses of cylindrical DRA with single and dual annular slot.

Figure 5.8 demonstrates the return loss of the CP antenna where it can be noticed that inserting the parasitic annular slot has improved the bandwidth from 7.7% to 9.2% and from 7.4% to 19.01%, for the lower and upper frequency bands, respectively. Figures 5.9 illustrates the axial ratio of the CP antennas with and without the parasitic slot, respectively. It is confirmed that adding a gap in the parasitic slot increases the AR bandwidth considerably. The axial ratio bandwidth has been increased at 40 GHz from 0.00% to 4.63% and for the second resonance, at 60 GHz, the bandwidth has been increased from 4.52% to 7.75% by adding a gap in the parasitic slot. Furthermore, the proposed DRA demonstrates good radiation characteristics. At the dual band, i.e., at 38 GHz and 60 GHz, the gain is equal to 5.5 dBi and 7.18 dBi, respectively. The radiation efficiency is equal to 91.2%.

5.4 Fabrication process and measurement of cylindrical DRA

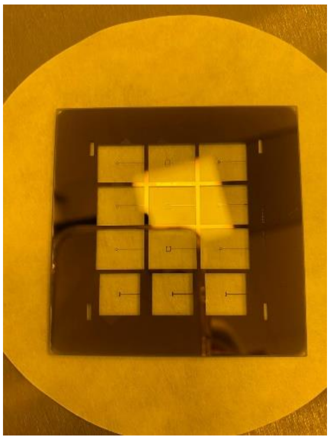

Figure 5.10: Fabricated mask of DRA feeding structures that included more than one feed to reduce the cost and time.

This section illustrates the fabrication and measurement processes that have been carried out for the cylindrical DRA. The silicon wafer has a resistivity of 2000 Ω.cm, a dielectric loss tangent (tan δ) of 0.004, and a permittivity ϵr = 11.9. Additionally, the thickness of the silicon wafer was 670 μm thick.

Figure 5.10 illustrates the mask that is used in the fabrication and measurement process of the cylindrical DRA. After choosing the silicon wafer, the mask is fabricated. It is fabricated in the clean room facility, and it contains the feeding structure. The layout of the mask is fabricated by exposing, developing, etching and cleaning it until it’s ready for use.

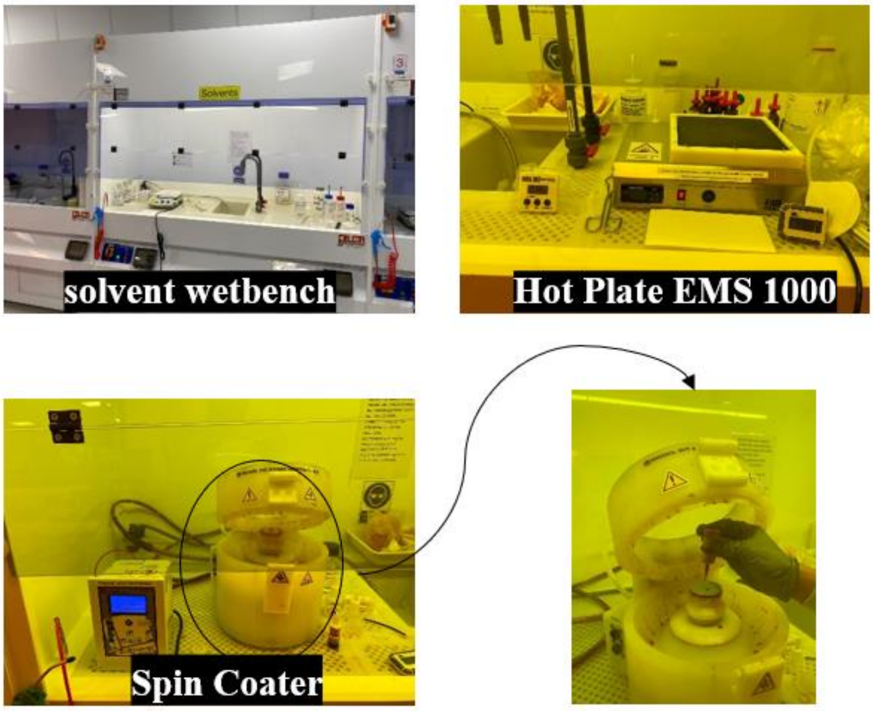

Figure 5.11: Fabrication process of the silicon wafer (cleaning, baking and spinning).

Figure 5.11 illustrates the method that is carried out to clean the silicon wafer from any impurities. Beakers for solvent cleaning that contain N-buty acetate, Acetone, and isopropyl alcohol are used to clean the sample. Then, the baking process is carried out at a chemical station called the yellow room. The sample is placed in the chemical station that contains a baker to bake the sample at 100 degrees Celsius for 60 seconds. Figure 5.11 also illustrates the spinning process where the sample is placed in a spinner where some drops of AZ1514H (photoresist) are added for coating. While holding down the lid to close the spinner, Vacuum will be applied to keep the sample firmly in place. Then, the spinning will be processed for about 60 seconds. After the spinning process, the sample is placed for baking for 60 seconds.

(a) (b)

Figure 5.12: Fabrication process of the silicon wafer.

Figure 5.12 illustrates the photolithography process. The mask is aligned to choose the feeding structure that it should be exposed to. After baking the silicon wafer sample, it is placed in the station of photolithography to be exposed to the feeding structure. Then, the sample and mask are exposed for 5.5 seconds.

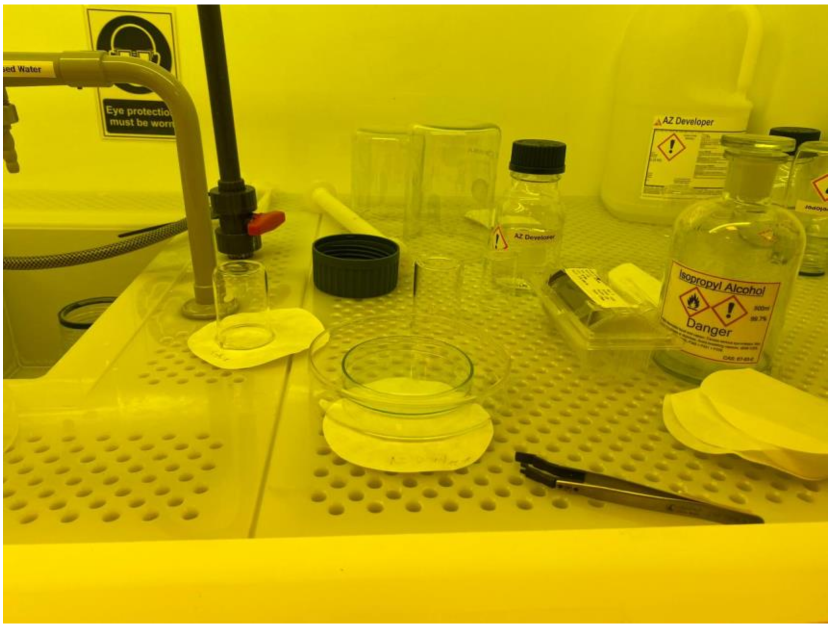

Figure 5.13: Fabrication process of developer the sample.

Figure 5.13 illustrates the developer process. After the photolithography process, the sample is first placed in acetone for 60 seconds and then in water to develop the sample. Then, it is placed under running water to clean it. To dehydrate the sample, nitrogen air is applied onto it. The sample is placed under the microscope, as shown in Figure 5.12, to ensure that there are no defects in the sample and that it can be used in future processes.

After examining the sample, it was taken to do the metallisation process whereby gold was used as the metal. Figure 5.14 (a) illustrates the device that has been used to carry out the metallisation process. Figure 5.14 (b) illustrates the sample after metallisation, which is then applied for lift-off to result in the design illustrated in Figure 5.14 (c).

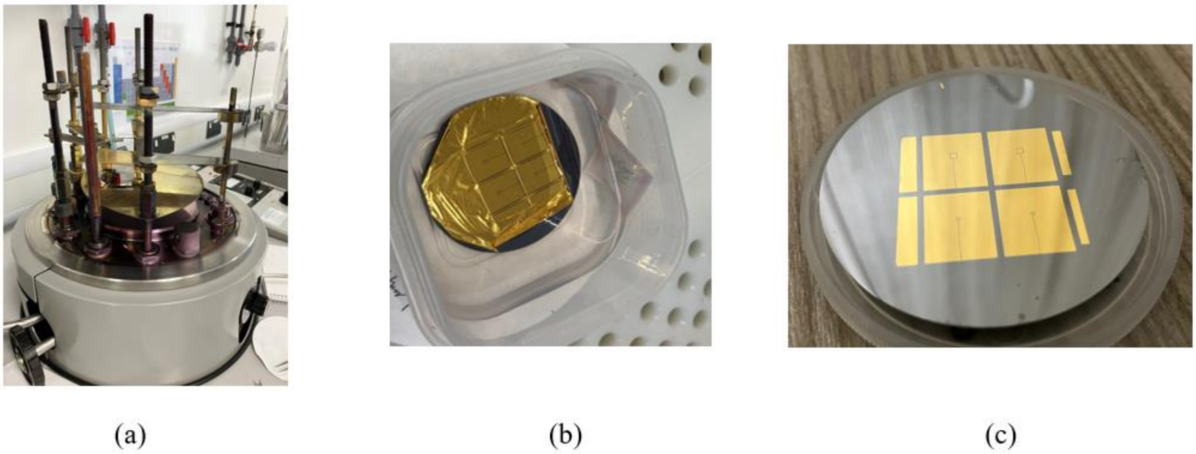
(a) (b) (c)

Figure 5.14: Fabrication process of metallization the sample

Various equipments have been used in the lab for the measurement of parameters. The wafer probe station (MPI TS150-THZ) is a manual probe system that had been designed for precise analysis of substrates, 150 mm wafers, or single dies. To do so, the thin needles are precisely positioned on the surface of any devices like antenna.

Three kinds of probes are available at the lab. The MPI Titan Probe has 150 µm pitch. There are two types of picoprobe with slight differences between them, as one of them has 150 µm pitch and operates between 75 GHz and 110 GHz, while the other one has 100 µm pitch and operates between 50 and 75 GHz. For the design, the picoprobe that has pitch of 100 µm and operates at a frequency that ranges between 50 and 75 GHz has been chosen. The vector network (N5245B) has four ports and can measure a frequency up to 50 GHz. Nevertheless, the proposed design operates at a frequency above 50 GHz, so VDI frequency extenders have been used to extend the capacity of the operating frequency so that it measures frequencies that range between 50 GHz and 110 GHz.

The spherical measurement system, that has been designed by NSI-MI technologies, is used to measure the radiation pattern, gain, and axial ratio. However, at frequencies higher than 50 GHz, another probe station should be used to do the measurements accurately. Yet, the probe station has not been offered at lab. Since axial ratio cannot be measured, the following section will investigate measurements of linear polarization only.

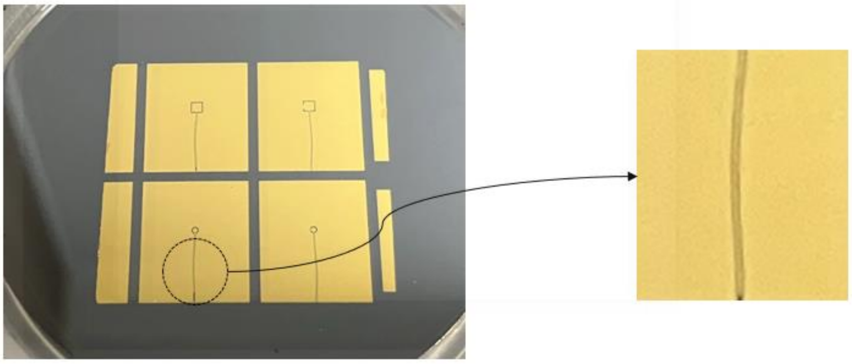

Figure 5.15: Fabricated sample of feeding structure with tilted lines.

As shown in Figure 5.15, it has been observed that the lines are tilted and that the results are inaccurate. This is because the length of the lines is inaccurate and inconsistent. Also, the adjacent distance between the lines is incoherent throughout such that some parts result in a short circuit. This affected the results and has made it more challenging to attain accurate results. Also, this process is time-consuming and is not cost-effective. Therefore, this fabrication process was not implemented in the study because it is not a precise fabrication process since it could result in major errors.

As mentioned earlier, the process of fabrication in clean room is time and money consuming, and the equipment used result in some defects as the results attained are not very precise. As a result, the cost is higher in terms of materials, solutions, and equipments. Therefore, to overcome these limitations, the next section proposes a design that can obtain the desired prototype using 3D printing. The implementation of the 3D printing can reduce the burden of time and cost that have been a challenge during the fabrication process in the clean room. The material used is equivalent to one of the semiconductor materials, and as shown in Figure 5.16, the materials are organised in order of decreasing permittivities, and it is notable that Alumina and GaN have close permittivities. Therefore, Alumina was used for the fabrication of the integrated DRA. Yet, it’s important to mention that silicon was used in earlier designs because it was available at lab.

Also, GaN is considered to be the future material since it’s more advantageous for use than silicon in terms of the bandgap and electron mobility as stated earlier. Thus, the material chosen in the design is relatively close to GaN in terms of permittivity and bandwidth.

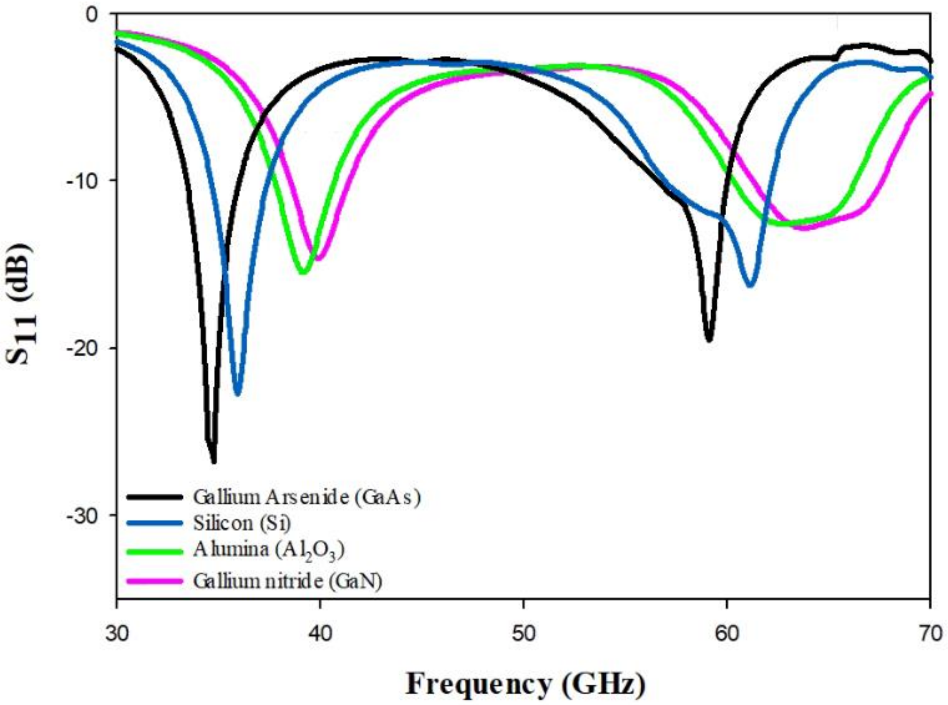

Figure 5.16: Reflection coefficient of cylindrical DRA with different material (Silicon, Gallium Arsenide, Alumina and Gallium Nitride).

5.5 Integrated Cylindrical DRA

The cylindrical DRA has been integrated into the substrate that has the same material, i.e., Alumina as illustrated in Figure 17 (a). The integrated DRA has been fabricated using 3D printing technology. The cylindrical DRA has a height h and radius a. The length, width and thickness of the integrated substrate have been defined as y_s, x_s and h_s, respectively. The feeding structure constitutes a Rogers lower substrate with relative permittivity of 2.2 and thickness of 0.256 mm. On the top of the substrate is a metal ground plane in which the CPW, two concentric annular slots have been etched and used to excite the DRA as demonstrated in Figure 5.17(b). The first annular slot has an annular radius of (r_1) and width of (w_1), while the inner parasitic slot has a radius of (r_2) and width of (w_2). The CPW feed has a spacing between the slots that is defined as s and with a slot width of t. It is worth mentioning that the width of the feeding structure has been chosen to be the same as that of the integrated substrate to simplify the assembly of the structure. On the other hand, the length of the feeding structure is 2 mm longer than that of the integrated substrate to ease the connection between the wafer probe and CPW feeding during the measurements.

5.5.1 Optimization of the feeding annular slot

The aim of this section is to examine the effects of changing the dimensions of the slot on the DRA performance in order to achieve wider and multiband. Three frequency ranges have been considered 47-55 GHz, 55-65 GHz and 65-77 GHz based on the available ranges of the available wafer probe in the lab that is capable of measuring the range of 47 to 77 GHz. The cylindrical DRA has a height and radius of 0.4 mm and 1.3 mm, respectively, which have been determined using the numerical equation (5.3), such that the fundamental mode TE_{111} can be excited.

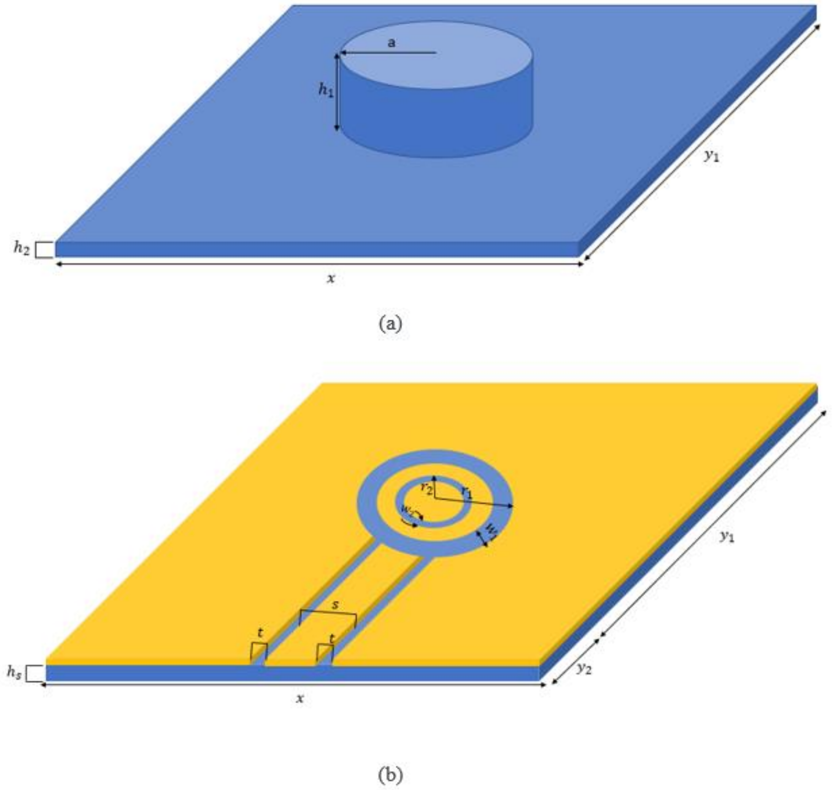

Figure 5.17: (a) 3D printed Alumina cylindrical DRA and substrate (b) CPW feeding structure.

The parametric study aims to determine the optimum radius and width of the outer annular slot while the inner slot is fixed at $r_2 = 0.3$ mm and w_2= 0.07 mm. Initially, the radius of the annular slot was changed from 0.5 mm to 0.9 mm at a step size of 0.1 mm, and the width was kept fixed at 0.2 mm. Also, the radius and height of cylindrical DRA were kept at 1.3 mm and 0.4 mm, respectively.

As illustrated in Figure 5.18, when the radius of the annular slot is $0.5 \leq a \leq 0.8$ mm, a dual band is attained. However, at 0.9 mm, only a single band is attained at 70 GHz albeit with a wider bandwidth. The optimum radius of the annular slot, as determined in the study, is 0.7 mm, as it has the potential to operate at 50 GHz and 60 GHz. When the outer slot's radius is 0.7 mm, the attained bandwidths are 4.5 % and 11.7 % at 50 GHz (HE_{111}) and 60 GHz (HE_{131}), respectively.

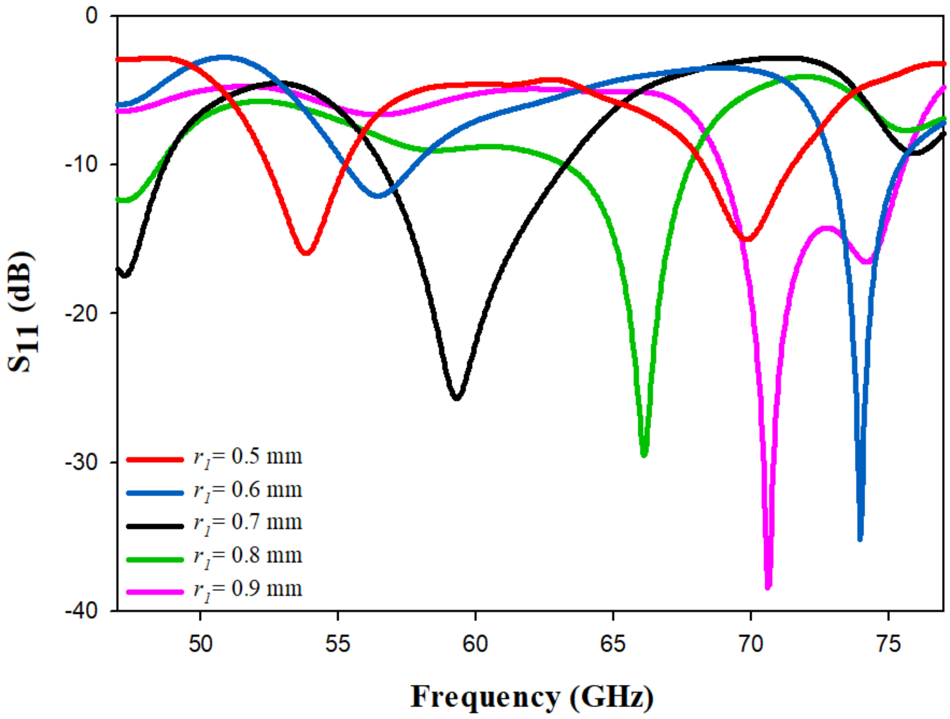

Figure 5.18: Impact of the outer annular slot's radius, r_1, on the reflection coefficient.

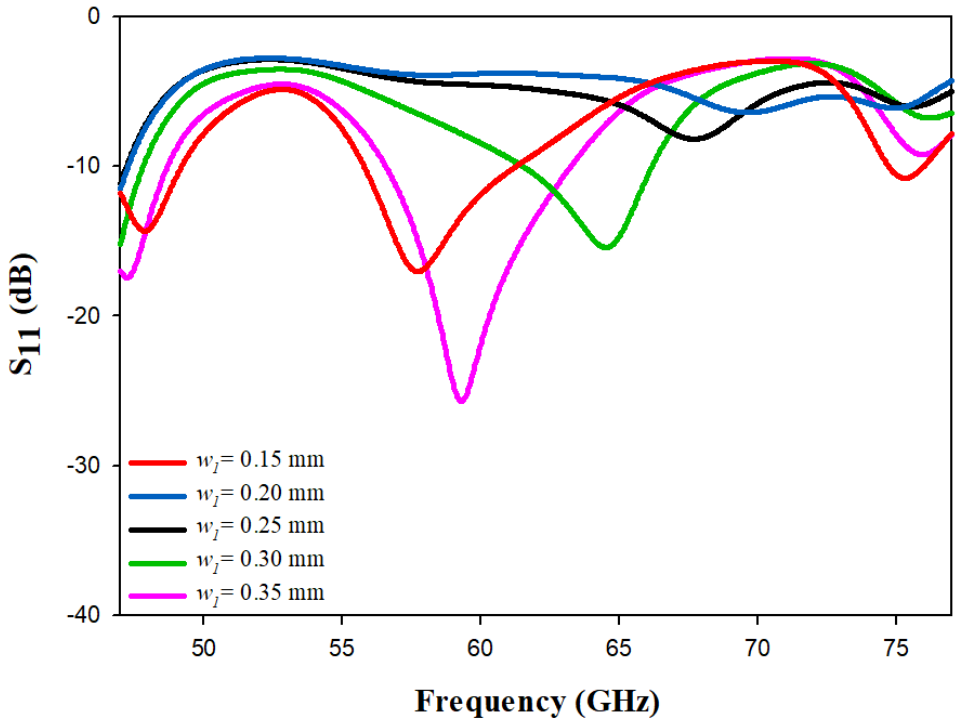

Figure 5.19: Impact of the outer annular slot width, w_1, on the reflection coefficient.

Figure 5.19 illustrates the effect of changing the width, w_1, of the outer annular slot on the bandwidth. Varying w_1 from 0.15 mm to 0.35 mm, demonstrates that when w_1 = 0.3 mm or 0.35 mm, only a single band is attained at lower frequencies, i.e., at 50 GHz. However, when w_1 = 0.20 mm or 0.25 mm, a dual band is attained at 50 GHz and 60 GHz. Additionally, when the width of the annular slot is equal to 0.15 mm, a multi-band is attained at 50 GHz, 60 GHz, and 70 GHz. Therefore, w_1 = 0.15 mm has been chosen as the optimum width of the outer annular slot. Yet, it is essential to note that it is not possible to choose a width that is less than 0.07 mm because of the fabrication limitations, as a very high tolerance would be required, which could adversely affect the measured results at higher frequencies.

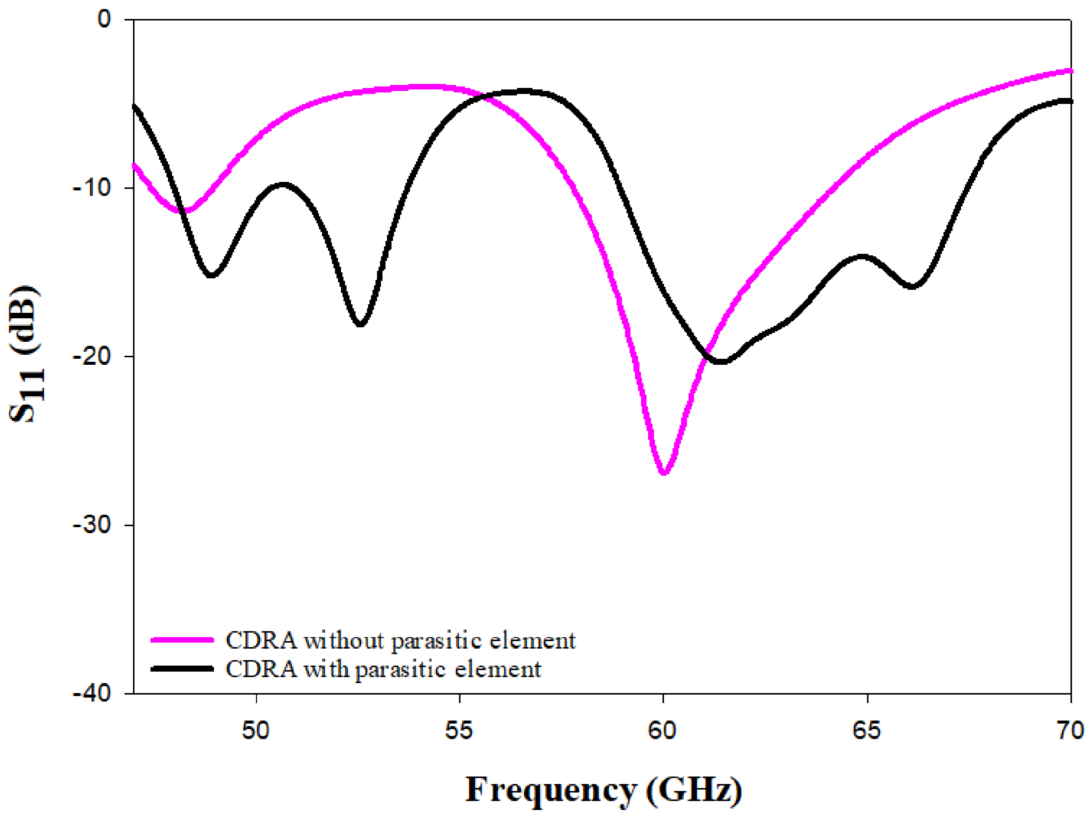

Figure 5.20: Effects of the parasitic slot on the reflection coefficient at $r_2 = 0.3\ mm, w_2 = 0.07\ mm, CDRA_r = 1.3\ mm\ and\ \ CDRA_h = 0.4\ mm$.

The parasitic slot has been utilized to achieve a wider impedance bandwidth [129]. Figure 5.20 illustrates the impact of adding a parasitic slot on the bandwidth by comparing the results of the bandwidth of cylindrical DRA with and without the parasitic element. The bandwidth in the presence of a parasitic slot is 9.5% and 12.6% at dual band, i.e., at the lower and higher frequency respectively. The parasitic element has a radius of r_2 and a width of w_2. The dimension chosen was dependent on the convenience of fabrication.

Section 5.2.4 demonstrates the measurement and fabrication with respect to the simulated and measured results as well as the techniques used for measurement and fabrication of various parameters of the cylindrical DRA.

5.5.2 Fabrication and measurement of cylindrical DRA

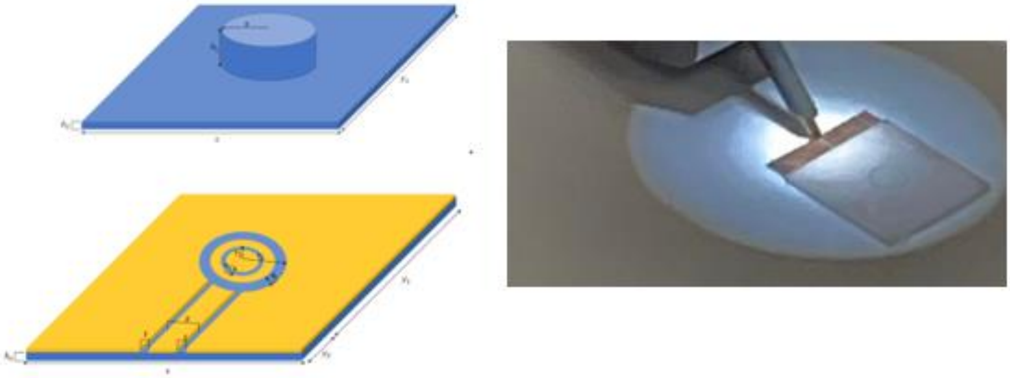
(a) (b)

Figure 5.21: (a) 3D printed Alumina cylindrical DRA and substrate (b) fabricated prototype under test.

As shown in Figure 5.21 (a), the optimal dimensions of the cylindrical DRA were obtained to be r = 1.3 mm; h_1= 0.35 mm; h_2 = 0.2 mm; x = 10mm; y_1= 10 mm. The cylindrical DRA was fabricated using 3D printing, and the material used was alumina which has a permittivity of 9.9.

Figure 5.21 (b) illustrates the optimal dimensions of the feeding structure that was fabricated using the PCB process. The substrate is attached to the ground plane made from Roger material, and it has a CPW feed attached to it. The substrate has dimensions of h_s= 0.256; x = 10 mm; y_1 + y_2= 12 mm. It is remarkable that the widths of the integrated cylindrical DRA and the feeding structure are equal, however, the y_1 is further extended by y_2 in order to increase the area and allow the probe to operate at the CPW feed.

To assemble the integrated cylindrical DRA and feeding structure, a glue brush has been used, and it will be discussed in further details in section 5.5.3.


(a) (b) (c)

Figure 5.22: (a) vector network analyser (b) wafer probe station (c) WR15 wafer probe.

The vector network analyser mm-wave converter, with a model of N5245B, is used to measure the bandwidth at 50 GHz as shown in figure 5.22 (a). However, it cannot measure higher frequencies, so Virginia Diodes (VDI) frequency extender has been used to increase its capability to operate at mm-wave bands beyond 50 GHz up to 110 GHz.

The wafer probe used to measure the reflection coefficient (S_{11}) is model N5262BR15 WR15, as shown in Figure 5.22 (c). The probe has three pins which are with a patch of 100 µm, i.e., the distance between two adjacent pins is equal to 100 µm. The probe can measure frequencies that range between 47 GHz and 77 GHz.

Figure 5.23 illustrates reflection coefficient for the measured and simulated results. As shown, there is dual band for the measured and simulated at 50 GHz and 60 GHz. At 50 GHz, the return loss was equal to 5.9 % and 10.2 % for the measured and simulated, respectively. At 60 GHz, the return loss was equal to 12.42 % and 13.75 % for the measured and simulated, respectively. At 60 GHz, there is close agreement between the measured and simulated results. However, at 50 GHz, there is less agreement between the measured and simulated results. This is a result of fabrication errors and experimental tolerances.

The simulated radiation patterns, gain, and efficiency at 50 GHz and 60 GHz are illustrated in Figure 5.24. The simulated efficiency is 90% at the operating frequency range.

The simulated gain at 50 GHz and 60 GHz is equal to 5.9 dBi and 7.15 dBi, respectively. It is noteworthy that the measured results could not be attained in the lab because there are no sufficient stations available to perform accurate investigations of the above-mentioned parameters.

It is worth mentioning that a limitation has been observed while employing the cylindrical shape of the DRA. The side walls of the cylindrical shape cannot be as well defined as the side walls of the rectangular shape. This finding was observed after the fabrication of the proposed design was discussed with the clean room leader. Therefore, in order to overcome this limitation, a rectangular DRA will be introduced in the next section.

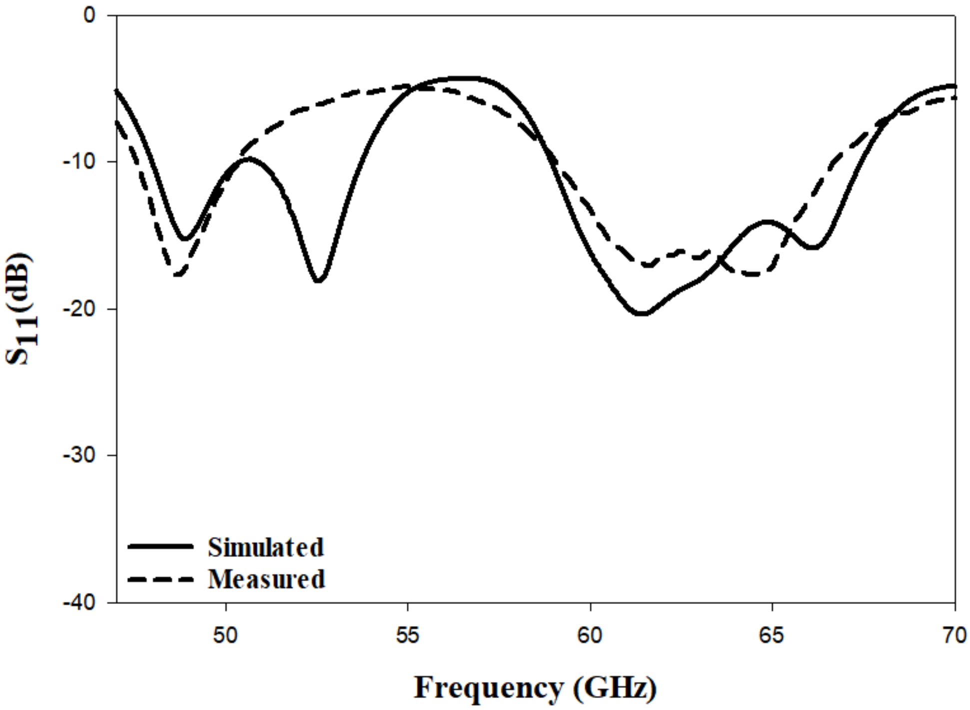

Figure 5.23: Simulated and measured of reflection coefficient of cylindrical DRA at $r_2 = 0.3\ mm, w_2 = 0.07\ mm, CDRA_r = 1.3\ mm\ and\ \ CDRA_h = 0.4\ mm$..

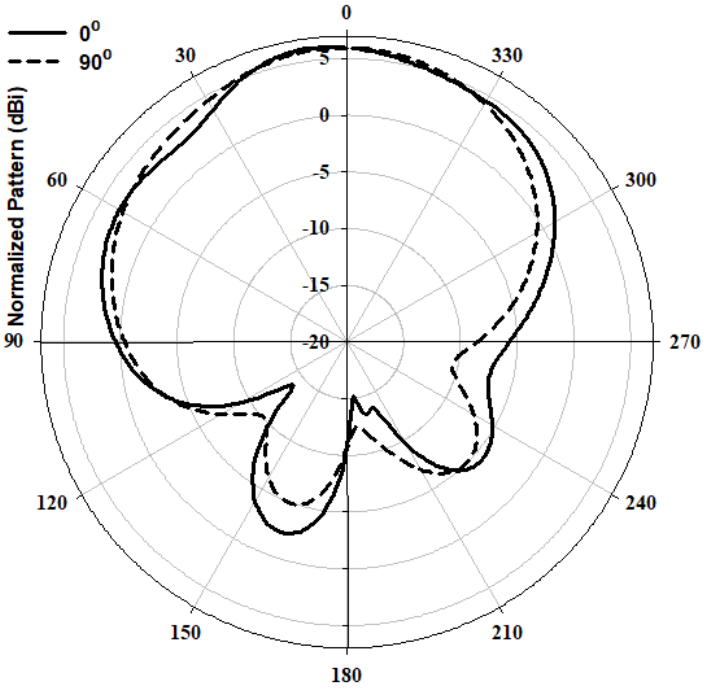

(a)

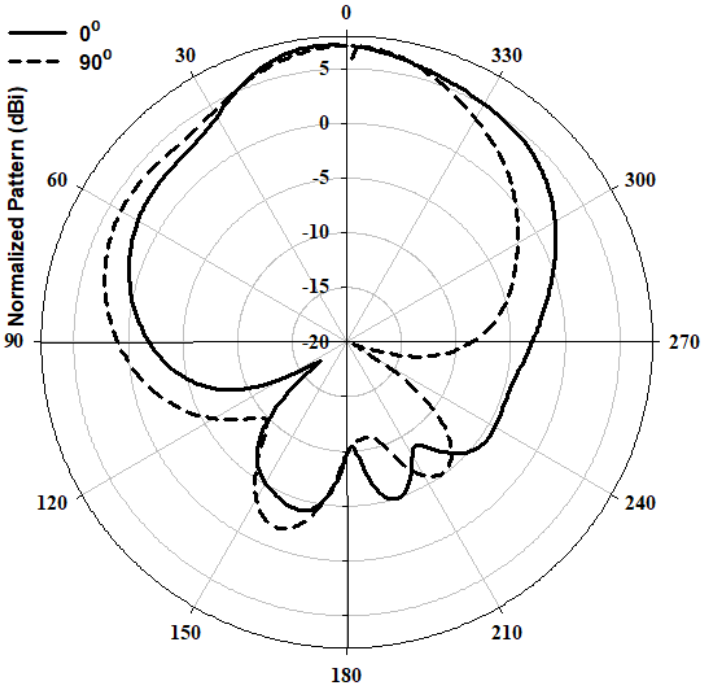

(b)

Figure 5.24: Radiation patterns of cylindrical DRA at (a) 50 GHz and (b) 60 GHz.

5.6 Integrated Rectangular DRA

5.6.1 Configuration design of rectangular DRA

Figure 5.25 illustrates the configuration and dimensions of a rectangular DRA that was used in the study. The rectangular DRA is integrated into a substrate using 3D printing. They also are made of the same material, i.e., alumina with a dielectric permittivity of 9.9. The rectangular DRA has a length, width, and height of l, w, and h, respectively. It is notable that l = w for the rectangular DRA. The integrated substrate has a thickness of 0.2 mm, and a width and length of x and y_1, respectively.

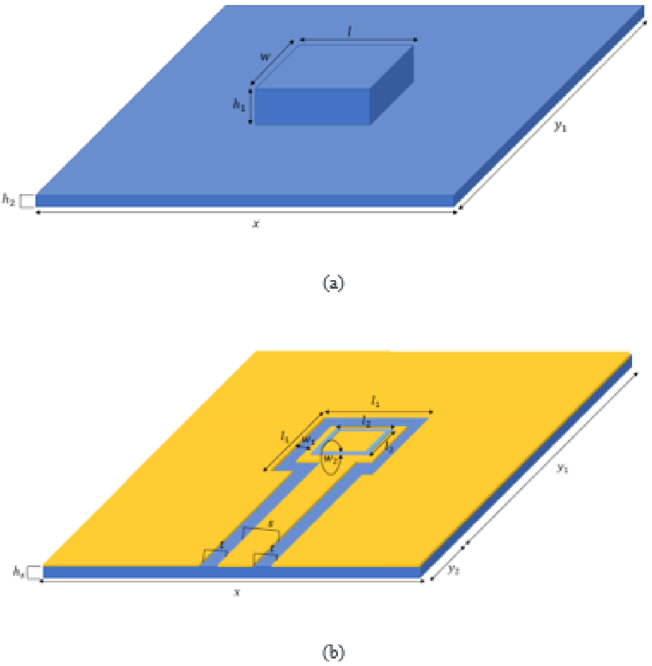

(a)

(b)

Figure 5.25: (a) 3D printed Alumina rectangular DRA and substrate (b) CPW feeding structure.

The feeding structure has a substrate made of Roger with a permittivity of 2.2. It has dimensions of x, $y_{1,2}$, and h. The CPW is used to excite the DRA, and it has slot separation (s), and slot width (t). The square slot has a length and width of l_1 and w_1. The parasitic slot was etched inside the bigger square slot and had a length and width of l_2 and w_2. The integrated DRA is placed on the feeding structure. They have equal widths to facilitate the alignment.

However, the length of the feeding structure is 2 mm longer than that of the integrated DRA to provide sufficient space for the wafer probe to be in contact and to connect with the CPW.

The dielectric waveguide model (DWM) defines the DRA's dimensions. Two families of mode can be used to constitute the modes of the rectangular dielectric waveguide, namely TM_{mnl} and TE_{mnl}, whereby m, n, and l represent the extrema number inside the dielectric waveguide the x, y, and z- directions, respectively. The following equations are used to attain the fundamental resonant frequency of rectangular DRA at TE_{111} mode, where k_x, k_y,and k_z, represent that wave numbers across the x, y, and z axis respectively. c represents the speed of light:

$$f_0 = \frac{c}{2\pi\varepsilon_r}\sqrt{\left(k_x^2 + k_y^2 + k_z^2\right)} \tag{5.4}$$

The wafer probe is limited to measuring frequencies between 47 GHz and 77 GHz. Thus, the dimensions of the DRA have been designed in an attempt to resonate at a target frequency band. This prototype excites multi-boards which allows the DRA to operate at multi-bands.

5.6.2 Parametric study

The rectangular DRA has a length, width, and height of 3 mm, 3 mm, and 0.9 mm. These dimensions have been chosen based on equation (5.4). This design proposes that using a square slot can excite different modes. Thus, the chosen dimensions are expected to operate at multi-modes. Also, the implementation of a slot to excite the DRA may shift the frequency higher or lower at optimum conditions. To facilitate the discussion of details, the frequency ranges have been categorized into regions, such that 50 GHz, 60 GHz, and 70 GHz region represents the frequency from 47 GHz to 55 GHz, 55 GHz to 65 GHz, and 65 GHz to 75 GHz, respectively.

The square slot had a length and width of l_1 and w_1. This section aims to examine the effect of changing the dimensions of the slot. To begin, the l_1 has been changed from 1.1 mm to 1.5 mm by a step size of 0.1 mm, while the w_1 has been kept constant at 0.2 mm. Then, the bandwidth is noted for each dimension, as shown in Figure 5.26. Figure 26 illustrates the effect of changing the S-parameter on the bandwidth.

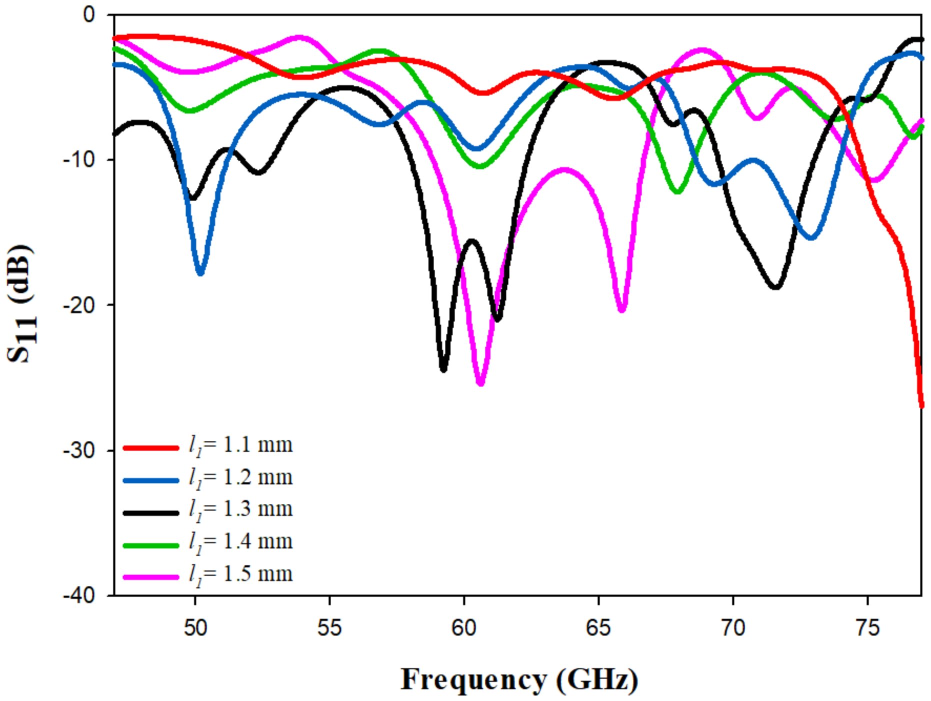

Figure 5.26: Effects of the square slot dimensions on the reflection coefficient (l_1).

As shown, at 70 GHz, the antenna at all the examined parameters can operate at 70 GHz. However, it is evident that not all parameters have sufficient bandwidth at 70 GHz. At 50 GHz and 60 GHz, it is evident that as the parameter size increases, the bandwidth increases. At 50 GHz, the bandwidth for the dimension of 1.2 mm and 1.3 mm is equal to 3.9% and 7.1%, respectively. Similarly, at 60 GHz, the bandwidth for the dimension of 1.3 mm is equal to 7.8%. On the contrary, at 70 GHz, it is evident that as the parameter size increases, the bandwidth decreases. At 70 GHz, the bandwidth for the dimension of 1.2 mm and 1.3 mm is equal to 7.1% and 5%, respectively. The aim of this design is to identify the dimensions that would have sufficient bandwidth in all bands.

The most suitable bandwidth was attained when l_1 = 1.3 mm. Thus, l_1 was kept constant at 1.3 mm while changing the w_1 from 0.09 mm to 0.21 mm by a step size of 0.03 mm. The bandwidth for each dimension was also noted, as shown in Figure 5.27. Figure 5.27 illustrates the effect of changing the width of the square slot on the bandwidth. The length (l_1) was maintained at 1.3 mm. Also, there is not a significant impact on the bandwidth at 50 GHz. Reducing the width makes the bandwidth shift upwards, and there is no matching at 60 GHz. Reducing the width shifts the resonance frequency to a higher frequency and vice versa at 70 GHz. Moreover, the bandwidth attained at 50 GHz, 60 GHz, and 70 GHz when w_1 = 0.18, is 3.5%, 7.2%, and 6.8%.

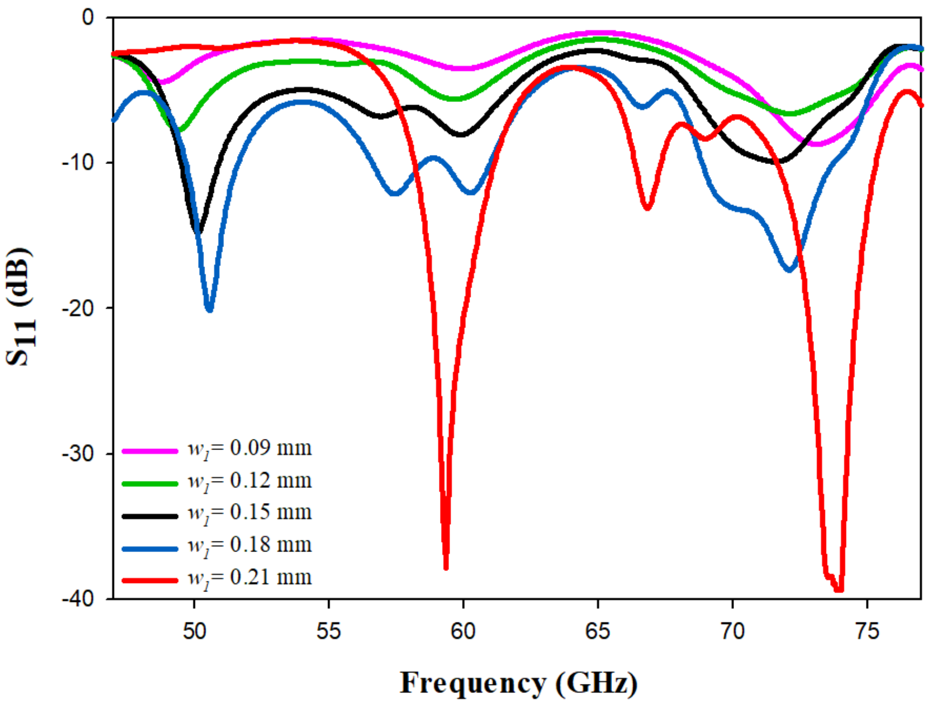

Figure 5.27: Effects of the square slot dimensions on the reflection coefficient (w_1).

To further improve the bandwidth, a parasitic slot has been added into the main square slot. The parasitic slot dimensions have been chosen to be suitable to be inserted inside the square slot and based on convenience concerning the capability of fabricating its dimensions. The parasitic slot has a length and width of l_2 and w_2, respectively. In Figure 5.28, the effect of adding a parasitic slot has been shown by comparing the bandwidth of the rectangular DRA with and without parasitic slot. Figure 5.28 shows that adding parasitic slot results in triple band at 50 GHz, 60 GHz, and 70 GHz which excited in TE_{111}, TE_{311}, and TE_{331}, respectively. On the contrary, not adding parasitic slot results in a narrower band, as it only achieves a dual band at 50 GHz and 70 GHz. At 50 GHz, 60 GHz, and 70 GHz, the bandwidth is equal to 0.35 mm is 2.4%, 7.3%, and 5.3%, respectively.

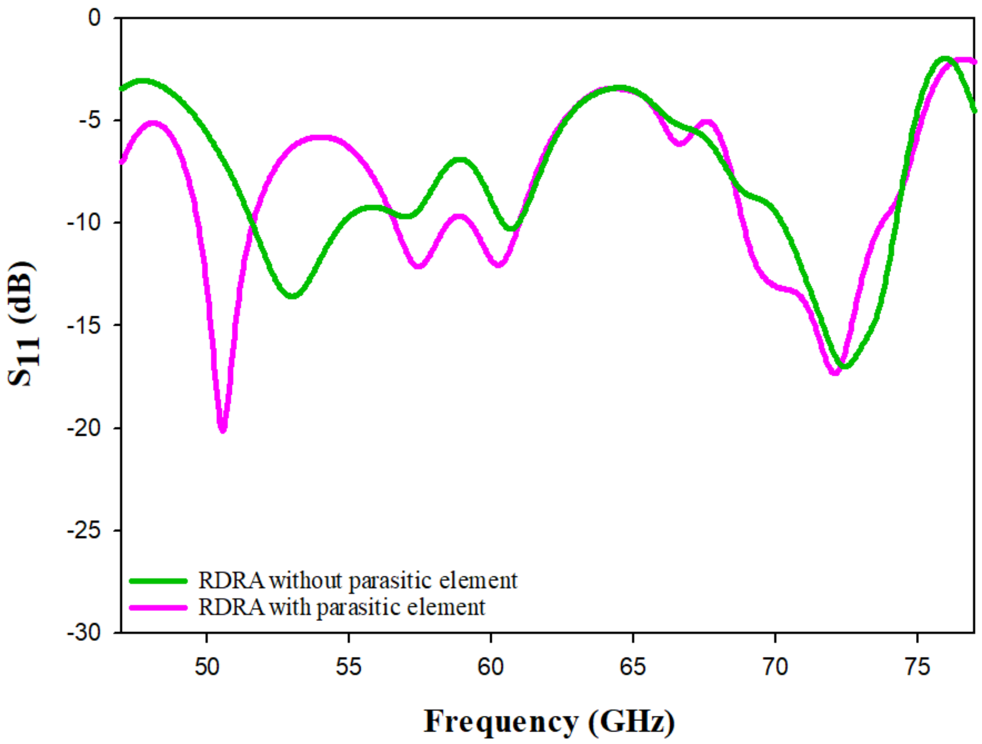

Figure 5.28: Effects of the parasitic slot on the reflection coefficient.

5.6.3 Fabrication and measurement of rectangular DRA

This section discusses the fabrication and measurement of the proposed prototype of the rectangular DRA. Also, the alignment and the fixture techniques that have been used are discussed in detail.

As shown in Figure 5.29 (a), the optimal dimensions of the rectangular DRA are: h_1= 0.9 mm; h_2 = 0.2 mm; x = 10 mm; y_1 = 10 mm; l= w = 3 mm. The rectangular DRA was fabricated using 3D printing and alumina with a permittivity of 9.9.

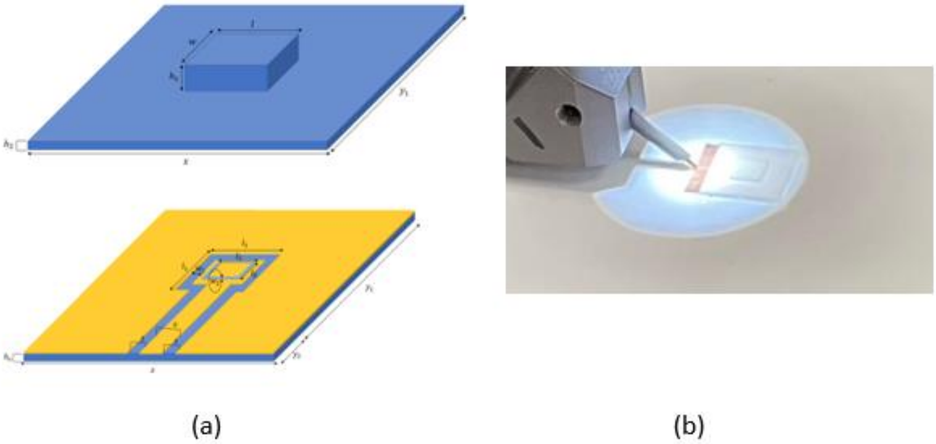

(a) (b)

Figure 5.29: (a) 3D printed Alumina rectangular DRA and substrate (b) fabricated prototype under test.

Figure 5.29 (b) shows the feeding structure was fabricated through the PCB process. The substrate has dimensions of h_s = 0.256; x = 10 mm; y_1+ y_2= 12 mm, whereby width of feeding substrate is equal to width of integrated rectangular DRA. However, the y_1 is further extended by 12 mm in order to increase the area and allow the probe to operate at the CPW feed. The CPW feed has a square slot, whereby the l_1 = 1.3 mm, and w_1 = 0.18 mm.

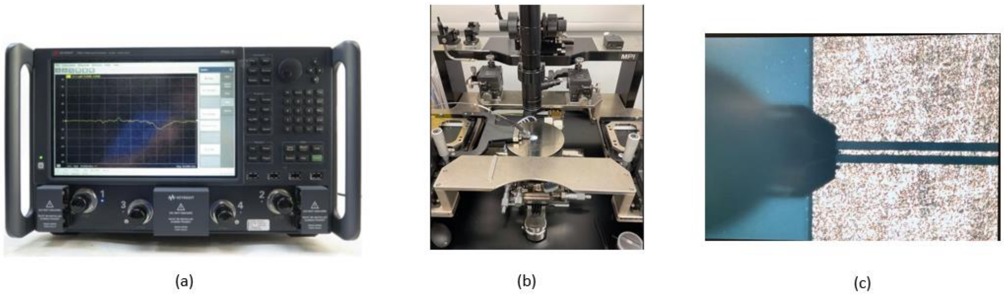
(a) (b) (c)

Figure 5.30: (a) vector network analyser (b) wafer probe station (c) WR15 wafer probe.

The devices used to measure the bandwidth and return loss are identical to the ones used in the previous section - Section 5.2.3. To measure the bandwidth at 50 GHz, the vector network analyser mm-wave converter, with a model of N5245B, is used. However, to measure the bandwidth at higher frequencies such as 50 GHz to 110 GHz, the Virginia Diodes (VDI) frequency extender is used. The VDI is capable of operating at mm-wave bands beyond 50 GHz. As shown in Figure 5.30, the vector network analyser N5245B is used to measure the $S11$ bandwidth. The vector network analyser has four ports. The wafer probe station with model N5262BR15 WR15 is used. The wafer probe has three pins which are 100 micrometres distant adjacently. It can measure frequencies that range between 47 GHz and 77 GHz.

It is remarkable that the widths of the integrated rectangular DRA and the feeding structure are equal. To align the integrated rectangular DRA and feeding structure, a glue brush has been used. As shown in Figure 5.31, the glue was placed on points a, b, c, d, and e on the feeding structure, such that the integrated rectangular DRA will stick onto the feeding structure. Pressure has been used to ensure that the glue does not escape further into or out of the structure. The glue has permittivity of ~2.5 which was manufactured by MULTICOMP.

As shown in Figure 5.32, the return losses were measured, and multi-band frequencies have been recorded. The measured and simulated bandwidth were equal to 5% and 4% at 50 GHz; 6% and 6.2% at 60 GHz; and 8% and 10% at 70 GHz, respectively. At 50 GHz and 60 GHz, the simulated and measured results are in good agreement. However, at 70 GHz, there is slight discrepancy between the bandwidth of the simulated and measured results. This is because of the fabrication errors and experimental tolerances.

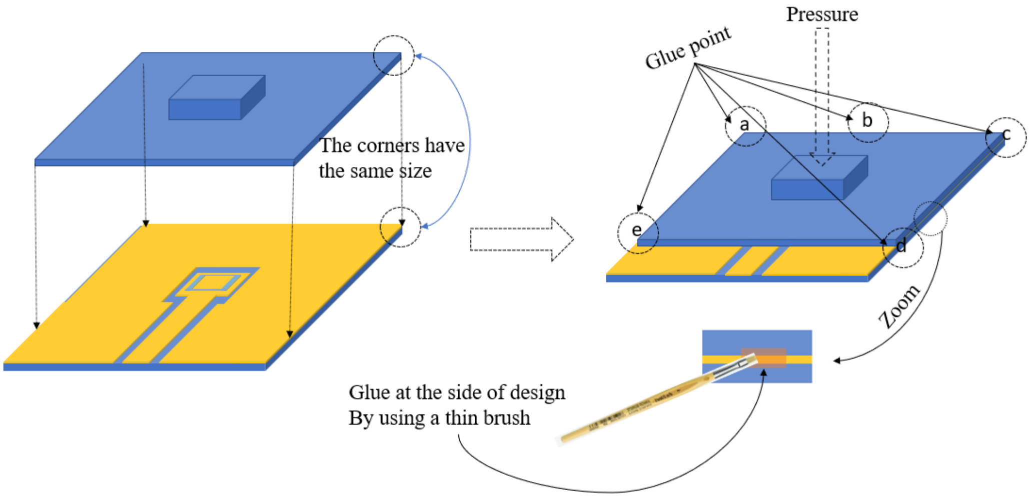

Figure 5.31: Procedure to align and assembly the integrated rectangular DRA with the feeding structure.

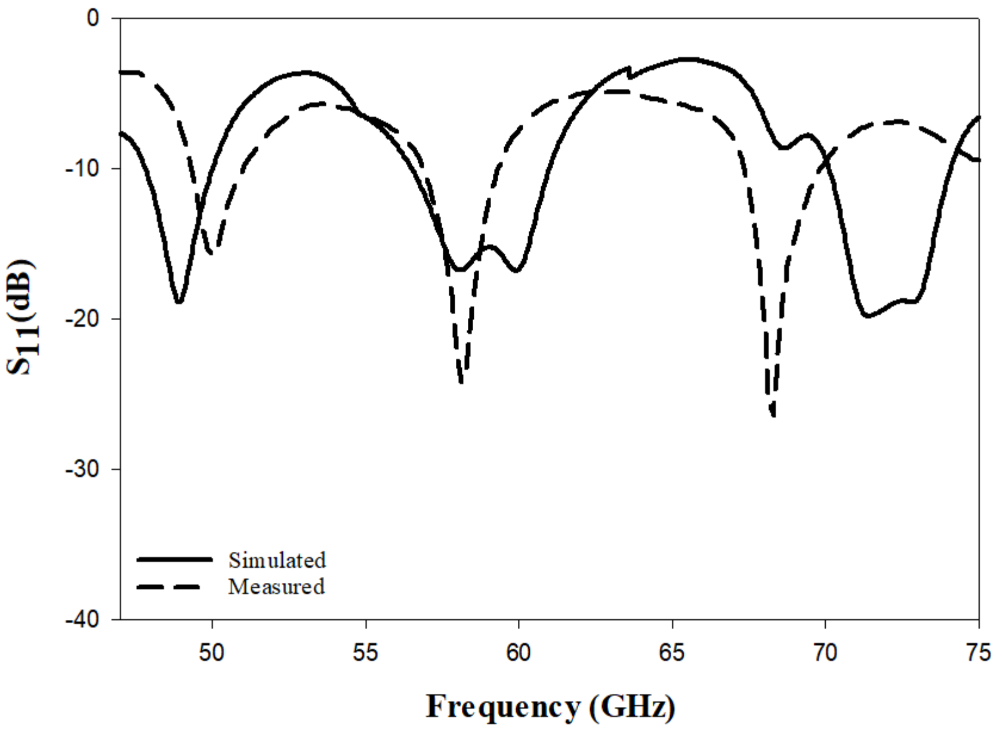

Figure 5.32: Simulated and measured of reflection coefficient of rectangular DRA at $l_1 = 1.3\ mm, w_1 = 0.18\ mm, RDRA_l = 10\ mm\ and\ \ RDRA_h = 0.2\ mm.$

.

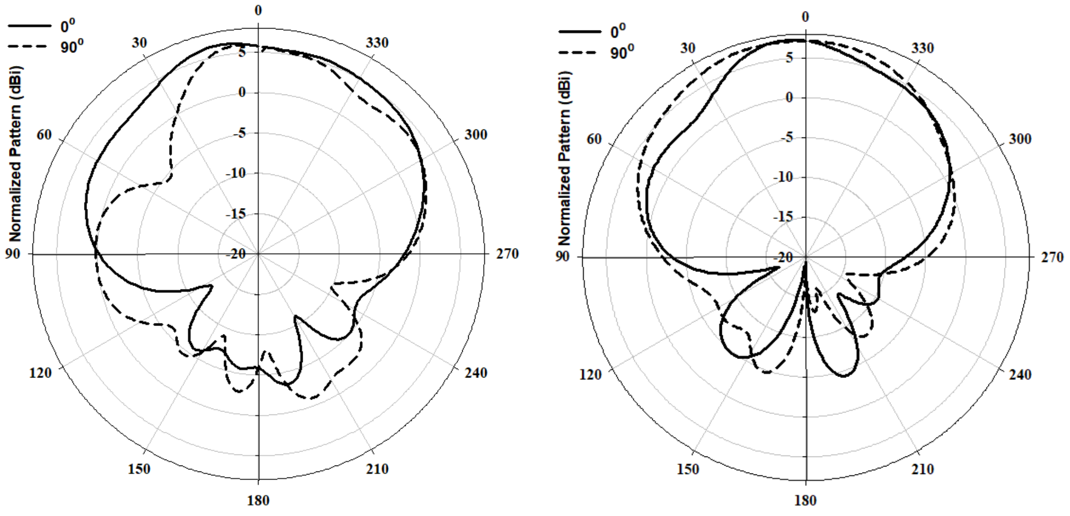

(a) (b)

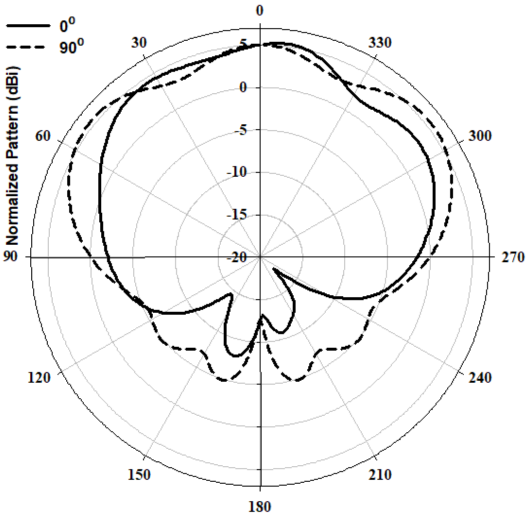

(c)

Figure 5.33: Radiation patterns of rectangular DRA at (a) 49 GHz, (b) 60 GHz, (c) 72 GHz at $l_1 = 1.3\,mm, w_1 = 0.18\,mm, RDRA_l = 10\,mm\ and\ \ RDRA_h = 0.2\,mm.$

Figure 5.33 illustrates the simulated radiation patterns at 49 GHz, 60 GHz, and 72 GHz. At 49 GHz, 60 GHz, and 70 GHz, the simulated gain is equal to 5.2 dBi, 7.11 dBi, and 6 dBi, respectively. The measured results have not been attained in the lab since there are no suitable stations available to perform accurate investigations of the above-mentioned parameters.

5.7 Conclusion

At V band, the misalignment, compact size, and wide/multiband bandwidth have been investigated in Chapter 5. Since the non-planar antenna will be more complex and less accurate in terms of fabrication, the cylindrical and rectangular DRA has been investigated. A square and annular slot have been chosen for the rectangular and cylindrical DRAs, respectively, to improve the impedance bandwidths. Both configurations have been integrated with a substate using 3D printing that provided more mechanical stability since the wavelength of 60 GHz is too small compared to lower frequencies. It is evident that the rectangular and cylindrical DRAs offer a dual band with a good impedance bandwidth that make them suitable for more than one application.

The importance of operating at 60 GHz has been discussed in detail earlier in this chapter. It is shown to be the optimum frequency of operating for the DRA since it has a potential future for mm-wave applications. The material used, i.e., Alumina, has a low profile and it has a permittivity that is close to gallium nitride (GaN), since alumina and GaN have a permittivity of 9.5 and 10, respectively. Additionally, CP and LP are investigated in the study. Adding gaps in annular and parasitic slots generate the CP and achieved dual band. Yet, the CP cannot be measured in the lab, therefore, LP was measured instead. Furthermore, the fabrication of the on-chip antenna results in many limitations like being cost and time-consuming and having inaccurate dimensions. The integrated substrate that has been fabricated using 3D printing gives advantages of not using any adhesive materials or texturing techniques to fix the DRA and substrate. Additionally, the position of the DRA is well-aligned which helps avoid any error that could occur as a result of misalignment. Furthermore, it can ensure that it would be aligned to the feeding structure in a more convenient way and would not require the use of high technology.

The cylindrical and rectangular DRAs operate at more than one band, i.e., at dual band and triple band, respectively. Thus, they are useful for operation at different frequencies simultaneously, which implies that they would reduce the cost. A parasitic slot has been implemented in both designs, and it is advantageous because it helps improve the band further. A good validation has been achieved between the simulated and measured results. Nevertheless, it is important to remark that the rectangular DRA was implemented because it has side walls that are more defined than that of the cylindrical DRA. In sum, the proposed design is useful for various 5G applications in the future.

Chapter 6

Conclusions and Future Work

6.1 Conclusions

This thesis focused on several key ideas: alignment, fixture, wider linear polarisation and circular polarisation bands, dual bands, multi-bands, and higher data rates. Chapter one included the introduction, the research objectives, and literature review on existing studies, as well as the novelty of contribution for this thesis. Chapter two focused on methods that can be used to attain better alignment, fixture, wider band, and higher gain. Chapter three was about Circular Polarisation (CP) in which the bandwidth is increased, and alignment is improved. Chapter four was about high data rate and dual band. Chapter two, three, and four conducted studies on frequencies between 20 and 38 GHz. On the contrary, chapter five conducted studies at higher frequencies, i.e., at 60 GHz to examine techniques to maintain alignment at dual and multi-bands.

Chapter two first focused on determining the slot shape that would achieve a wider bandwidth for the excited high order mode of hemispherical DRA and it found that it is the annular slot. Yet, the wider band was challenging because it is not easy to place the DRA on the right position. For that, three techniques were applied to align the hemispherical DRA. The first technique involved highlighting the position of the single element and array through 3D printing, which was shown to have good performance, but it is limited because adhesive material had to be used. The second technique is known as ground-grooving and it involved creating a hole in the upper ground plane in accordance to the dimensions of the hemispherical DRA as much as possible to fit it, which also showed good results, but it was limited because the size of the hemispherical DRA is too small. The third technique involved integrating the

DRA with the substrate, which made alignment and assembly easier since it is better for use for smaller dimensions and there was no need to use any adhesive material. It gave better results in terms of assembly. It is noteworthy that all of the aforementioned techniques are fit candidates for alignment, however, it is important to consider three factors when choosing which one to apply, namely: dimensions, time, and cost.

Chapter 3 proposed a circularly polarised hemispherical DRA and techniques that have been used to increase the AR bandwidth and to enhance the freedom of choosing material that is available in the market. The cross-slot shape was chosen because unlike the annular slot, it is more flexible to change that could be subjected in the parameters. The limitation of using hemispherical DRA as compared to other DRA shapes, however, is that it is more challenging to achieve wider axial ratios (AR) because it is limited to one degree of freedom. Therefore, adding a substrate under the hemispherical DRA gave more freedom of change, and that subsequently contributed to improving the AR bandwidths. It is important to mention the substrate that has been added under the hemispherical DRA did not only improve the AR bandwidths, but also reduced the sensitivity of misalignment of the hemispherical DRA. Thus, the integrated substrate was used to improve the AR bandwidth and to avoid using any adhesive material that could affect the performance of the DRA. Another substrate which was perforated was later introduced to overcome the limitation of the unavailability of material in the market, and to provide more flexibility of changing the permittivity at lower costs and lesser time. The aforementioned techniques have shown a good agreement between the measurement results, which means that they are more suitable to apply on other DRA shapes to increase the AR bandwidth.

In mm-wave applications, it is important to maintain a high data rate, low profile, low cost, and low mutual coupling. Chapter 4 proposed a MIMO rectangular DRA that offered a dual band in conjunction with a good bandwidth, high gain and high efficiency. Furthermore, the slot configuration that has been used in this chapter is a contribution to the experiment since the cross slot and square slot are integrated together to produce a dual band. To reduce the mutual coupling between the rectangular DRAs, the positions of the feeding structures were investigated. In addition to that, it has been shown that the position of the rectangular DRAs helps to improve the mutual coupling which leads to having a good performance for the MIMO rectangular DRA without adding any extra materials that could increase the profile or implementing a metal vias that could lead to making it more complex. Moreover, the performance of the MIMO has been examined based on different parameters, namely: the envelope correlation coefficient, the channel capacity loss, diversity gain, total active reflection coefficient, the mean effective gain and the multiplexing efficiency. All these parameters showed a good performance that make the proposed design a good candidate for 5G mm-wave applications. It is also remarkable that the measured and simulated results show a good an agreement.

Chapter 5 investigated misalignment, compact size, and wide (dual and multi) bandwidths at frequencies between 40 GHz and 75 GHz. The DRAs used in the study are generally rectangular and cylindrical DRAs, which have planar top surfaces. However, the reason why hemispherical DRA is considered non-planar compared to them is that the hemispherical DRA does not have a planar top surface but a convex one.. Also, semiconductor materials, like GaN, have not been used in this study due to the limitations of the lab, hence, alumina, which has a close permittivity, has been used. In an attempt to improve the impedance bandwidth and to excite the rectangular DRA and CRDA, a square and annular slot with parasitic slots have been used to increase the bandwidth, respectively. Highlighting and Grooving methods were not used in this study, because as shown in Chapter 2, they are not suitable for use in DRAs that are small in size. Also, these methods require the use of adhesive material which could affect the performance of a DRA at 60 GHz, since the size is too small, and could lead to misalignment. The wavelength at 60 GHz is too small, as it is 5 mm which is much smaller than wavelengths at lower frequencies. Both configurations were integrated with a substrate through 3D printing. This method ensured better assembly, alignment, and mechanical stability for the DRA. The rectangular and cylindrical DRA offer more than one band with a good impedance bandwidth that is suitable for more than one application. It is worth to mention that the rectangular DRA has been employed since its side walls are more well-defined than that of the cylindrical DRA. Moreover, a good validation has been achieved between the simulated and measured results.

6.2 Future Work

This section presents implications that have been identified based on the findings of the thesis so that they would be applied to improve the findings of studies that would be conducted in the future.

As investigated in this thesis, the excited higher order modes and shape of slots offer a higher gain and wider bandwidths, respectively. Additionally, the aim was to overcome the challenges of improving the alignment and fixturing of their physical structure, as well as addressing the bonding between the ceramic DRA and feeding substrate layer by using 3D printing. Also, the air gaps exist among the layers that may affect the antenna performance substantially at high frequencies. Hence, innovative manufacturing methods like 3D printing of integrated DRA need to be identified to ensure that no air gaps exist between DRA and the feeding substrate.

A single element technique has been proven to be an effective technique for fixture and alignment of the DRA. Future studies can use arrays instead of single elements. Using arrays can further increase the gain, and using the technique proposed in Chapter 1 of this thesis, the fixture and alignment of the DRA would not be a concern.

The findings of this thesis have added to the literature of works and have also proposed techniques that could be implemented to overcome the challenges and to attain better results in terms of the CP bandwidth. Cross-slot feeding with unequal lengths was used in this thesis. One of the promising research fields that should be further investigated is the perforated hemispherical DRA with different kind of slots, like spiral and parasitic patch since the use of a hemispherical DRA with cross slot without the integration technique significantly limits the CP bandwidth. Therefore, studies should investigate suitable feeding techniques to improve the CP bandwidth while using perforated DRA. Furthermore, to facilitate the switching between the LP and CP, reconfigurable DRAs could be used. They can be useful in modern wireless systems, as studying them will be an interesting research topic in the future.

The single element MIMO technique has been implemented in chapter 4, and it has shown good results in terms of attaining improved isolation and dual band. To further improve the diversity performance and to overcome the constraints of the MIMO system at 5G and future applications, more elements can be used. For instance, 2x2 array, 4x4 array, and array MIMO can be used.

The 3D printing methodology increases the fabrication accuracy, which is particularly useful for antennas operating at around 40 GHz and 60 GHz, as their dimensions are very small to be fabricated precisely using chemical etching procedures. Thus, 3D printing has been used to demonstrate low-profile and multi-band characteristics. Different kinds of slots (square slot and annular slot) with a parasitic slot have been proposed in Chapter 5 using alumina material. Future studies can repeat the study using semi-conductive materials in compatible labs for fabrication. In addition to that, the array can be used instead of single elements to further improve the gain.

References

[1] R. Pethrick, D. Hayward, K. Jeffrey *et al.*, “Investigation of the hydration and dehydration of aluminium oxide-hydroxide using high frequency dielectric measurements between 300 kHz-3 GHz,” *Journal of materials science,* vol. 31, no. 10, pp. 2623-2629, 1996.

[2] J. S. Vardakas, I. T. Monroy, L. Wosinska *et al.*, "Towards high capacity and low latency backhauling in 5G: The 5G STEP-FWD vision." pp. 1-4.

[3] T. P. Budka, “Wide-bandwidth millimeter-wave bond-wire interconnects,” *IEEE Transactions on Microwave Theory and Techniques,* vol. 49, no. 4, pp. 715-718, 2001.

[4] A. V. Lopez, A. Chervyakov, G. Chance *et al.*, “Opportunities and Challenges of mmWave NR,” *IEEE Wireless Communications,* vol. 26, no. 2, pp. 4-6, 2019.

[5] T. S. Rappaport, S. Sun, R. Mayzus *et al.*, “Millimeter wave mobile communications for 5G cellular: It will work!,” *IEEE access,* vol. 1, pp. 335-349, 2013.

[6] M. T.S., A. 2022.09.05, and http://www.tst-sistemas.es/en/rd/miwaves/, 2022.

[7] S. R. Govindarajulu, and E. A. Alwan, "Range optimization for DSRC and 5G millimeter-wave vehicle-to-vehicle communication link." pp. 228-230.

[8] M. Medin, and G. Louie, *The 5G ecosystem: Risks and opportunities for DoD*, Defense Innovation Board Washington DC United States, 2019.

[9] E.-L. Li, and W.-J. Wang, “5G will drive the development of health care,” *Chinese Medical Journal,* vol. 132, no. 23, pp. 2895-2896, 2019.

[10] F. Giannetti, M. Luise, and R. Reggiannini, “Mobile and personal communications in the 60 GHz band: A survey,” *Wireless Personal Communications,* vol. 10, no. 2, pp. 207-243, 1999.

[11] A. Bani-Bakr, K. Dimyati, M. N. Hindia *et al.*, “Feasibility study of 28 GHz and 38 GHz millimeter-wave technologies for fog radio access networks using multi-slope path loss model,” *Physical Communication,* vol. 47, pp. 101401, 2021.

[12] Z. Qingling, and J. Li, "Rain attenuation in millimeter wave ranges." pp. 1-4.

[13] R. Richtmyer, “Dielectric resonators,” *Journal of applied physics,* vol. 10, no. 6, pp. 391-398, 1939.

[14] P. Rezaei, M. Hakkak, and K. Forooraghi, “Design of wide-band dielectric resonator antenna with a two-segment structure,” *Progress In Electromagnetics Research,* vol. 66, pp. 111-124, 2006.

[15] S. B. Cohn, “Microwave bandpass filters containing high-Q dielectric resonators,” *IEEE Transactions on microwave theory and techniques,* vol. 16, no. 4, pp. 218-227, 1968.

[16] S. Fiedziuszko, “Microwave dielectric resonators,” *Microwave Journal,* vol. 29, pp. 189-196, 1986.

[17] A. Okaya, and L. Barash, “The dielectric microwave resonator,” *Proceedings of the IRE,* vol. 50, no. 10, pp. 2081-2092, 1962.

[18] M. Gastine, L. Courtois, and J. L. Dormann, “Electromagnetic resonances of free dielectric spheres,” *IEEE Transactions on Microwave Theory and Techniques,* vol. 15, no. 12, pp. 694-700, 1967.

[19] D. Kajfez, and P. Guillon, “Dielectric resonators,” *Norwood*, 1986.

[20] J. Van Bladel, “On the resonances of a dielectric resonator of very high permittivity,” *IEEE Transactions on Microwave Theory and Techniques,* vol. 23, no. 2, pp. 199-208, 1975.

[21] J. Van Bladel, “The excitation of dielectric resonators of very high permittivity,” *IEEE Transactions on Microwave Theory and Techniques,* vol. 23, no. 2, pp. 208-217, 1975.

[22] D. Kajfez, A. W. Glisson, and J. James, “Computed modal field distributions for isolated dielectric resonators,” *IEEE transactions on Microwave Theory and Techniques,* vol. 32, no. 12, pp. 1609-1616, 1984.

[23] M. McAllister, and S. A. Long, “Resonant hemispherical dielectric antenna,” *Electronics Letters,* vol. 20, no. 16, pp. 657-659, 1984.

[24] M. McAllister, S. A. Long, and G. Conway, “Rectangular dielectric resonator antenna,” *Electronics letters,* vol. 19, pp. 218, 1983.

[25] A. Petosa, and A. Ittipiboon, “Dielectric resonator antennas: A historical review and the current state of the art,” *IEEE antennas and Propagation Magazine,* vol. 52, no. 5, pp. 91-116, 2010.

[26] X.-L. Liang, T. A. Denidni, and L.-N. Zhang, “Wideband L-shaped dielectric resonator antenna with a conformal inverted-trapezoidal patch feed,” *IEEE Transactions on Antennas and Propagation,* vol. 57, no. 1, pp. 271-274, 2009.

[27] L. Qinghua, G. Almpanis, C. Fumeaux *et al.*, “Comparison of the Radiation Efficiency for the Dielectric Resonator Antenna and the Microstrip Antenna at Ka Band,” *IEEE Transactions on Antennas and Propagation,* vol. 56, no. 11, pp. 3589-3592, 2008.

[28] Y.-M. Pan, K. W. Leung, and K.-M. Luk, “Design of the Millimeter-wave Rectangular Dielectric Resonator Antenna Using a Higher-Order Mode,” *IEEE Transactions on Antennas and Propagation,* vol. 59, no. 8, pp. 2780-2788, 2011.

[29] A. A. Abdulmajid, S. Khamas, and S. Zhang, “Wideband High-gain millimetre-wave three-layer hemispherical dielectric resonator antenna,” *Progress In Electromagnetics Research C,* vol. 103, pp. 225-236, 2020.

[30] I. A. Zubir, M. Othman, U. Ullah *et al.*, “A Low-Profile Hybrid Multi-Permittivity Dielectric Resonator Antenna With Perforated Structure for Ku and K Band Applications,” *IEEE Access,* vol. 8, pp. 151219-151228, 2020.

[31] E. Baldazzi, A. Al-Rawi, R. Cicchetti *et al.*, “A High-Gain Dielectric Resonator Antenna With Plastic-Based Conical Horn for Millimeter-Wave Applications,” *IEEE Antennas and Wireless Propagation Letters,* vol. 19, no. 6, pp. 949-953, 2020.

[32] M.-R. Nezhad-Ahmadi, M. Fakharzadeh, B. Biglarbegian *et al.*, “High-Efficiency On-Chip Dielectric Resonator Antenna for mm-Wave Transceivers,” *IEEE Transactions on Antennas and Propagation,* vol. 58, no. 10, pp. 3388-3392, 2010.

[33] K. Gong, and X. H. Hu, “Low-Profile Substrate Integrated Dielectric Resonator Antenna Implemented With PCB Process,” *IEEE Antennas and Wireless Propagation Letters,* vol. 13, pp. 1023-1026, 2014.

[34] M. Mrnka, M. Cupal, Z. Raida *et al.*, "Millimeter-wave directive dielectric resonator antenna based on LTCC." pp. 1-4.

[35] W. M. A. Wahab, D. Busuioc, and S. Safavi-Naeini, “Low Cost Planar Waveguide Technology-Based Dielectric Resonator Antenna (DRA) for Millimeter-Wave Applications: Analysis, Design, and Fabrication,” *IEEE Transactions on Antennas and Propagation,* vol. 58, no. 8, pp. 2499-2507, 2010.

[36] W. M. Abdel-Wahab, Y. Wang, and S. Safavi-Naeini, “SIW Hybrid Feeding Network-Integrated 2-D DRA Array: Simulations and Experiments,” *IEEE Antennas and Wireless Propagation Letters,* vol. 15, pp. 548-551, 2016.

[37] W. M. Abdel-Wahab, M. Abdallah, J. Anderson *et al.*, “SIW-Integrated Parasitic DRA Array: Analysis, Design, and Measurement,” *IEEE Antennas and Wireless Propagation Letters,* vol. 18, no. 1, pp. 69-73, 2019.

[38] W. Mazhar, D. M. Klymyshyn, G. Wells *et al.*, “Low-Profile Artificial Grid Dielectric Resonator Antenna Arrays for mm-Wave Applications,” *IEEE Transactions on Antennas and Propagation,* vol. 67, no. 7, pp. 4406-4417, 2019.

[39] W. M. Abdel-Wahab, D. Busuioc, and S. Safavi-Naeini, “Millimeter-Wave High Radiation Efficiency Planar Waveguide Series-Fed Dielectric Resonator Antenna (DRA) Array: Analysis,

Design, and Measurements," *IEEE Transactions on Antennas and Propagation,* vol. 59, no. 8, pp. 2834-2843, 2011.

[40] M. Niayesh, and A. Kouki, "LTCC-Integrated Dielectric Resonant Antenna Array for 5G Applications," *Sensors (Basel),* vol. 21, no. 11, May 31, 2021.

[41] M. Mrnka, M. Cupal, Z. Raida *et al.*, "Millimetre-wave dielectric resonator antenna array based on directive LTCC elements," *IET Microwaves, Antennas & Propagation,* vol. 12, no. 5, pp. 662-667, 2018.

[42] W. Luo, L. Shi, W. Xu *et al.*, "High Gain Dielectric Resonance Antenna Array for Millimeter Wave Vehicular Wireless Communication," *Progress In Electromagnetics Research,* vol. 108, pp. 63-78, 2021.

[43] Y.-T. Liu, B. Ma, S. Huang *et al.*, "Wideband Low-Profile Connected Rectangular Ring Dielectric Resonator Antenna Array for Millimeter-Wave Applications," *IEEE Transactions on Antennas and Propagation*, 2022.

[44] A. Perron, T. A. Denidni, and A. R. Sebak, "High-Gain Hybrid Dielectric Resonator Antenna for Millimeter-Wave Applications: Design and Implementation," *IEEE Transactions on Antennas and Propagation,* vol. 57, no. 10, pp. 2882-2892, 2009.

[45] M. O. Sallam, M. Serry, S. Sedky *et al.*, "Micromachined On-Chip Dielectric Resonator Antenna Operating at 60 GHz," *IEEE Transactions on Antennas and Propagation,* vol. 63, no. 8, pp. 3410-3416, 2015.

[46] L. Ohlsson, T. Bryllert, C. Gustafson *et al.*, "Slot-Coupled Millimeter-Wave Dielectric Resonator Antenna for High-Efficiency Monolithic Integration," *IEEE Transactions on Antennas and Propagation,* vol. 61, no. 4, pp. 1599-1607, 2013.

[47] M. D. Ardakani, M. Farahani, M. Akbari *et al.*, "A Compact Wideband Cubic Dielectric Resonator Antenna for Integrated 60-GHz MHMIC Short-range Transceivers," in 2020 IEEE International Symposium on Antennas and Propagation and North American Radio Science Meeting, 2020, pp. 71-72.

[48] Z. Chen, C. Shen, H. Liu *et al.*, "Millimeter-Wave Rectangular Dielectric Resonator Antenna Array With Enlarged DRA Dimensions, Wideband Capability, and High-Gain Performance," *IEEE Transactions on Antennas and Propagation,* vol. 68, no. 4, pp. 3271-3276, 2020.

[49] A. A. Qureshi, D. M. Klymyshyn, M. Tayfeh *et al.*, "Template-Based Dielectric Resonator Antenna Arrays for Millimeter-Wave Applications," *IEEE Transactions on Antennas and Propagation,* vol. 65, no. 9, pp. 4576-4584, 2017.

[50] A. Dadgarpour, B. Zarghooni, B. S. Virdee *et al.*, "Mutual Coupling Reduction in Dielectric Resonator Antennas Using Metasurface Shield for 60-GHz MIMO Systems," *IEEE Antennas and Wireless Propagation Letters,* vol. 16, pp. 477-480, 2017.

[51] M. Farahani, J. Pourahmadazar, M. Akbari *et al.*, "Mutual Coupling Reduction in Millimeter-Wave MIMO Antenna Array Using a Metamaterial Polarization-Rotator Wall," *IEEE Antennas and Wireless Propagation Letters,* vol. 16, pp. 2324-2327, 2017.

[52] R. Karimian, A. Kesavan, M. Nedil *et al.*, "Low-Mutual-Coupling 60-GHz MIMO Antenna System With Frequency Selective Surface Wall," *IEEE Antennas and Wireless Propagation Letters,* vol. 16, pp. 373-376, 2017.

[53] Y. M. Pan, X. Qin, Y. X. Sun *et al.*, "A simple decoupling method for 5G millimeter-wave MIMO dielectric resonator antennas," *IEEE Transactions on Antennas and Propagation,* vol. 67, no. 4, pp. 2224-2234, 2019.

[54] Y. Zhang, J.-Y. Deng, M.-J. Li *et al.*, "A MIMO Dielectric Resonator Antenna With Improved Isolation for 5G mm-Wave Applications," *IEEE Antennas and Wireless Propagation Letters,* vol. 18, no. 4, pp. 747-751, 2019.

[55] M. S. Sharawi, S. K. Podilchak, M. T. Hussain *et al.*, "Dielectric resonator based MIMO antenna system enabling millimetre-wave mobile devices," *IET Microwaves, Antennas & Propagation,* vol. 11, no. 2, pp. 287-293, 2017.

[56] N. K. Sahu, and R. K. Gangwar, “Dual-Port Compact MIMO-DRAs: Exploiting Metallic Sheets to Increase Inter-Port Isolation at 28 GHz 5G-Band,” *IEEE Transactions on Circuits and Systems II: Express Briefs*, 2022.

[57] H. Chu, and Y.-X. Guo, “A Novel Approach for Millimeter-Wave Dielectric Resonator Antenna Array Designs by Using the Substrate Integrated Technology,” *IEEE Transactions on Antennas and Propagation,* vol. 65, no. 2, pp. 909-914, 2017.

[58] A. A. Abdulmajid, S. Khamas, and S. Zhang, “Wide bandwidth high gain circularly polarized millimetre-wave rectangular dielectric resonator antenna,” *Progress In Electromagnetics Research M,* vol. 89, pp. 171-177, 2020.

[59] M.-D. Yang, Y.-M. Pan, Y.-X. Sun *et al.*, “Wideband Circularly Polarized Substrate-Integrated Embedded Dielectric Resonator Antenna for Millimeter-Wave Applications,” *IEEE Transactions on Antennas and Propagation,* vol. 68, no. 2, pp. 1145-1150, 2020.

[60] A. Kesavan, M. Al-Hassan, I. Ben Mabrouk *et al.*, “Wideband Circular Polarized Dielectric Resonator Antenna Array for Millimeter-Wave Applications,” *Sensors (Basel),* vol. 21, no. 11, May 22, 2021.

[61] A. Bansal, and A. Vaish, “Deminiaturized mode control rectangular dielectric resonator antenna,” *Progress In Electromagnetics Research,* vol. 86, pp. 173-182, 2016.

[62] A. Gaya, M. H. Jamaluddin, B. Alali *et al.*, “A novel wide dual band circularly polarized dielectric resonator antenna for milli meter wave 5G applications,” *Alexandria Engineering Journal,* vol. 61, no. 12, pp. 10791-10803, 2022.

[63] G. Zhao, Y. Zhou, J. R. Wang *et al.*, “A Circularly Polarized Dielectric Resonator Antenna Based on Quasi-Self-Complementary Metasurface,” *IEEE Transactions on Antennas and Propagation*, 2022.

[64] H. Xu, Z. Chen, H. Liu *et al.*, “Single-Fed Dual-Circularly polarized Stacked Dielectric Resonator Antenna for K/Ka-Band UAV Satellite Communications,” *IEEE Transactions on Vehicular Technology,* vol. 71, no. 4, pp. 4449-4453, 2022.

[65] L. Qinghua, C. Fumeaux, H. Wei *et al.*, “60 GHz Aperture-Coupled Dielectric Resonator Antennas Fed by a Half-Mode Substrate Integrated Waveguide,” *IEEE Transactions on Antennas and Propagation,* vol. 58, no. 6, pp. 1856-1864, 2010.

[66] Y.-X. Sun, and K. W. Leung, “Circularly Polarized Substrate-Integrated Cylindrical Dielectric Resonator Antenna Array for 60 GHz Applications,” *IEEE Antennas and Wireless Propagation Letters,* vol. 17, no. 8, pp. 1401-1405, 2018.

[67] W. Lin, R. W. Ziolkowski, and T. C. Baum, “28 GHz compact omnidirectional circularly polarized antenna for device-to-device communications in the future 5G systems,” *IEEE Transactions on Antennas and Propagation,* vol. 65, no. 12, pp. 6904-6914, 2017.

[68] W. Hong, “Solving the 5G mobile antenna puzzle: Assessing future directions for the 5G mobile antenna paradigm shift,” *IEEE microwave magazine,* vol. 18, no. 7, pp. 86-102, 2017.

[69] I. Ali, M. H. Jamaluddin, A. Gaya *et al.*, “A dielectric resonator antenna with enhanced gain and bandwidth for 5G applications,” *sensors,* vol. 20, no. 3, pp. 675, 2020.

[70] W. El-Halwagy, R. Mirzavand, J. Melzer *et al.*, "A substrate-integrated fan-beam dipole antenna with varied fence shape for mm-wave 5G wireless." pp. 251-252.

[71] J. Yin, Q. Wu, C. Yu *et al.*, “Broadband symmetrical E-shaped patch antenna with multimode resonance for 5G millimeter-wave applications,” *IEEE Transactions on Antennas and Propagation,* vol. 67, no. 7, pp. 4474-4483, 2019.

[72] J. Wang, Y. Li, and J. Wang, "Millimeter-Wave Low-Profile Wideband Magneto-Electric Monopole Antenna." pp. 1-2.

[73] A. Petosa, A. Ittipiboon, Y. Antar *et al.*, “Recent advances in dielectric-resonator antenna technology,” *IEEE Antennas and Propagation Magazine,* vol. 40, no. 3, pp. 35-48, 1998.

[74] H. I. Kremer, K. W. Leung, W. C. Wong *et al.*, “Design of dielectric resonator antenna using dielectric paste,” *Sensors,* vol. 21, no. 12, pp. 4058, 2021.

[75] E. K. Chemweno, P. Kumar, and T. J. Afullo, “Substrate Integrated Waveguide-Dielectric Resonator Antenna for Future Wireless Communication,” *SAIEE Africa Research Journal,* vol. 113, no. 3, pp. 119-128, 2022.

[76] J. Wen, Y. C. Jiao, Y. X. Zhang *et al.*, “Wideband circularly polarized dielectric resonator antenna loaded with partially reflective surface,” *International Journal of RF and Microwave Computer-Aided Engineering,* vol. 29, no. 12, pp. e21962, 2019.

[77] R. n. D. G. Enriquez, F. GallÉe, and C. Kärnfelt, "Novel 60 GHz DRA topology adapted to the LTCC process."

[78] G. A. Sarkar, S. Ballav, A. Chatterjee *et al.*, “Four element MIMO DRA with high isolation for WLAN applications,” *Progress In Electromagnetics Research Letters,* vol. 84, pp. 99-106, 2019.

[79] C. Sarkar, D. Guha, and C. Kumar, “Glueless Compound Ground Technique for Dielectric Resonator Antenna and Arrays,” *IEEE Antennas and Wireless Propagation Letters,* vol. 16, pp. 2440-2443, 2017.

[80] Z.-X. Xia, K. W. Leung, and K. Lu, “3-D-Printed Wideband Multi-Ring Dielectric Resonator Antenna,” *IEEE Antennas and Wireless Propagation Letters,* vol. 18, no. 10, pp. 2110-2114, 2019.

[81] M. Liang, W.-R. Ng, K. Chang *et al.*, “A 3-D Luneburg lens antenna fabricated by polymer jetting rapid prototyping,” *IEEE Transactions on Antennas and Propagation,* vol. 62, no. 4, pp. 1799-1807, 2014.

[82] T. S. Rappaport, and D. A. Hawbaker, “Wide-band microwave propagation parameters using circular and linear polarized antennas for indoor wireless channels,” *IEEE Transactions on Communications,* vol. 40, no. 2, pp. 240-245, 1992.

[83] R. K. Chaudhary, R. Kumar, and R. Chowdhury, *Circularly Polarized Dielectric Resonator Antennas*: Artech House, 2021.

[84] K. Leung, “Efficient computation for the general solution of a slot loaded by a hemispherical dielectric and/or backing cavity,” *IEEE Transactions on Antennas and Propagation,* vol. 50, no. 12, pp. 1859-1862, 2002.

[85] L. Kwok Wa, and N. Hoi Kuen, “The slot-coupled hemispherical dielectric resonator antenna with a parasitic patch: applications to the circularly polarized antenna and wide-band antenna,” *IEEE Transactions on Antennas and Propagation,* vol. 53, no. 5, pp. 1762-1769, 2005.

[86] K. W. Leung, and H. K. Ng, “Theory and experiment of circularly polarized dielectric resonator antenna with a parasitic patch,” *IEEE Transactions on Antennas and Propagation,* vol. 51, no. 3, pp. 405-412, 2003.

[87] Z. Qian, K. Leung, and R.-S. Chen, “Analysis of circularly polarized dielectric resonator antenna excited by a spiral slot,” *Progress In Electromagnetics Research,* vol. 47, pp. 111-121, 2004.

[88] K. Leung, and K. So, “Frequency-tunable designs of the linearly and circularly polarized dielectric resonator antennas using a parasitic slot,” *IEEE Transactions on Antennas and Propagation,* vol. 53, no. 1, pp. 572-578, 2005.

[89] K. Leung, “Circularly polarized dielectric resonator antenna excited by a shorted annular slot with a backing cavity,” *IEEE transactions on antennas and propagation,* vol. 52, no. 10, pp. 2765-2770, 2004.

[90] K. So, K. Leung, and H. Ng, "Frequency design of the circularly polarized dielectric resonator antenna." pp. 1090-1093.

[91] H. Lam, and K. Leung, “Analysis of U-slot-excited dielectric resonator antennas with a backing cavity,” *IEE Proceedings-Microwaves, Antennas and Propagation,* vol. 153, no. 5, pp. 480-482, 2006.

[92] R. K. Mongia, and A. Ittipiboon, “Theoretical and experimental investigations on rectangular dielectric resonator antennas,” *IEEE Transactions on antennas and propagation,* vol. 45, no. 9, pp. 1348-1356, 1997.

[93] I. Nadeem, and D.-Y. Choi, “Study on mutual coupling reduction technique for MIMO antennas,” *IEEE Access,* vol. 7, pp. 563-586, 2018.

[94] V. Kuhn, *Wireless communications over MIMO channels: applications to CDMA and multiple antenna systems*: John Wiley & Sons, 2006.

[95] Z. Wani, M. P. Abegaonkar, and S. K. Koul, “A 28-GHz antenna for 5G MIMO applications,” *Progress In Electromagnetics Research Letters,* vol. 78, pp. 73-79, 2018.

[96] N. Hussain, M.-J. Jeong, J. Park *et al.*, “A broadband circularly polarized fabry-perot resonant antenna using a single-layered PRS for 5G MIMO applications,” *IEEE Access,* vol. 7, pp. 42897-42907, 2019.

[97] M. Khalid, S. Iffat Naqvi, N. Hussain *et al.*, “4-Port MIMO antenna with defected ground structure for 5G millimeter wave applications,” *Electronics,* vol. 9, no. 1, pp. 71, 2020.

[98] S. F. Jilani, and A. Alomainy, “Millimetre-wave T-shaped MIMO antenna with defected ground structures for 5G cellular networks,” *IET Microwaves, Antennas & Propagation,* vol. 12, no. 5, pp. 672-677, 2018.

[99] A. Sharma, A. Sarkar, M. Adhikary *et al.*, "SIW fed MIMO DRA for future 5G applications." pp. 1763-1764.

[100] A. Sharma, and A. Biswas, “Wideband multiple-input–multiple-output dielectric resonator antenna,” *IET Microwaves, Antennas & Propagation,* vol. 11, no. 4, pp. 496-502, 2017.

[101] G. Das, A. Sharma, R. Gangwar *et al.*, “Compact back-to-back DRA-based four-port MIMO antenna system with bi-directional diversity,” *Electronics Letters,* vol. 54, no. 14, pp. 884-886, 2018.

[102] J. Mu'Ath, T. A. Denidni, and A. R. Sebak, “Millimeter-wave compact EBG structure for mutual coupling reduction applications,” *IEEE Transactions on Antennas and Propagation,* vol. 63, no. 2, pp. 823-828, 2014.

[103] R. Karimian, A. Kesavan, M. Nedil *et al.*, “Low-mutual-coupling 60-GHz MIMO antenna system with frequency selective surface wall,” *IEEE Antennas and Wireless Propagation Letters,* vol. 16, pp. 373-376, 2016.

[104] M. D. Alanazi, and S. K. Khamas, "On-Chip Multiband MIMO Dielectric Resonator Antenna for MillimeterWave Applications." pp. 174-177.

[105] G. Das, A. Sharma, R. K. Gangwar *et al.*, “Performance improvement of multiband MIMO dielectric resonator antenna system with a partially reflecting surface,” *IEEE Antennas and Wireless Propagation Letters,* vol. 18, no. 10, pp. 2105-2109, 2019.

[106] G. Das, N. K. Sahu, A. Sharma *et al.*, “FSS-based spatially decoupled back-to-back four-port MIMO DRA with multidirectional pattern diversity,” *IEEE Antennas and Wireless Propagation Letters,* vol. 18, no. 8, pp. 1552-1556, 2019.

[107] A. Sharma, G. Das, and R. K. Gangwar, “Dual polarized triple band hybrid MIMO cylindrical dielectric resonator antenna for LTE2500/WLAN/WiMAX applications,” *International Journal of RF and Microwave Computer-Aided Engineering,* vol. 26, no. 9, pp. 763-772, 2016.

[108] A. Sharma, G. Das, and R. K. Gangwar, “Design and analysis of tri-band dual-port dielectric resonator based hybrid antenna for WLAN/WiMAX applications,” *IET Microwaves, Antennas & Propagation,* vol. 12, no. 6, pp. 986-992, 2018.

[109] A. M. Al-Samman, T. A. Rahman, M. N. Hindia *et al.*, “Path loss model for outdoor parking environments at 28 GHz and 38 GHz for 5G wireless networks,” *Symmetry,* vol. 10, no. 12, pp. 672, 2018.

[110] A. Patnaik, and M. Kartikeyan, “Compact dual and triple band antennas for 5G-IOT applications,” *International Journal of Microwave and Wireless Technologies,* vol. 14, no. 1, pp. 115-122, 2022.

[111] M. Zou, and J. Pan, “Investigation of a cross-slot-coupled dual-band circularly polarized hybrid dielectric resonator antenna,” *Progress In Electromagnetics Research C,* vol. 53, pp. 187-195, 2014.

[112] R. Shao, X. Chen, J. Wang *et al.*, “Design and Analysis of an Eight-Port Dual-Polarized High-Efficiency Shared-Radiator MIMO Antenna for 5G Mobile Devices,” *Electronics,* vol. 11, no. 10, pp. 1628, 2022.

[113] S. Gregson, J. McCormick, and C. Parini, *Principles of planar near-field antenna measurements*: IET, 2007.

[114] S.-H. Kim, and J.-Y. Chung, “Analysis of the envelope correlation coefficient of MIMO antennas connected with suspended lines,” *Journal of Electromagnetic Engineering and Science,* vol. 20, no. 2, pp. 83-90, 2020.

[115] P. Sharda, and M. R. Bhatnagar, “Diversity-multiplexing tradeoff for MIMO-FSO system under different transmission scenarios with limited quantized feedback,” *IEEE Access,* vol. 8, pp. 114266-114286, 2020.

[116] S. Pandit, A. Mohan, and P. Ray, “A compact four-element MIMO antenna for WLAN applications,” *Microwave and Optical Technology Letters,* vol. 60, no. 2, pp. 289-295, 2018.

[117] R. Hussain, M. Abou-Khousa, N. Iqbal *et al.*, “A Multiband Shared Aperture MIMO Antenna for Millimeter-Wave and Sub-6GHz 5G Applications,” *Sensors,* vol. 22, no. 5, pp. 1808, 2022.

[118] M. Morsy, “4-Port Planar MIMO Antenna Using Open-Slot Radiators for 5G New Radio (NR) Frequency Bands n38 (2570 to 2620 MHz) and n41 (2496 MHz–2690 MHz) Applications,” *Progress In Electromagnetics Research Letters,* vol. 104, pp. 87-94, 2022.

[119] W. Yin, S. Chen, J. Chang *et al.*, “CPW fed compact UWB 4-element MIMO antenna with high isolation,” *Sensors,* vol. 21, no. 8, pp. 2688, 2021.

[120] D. Fritsche, G. Tretter, C. Carta *et al.*, “Millimeter-wave low-noise amplifier design in 28-nm low-power digital CMOS,” *IEEE Transactions on Microwave Theory and Techniques,* vol. 63, no. 6, pp. 1910-1922, 2015.

[121] A. Kapoor, and G. Singh, “Mode classification in cylindrical dielectric waveguides,” *Journal of lightwave technology,* vol. 18, no. 6, pp. 849-852, 2000.

[122] K. M. L. a. K. W. Leung, *Dielectric resonator antennas*, Baldock, Hertfordshire, England; Philadelphia, PA; Williston, VT: Research Studies Press Distribution,North America [by] AIDC, 2003.

[123] J. Sethares, and S. Naumann, “Design of microwave dielectric resonators,” *IEEE Transactions on Microwave Theory and Techniques,* vol. 14, no. 1, pp. 2-7, 1966.

[124] S. Long, M. McAllister, and L. Shen, “The resonant cylindrical dielectric cavity antenna,” *IEEE Transactions on Antennas and Propagation,* vol. 31, no. 3, pp. 406-412, 1983.

[125] R. De Smedt, “Correction due to a finite permittivity for a ring resonator in free space,” *IEEE transactions on microwave theory and techniques,* vol. 32, no. 10, pp. 1288-1293, 1984.

[126] M. Tsuji, H. Shigesawa, and K. Takiyama, “Analytical and experimental investigations on several resonant modes in open dielectric resonators,” *IEEE transactions on microwave theory and techniques,* vol. 32, no. 6, pp. 628-633, 1984.

[127] M. Riaziat, R. Majidi-Ahy, and I.-J. Feng, “Propagation modes and dispersion characteristics of coplanar waveguides,” *IEEE transactions on microwave theory and techniques,* vol. 38, no. 3, pp. 245-251, 1990.

[128] S. Fakhte, H. Oraizi, and R. Karimian, “A novel low-cost circularly polarized rotated stacked dielectric resonator antenna,” *IEEE Antennas and Wireless Propagation Letters,* vol. 13, pp. 722-725, 2014.

[129] K. So, and K. Leung, “Bandwidth enhancement and frequency tuning of the dielectric resonator antenna using a parasitic slot in the ground plane,” *IEEE Transactions on Antennas and Propagation,* vol. 53, no. 12, pp. 4169-4172, 2005.